UNIVERSITY OF OKLAHOMA

GRADUATE COLLEGE

THE ATMOSPHERIC IMAGING RADAR FOR HIGH RESOLUTION OBSERVATIONS OF SEVERE WEATHER

A DISSERTATION

SUBMITTED TO THE GRADUATE FACULTY

in partial fulfillment of the requirements for the

Degree of

DOCTOR OF PHILOSOPHY

By

BRADLEY ISOM
Norman, Oklahoma
2012

THE ATMOSPHERIC IMAGING RADAR FOR HIGH RESOLUTION OBSERVATIONS OF SEVERE WEATHER

A DISSERTATION APPROVED FOR THE
SCHOOL OF ELECTRICAL AND COMPUTER ENGINEERING

BY

Dr. Robert Palmer, Chair

Dr. Mark Yeary

Dr. Tian-You Yu

Dr. Yan Zhang

Dr. Richard Doviak

Dr. Michael Biggerstaff

Dedication

For my loving wife, Lacy Dawn

Acknowledgments

First and foremost I must thank my wife, Lacy, for her support and love throughout my time in graduate school. Thank you for understanding the purpose of this journey and reminding me that the sacrifice and investment was worth it. I can't wait to find out what new adventures life will bring us and know that whatever it is, I am extremely lucky to get to share it with you.

I also thank my parents, Janet and Ed Isom, for giving me the values and metrics by which I define my life today. I learned to work hard, but also enjoy the small things in life. I learned to be humble and be thankful for what I have. My love of science and engineering was encouraged and, though my path wasn't always the straightest, I could always count you to support me. Also, my sister, Kim "Mimi" Isom, thank you for lifting my spirits when no one else could.

I thank my grandparents, June and Dalbert Isom and Frank and Eula-Jean Roberts. I am extremely proud of my Nebraska/Iowa heritage and am thankful for my blue eyes, the summer school sessions in Gowrie, and sharing my birthday with Grandma Roberts.

I thank my late father-in-law, Jay Anderson, for his Saturday decompression cochon de laits, infinite generosity, and more perfectly cooked steaks than I can count. I miss you Jay.

Next I must thank my advisor and mentor, Dr. Robert Palmer. You spotted something in me that few people saw in Nebraska and set me on a path to success. I have enjoyed being a part of a program that gives students opportunities that

few universities offer. I gained a tremendous amount of knowledge from you, not only in engineering and science, but in work ethic, dissemination, and numerous other professional skills. I owe my future successes to your guidance and support.

I thank my committee members, Dr. Tian-You Yu, Dr. Mark "Bradley" Yeary, Dr. Yan "Rockee" Zhang, Dr. Michael Biggerstaff, and Dr. Richard Doviak. I have enjoyed working with each of you and appreciate your help and support, not only with the AIR project, but with my education and professional career. I look forward to continued contact and collaborations.

I thank the team of students and staff that helped make the AIR happen. Without the support of this stellar group of people, this project would not have been a success. I sincerely appreciate all of your help and thank you for your efforts.

And finally I thank my buddies from Omaha who define the meaning of friendship -Bones-

Table of Contents

List Of Tables

List Of Figures

Abstract

Mobile weather radars often utilize rapid scan strategies when collecting observations of severe weather. Various techniques have been used to improve volume update times, including the use of agile and multi-beam radars. Imaging radars, similar in some respects to phased arrays, steer the radar beam in software, thus requiring no physical motion. In contrast to phased arrays, imaging radars gather data for an entire volume simultaneously within the field-of-view of the radar, which is defined by a broad transmit beam. As a result, imaging radars provide update rates significantly exceeding those of existing mobile radars, including phased arrays. The Atmospheric Radar Research Center at the University of Oklahoma is engaged in the design, construction and testing of a mobile imaging weather radar system called the Atmospheric Imaging Radar (AIR).

Initial tests performed with the AIR demonstrate the benefits and versatility of utilizing beamforming techniques to achieve high spatial and temporal resolution. Specifically, point target analysis was performed using several digital beamforming techniques. Adaptive algorithms allow for the improved resolution and clutter rejection when compared to traditional techniques. Additional experiments were conducted during three severe weather events in Oklahoma, including an isolated cell event with high surface winds, a squall line, and a non-tornadic cyclone. Several digital beamforming techniques were tested and analyzed, producing unique, simultaneous multi-beam measurements using the AIR.

The author made specific contributions to the field of radar meteorology in several areas. Overseeing the design and construction of the AIR was a significant effort and involved the coordination of many smaller teams. Interacting with the members of each group and ensuring the success of the project was a primary focus throughout the venture. Meteorological imaging radars of the past have typically focused on boundary layer or upper atmospheric phenomena. The AIR's primary focus is to collect precipitation data from severe weather. Applying well defined beamforming techniques, ranging from Fourier to adaptive algorithms like robust Capon and Amplitude and Phase Estimation (APES), to precipitation phenomena was a unique effort and has served to advance the use of adaptive array processing in radar meteorology. Exploration of irregular antenna spacing and drawing from the analogies between temporal and spatial processing led to the development of a technique that reduced the impact of grating lobes by unwrapping angular ambiguities. Ultimately, the author leaves having created a versatile platform capable of producing some of the highest resolution weather data available in the research community today, with opportunities to significantly advance the understanding of rapidly evolving weather phenomena and severe storms.

Chapter 1

Introduction

1.1 The Atmosphere: A Brief Review

The atmosphere that surrounds the earth's surface is layered. If a gas-filled balloon equipped with temperature and pressure recording devices, called a radiosonde, were to be released at the surface and allowed to rise through each layer, the data would appear similar to the diagram given in Figure 1.1. Isothermal regions denote transitions from one layer to another (Wallace and Hobbs 1977; Ahrens 2007). Each layer also has a temperature trend called a lapse rate, or the rate of temperature change per unit height. For the troposphere, the average lapse rate is approximately 6.5° C km^{-1} (Ahrens 2007). By looking at the pressure change with height and the ideal gas law:

$$\mathsf{P} = \rho \mathcal{R} \mathsf{T}, \tag{1.1}$$

where P is pressure, ρ is density, $\mathcal{R}$ is the individual gas constant and T is temperature, it is apparent that the temperature is proportional to pressure, and thus should decrease with height (Rogers and Yau 1989). The individual gas constant is calculated by dividing the universal gas constant, 8.314 J mole^{-1} K^{-1}, by the molecular weight of the gas. In the case of dry air, this is found to be 28.96 g/mole, making $\mathcal{R}$ = 287 J kg^{-1} K^{-1}. One may notice, though, that for two of the layers, the stratosphere and thermosphere, temperature increases with

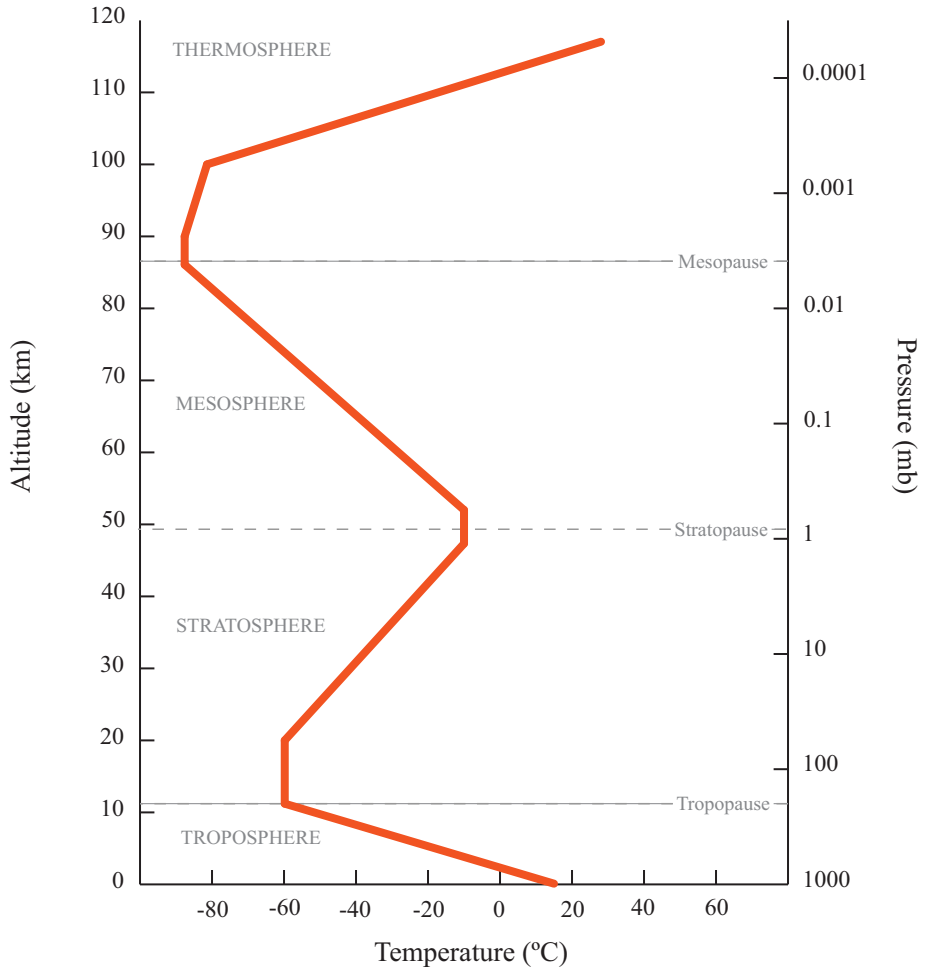

Figure 1.1: An illustration of the vertical temperature (left axis) and pressure (right axis) profile of the earth's atmosphere (Wallace and Hobbs 1977; Ahrens 2007). The four distinct layers are separated by isothermal regions denoted by the tropopause, stratopause and mesopause. While each layer has its own properties, the troposphere is of primary importance to this work due to the formation of clouds, precipitation and severe weather, all of which affect people and their day-to-day activities.

height. For the stratosphere, this increase in temperature is caused by the absorption of solar radiation at ultraviolet wavelengths by the large quantities of ozone (O_3) (Ahrens 2007). In the thermosphere, the temperature increase can be attributed to the large mean free path, or distance between molecules, and the oxygen (O_2) molecules' ability to absorb energetic solar rays (Wallace and Hobbs 1977; Ahrens 2007).

It is also important to note that the molecular makeup of the atmosphere is essential to understanding and predicting how it reacts to different conditions and variables. As a reference, a table of molecules found in the earth's atmosphere and their concentrations are given in Table 1.1.

Table 1.1: Composition of Earth's Atmosphere

STEADY STATE GASES			**TRANSIENT GASES**		
		Percent (by Volume)			**Percent**
Gas	**Symbol**	**Dry Air**	**Gas (and Particles)**	**Symbol**	**(by Volume)**
Nitrogen	N_2	78.08	Water Vapor	H_2O	0 to 4
Oxygen	O_2	20.95	Carbon Dioxide	CO_2	0.038
Argon	Ar	0.93	Methane	CH_4	0.00017
Neon	Ne	0.0018	Nitrous Oxide	N_2O	0.00003
Helium	He	0.0005	Ozone	O_3	0.000004
Hydrogen	H_2	0.00006	Dust/Soot		0.000001
Xenon	Xe	0.000009	Chloroflourocarbons		0.00000002

Through Figure 1.1, it has been illustrated how the concentration of ozone can increase the temperature of a volume despite a drop in pressure. Another molecule is water vapor, or H_2O, one of the most important present in the earth's atmosphere and directly affects the generation of clouds, precipitation and severe weather. Water can exist in all three physical states within the realm of the earth's atmosphere. As a gas, water vapor causes air to become more buoyant than it would be otherwise (H_2O is less dense than both Nitrogen and Oxygen).

Given the fact that liquid water will be formed as water vapor cools and, as a result, releases latent heat, a parcel of air rising through the atmosphere will not decrease in temperature as quickly as it would were it absent of H_2O. This difference is denoted by the reference to the dry adiabatic and moist adiabatic lapse rates, where the dry rate is 10° C km^{-1} and the moist is at a lower rate, around 5° C km^{-1} (Rogers and Yau 1989; Ahrens 2007). Similarly, as a parcel is lowered, the water will evaporate, absorbing heat and causing the temperature to increase at a rate slower than 10° C km^{-1}. An adiabatic process is one in which the parcel of air changes pressure or temperature without exchanging energy with its surroundings. This is a useful definition for thought experiments and in fact is used in forecasting and severe weather warning via the examination of Skew-T and Stüve diagrams.

Due to the difference between dry and moist lapse rates, the atmosphere can exist in one of several states denoted by the stability of the system. An illustration given in Figure 1.2 will help in the understanding of this principle. As previously stated, the moist adiabatic lapse rate is lower than the dry lapse rate. Thus, depending on the actual environmental lapse rate measured by radiosondes, the environment can be stable, conditionally unstable, or unstable, denoted by the blue, yellow and red regions in Figure 1.2, respectively (Rogers and Yau 1989; Ahrens 2007). For example, if the environmental lapse rate is located in the red region, and a parcel of air is lifted at either the dry or moist adiabatic rates, the parcel will always be warmer than the surrounding air and will thus be more buoyant and would rise. Similar experiments can be conducted with the aid of the figure by varying the location and shape of the environmental profile. It is through these definitions that environmental conditions are identified at any given time, which is essentially the definition of weather (Ahrens 2007).

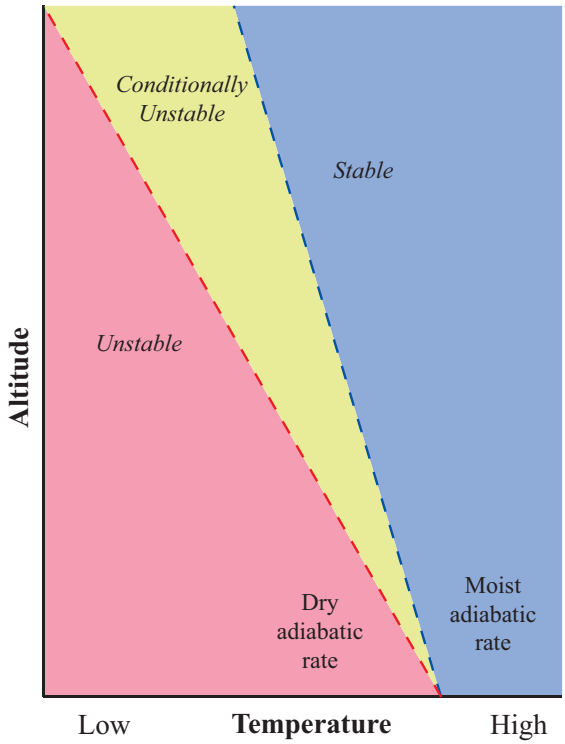

Figure 1.2: An illustration depicting the possible states of the atmosphere. The blue region denotes an unconditionally stable state. That is, if the environmental lapse rate were to exist within the blue zone, a parcel of air lifted at either the dry or moist adiabatic rate would always be cooler than the environment and would sink back to the ground. Similar experiments can be conducted with both the unstable red and conditionally unstable yellow regions.

As parcels rise, the water vapor in the air will condense and form liquid water droplets. These droplets (0.01 to 0.1 mm radius) aggregate and coalesce to form larger drops (0.1 to 4 mm radius) (Rogers and Yau 1989). If the temperature is cold enough, the solid form of H_2O, ice, forms instead. Once the drops or ice particles have reached sufficient size to overcome gravity and vertical winds, they begin to descend and fall to the surface of the earth as precipitation. Rain, snow, hail and sleet are some of the many forms of precipitation that can have significant, if not extreme, impacts on peoples' lives. It is this that prompted the desire and need to detect and monitor these phenomena that occur on a daily basis within the earth's atmosphere.

Radiosondes are one method for retrieving information that can aid in the understanding and prediction of the weather. Other, more advanced techniques that make use of electromagnetic signals and exploit the interaction of these signals with the molecules of the atmosphere have been developed over the last century. Specifically, the use of radio waves to detect variations in the wave path have become widely used and accurate methods for atmospheric observation. The next section will give a detailed overview of the many types of radar systems that are used to retrieve information about the earth's atmosphere.

1.2 Radar Observations of the Atmosphere

The word *radar* was coined by Commander S. M. Tucker, according to Navy records, and is derived from the fact that radar is used for **ra**dio **d**etection **a**nd **r**anging (Dunlap Jr. 1946). In other words, a radio wave is transmitted and, if its path is interrupted, scatters a part of the energy along the transmitted path. The palindromic nature of the word itself seems to fit this description perfectly. Radar was developed through the efforts put forth by many brilliant

scientists and innovators, including, Hertz and Marconi, Tesla and Thompson, Edison, Braun and many others (Dunlap Jr. 1946). Much of the advancement in this area of science came out of necessity during World War II. By March of 1940, Britain's secret expenditures on radar technology totaled $36 million (more than $585 million in today's dollars) (Dunlap Jr. 1946). The new radar technology enabled Britain to deploy its Royal Air Force to intercept the Luftwaffe of Germany at night, through fog and clouds. The use of radar saved countless lives and undoubtedly aided the allies in their victory over Germany and Japan.

Following the war, peace brought new pursuits for the infant technology of radar. Some desired to prevent ship collisions, others to cure the blind. November 17, 1946, however, brought a new era in radar science: a hurricane was detected and recorded using an airborne radar system (Dunlap Jr. 1946). Said one interviewed Navy sailor,

> *It has been long known that radar pulses of appropriate frequency are echoed by water droplets in the air. These rain echoes form characteristic patterns which can be identified by trained observers.*

This statement foreshadowed what would become one of the great scientific pursuits of the modern era: Doppler radar for weather observations.

Over the next decades, many different forms of radars took shape. For this work, the author will focus on two atmospheric radars: profilers and precipitation radars.

1.2.1 Clear Air Observations: Profiling Radars

Profiling radars are vertically pointing and typically operate at VHF and UHF radio frequencies, which are 3 to 300 MHz and 300 to 1000 MHz, respectively (Martner et al. 1993). Profiling radars are typically used to detect inhomogeneities in

the refractive index produced by turbulence that are on the scale of one half the radar wavelength Bragg-scale (Gage et al. 1994). The perturbations in the refractive index are advected by the wind and it is this motion that is detected by the wind profiler. The mechanism for detection is also known as Bragg scattering and is the process by which all profiling radars operate. An image of a typical wind profiling radar is given in Figure 1.3.

Figure 1.3: Installation of the wind profiler located at Kessler Atmospheric and Ecological Field Station (`http://kffl.ou.edu`). The wind profiler operates at 915 MHz and 500 W peak power.

Typical profiling radars operate with a peak power of around 0.5 to 20 kW and dwell times of 30 seconds to 2 minutes. As it will be seen, this is a unique property that differs greatly from most precipitation radars (Gage et al. 1994). It is the long dwell times coupled with coherent integration that facilitate the detection of weak signals, deep temporal ground clutter filtering, and extraction of velocity

data from the preserved phase information. Additionally, the vertical extent of wind profilers' range rarely exceeds 20 km. One of the factors in determining the maximum range of a wind profiler is the operating frequency. Typically this is chosen based on the type/size of Bragg scatter of interest (Doviak and Zrnić 1993). While profilers can operate at a broad range of frequencies, it is common to find that most operate at the specific frequencies of 50, 404, 440, and 915 MHz (Martner et al. 1993). Lower frequency profilers are capable of observations approaching 20 km while 915 MHz radars are used to observe the boundary layer and lower regions of the atmosphere, mainly due to their sensitivity to the scale of turbulence at these lower levels.

As the name indicates, wind profilers are used to gather information about the wind, with a three-dimensional field being the desired output. To measure the three-dimensional wind field, wind profilers collect data at several different (nearly vertical) angles and combine the measured Doppler velocities to extract the zonal, meridional and vertical winds (Strauch et al. 1984). Typically, measurements are collected at a 90° elevation angle interleaved with off-broadside measurements aligned with the cardinal directions (Rogers et al. 1993). Often this is performed electronic steering of the beam, though some utilize mechanical methods. At least three angles must be used in order to fully determine the winds and an assumption is made that the winds are homogeneous at a given height. An elevation angle of 75° is often chosen because it allows for sufficiently accurate detection of the horizontal winds while maintaining a beam shape similar to that produced when pointing as zenith (Strauch et al. 1984). Of course, the beam degradation is an issue only for electronically steered profilers.

UHF (and VHF) profilers have the added capability to detect precipitation in both liquid and solid forms, while also detecting the atmospheric winds (Fukao

et al. 1985; Gage et al. 1994). VHF radars typically receive approximately equivalent power returns for both precipitation and clear air while radars operating at frequencies higher than UHF are often dominated by precipitation (Fukao 2007). It is advantageous to detect precipitation because it allows the removal of biases in air velocity measurements caused by hydrometeor descent. Typically this is achieved by observing both the Bragg scatterers and precipitation simultaneously via the Doppler spectra. Through discrimination of the precipitation type via return power estimates and fall velocities, it is possible to identify storm type and structure by identifying precipitation intensity, depth, and melting layer levels (Gage et al. 1994).

Another, substantially larger, and typically more powerful version of a wind profiler is a Mesosphere-Stratosphere-Troposphere radar, also known as a MST radar. Several such radars have been constructed and used to observe far above the earth's surface, even to heights of 800 km (Farley 1969a). Some notable MST radars include Jicamarca near Lima, Peru (Farley 1969a,b; Woodman et al. 1972; Fukao et al. 1978), Arecibo in Puerto Rico (Fukao et al. 1980b), the Middle and Upper (MU) atmosphere radar near Shigaraki, Japan (Fukao et al. 1980a), and the SOUSY (sounding system) radar located originally in the Harz mountains in Germany, now at Jicamarca (Rüster and Czechowsky 1980; Woodman et al. 2003). All of these radars operate near the 50 MHz VHF frequency and pulse modulation is used to achieve fine range resolution. A collection of images showing these MST radar systems are given in Figure 1.4.

With the exception of one of the Arecibo Observatory, all of these radars have a commonality: they are phased array systems[1]. Formations of Yagi antennas

[1]In actuality, additional hardware was added to the Arecibo Observatory making spatial interferometry possible, which is a precursor to phased array electronic beam steering (Palmer et al. 1997).

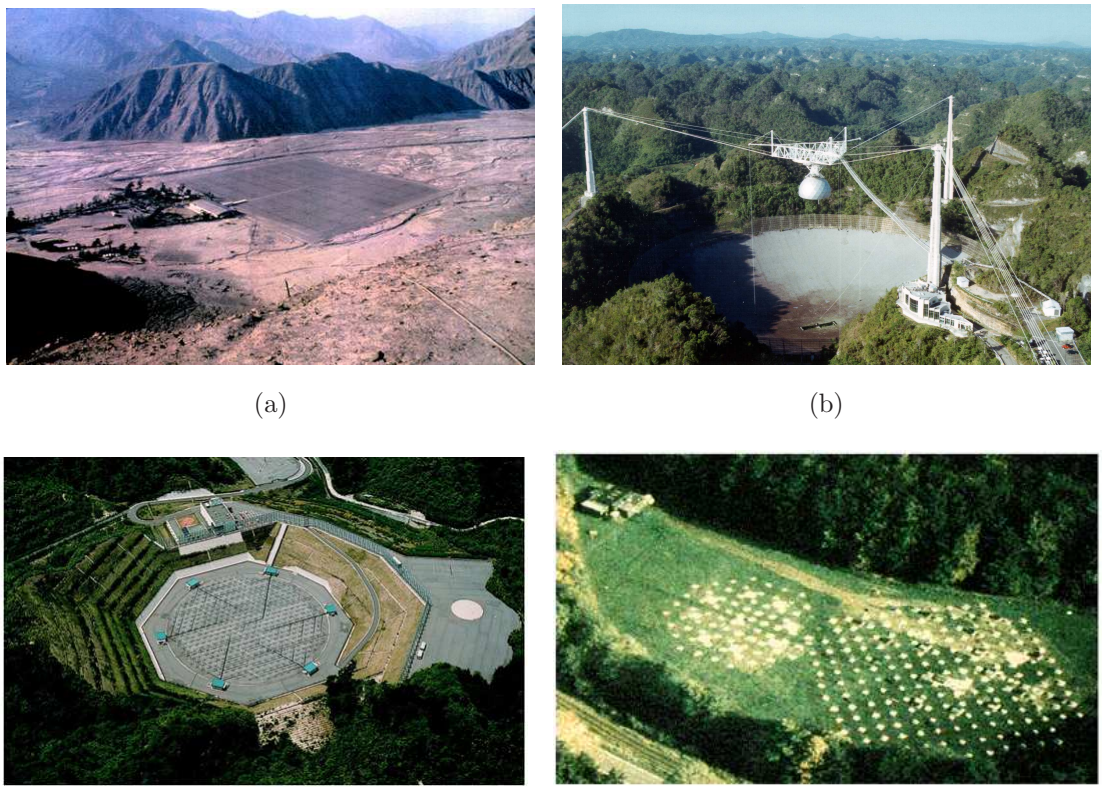

(a) (b)

(c) (d)

Figure 1.4: MST radars from around the world. (a) Jicamarca observatory near Lima, Peru (`http://jicamarca.ece.cornell.edu`) (b) Arecibo observatory on the island of Puerto Rico (`http://naic.edu`) (c) MU radar near Shigaraki, Japan (`http://www.rish.kyoto-u.ac.jp`) and (d) SOUSY in Germany (`http://www.mps.mpg.de`). All of these radars are much larger than a UHF wind profiler and operate in the VHF frequency of 50 MHz.

are used to transmit and receive electromagnetic signals. Depending on the system architecture, linear and circular polarization transmission and reception are possible, allowing for a diverse set of data collection techniques to be performed. While, early on, some MST radars used a few fixed beams, the MU radar in Japan has the ability to steer the beam with 0.45° resolution (Fukao et al. 1980a; Doviak and Zrnić 1993). Latter experiments with these systems made use of interferometer techniques which allow for simultaneous beam steering through the calculation of the so called "angular spectrum" (Farley et al. 1981; Röttger and Ierkic 1985). A co-located transmitter is used to illuminate a desired angular domain and several receive antennas form the narrower receive beam. Subsequent work applied the steering to signal statistics instead of the signal itself (Palmer et al. 1990). Much advancement came with the application of coherent radar imaging techniques, like Capon's method, to MST radars (Kudeki and Sürücü 1991; Sürücü et al. 1992; Hysell and Woodman 1997; Palmer et al. 1998).

One of the most advanced coherent imaging systems was developed at the University of Massachusetts (UMass) at Amherst (Mead et al. 1998). Known as the Turbulent Eddy Profiler (TEP), this radar operates at 915 MHz and has a peak power of 25 kW. Like the above MST systems, it uses a phased array antenna. An image of the TEP is given in Figure 1.5. A transmit horn illuminates a 25° by 25° angular volume and 90 receive elements provide signals that are combined digitally to form simultaneous beams (Mead et al. 1998). The two-dimensional array is reconfigurable to examine various spatial array patterns and it is this versatility that makes the system a valuable tool for exploring imaging techniques and applications. One of the main advantages of the TEP is the ability to apply adaptive beamforming algorithms to the received signals (Cheong et al. 2004; Palmer et al. 2005; Cheong et al. 2006). Further, by removing the need to even steer the beam pulse-to-pulse, the temporal resolution of the radar improves

Figure 1.5: An image of the TEP radar at UMass (courtesy of Dr. Robert Palmer). Each of the panels for this 915 MHz imaging wind profiler can be rearranged to examine the effects of alternative array patterns. Further, the use of digital beamforming allows for adaptive algorithms to enhance the quality of the radar signals.

dramatically over traditional profiling radars. Adaptive algorithms can improve angular resolution and aid in clutter rejection. It is this advancement in radar technology that motivated the author's work outlined in this dissertation.

While clear-air observations of the atmosphere have provided a vehicle for the advancement of many new technologies in the field of radars, it is the observation of precipitation which has a large impact on day-to-day activities. A detailed look at precipitation radars is given next.

1.2.2 Precipitation Observations

Clear air radar systems discussed thus far are quite useful in understanding the thermodynamics of the atmosphere as a whole. For the most part, however, it is the lowest layer of the atmosphere, the troposphere, that concerns people. This is where clouds and hydrometeors form, damaging winds develop, and tornadoes and hurricanes exist. Further, most people live there as well. Due to this fact, significant efforts have been focused on the detection and quantification of hydrometeors through precipitation observations. The creation of Doppler weather radars in the first half of the twentieth century has provided an invaluable tool that has completely changed the way the study of tropospheric phenomena is conducted.

1.2.2.1 A Brief History of Weather Radars

Even prior to World War II, weather echoes were observed using wireless detection techniques in the United Kingdom through work headed by Sir Robert A. Watson-Watt (Whiton et al. 1998a). Subsequent works during and following the last World War facilitated not only the technology and expertise that led to the

development of weather radars, it produced a significant amount of surplus components that made radars affordable (Best 1973; Doviak and Zrnić 1993; Whiton et al. 1998a; Brown and Lewis 2005).

The first manned weather radar stations were operated by the Air Weather Service (AWS) in both Panama and India during World War II (Best 1973; Whiton et al. 1998a). For the Indian locations, aircraft AN/APQ-13 radars were converted for ground use to lessen the cost of data collection. These X-band radars proved that forecasting weather events was possible using remote sensing systems. Following the war, the United States Weather Bureau (now the National Weather Service (NWS)) obtained several airborne S-band radar systems and converted them for weather surveillance purposes, changing the APS-2F moniker to WSR-1s, -2s, -3s, or -4s, the differences arising in the control panels (Whiton et al. 1998a).

Also during this time, the first radar designed purely for weather observation, the AN/CPS-9, was created (Whiton et al. 1998a). Considerable research went into the choice of frequency for this system, with X-band ultimately chosen because of size and power considerations. While widely used at military locations, the use of this radar exposed the potential for substantial attenuation at great distances and would prompt a reevaluation of the use of X-band in future systems. At the same time, the Weather Bureau expanded its network of WSRs after an Illinois State Water Survey radar operator, D. Staggs, observed and recorded a hook-shaped echo on the radar display that was associated with a tornadic storm (Whiton et al. 1998a). Two additional storms displaying a similar echo structure prompted the creation of the Texas Tornado Warning Network through a partnership with Texas A&M University. It was at this time that radars began to be used to identify tornadoes before volunteer spotters on the ground reported them and warnings were issued in advance of severe weather.

In 1956, following the success of the early WSR series radars and what was a particularly costly hurricane season, the Weather Bureau submitted a budgetary proposal for a new flagship radar, the WSR-57 (Whiton et al. 1998a). An image of the radar console for the WSR-57 is given in Figure 1.6. While the WSR-57

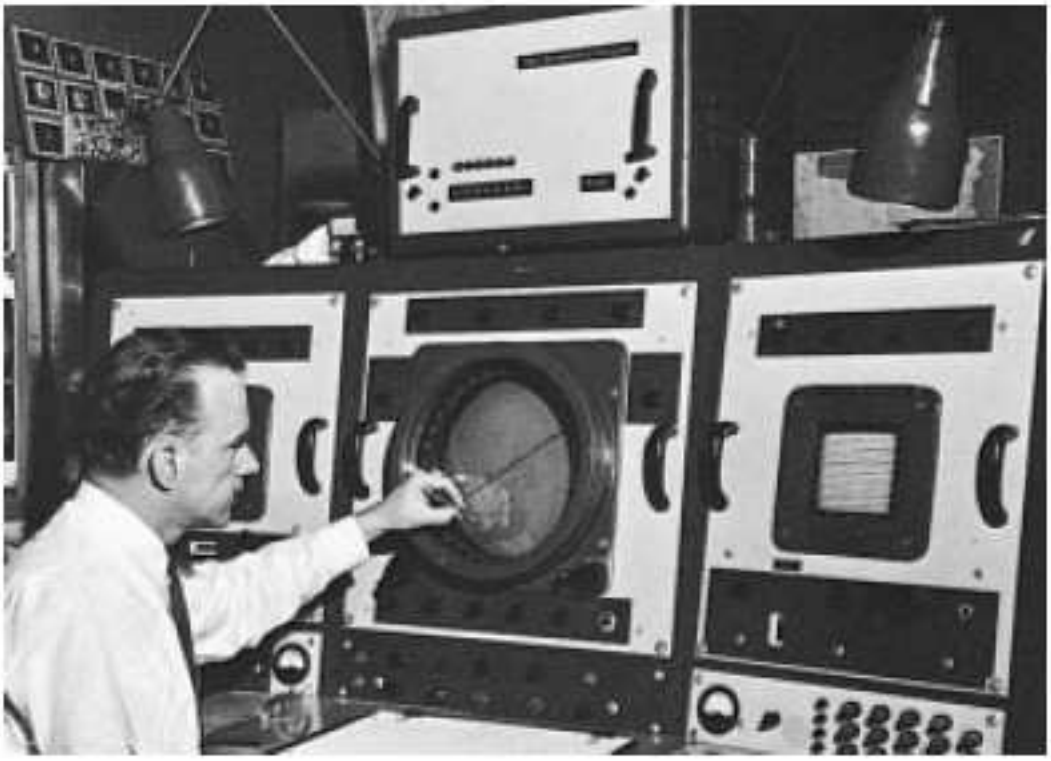

Figure 1.6: An image of the operator's console for the WSR-57 (Whiton et al. 1998a). One of the earliest radars used by the Weather Bureau (later the NWS), the WSR-57 proved useful in detecting and tracking severe weather for many years. Mechanical insufficiencies prompted the creation of the WSR-74C/S radars as replacements.

system had many technical issues, including open loop servo drives that prevented the operator from knowing where the radar was pointing and bull gears that only lubricated while moving, it served for decades as the primary weather surveillance radar at many locations.

By 1969, a small group of engineers in Alabama formed a company, Enterprise Electronics Corporation (EEC), and had created a new generation of C-band weather radars (Whiton et al. 1998a). A multitude of these systems, known as the WSR-74C within the NWS, as well as an S-band cousin, the WSR-74S, were purchased and in fact, one C-band radar still in operation today, but its shutdown is imminent (Smith 2011). EEC continued to innovate and contribute to the commercial production of weather radars, including the first commercial Doppler radar that was produced in 1981 and sold to KWTV-9 in Oklahoma City. An image of the disreputable Gary England operating this radar is given in Figure 1.7. These served as the last large purchases by the federal weather

Figure 1.7: Image of Gary England, a television meteorologist in command of a commercial Doppler weather radar produced by Enterprise Electronics Corporation in 1981 (photo taken at the offices of EEC in Enterprise, Alabama).

service before the weather radar community evolved into its current stage.

The 1960's brought about a significant effort to improve the knowledge of severe storms through the use of radars. With programs like the National Severe

Storms Project (later to become the National Severe Storms Laboratory (NSSL)) and Project Rough Rider, top engineers were collected and put to the task of gleaning every useful piece of information from radar signals. The leadership of Edwin Kessler and Roger Lhermitte, and dedication of engineers, facilitated the creation of the 3-cm pulsed Doppler radar (Brown and Lewis 2005). Over the next decade, two 10-cm Doppler radars were constructed. An image of one of the pulsed Doppler radars is given in Figure 1.8. The exploration of radar signals yielded

Figure 1.8: Image of the NSSL Doppler radar in Norman, Oklahoma (Brown and Lewis 2005). Also shown are the WSR-57 research radar and two aircraft tracking radars. It was through this testbed that the modern era of weather radar technology was developed and evaluated. A similar system was constructed in Cimarron, Oklahoma.

tremendous scientific impact. It is through this undertaking that pulsed Doppler radar was used to develop real-time pulse-pair processing schemes (Sirmans and

Doviak 1973), identify vortices in Doppler spectra (Zrnić and Doviak 1975) and conduct dual-Doppler analysis of tornadic data (Ray et al. 1975), thus ushering in the Next Generation [of] Weather Radars (NEXRAD).

A joint effort put forth by the United States Department of Commerce (DOC), Defense (DOD), and Transportation (DOT) resulted in the funding of a program to develop, procure and sustain the launch of a new weather radar system: the WSR-88D. Established in 1976 at NSSL, the Joint Doppler Operational Project (JDOP) investigated the use of real-time Doppler weather radar data for use in identifying and forecasting severe or tornadic storms (Crum and Alberty 1993). Pre-production designs by Raytheon and Unisys were scrutinized and the design put forth by Unisys Corporation won the contract (Crum and Alberty 1993). JDOP was filled with leaders in the field of weather radar who were major proponents of developing an extensive network of Doppler weather radars that had the capability to perform complex data processing algorithms in near real time while delivering data products to a wide variety of end users (Crum and Alberty 1993; Whiton et al. 1998b).

Many technical improvements over existing WSR-57 and WSR-74C/S radars were implemented in the WSR-88D system. With a 1° beamwidth and 750 kW of peak power, the NEXRAD network would have a resolution and sensitivity not seen in previous systems. Further, a network of 140 individual radars was originally planned with the final number reaching 158, which covers nearly the entirety of the continental United States (Crum and Alberty 1993; Whiton et al. 1998b). An image displaying the NEXRAD network is given in Figure 1.9. Many factors went into the selection of radar sites. The distribution of population, approach directions of severe weather, local terrain and obstructions, airports and military installations were all influential in the identification of ideal radar

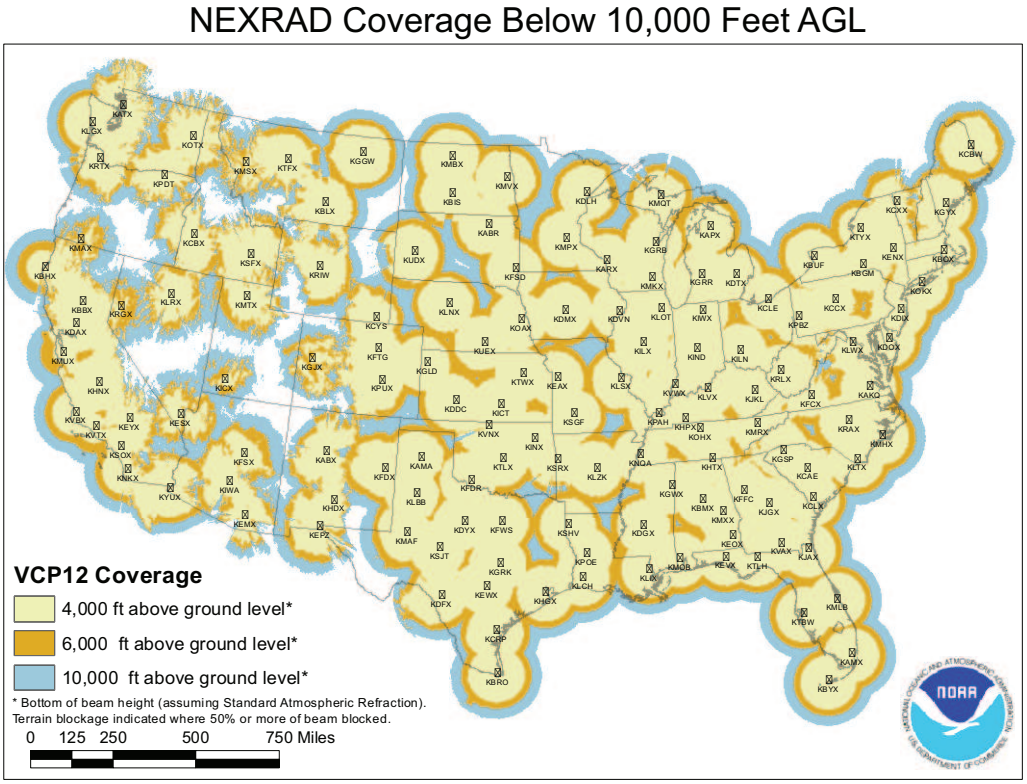

Figure 1.9: An image depicting the locations of the NEXRAD sites (`http://-roc.noaa.gov`) within the continental United States. Yellow rings indicate the coverage up to 10,000 feet above ground level.

locations (Leone et al. 1989). Data from the United States Census Bureau and the United States Geological Survey helped to identify high impact locations.

Data produced by the WSR-88D is divided into three categories: Level I, II, III and IV (Crum et al. 1993). Raw, digital data signals generated by the digital receiver are considered Level I data. Level II data are available once the raw data are processed and the three spectral moments, power, velocity and spectrum width, are calculated. A multitude of products are generated from the spectral moments and these radar products comprise the Level III data. A subset of Level III data can be viewed and recorded on a Principle User Processor (PUP) and these recorded data are recategorized as Level IV data (Crum et al. 1993).

Following the release of the WSR-88D, the team at NSSL began to look at the next upgrade for weather remote sensing technology: polarimetric radar (Doviak et al. 2000). It was already established that utilizing orthogonal polarization planes could provide benefits in rainfall estimation, hydrometeor classification and was even considered a possible solution to the Doppler delimma (Doviak and Sirmans 1973; Doviak et al. 2000; Scharfenberg et al. 2005). NSSL had been using a dual-polarization radar in Cimarron, OK when the decision was made to upgrade a WSR-88D radar, KOUN, to incorporate a simultaneous horizontal and vertical transmitting and receiving capabilities. In addition, the CSU-CHILL radar operated by Colorado State University had also been experimenting with dual-polarization techniques (Hubbert et al. 1998). Following the completion of the KOUN upgrade, a Joint Polarization Experiment (JPOLE) was conducted and data recorded during the experiment were evaluated by forecasters (Scharfenberg et al. 2005). Subsequent research yielded highly accurate rainfall estimation algorithms (1.7 times RMS error reduction over non-polarimetric techniques) (Ryzhkov et al. 2005), hidden secrets of tornado dynamics (Kumjian et al.

2010), and proved S-band polarimetric radar to be a tool for mapping Bragg scatter (Melnikov et al. 2011).

Leveraging wind profiler technology and military surplus, the next phase of weather radar took shape. By utilizing arrays of antennas and carefully controlling the phase, nearly instantaneous steering of the radar beam can be achieved, between pulses if necessary. Acquiring an AN/SPY-1 antenna, NSSL commissioned the first phased array radar for use in weather detection (Forsyth et al. 2002; Zrnić et al. 2007). An illustration of the National Weather Radar Testbed (NWRT) is given in Figure 1.10. Further research indicated benefits to the elec-

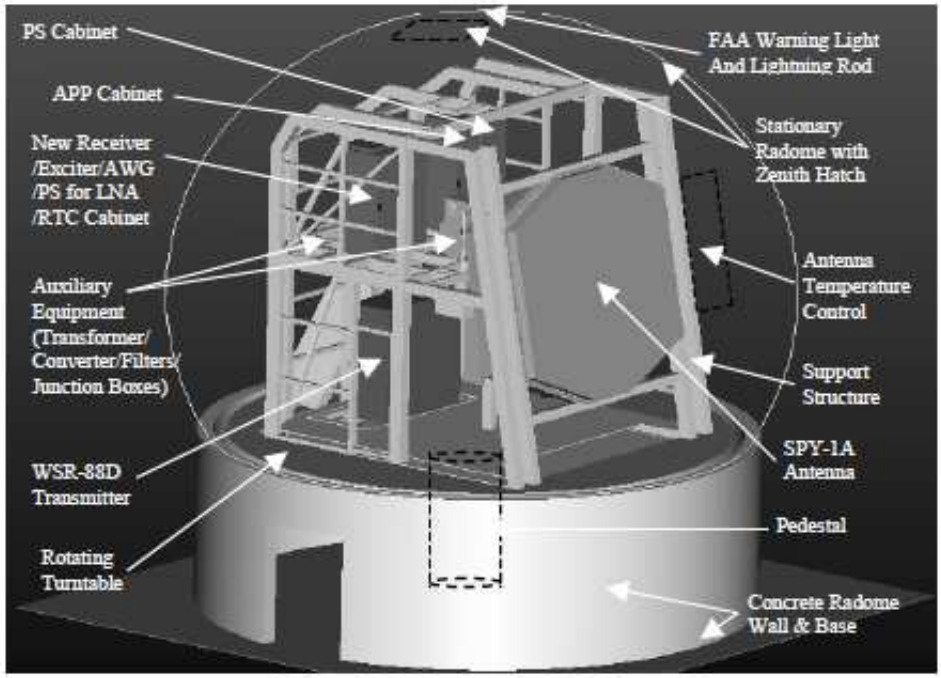

Figure 1.10: An illustration of the NWRT (Forsyth et al. 2002). A surplus SPY-1 phased array radar is fitted for fixed-site operation, much like the earlier systems following World War II. Electronic steering allows for complex scan strategies and multi-purpose functionality. In the future, radars that comprise the national network may all employ phased array technology.

tronic steering approach through beam multiplexing, which allows shorter volume coverage times by improving the statistical accuracy of radar measurements (Yu et al. 2007). With the addition of auxiliary elements around the perimeter of the array, clutter cancellation techniques could be employed to reduce the impact of undesirable targets (Le et al. 2009; Yeary et al. 2011).

Over the last few decades, weather radar technology has evolved considerably and the understanding of weather phenomena has expanded. One limitation of the weather radars discussed thus far is the resolution of the data collected, both spatial and temporal. Detectable atmospheric phenomena change in range due to the effect of beam broadening at large distances. To achieve high spatial resolution, frequency bands and antenna diameter are the traditional parameters that can be adjusted for fixed-site radars. It is due to this fact that a series of mobile platforms were developed to allow radars to gather data at close range with high spatial resolution.

1.2.2.2 Mobile Radars

It is difficult to capture rapidly evolving severe weather phenomena at low levels and high spatial resolution with traditional fixed-site radars due to the need for close proximity. Thus, mobile weather radar systems are used to increase the likelihood of near-storm observations. For a number of years now, it has been common in mid-western towns to see one or more mobile radar systems inroute to a potential high-impact weather event. Some images of typical mobile radars used in field campaigns are given in Figure 1.11. One of the original mobile systems was tfhe Center for Severe Weather Research (CSWR) Doppler on Wheels (DOW) (Wurman et al. 1997) followed by the Shared Mobile Atmospheric Research and Teaching Radar, or SMART Radar (Biggerstaff et al. 2005). Additional systems, such as the UMass X-Pol (Venkatesh et al. 2008) and the NSSL

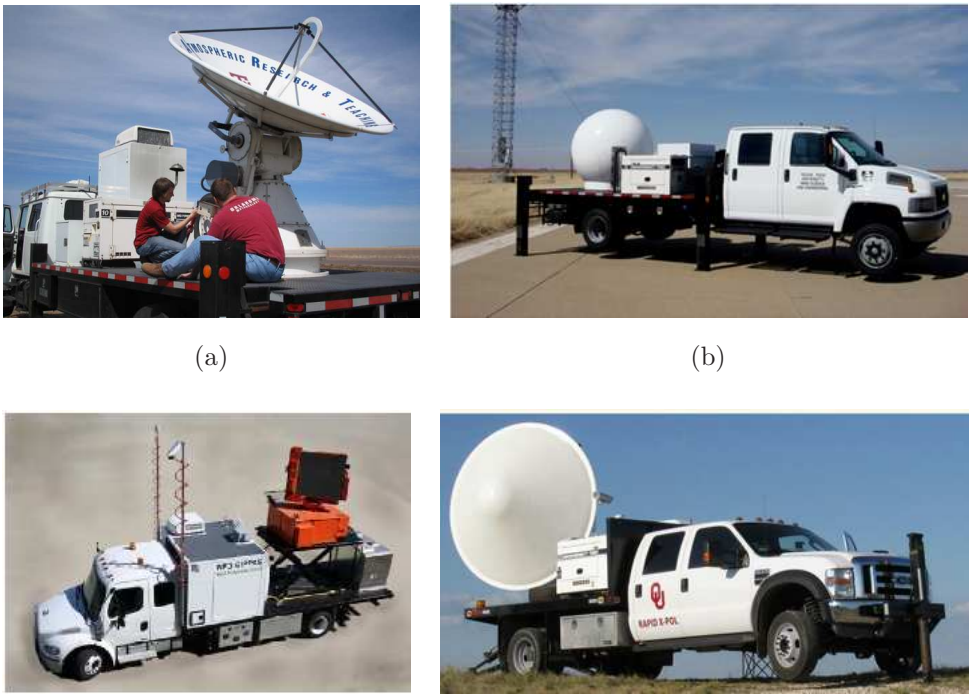

(a) (b)

(c) (d)

Figure 1.11: Images depicting mobile radar systems in use today. (a) The SMART-R systems maintained by the University of Oklahoma (b) Ka-band radars maintained by Texas Tech University (`http://-www.depts.ttu.edu/weweb/WindEnergy`) (c) MWR-05XP phased array system maintained by the Navy Postgraduate School(`http://www.cirpas.org`) and (d) RaXpol built by Prosensing and maintained by the Atmospheric Radar Research Center (`http://arrc.ou.edu`). Many of these radars employ both dual-polarization and methods to expedite the scanning process. Additionally, all of these radars have been used in the gathering of severe weather data.

NO-XP (Schwarz and Burgess 2010), improved mobile radar measurements by incorporating dual-polarization capabilities, which allow for attenuation correction and hydrometeor classification (Ryzhkov and Zrnić 1994) among other benefits. Other systems advance mobile radar performance by enhancing spatial resolution through the utilization of higher frequencies. The Texas Tech University Ka-band (TTUKa) radar (Weiss et al. 2009) and the UMass W-Band radar (Bluestein et al. 1997; Seliga and Mead 2009) are two such systems. One common feature of all of the systems mentioned, is their use of a traditional parabolic dish. In other words, the systems utilize a pencil beam to gather volumetric storm data. Temporal resolution is thus limited and has prompted further exploration for technological advancement in the mobile radar community.

As a result of the high spatial resolution gained by the use of mobile radars, temporal resolution can be increased to observe small-scale phenomena as they form. A relationship between the necessary temporal resolution for a given spatial resolution can be derived from the spatial decorrelation time of a specific weather event, as shown by Bodine et al. (2009) for a simulated tornado case. Results of the analysis indicate that the spatial structure of the vortex (sampled at 25, 50 and 100 m) decorrelates in approximately two seconds. A more qualitative study provided by Wurman (2005) illustrates the relationship between spatial and temporal resolution as well as indicating the ability of a variety of systems to detect quickly evolving phenomena and an illustration is presented in Figure 1.12. In general, spatial resolution is proportional to the temporal scale, meaning, smaller features of a phenomena require less time between samples to be detected and analyzed. For instance, multiple vortices are indicated by the black box outlined in the lower left corner of Figure 1.12, requiring 50 m resolution with 20 s samples. None of the radars indicated in the figure are able to achieve this temporal or spatial scale.

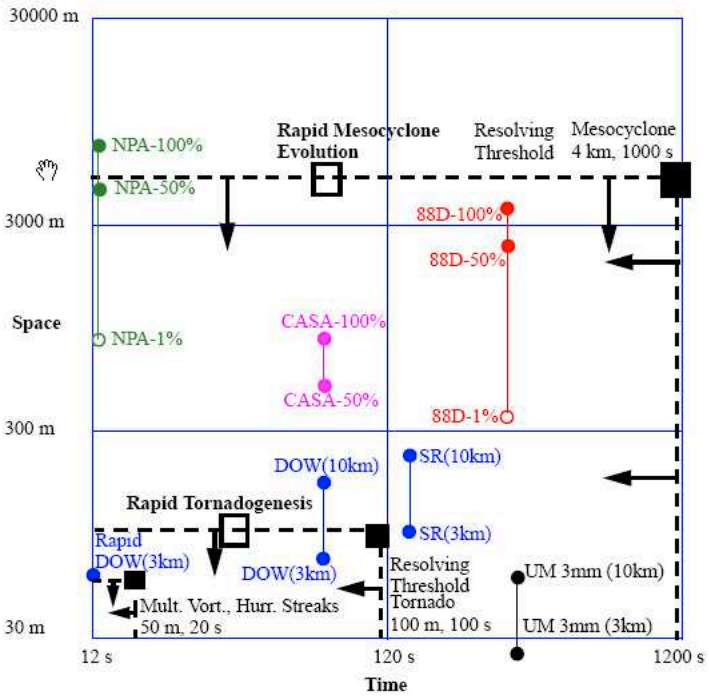

Figure 1.12: An illustration from Wurman (2005) indicating the relationship between spatial and temporal resolution. Additionally, several radar systems, both fixed and mobile, are denoted, indicating the ability to detect various meteorological phenomena. The Atmospheric Imaging Radar (discussed later) would be located in the lower left corner, exceeding the 12 s minimum time scale shown in the figure.

To improve the update time of volumetric storm data, mobile radars have employed various techniques. Electronic beam steering and frequency hopping are two, somewhat unrelated techniques that aim to improve temporal resolution. Electronic steering can be accomplished in a fraction of the time it takes to mechanically steer the dish of the radar. The CSWR Rapid Scan DOW (Wurman and Randall 2001) makes use of multiple frequencies to generate several beams fixed in elevation while mechanically scanning in azimuth. The Rapid Scanning X-band Polarimetric Radar (RaXpol), employs a frequency hopping technique to allow for high-speed antenna rotation. Similar to the beam multiplexing idea put forth by Yu et al. (2007), data accuracy is determined by the number of independent samples acquired. Utilizing multiple, independent frequencies nearly simultaneously, the radar is able to increase its rotation rate because it is collecting multiple independent samples where a conventional radar collects one, thus reducing the time required to collect volumetric storm data (Pazmany and Bluestein 2009). The Meteorological Weather Radar 2005 X-band (MWR-05XP) uses both phase and frequency scanning to steer the beam in elevation and azimuth, but also relies on mechanical steering to a large extent (Bluestein et al. 2010).

Many significant experiments have been completed with these systems, including the Verifications of the Origins of Rotation in Tornadoes Experiment 2 (VORTEX2) project (Bluestein et al. 2009), where a fleet of radars, including those mentioned above, were deployed over several weeks and two spring seasons primarily in search of tornado events. Data collected during these experiments have improved the understanding of tornado life cycle and helped to enhance radar tornado detection algorithms. Some cases could potentially lead to a reduction in lives lost to severe weather through the construction of structures better able to withstand the force of tornadic winds (Metzger et al. 2011).

While the aforementioned techniques are valid in the attempt to improve temporal and spatial resolution of Doppler weather radars, additional approaches exist. As an example, this work presents the Atmospheric Imaging Radar (AIR), developed by the Atmospheric Radar Research Center (ARRC) at the University of Oklahoma (OU), which employs imaging techniques to *simultaneously* gather volumetric data on a mobile platform.

1.3 Imaging Applications for High Resolution Weather Observations: The Atmospheric Imaging Radar

Through a combination of clear air imaging technology and precipitation-based Doppler radar designs, the Atmospheric Imaging Radar (AIR) provides the latest advancement in radar technologies. Similar to the imaging work completed on the MU radar in Japan (Hysell and Woodman 1997; Palmer et al. 1998) and the TEP radar at UMass (Mead et al. 1998), a broad field-of-view (FOV) is defined by the transmit beam while multiple radar receivers collect the atmospheric returns. By combining the signals from each of the receivers in the digital domain, instantaneous beam formation can be achieved. Essentially, an infinite number of beams can be generated within the FOV simultaneously through the process of digital beamforming (DBF). Typically, beam positions are chosen such that the 3-dB beamwidths of adjacent beams overlap so as to produce practically independent spatial samples.

By selecting the carrier frequency to be 9.55 GHz, the radar is responsive to hydrometeor backscatter, thus making it a precipitation radar. Additionally, the use of a distributed clock signal allows the system to remain coherent and Doppler retrieval is possible. Further capability is added through the use of a

traveling wave tube (TWT) amplifier, which makes pulse compression available to the system and recovers some of the sensitivity losses associated with the broad transmit beam. Like the mobile systems mentioned earlier, mechanical azimuthal steering is necessary for this system as the 36 receive antennas are arranged linearly in the vertical dimension. Spatial resolution, at a minimum, matches that of existing mobile radars with the added benefit of adaptive beam shaping in the beamforming dimension. With 5-second volumetric update times, and 1° by 1°angular resolution, the temporal and spatial resolution of the AIR make it an ideal platform for monitoring and collecting data from severe weather events. Through analysis and study, a greater understanding of short time scale phenomena can be achieved.

It will be shown through this document that the AIR provides a testbed for the use of imaging technology for precipitation sensing and severe weather observation. The following chapter will review the background and theory behind Doppler weather radar. Chapter 3 will summarize array and signal processing techniques and Chapter 4 details the AIR system hardware, software and operation. Results from initial experiments and field campaigns are given in Chapter 5 while recommendations for future work and conclusions are presented in Chapter 6.

Figure 1.13: An image of the AIR collecting data near Willow, Oklahoma March 18, 2012. A supercell can be observed in the background, which is the object of interest for the AIR.

Chapter 2

Fundamentals of Doppler Weather Radar

2.1 Waves and Propagation

The basic principle of all radar systems relies on the transmission and reception of electromagnetic waves. These waves are composed of **E** and **H** force fields that travel at the speed light ($c \approx 2.998 \times 10^8$ m s^{-1}). Interactions between these waves and matter along the propagation path cause the waves to scatter, diffract, and refract (Doviak and Zrnić 1993). Electromagnetic waves have sinusoidal spatial and temporal variations where the distance from peak to peak is defined by the wavelength, λ. Wavelength and frequency are related through the speed of light:

$$f = c/\lambda \text{ (Hz)}. \tag{2.1}$$

Microwaves are typically defined as frequencies within the range of 3 to 300 GHz (wavelengths 10^{-3} to 10^{-1} m). Typically, the longer microwave wavelengths are used in the weather radar community. In the far field, defined as distances greater than $2D^2/\lambda$ where D is the diameter of the dish or antenna, the electric field can be described as

$$\mathbf{E}(r, \theta, \phi, t) = \frac{\mathbf{A}(\theta, \phi)}{r} \cos\left[2\pi f\left(t - \frac{r}{c}\right) + \psi\right] \text{ (Vm}^{-1}\text{)}, \tag{2.2}$$

where ψ is the transmitter phase (known or random depending on the electromagnetic source), t is time, and r, θ, and ϕ are described by Figure 2.1. Since the

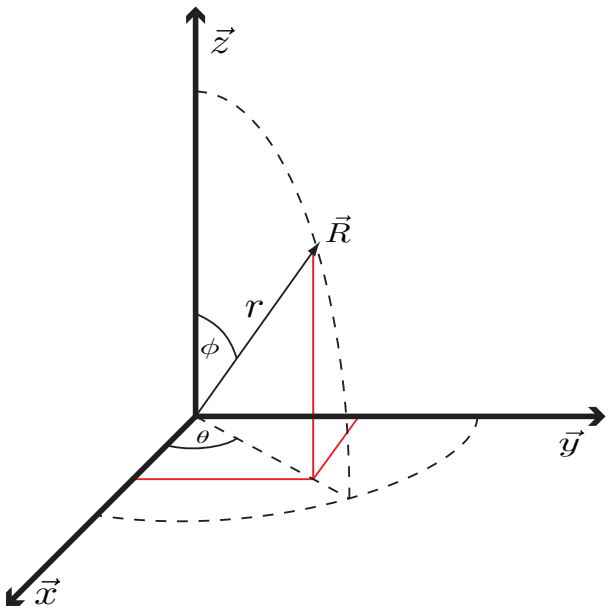

Figure 2.1: An illustration of the spherical coordinate system used in this chapter. θ is the angle measured from the positive $\vec{x}$ axis toward the positive $\vec{y}$ axis while ϕ is measured from the positive $\vec{z}$ axis.

electromagnetic waves are primarily determined by the amplitude, $\mathbf{A}$, and phase, $(2\pi f(t - r/c) + \psi)$, it is straightforward to represent the electromagnetic wave in phasor notation:

$$\mathbf{E}(r, \theta, \phi, t) = \frac{\mathbf{A}(\theta, \phi)}{r} \exp\left[j2\pi f\left(t - \frac{r}{c}\right) + j\psi\right] \ (\mathrm{Vm}^{-1}). \tag{2.3}$$

Using this notation, it is important to discuss another important electromagnetic quantity called the power density $S(r, \theta, \phi)$ given by:

$$S(r, \theta, \phi) = \frac{1}{2}\frac{\mathbf{E} \cdot \mathbf{E}^*}{\eta_0} = \frac{A^2(\theta, \phi)}{2\eta_0 r^2} \ (\mathrm{Wm}^{-2}), \tag{2.4}$$

where A^2 is the magnitude squared of $\mathbf{A}$ and $\{\cdot\}^*$ indicates the complex conjugate. η_0 is the wave impedance of the earth's atmosphere and has a constant value of 377 Ohms.

An electromagnetic wave follows a straight path in free space. However, the earth's atmosphere has a dielectric constant greater than ε_0 and thus waves travel

at speeds slower than the speed of light ($\nu < c$). Since the atmosphere is stratified, beams follow a curved path from their source and this path is determined by the magnitude of the refractive index, n:

$$\mathsf{n} = \frac{c}{\nu} = \sqrt{\varepsilon_r} = \sqrt{\frac{\varepsilon}{\varepsilon_0}}. \tag{2.5}$$

Related to the refractive index is a term called Refractivity.

$$\mathsf{N} = (\mathsf{n} - 1) \times 10^6 \tag{2.6}$$

and

$$\mathsf{N} = (77.6/\mathsf{T})(\mathsf{P} + 4810\mathsf{P}_\mathrm{w}/\mathsf{T}) \ , \tag{2.7}$$

where T is temperature in $^\circ$ C, P is pressure in millibars and P_w is water vapor pressure, also in millibars.

As previously mentioned, the refractive index of the atmosphere is not constant with height. As such, a radar beam will bend, or *refract* as it propagates through the air. Additionally, the curvature of the earth causes a similar effect as the ground appears to fall away from the beam as range increases. In the first two kilometers of atmosphere, it is approximated that the gradient of n with height is typically $-(4\mathsf{a})^{-1}$ where a is the earth's radius, 6371 km. Using this model, the height of an electromagnetic wave originating at the earth's surface with an elevation angle of θ_e can be approximated as:

$$h = [r^2 + \mathsf{a}_\mathrm{e}^2 + 2r\mathsf{a}_\mathrm{e}\sin\theta_\mathrm{e}]^{1/2} - \mathsf{a}_\mathrm{e} \ (\mathrm{km}), \tag{2.8}$$

where

$$\mathsf{a}_\mathrm{e} = \frac{4}{3}\mathsf{a}. \tag{2.9}$$

Examples of the beam height at several elevation angles are shown in Figure 2.2. At times, the refractive index of the atmosphere can become large enough to cause significant deviations in the electromagnetic wave path. For example, situations

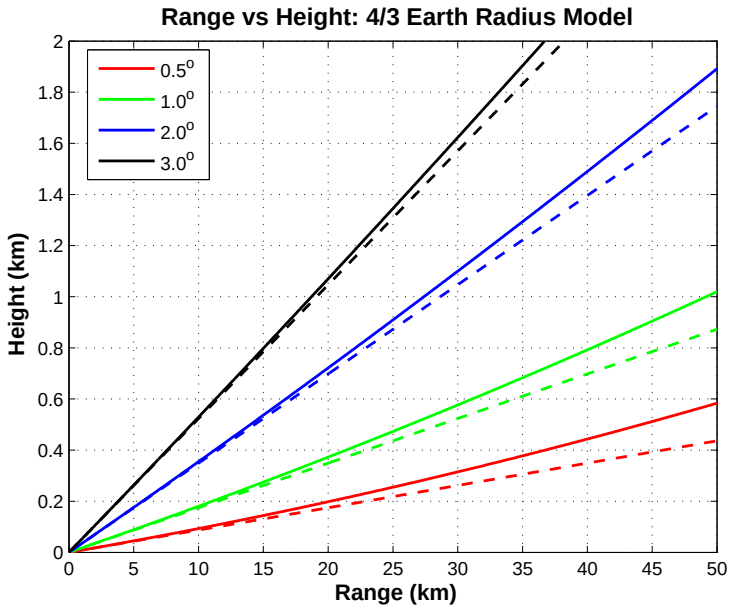

Figure 2.2: Electromagnetic beam paths for elevation angles 0.5, 1.0, 2.0 and 3.0 degrees depicted by black, red, green and blue lines, respectively. Solid lines represent paths calculated utilizing the 4/3-earth radius model and dashed lines represent the path determined purely geometrically. The geometric calculations consistently underestimate the beam position relative to the 4/3 model.

in which the refractive index changes more drastically with height would cause the beam to bend back toward the earth. This is known as *super-refraction*. In contrast, a refractive index gradient lower than $-(4\mathsf{a})^{-1}$ results in an upward-bending beam and is called *sub-refraction*.

2.1.1 Radar Beam Interactions

Thus far, a discussion of generic electromagnetic propagation has been given. For radar systems, it is useful to describe the electromagnetic wave interaction with the environment through the *radar range equation*. The following discussion will follow the derivation of this equation.

2.1.1.1 Radar Range Equation

Radars typically will focus the generated electromagnetic radiation into a specific angular shape ($1^\circ \times 1^\circ$ is typical for weather radars), known hereafter as a radar *beam*. A measure of this focusing, relative to an omnidirectional antenna, is called directivity, or a related term, directive gain, g. Once a focused beam is transmitted, its interaction with an object in the environment begins with the incident power density:

$$S_i(\theta, \phi) = P_t g_t f^2(\theta, \phi)/4\pi r^2, \tag{2.10}$$

where P_t is the transmitted power delivered to the antenna, g_t is the transmit directive gain along the beam axis and $f^2(\theta, \phi)$ is the normalized power gain pattern. Note that as this is a power density, the division by $4\pi r^2$ refers to the solid angle on the unit sphere, where $\int_0^{2\pi} \int_0^{\pi} r^2 \sin\theta \; d\theta \; d\phi = 4\pi r^2$.

Electromagnetic energy incident upon an object will either be scattered or absorbed by the object. For an object of cross section σ, the reflected power density detected at the receiver can be described as:

$$S_r = S_i \sigma(\theta', \phi')/4\pi r^2. \tag{2.11}$$

It is apparent from the equation that the magnitude of the received power density depends on the location of the scatterer and the angles describing the relative return path to the antenna, denoted by θ' and ϕ'. Some typical cross section values for various objects are given in Table 2.1 (Richards 2005). For radars, the

Table 2.1: Common Cross Section Values

Target	σ **(m^2)**
missile	0.5
fighter aircraft	2-6
pickup truck	200
bicycle	2
human	1
insect	0.00001

parameter of interest is typically the backscattered cross section, or the energy reflected along the same path as the incident radar beam. For a spherical water drop of diameter $\mathsf{D} \leq \lambda/16$, the backscattered cross section is given via the Rayleigh approximation by

$$\sigma_b \approx \frac{\pi^5}{\lambda^4} |\mathsf{K}_m|^2 \mathsf{D}^6, \tag{2.12}$$

where $\mathsf{K}_m = (\mathsf{m}^2 - 1)/(\mathsf{m}^2 + 2)$, $\mathsf{m} = \mathsf{n} - j\mathsf{n}\kappa$ is the complex refractive index of water, and κ is the index of attenuation. For cases in which $\mathsf{D} > \lambda/16$, which

is often the case with X-band or higher frequency radars, the scatterers occupy the Mie regime and alternative techniques are used to calculate the backscattered cross section as the Rayleigh approximation is no longer valid.

Mie Scattering Mie (1908) formulated a solution to the wave equation for spheres that will now be applied to rain drops. The full derivation of these solutions is beyond the scope of this study but the reader is directed to additional resources (Bohren and Huffman 1983; Bringi and Chandrasekar 2001; Ishimaru 1997; van de Hulst 1957). The following again applies to drops that are spherical in shape.

Since energy incident upon an object is either scattered or absorbed, it is useful to define the *extinction cross section* as the sum of the scattered and absorbed cross sections ($\sigma_e = \sigma_s + \sigma_a$). Dividing the cross sections by the physical area yields the associated efficiency, which can be calculated via

$$Q_i = \frac{\sigma_i}{\pi a^2} \ , \tag{2.13}$$

where i can indicate extinction, absorption or scattering (backscattering) and a is the particle radius. From Mie theory, it is known that

$$Q_e = \frac{1}{2}\left(\frac{\lambda}{\pi a}\right)\sum_{n=1}^{\infty}(2n+1)\mathrm{Re}\{a_n^S + b_n^S\}, \tag{2.14}$$

$$Q_s = \frac{1}{2}\left(\frac{\lambda}{\pi a}\right)\sum_{n=1}^{\infty}(2n+1)(|a_n^S|^2 + |b_n^S|^2), \tag{2.15}$$

$$Q_b = \frac{1}{4}\left(\frac{\lambda}{\pi a}\right)\left|\sum_{n=1}^{\infty}(2n+1)(-1)^n(a_n^S - b_n^S)\right|^2 \ , \tag{2.16}$$

where a_n and b_n are the expansion coefficients of the scattered fields (Bohren and Huffman 1983; Oguchi 1983). While the equations appear as infinite sums, realistic approximations must be made to provide an analytical solution. Thus, the series is truncated at $n_{\max} = x + 4x^{1/3} + 2$, where $x = 2\pi/(\lambda a)$ and is referred

to as the size parameter (Bohren and Huffman 1983). Code provided by Bohren and Huffman (1983) is used in order to calculate the backscattering efficiencies with the size parameter and refractive index as inputs and the results are given in Figure 2.3. Calculation of the refractive index is dependent upon the temperature

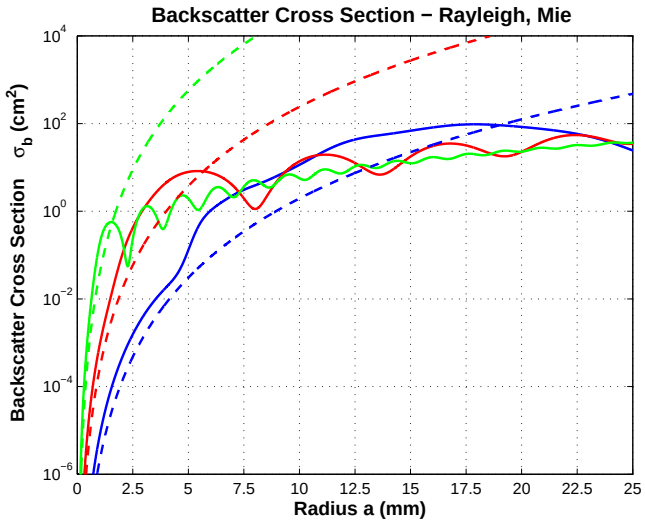

Figure 2.3: Backscattered cross sections for various spherical water drop diameters at $\mathsf{T} = 0°\mathrm{C}$. Mie cross sections are shown as solid lines for frequencies of 3, 10 and 35 GHz (blue, red and green, respectively). The dashed lines indicate the Rayleigh approximate backscattered cross sections.

of the particle and the radar frequency and is covered in Appendix A.

Attenuation Extinction cross sections, and the parameters comprising them, not only determine the ability of the radar to detect an object, but also influence the ability of the radar to detect objects downrange, or at greater distances. As a radar beam propagates along its path, the incident power density is reduced as the beam comes in contact with obstructions and is a phenomenon known as

attenuation. A model for the energy lost upon an object within the radar beam is given as

$$P_L = \sigma_e S_i \ , \tag{2.17}$$

where P_L is the power lost to attenuation. Expanding this idea to distributed targets (such as a field of hydrometeors) is necessary for the rest of this work. So, if it assumed that a wave is incident on a volume ΔV of particles, then the change in the incident power density over a distance Δr is

$$\Delta S_i = -\frac{\Delta r}{\Delta V} \sum_{n=1}^{N} (\sigma_{an} + \sigma_{sn}) S_i \ , \tag{2.18}$$

where σ_{an} and σ_{sn} represent the absorption and scattering cross section for the nth particle, respectively. As the limit of $\Delta r \to 0$, S_i is considered constant within ΔV and

$$\lim_{\Delta r \to 0} \left(\frac{\Delta S_i}{\Delta r} \right) = \frac{dS_i}{dr} = - \left(\lim_{\Delta r \to 0} \sum_{n=1}^{N} \frac{\sigma_{an} + \sigma_{sn}}{\Delta V} \right) S_i = -\mathsf{k} S_i \ , \tag{2.19}$$

where k is the specific attenuation and has units of inverse meters. An equivalent expression for the specific attenuation is given as

$$\mathsf{k} = \int_0^\infty N_{\mathrm{DSD}}(\mathsf{D}, \mathbf{r}) \sigma_e(\mathsf{D}) \ d\mathsf{D} \ . \tag{2.20}$$

Note that the absorption and scattering cross sections have been combined to form the extinction cross section and $N_{\mathrm{DSD}}(\mathsf{D})$ is the drop size distribution (DSD). Since, in general, the radar path and signal power are represented in kilometers and decibels, respectively, it is useful to express the specific attenuation as

$$\mathsf{K} = 4.34 \times 10^3 \mathsf{k} \ \ (\mathrm{dB\ km^{-1}}) \ . \tag{2.21}$$

Drop Size Distribution Because the DSD estimation is essential to not only the specific attenuation calculation but, prophetically, for the ubiquitous reflectivity factor used by most weather radars, significant theoretical and experimental

research has been conducted. Experimental work done by Marshall and Palmer (1948) resulted in a negative exponential model for the DSD, expressed by

$$\begin{aligned} N_{\mathrm{DSD}}(\mathsf{D}) &= N_0 \exp\left[-\Lambda \mathsf{D}\right] \quad (\mathrm{mm}^{-1}\ \mathrm{m}^{-3}) \ , \qquad (2.22) \\ \Lambda &= 4.1\mathsf{R}^{-0.21} \quad (\mathrm{mm}^{-1}) \ , \\ N_0 &= 8 \times 10^3 \quad (\mathrm{mm}^{-1}\ \mathrm{m}^{-3}) \ , \qquad (2.23) \end{aligned}$$

where N_0 denotes the number concentration parameter, Λ is the slope parameter and R is the rainfall rate. Work conducted by Laws and Parsons (1943) can be represented closely by a negative exponential distribution as well, with $N_0 = 5.1 \times 10^3 \mathsf{R}^{-0.03}$ and $\Lambda = 3.8\mathsf{R}^{-0.20}$ (Ulbrich 1983). It is noted that the exponential distribution is inaccurate for small drop sizes and does not closely match data from disdrometers capable of measuring such particles. The accuracy of the negative exponential DSD model is also variable depending upon the type of rain and geographical location (Doviak and Zrnić 1993). As a result, additional attempts to define the exponential model parameters N_0 and Λ for specific classes of rain events were made. Joss et al. (1968) developed two such definitions, one for convective rain and the other for light, stratiform rain. The exponential model parameters for each are

- Thunderstorm

$$\begin{aligned} \Lambda &= 3\mathsf{R}^{-0.21} \\ N_0 &= 1.4 \times 10^3 \qquad (2.24) \end{aligned}$$

- Drizzle

$$\begin{aligned} \Lambda &= 5.7\mathsf{R}^{-0.21} \\ N_0 &= 30 \times 10^3 \ . \qquad (2.25) \end{aligned}$$

To better represent DSDs, a new distribution function was developed that incorporated a better representation of the smaller drops. Ulbrich (1983) developed what is known as the gamma distribution and is defined as

$$N_{\mathrm{DSD}}(\mathsf{D}) \;=\; N_0 \mathsf{D}^{\mu} \exp\left[-\Lambda \mathsf{D}\right] \;, \tag{2.26}$$

where μ is the distribution shape parameter. Note that the units for N_0 are now $\mathrm{mm}^{-1-\mu}\ \mathrm{mm}^{-3}$. Contributions to the accuracy of the gamma distribution have been supplied by Cao et al. (2010) and Zhang et al. (2001, 2006) in the form of the constrained-gamma DSD, which exploits the interdependence of the three parameters: N_0, Λ and μ. The constrained-gamma DSD is so named because it removes one degree of freedom from the underdetermined system, thus constraining one basis within the solution set. The constrained-gamma distribution shows improvements in the estimations of the DSD and its impact on downstream measurements such as rainfall rate and is primarily used in conjunction with polarimetric radars.

Generally, the DSD is not known and therefore must be calculated from either disdrometer measurements or radar parameters. In many cases, it suffices that a DSD is assumed and utilized in downstream calculations.

Radar Range Equation Combining the discussion thus far, it can be seen that

$$S_r(r,\theta,\phi) = \frac{P_t g_t f^2(\theta,\phi)\sigma_b}{(4\pi r^2)^2 \mathsf{l}^2} \ \ \mathrm{Wm}^{-2}, \tag{2.27}$$

$$\mathsf{l} = \exp\left(\int_0^r \mathsf{k}_t \ dr\right) \tag{2.28}$$

where l is the one-way transmission loss and k_t is the total specific attenuation (sum of losses due to gasses, hydrometeors, clouds, etc.). From here, the return density is converted to a power measurement by

$$P_r = S_r(r,\theta,\phi) A_e(\theta,\phi) \ \ W, \tag{2.29}$$

where A_e is the effective aperture of the antenna collecting the returned power density

$$A_e = \frac{g_r \lambda^2 f^2(\theta, \phi)}{4\pi} \ \ \mathrm{m}^2, \tag{2.30}$$

and P_r is the power returned to the receiver. g_r is the receive antenna directive gain, which is equal to g_t if the system is mono-static.

Expanding the above equation, it is found that, for a system measuring a small object with backscatter,

$$P_r = \frac{P_t g_t g_r \lambda^2 \sigma_b f^4(\theta, \phi)}{(4\pi)^3 r^4 l^2}. \tag{2.31}$$

The above radar range equation is useful in defining or fully characterizing a specific radar system.

Weather Radar Equation Many different forms of the radar equation exist and, depending on the application, various parameters are considered. In the case of weather radar, distributed targets are present and thus require the reference to the radar resolution volume. For this, a differential volume $dV = r^2 \sin\theta \; dr \; d\theta \; d\phi$ is used and the backscatter cross section is expanded to include a distribution of scatterers per unit volume. To do so, a term called *reflectivity* is introduced as:

$$\frac{E\{\sigma_b\}}{dV} = \eta(r) = \int_0^\infty \sigma_b(\mathsf{D}) N_{\mathrm{DSD}}(\mathsf{D}, r) \; d\mathsf{D}. \tag{2.32}$$

Further refinement can be made by incorporating the Rayleigh assumption of (2.12)

$$\eta(r) = \int_0^\infty \frac{\pi^5}{\lambda^4} |K_m|^2 \mathsf{D}^6 N(\mathsf{D}, r) \; d\mathsf{D} \tag{2.33}$$

$$= \frac{\pi^5}{\lambda^4} |K_m|^2 Z_e \ , \tag{2.34}$$

where Z_e is the equivalent reflectivity factor. The familiar dBZ log scale is used for reflectivity measurements because of the large range of values that appear in most weather scenarios and is calculated by

$$\mathrm{dBZ} = 10 \log_{10}\{Z_e(\mathrm{mm}^6/\mathrm{m}^3)\} \ . \tag{2.35}$$

The resolution volume itself is weighted according to the shape of the electromagnetic beam, which in this case will be represented by a Gaussian shape in the $d\theta$ and $d\phi$ dimensions with half power points at $\pm\theta_{3\text{dB}}/2$. For the dr dimension, a rectangular pulse is assumed and the system response $|W_s(r)|^2$ is known as the range weighting function. Now it remains to integrate over the full volume dV to obtain the expected echo power

$$\bar{P} = \int_0^{r_2} \int_0^{\pi} \int_0^{2\pi} \frac{P_t g_t g_r \lambda^2 |W_s(r)|^2 f^4(\theta,\phi)\eta(r)}{(4\pi)^3 r^4 \mathsf{l}^2} \; r^2 \sin\theta \; dr \; d\theta \; d\phi, \tag{2.36}$$

while

$$\int_0^{r_2} |W_s(r)|^2 \; dr = \frac{c\tau}{2} \tag{2.37}$$

and

$$\int_0^{\pi} \int_0^{2\pi} f^4(\theta,\phi) \; \sin\theta \; d\theta \; d\phi = \pi\theta_{3\text{dB}}^2/8\ln 2. \tag{2.38}$$

It is assumed that the attenuation, l, and the reflectivity, $\eta(r)$ are constant over the dr range. Thus,

$$\bar{P} = \frac{P_t g_t g_r c\tau \theta_{3\text{dB}}^2 \pi^3 |K_m|^2 Z_e}{2^{10} r^2 \mathsf{l}^2 \ln 2 \lambda^2} \; . \tag{2.39}$$

This equation is known as the *weather radar equation* and is the basis for sensitivity measurements throughout the remainder of this work.

2.2 Doppler Radar Theory

The main principle behind Doppler radar is similar to that of echo-location used by bats and dolphins. Instead of using sound waves, radars use radio or electromagnetic waves. Specifically, a transmitter emits electromagnetic waves at a particular frequency and then *listens* for the backscattered energy as the waves collide with scatterers.

2.2.1 Pulse Modulated Radar

A modern pulsed radar operates by transmitting a single pulse of a specific carrier frequency and extracting practical information from the returned signal. As can be seen in Figure 2.4, the carrier frequency, or RF (radio frequency) signal, is

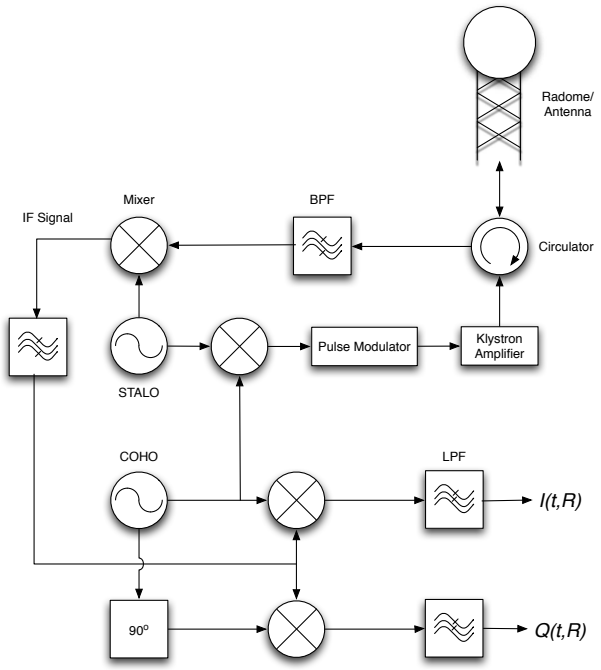

Figure 2.4: An illustration of a typical radar system. Note that the coherent radar has two down-conversion stages: the first to an intermediate frequency and the second to baseband, where only the Doppler frequency is present. As this is a model of a typical system, the amplifier need not be a klystron. Several other amplification options exist, including, traveling wave tube and solid state transistor amplifiers.

generated by the combination of the stable local oscillator (STALO) and coherent oscillator (COHO) signals. Next, the RF signal is passed, for a brief period due to the pulse modulator, to a microwave amplifier, which then emits an electromagnetic wave at the carrier frequency. From here, the pulsed wave is then focused

using a directive antenna into a particular beam shape. Beam shapes can vary greatly depending on antenna design parameters and define the volume illuminated by the radar. The pulse then propagates through the atmosphere where it strikes a target and is scattered back to the radar. Meanwhile, the radar has changed to receive mode and awaits the return signal. Under perfect reflection conditions, the received signal replicates the transmitted pulse with a time delay and is expressed as follows:

$$V(t,r) = A\exp\{j2\pi f(t-2r/c) + j\psi_{\mathrm{t}}\}U(t-2r/c)\,, \tag{2.40}$$

where A is the complex amplitude at the receiver, f is the carrier frequency, and $U(t)$ is the transmitted pulse shape defined as

$$U(t) = \begin{cases} 1 & 0 \le t \le \tau \\ \\ 0 & \text{otherwise} \end{cases}\,, \tag{2.41}$$

with r as the one-way range to the target, and τ as the pulse width. The echo phase of the signal (ψ_e) is defined as

$$\psi_e \equiv -\frac{4\pi r}{\lambda} + \psi_{\mathrm{t}} + \psi_{\mathrm{s}}\,, \tag{2.42}$$

which includes the carrier signal wavelength (λ), transmitted phase (ψ_{t}), and the scattering phase shift (ψ_{s}) (Doviak and Zrnić 1993). The ωt term is omitted because it has nothing to do with the echo and will be removed in the final processing stage. The received RF signals are then filtered and mixed with the STALO to create an intermediate frequency (IF) (generated by the COHO) that is more easily managed in the the final mixing to baseband, where the only dominate spectral component present is that of the Doppler frequency. The COHO also generates two reference signals used in the final mixing stages, called, *in-phase* and *quadrature*, which are separated in phase by 90°. When the received signal

is mixed with the in-phase and quadrature signals and after the application of a matched filter, the real (I) and imaginary (Q) components of the complex receive signal $V(t, r)$ are derived (Battan 1959; Doviak and Zrnić 1993; Meischner 2004). Specifically,

$$I(t,r) = \frac{|A|}{2}\cos(\psi_e)U(t-2r/c) \tag{2.43}$$

$$Q(t,r) = -\frac{|A|}{2}\sin(\psi_e)U(t-2r/c)\,. \tag{2.44}$$

While this model for a weather radar provides a good illustration of many traditional systems, much advancement in technology has changed the general form of weather radars today. For instance, a modern radar may utilize a digital receiver that is capable of performing the IF to baseband conversion using software defined radio (Meier et al. 2012). Instead of mixing analog signals to baseband, which can cause amplitude and phase mismatches, the IF signal is translated directly into the digital domain. From there, the quadrature operation is performed through a multiplication with patterns of zero, one and negative one, replicating a cosine and its 90° counterpart, a sine wave. An illustration of one such system design is given in Figure 2.5. Many of the components, mainly dealing with the RF signal processing, remain the same. However the digital components now play a large role in the generation of the IQ signals as well as generating the transmitted waveform. The encroachment of digital functionality into waveform generation has facilitated the advancement of pulse compression and advanced waveform manipulation, which many modern radars utilize today (Isom et al. 2011; Kurdzo et al. 2012; Pazmany and Bluestein 2009).

Regardless of the method used, the IQ signals are produced and it is possible to extract the velocity of the target from the echo phase, ψ_e. The assumption is that the transmit phase is time independent and the scattering phase shift is uniformly distributed over many scatterers and thus average to zero over many

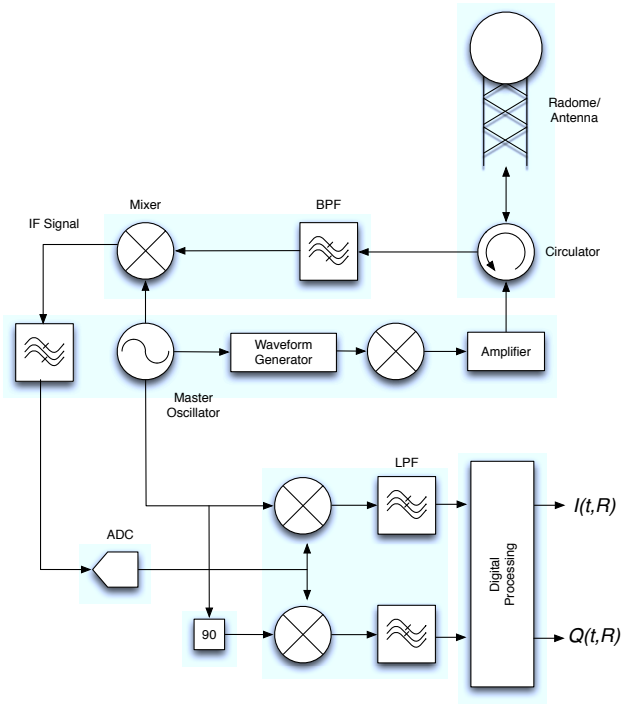

Figure 2.5: An illustration of a modern radar system. Again, the coherent radar has two down-conversion stages except this time, the final conversion to base-band is handled in the digital domain. The pulse modulator is replaced with an arbitrary waveform generator to facilitate pulse compression techniques.

samples. The time derivative of the signal phase is calculated to extract the *radial velocity* of the signal; the velocity component along the radar beam path

$$\frac{d\psi_e}{dt} = -\frac{4\pi}{\lambda}\frac{dr}{dt} = -\frac{4\pi}{\lambda}v_r = 2\pi f_d = \omega_d \,, \tag{2.45}$$

where ω_d is the angular Doppler frequency (radians per second).

2.2.2 Sampling Theory and Aliasing Effects

In order to process the signal, samples of both the in-phase and quadrature signals are taken at precise time intervals. The pulse width, τ, determines the *range resolution* by the following equation and is usually taken as the range-time sampling interval,

$$\Delta r = \frac{c\tau}{2} \,, \tag{2.46}$$

This process of transmitting and receiving pulses is repeated and a set of I and Q samples is gathered for future processing. The time between transmitted pulses is called the *pulse repetition time* (PRT). Similar to the dependence of the range resolution on the pulse width, the PRT determines the *maximum unambiguous range*, specifically,

$$r_{\mathrm{a}} = \frac{cT_s}{2} \,, \tag{2.47}$$

where T_s is the PRT. An illustration of a basic pulsed radar waveform is given in Figure 2.6.

The choice of PRT is critical in determining r_{a}, but it is also important in calculating the maximum unambiguous velocity or *aliasing velocity*, v_{a}. From Equation (2.45) it is known that $f_{\mathrm{d}} = -2v_r/\lambda$. Also, from the Nyquist sampling theorem, which states that a signal can be completely reconstructed provided that the highest frequency component present does not exceed one-half of the sampling

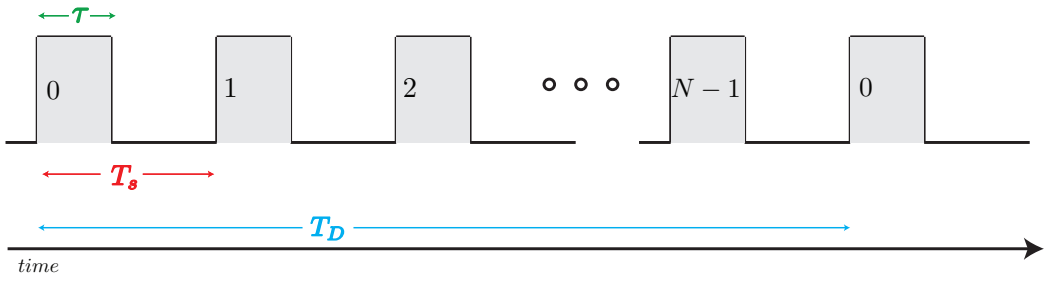

Figure 2.6: An illustration of a generic pulsed radar waveform. The width of the each pulse is represented by τ while the pulse repetition time is represented by T_s. The dwell time, or number of pulses utilized in calculating the spectral moments, is represented by T_D.

frequency (Stoica and Moses 2005; Mitra 2006), the following conclusion can be drawn:

$$f_{d,\max} = \frac{f_s}{2} \tag{2.48}$$

$$-\frac{2v_{r,\max}}{\lambda} = \frac{f_s}{2} \tag{2.49}$$

$$v_{\mathrm{a}} = \pm\frac{\lambda}{4T_s}\,. \tag{2.50}$$

Hence, both r_{a} and v_{a} depend upon the PRT creating what is known as the *Doppler dilemma*, i.e., $r_{\mathrm{a}}v_{\mathrm{a}} = c\lambda/8$ (Doviak and Zrnić 1993; Skolnik 2001). Thus, given a fixed wavelength, a trade-off must be investigated.

Many techniques have been developed that attempt to mitigate the Doppler dilemma. Utilizing alternating short and long PRTs, known as staggered PRTs, can remove velocity ambiguities (Tabary et al. 2006; Torres et al. 2004). Encoding the transmit pulse phase in a technique used to mitigate range ambiguities (Bharadwaj and Chandrasekar 2007; Sachidananda and Zrnić 1999). Additionally, multi-lag techniques have been shown to reduce the impact of second-trip contamination or radar returns from targets at distances greater than r_a (Cao

et al. 2011). Variations of these methods will be discussed further in subsequent sections.

2.3 Fundamentals of Weather Radar Signal Processing

2.3.1 Statistical Analysis of Weather Radar Signals

The in-phase and quadrature (I and Q) signals discussed previously can be considered as random variables if the motion of the scatterers is unpredictable, which is indeed the case (Doviak and Zrnić 1993). Further, if the scatterers within a radar resolution volume are large in number and no particular target is dominate, the *central limit theorem* holds and I and Q will have a Gaussian distribution. It is also important to note here that while physical processes are constantly evolving, the period over which the received samples are taken is small relative to the time necessary for substantial changes to occur in the atmosphere. Thus, it is appropriate to consider $V(t, r)$ as a *wide-sense stationary* (WSS) random process. Moreover, sample sequences produced by scatterers with statistically homogeneous properties are members of an *ergodic* ensemble, meaning, that temporal averages of a single member of the ensemble can be used to deduce the statistical parameters of the process (Doviak and Zrnić 1993; Shanmugan and Breipohl 1988).

To further explore weather signal statistics, it is beneficial to examine the *probability density function* (PDF). Both I and Q are independent random variables with Gaussian distribution and zero mean. Thus, the joint PDF of I and Q is a product of the individual PDFs

$$p(I, Q) = \frac{1}{2\pi\sigma^2} \exp\left(-\frac{I^2}{2\sigma^2} - \frac{Q^2}{2\sigma^2}\right) , \tag{2.51}$$

where σ^2 is the variance of I (same value for Q). The probabilities of the amplitude ($|V| = [I^2 + Q^2]^{1/2}$), phase (ψ_e), and power ($P = I^2 + Q^2$) can be shown to have Rayleigh, uniform, and exponential distributions, respectively, through the following equations:

$$p(|V|) = \frac{|V|}{2\sigma^2} \exp\left(-\frac{|V|^2}{2\sigma^2}\right) \tag{2.52}$$

$$p(\psi_e) = \begin{cases} \frac{1}{2\pi} & -\pi \leq \psi_e \leq \pi \\ 0 & \text{otherwise} \end{cases} \tag{2.53}$$

$$p(P) = \frac{1}{2\sigma^2} \exp\left(-\frac{P}{2\sigma^2}\right). \tag{2.54}$$

Example histograms of real weather data are presented in Figure 2.7. Note that the density functions do in fact approximately follow the Gaussian, Rayleigh, uniform, and exponential functions, as expected.

While the time-series samples gathered from the radar may reveal some information regarding the characteristics within the radar resolution volume, a more practical approach is to examine the *Doppler spectrum*, which is a power-weighted distribution of radial velocities within a radar resolution volume. Hence, a full characterization of the volume's scatterers can be obtained. It can be shown that the Doppler spectrum is the discrete time Fourier transform (DTFT) of the IQ sample autocorrelation function (ACF), which, for a complex WSS signal, the biased estimator is given by

$$\hat{R}(l) = \frac{1}{M} \sum_{m=0}^{M-|l|-1} V^*(m)V(m+l), \tag{2.55}$$

where $V(m)$ is the mth sample of M digitized complex received samples. The Doppler spectrum, or *power spectral density* (PSD), is then estimated by

$$\hat{S}(f) = T_s \sum_{l=-(M-1)}^{M-1} \hat{R}(l) e^{-j2\pi f T_s l}, \tag{2.56}$$

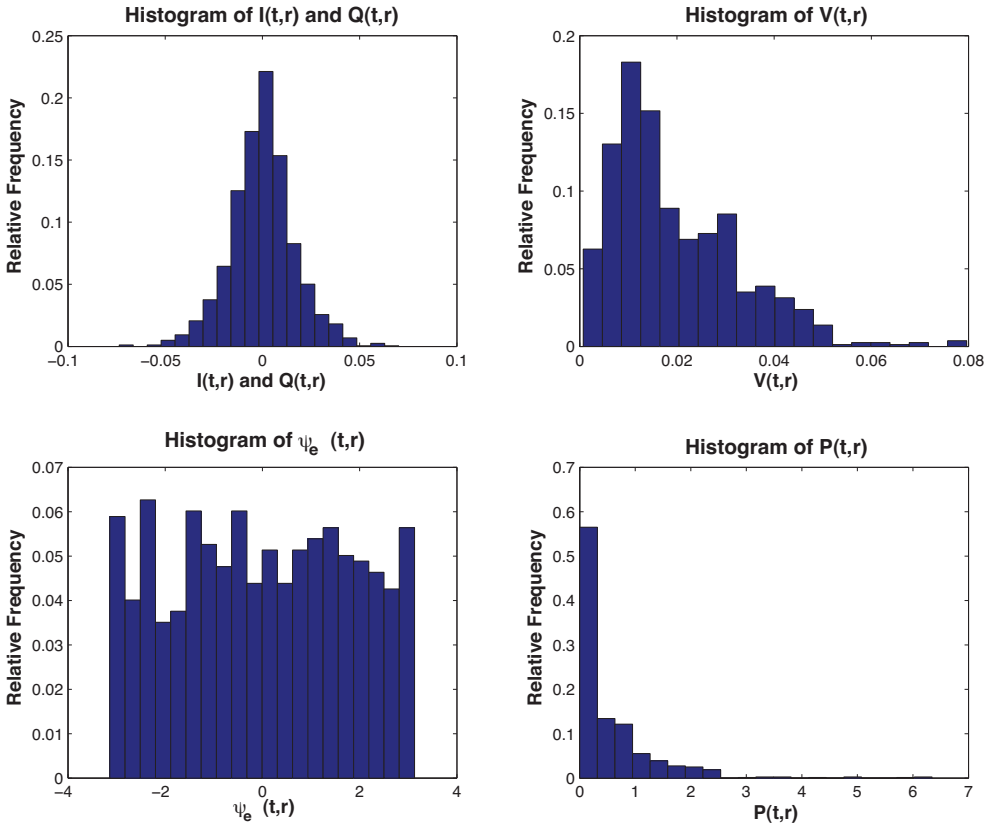

Figure 2.7: Histograms of real weather radar data acquired at the KDDC WSR-88D. The amplitude, phase, and power of the zero-mean Gaussian random variables I and Q produce Rayleigh, uniform, and exponential distributions, respectively.

which can also be written in the more common *periodogram* form

$$\hat{S}(f) = |Z(f)|^2 T_s/M\,, \tag{2.57}$$

where $Z(f)$ is the DTFT of the received signal $V(m)$ (Doviak and Zrnić 1993; Stoica and Moses 2005; Shanmugan and Breipohl 1988).

When using estimators to characterize signals, it is important to account for an attribute known as *bias*, or the difference between the expected value of the estimator and the true value. The bias is typically derived from the *mean squared error* (MSE), which is the bias squared summed with the estimate's *variance*. By the fact that $\hat{S}(f)$ was calculated with a finite set of pulses, there is an inherent bias resulting from the signal interaction with the rectangular window of length M (used to represent the truncated data). The spectral estimate is in fact the true spectrum convolved with a $sinc^2$ function and results in spectral *leakage*, or transferring power from bands containing most of the signal power to bands containing little or none (Stoica and Moses 2005). To reduce this effect, unit weights applied to the time-series data prior to the ACF calculation are modified according to an appropriate *window function*. Typical functions include the von Hann, Hammming, and Blackman-Harris windows (Mitra 2006). The window function amplitudes smoothly transition between zero and one in the time domain resulting in a wider spectral main lobe but lower sidelobes, which culminates to a loss in resolution, but less spectral leakage and lower variance when compared to a rectangular window (Stoica and Moses 2005).

Beyond window functions, there exist many other spectral processing techniques that improve the accuracy of the PSD estimation (Stoica and Moses 2005).

For example, the Bartlett Method splits the available samples into L separate groups of M samples, calculates the PSD of each subset and averages the results.

$$\hat{S}(f) = \frac{1}{L}\sum_{i=1}^{L}|Z_i(f)|^2 \tag{2.58}$$

$$Z_i(f) = \frac{1}{M}\sum_{m=1}^{M}V(m)e^{-j2\pi fT_s m} \tag{2.59}$$

This technique reduces the resolution of the PSD by a factor of L, but also reduces the variance of the estimate by the same factor.

A variation of this method, called the Welch Method, allows the sample subsets to overlap and additionally applies a window function weighting to each subset. It is recommended that a 50% overlap be maintained between subsets (Stoica and Moses 2005). The goal of this extension of the Bartlett Method is twofold. First, the overlapping samples provide more periodograms to be averaged thus reducing the variance. Second, the window functions attempt to gain some control over the bias of the PSD estimation (leakage). The windowing also *decorrelates* the adjacent subsets, resulting in an improved reduction in the variance.

There exist many additional varieties of PSD estimation techniques and they will be discussed further in Chapter 3. For now, the derivation of practical spectral parameters will be presented.

2.3.2 Spectral Moment Estimation

The Doppler spectrum is often assumed to have a Gaussian shape due to the independent factors that contribute to its broadening. When performing analysis on weather radar data, three primary parameters are considered:*reflectivity*, *radial velocity*, and *spectrum width*. The latter two are exactly the first and square root of the second spectral moments while reflectivity is a value derived from the radar equation and calibrated to normalize the zeroth moment, which is the expected

value of the weather signal and depends on the distance to the target (Doviak and Zrnić 1993; Shanmugan and Breipohl 1988). Thus, it is convenient to assume

$$S(v) = \frac{S}{(2\pi)^{1/2}\sigma_v} \exp[-(v_r - \bar{v}_r)^2/2\sigma_v^2] + \frac{2\tilde{N}T_s}{\lambda}\,, \tag{2.60}$$

where S is the signal power, $\tilde{N}$ is the noise power, $\bar{v}_r$ is the mean radial velocity, and σ_v is the velocity spectrum width. Note here that the frequency units in Equation (2.56) have been converted to Doppler velocity, for convenience. As before, the ACF is calculated as the inverse Fourier transform of $S(v)$.

$$R(mT_s) = S \exp\left\{[-8(\pi\sigma_v m T_s/\lambda)^2]\right\} \exp\left\{-j4\pi\bar{v}_r m T_s/\lambda\right\} + \tilde{N}\delta_m\,, \tag{2.61}$$

where δ_m is the Kronecker delta function.

Using the weather radar Equation (2.39), reflectivity is derived from the estimate of the zeroth moment of the radar signal, and is given by the following for a length-M set of samples,

$$\hat{P} = \frac{1}{M}\sum_{m=o}^{M-1} P_m\,, \tag{2.62}$$

where P_m is $|V(m)|^2$ and the M samples are separated by T_s. This is analogous to calculating the ACF at lag zero or

$$\hat{P} = \hat{R}(0) = \frac{1}{M}\sum_{m=0}^{M-1} V^*(m)V(m)\,, \tag{2.63}$$

A long dwell time is useful for improvement of the power estimation but lowers the update speed of the radar (Doviak and Zrnić 1993).

While spectral moment calculations can be performed in the frequency domain, it is more computationally efficient to utilize time domain covariance processing (Doviak and Zrnić 1993). Equation (2.61) is used in this manner to obtain the following estimators of radial velocity and spectrum width

$$\hat{v}_r = -(\lambda/4\pi T_s)\arg\left[\hat{R}(T_s)\right] \tag{2.64}$$

and

$$\hat{\sigma}_v = (\lambda/2\pi T_s 6^{1/2}) \left| \ln \frac{|\hat{R}(T_s)|}{|\hat{R}(2T_s)|} \right|^{1/2} \text{sgn} \left[\ln \frac{|\hat{R}(T_s)|}{|\hat{R}(2T_s)|} \right] . \tag{2.65}$$

Note that the sgn[·] function is used as an identifier of unusable data, i.e., when the logarithm is negative in the case of narrow spectrum width and low signal strength.

The spectral moment estimates are then used to produce the three primary radar products used by meteorologists: reflectivity, mean radial velocity, and spectrum width. As previously mentioned, the radial velocity and spectrum width estimates are used directly by meteorologists. However, to make use of the zeroth moment, it is essential that the values are normalized. The reflectivity is calculated by correcting the zeroth moment for losses to due range and atmospheric attenuation. Additional losses are accounted for by a calibration term determined after comparisons with other like radars. The estimates calculated hereto include both the desired weather signal as well as noise and unwanted clutter. Alternative methods exist to mitigate the influence of noise in the moment estimations. For example, multi-lag estimators have been used to calculate spectrum power and spectrum width. A discussion of the multi-lag technique follows.

2.3.2.1 Multi-Lag Estimators

Traditionally, the auto-correlation function (ACF) is used to calculate the three primary spectral moments: power, mean spectral frequency and spectrum width. It is well known that as the signal-to-noise (SNR) decreases, the quality of these estimates decrease as well, though the effect is more noticeable with the power estimation (see (2.61)). The equations for calculating the spectral power and width using several multi-lag techniques are given by Zhang et al. (2004), Lei et al. (2009), and Cao et al. (2011). Since these estimates are calculated without

utilizing the zero-lag parameter of the ACF, the accuracy of the estimates is improved in many cases.

Lag 1 – 2 Estimator

$$\hat{P} = \frac{|\hat{R}(T_s)|^{4/3}}{|\hat{R}(2T_s)|^{1/3}} \tag{2.66}$$

$$\hat{\sigma}_v = \frac{\lambda}{\sqrt{24}\pi T_s}(\ln|\hat{R}(T_s)| - \ln|\hat{R}(2T_s)|)^{1/3} \tag{2.67}$$

Lag 1 – 3 Estimator

$$\hat{P} = \frac{|\hat{R}(T_s)|^{6/7} \cdot \hat{R}(2T_s)||^{3/7}}{|\hat{R}(3T_s)|^{2/7}} \tag{2.68}$$

$$\hat{\sigma}_v = \frac{\lambda}{28\pi T_s}(11 \cdot \ln|\hat{R}(T_s)| + 2 \cdot \ln|\hat{R}(2T_s)| - 13 \cdot \ln|\hat{R}(3T_s)|)^{1/2} \tag{2.69}$$

Lag 1 – 4 Estimator

$$\hat{P} = \frac{|\hat{R}(T_s)|^{54/86} \cdot |\hat{R}(2T_s)|^{39/86} \cdot |\hat{R}(3T_s)|^{14/86}}{|\hat{R}(4T_s)|^{21/86}} \tag{2.70}$$

$$\hat{\sigma}_v = \frac{\lambda}{4\sqrt{129}\pi T_s}(13 \cdot \ln|\hat{R}(T_s)| + 7 \cdot \ln|\hat{R}(2T_s)| - 3 \cdot \ln|\hat{R}(3T_s)| - 17 \cdot \ln|\hat{R}(4T_s)|)^{1/2} \tag{2.71}$$

Note that the spectrum width lag 1-2 estimator is the same as was used in the previous section, Equation (2.65). In general, both the bias and standard deviation of the multi-lag estimators are lower than the conventional techniques. For a more detailed analysis of the multi-lag estimators, see Lei et al. (2009).

2.4 Generalization to Multi-Static Doppler Radar

Thus far, the discussion regarding the radar range equation and subsequent parameter estimation has been focused on mono-static systems, or a system in which a single radar acts as transmitter and receiver (see Figure 2.4). Some systems utilize radars separated over great distances to gather additional knowledge about a target (i.e., detect a target moving orthogonal to the beam direction). Such

systems can be comprised of two or more radars with one or more acting as the transmitting source. Other systems might have separate antennas used for transmitting and receiving while occupying nearly identical locations (co-located). For either arrangement, slight modifications to (2.31) are necessary for completeness.

Recall that σ_b refers to the backscatter cross section and is proportional to the amount of energy that is reflected back along the radar beam path. For a multi-static system, σ_b is replaced with the generic scatter term, $\sigma(\theta', \phi')$, which is proportional to the energy scattered toward θ' and ϕ'. An image depicting such a scenario is given in Figure 2.8. Note that the receive path and receive

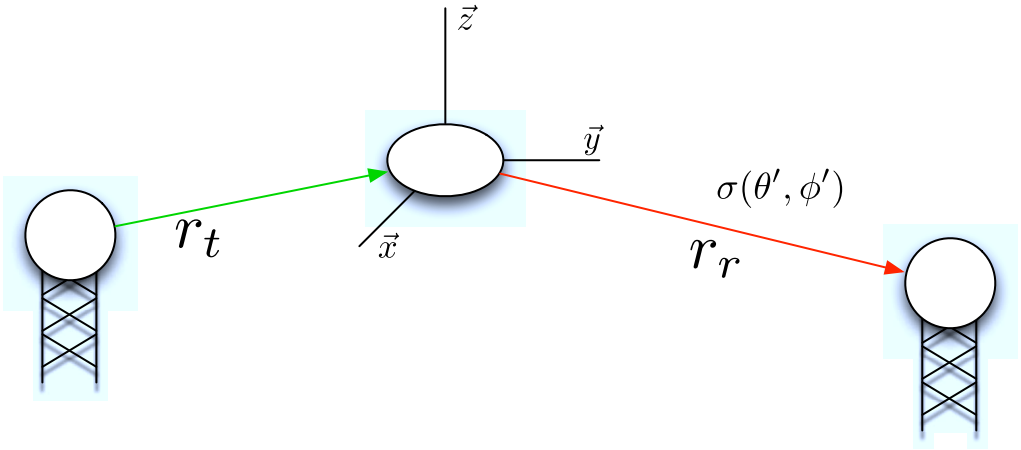

Figure 2.8: An illustration of a bi-static radar configuration based on a single scatterer. It is apparent that the radar range equation will be altered to reflect the differences in the transmit and receive beam paths, as well as the individual system characteristics. Note that the backscattered energy is now replaced with a generic scattering term, which can correspond to any desired direction, including back to the transmitting radar.

system need not be co-located with the transmitting system. Additionally, since multiple radar systems are involved, system specific parameters such as gain and beam patterns will not necessarily be identical. Thus, including separate terms

for the transmit and receive gain and normalized beam patterns is advisable. Moreover, the transmit→target and target→receive distances likely will differ (as will the attenuation) and must be included in the calculation separately.

Combining the above modifications into (2.31) gives:

$$P_r = \frac{P_t g_t g_r \lambda^2 \sigma(\theta', \phi') f_t^2(\theta, \phi) f_r^2(\theta, \phi)}{(4\pi)^3 r_t^2 r_r^2 l_t l_r}. \tag{2.72}$$

In the case of a co-located multi-static system, where the transmit and receive antennas are pointing in the same direction and located near each other, σ_b is still valid because of the relatively small difference between r_t and r_r.

In the next chapter, a detailed discussion of analogies between the temporal, frequency, spatial and angular domains is conducted. It will be shown that many of the same techniques applied in this chapter are equally valid when applied to spatially distributed antennas.

Chapter 3

Analogies in Signal and Array Processing

3.1 Radar Signal Processing

There are many techniques available for the extraction of meaningful parameters from time-series data. Auto-covariance techniques are well known and are quite robust in both accuracy and computation time. Modern computing technology has allowed additional techniques to become more prevalent and feasible for data processing with the the added benefit of reducing bias and variance of the estimates. What follows is a discussion of analysis techniques designed to provide accurate estimations of power distribution over frequency from finite records of stationary data sequences (Stoica and Moses 2005).

3.1.1 Signal Model

It is useful to define a model through which all the subsequent signal processing discussion will be facilitated. A common representation of signal processing algorithms is that of a linear time-invariant filter. Input, $e(t)$, passes through a system with impulse response h_k. Thus,

$$H(z) = \sum_{k=-\infty}^{\infty} h_k z^{-k} \tag{3.1}$$

where z^{-1} denotes the unit delay such that $z^{-1}e(t) = e(t-1)$ (Stoica and Moses 2005). The output of the linear time-invariant system is defined as

$$y(t) = H(z)e(t) = \sum_{k=-\infty}^{\infty} h_k e(t-k) \ . \tag{3.2}$$

If $z = e^{j\omega}$, with $\omega = 2\pi f$, the transfer function of the filter is

$$H(\omega) = H(z)\Big|_{z=e^{j\omega}} = \sum_{k=-\infty}^{\infty} h_k e^{-j\omega k} \ . \tag{3.3}$$

It is prudent at this point to review and define some terms that will be used throughout this chapter. First, the motivation for radar spectral processing has already been stated, but a particular emphasis is made on the informal statement of the goal:

From a finite record of a stationary data sequence, estimate how the total power is distributed over frequency. (3.4)

The definition of the desired power distribution is

$$S(\omega) = |Y(\omega)|^2 \ , \tag{3.5}$$

where

$$Y(\omega) = \sum_{t=-\infty}^{\infty} y(t)e^{-j\omega t} \tag{3.6}$$

is the DTFT of $y(t)$. Following a simple derivation, Parseval's Theorem states

$$\begin{aligned} \frac{1}{2\pi}\int_{-\pi}^{\pi} S(\omega)\ d\omega &= \frac{1}{2\pi}\int_{-\pi}^{\pi} \sum_{t=-\infty}^{\infty}\sum_{s=-\infty}^{\infty} y(t)y^*(s)e^{j\omega(t-s)}\ d\omega \\ &= \sum_{t=-\infty}^{\infty}\sum_{s=-\infty}^{\infty} y(t)y^*(s)\left[\frac{1}{2\pi}\int_{-\pi}^{\pi} e^{-j\omega(t-s)}\ d\omega\right] \\ &= \sum_{t=-\infty}^{\infty} |y(t)|^2 \ . \end{aligned} \tag{3.7}$$

Note that $\frac{1}{2\pi}\int_{-\pi}^{\pi} e^{j\omega(t-s)} = \delta_{t,s}$ where

$$\delta_{t,s} = \begin{cases} 1 & t = s \\ 0 & \text{otherwise} \end{cases} \tag{3.8}$$

is the Kronecker delta function (Mitra 2006; Shanmugan and Breipohl 1988). In a sense, Parseval's Theorem is a conservation of energy analogy since the energy content of the time-series data is the same as the frequency data.

The next pair of parameters that require definition are the autocorrelation and autocovariance sequences. In both cases, WSS random processes are assumed. The autocorrelation sequence is defined as

$$R(k) = \sum_{t=-\infty}^{\infty} y(t)y^*(t-k) \tag{3.9}$$

and the autocovariance sequence is

$$r(k) = \sum_{t=-\infty}^{\infty} (y(t) - \bar{y})(y(t-k) - \bar{y})^* = R(k) - \bar{y}^2 \ . \tag{3.10}$$

If it is assumed that the output of the system is a random variable with

$$E\{y(t)\} = 0 \ \forall \ t \ , \tag{3.11}$$

the autocovariance sequence is equivalent to the autocorrelation sequence (Stoica and Moses 2005). The autocovariance sequence has two properties that will prove useful, one being the symmetry of the function, that is $r(k) = r^*(-k)$, and the largest value occurs when $k = 0$. From the definition of the autocovariance sequence, an autocovariance matrix can be constructed as

$$\begin{aligned} \mathbf{R}_m &= \begin{bmatrix} r(0) & r^*(1) & \dots & r^*(m-1) \\ r(1) & r(0) & \ddots & \vdots \\ \vdots & \ddots & \ddots & r^*(1) \\ r(m-1) & \dots & r(1) & r(0) \end{bmatrix} \\ &= E\left\{ \begin{bmatrix} y^*(t-1) \\ \vdots \\ \vdots \\ y^*(t-m) \end{bmatrix} \begin{bmatrix} y(t-1) & \dots & y(t-m) \end{bmatrix} \right\} \end{aligned} \tag{3.12}$$

From the definition of the autocovariance, it is possible to return to the discussion of the power spectral density. From the previous sections, it is known that the PSD is the Fourier transform of the ACF, or redefined here

$$S(\omega) = \sum_{k=-\infty}^{\infty} R(k) e^{-j\omega k} \ . \tag{3.13}$$

The PSD can also be defined as (Stoica and Moses 2005; Mitra 2006)

$$S(\omega) = \lim_{N\to\infty} E\left\{ \frac{1}{N} \left| \sum_{t=1}^{M} y(t) e^{-j\omega t} \right|^2 \right\} \ . \tag{3.14}$$

The next section will explore several techniques for estimation of the PSD from temporal, discrete data.

3.1.2 Non-Parametric Spectral Estimation

3.1.2.1 Periodogram and Window Functions

The periodogram was used in the previous chapter to estimate the Doppler weather spectrum, though its applications are much broader. An estimate of the PSD can be obtained via the periodogram spectral estimator by

$$\hat{S}_p(\omega) = \frac{1}{N} \left| \sum_{t=1}^{N} y(t) e^{-j\omega t} \right|^2 \ . \tag{3.15}$$

Related to the periodogram is the correlogram defined as

$$\hat{S}_c(\omega) = \sum_{k=-(N-1)}^{N-1} \hat{R}(k) e^{-j\omega k} \tag{3.16}$$

where

$$\hat{R}(k) = \frac{1}{N} \sum_{t=k+1}^{N} y(t) y^*(t-k) \qquad 0 \le k \le N-1 \ , \tag{3.17}$$

and is known as the biased autocovariance sequence estimate (Stoica and Moses 2005). There are two reasons for using the biased estimator instead of the unbiased. First, the unbiased estimator can sometimes yield erratic values for large

k, which is mitigated by Equation (3.17). Second, the covariance matrix is not guaranteed to be positive definite if the unbiased estimator is utilized. This could result in negative PSD values, which is undesirable (Stoica and Moses 2005).

It can be shown that the periodogram and correlogram methods are equivalent through the following proof (Stoica and Moses 2005):

$$\begin{aligned}
\hat{S}_p(\omega) &= \frac{1}{N}\left|\sum_{t=1}^{N} y(t)e^{-j\omega t}\right|^2 \\
&= \frac{1}{N}\sum_{t=1}^{N}\sum_{s=1}^{N} y(t)y^*(s)e^{-j\omega(t-s)} \\
&= \sum_{s=1}^{N}\left(\frac{1}{N}\sum_{t=k+1}^{N} y(t)y^*(t-k)\right)e^{-j\omega k} \qquad 0 \le k \le N-1 \\
&= \sum_{t-k=1}^{t-k=N} \hat{R}(k)e^{-j\omega k} \\
&= \sum_{k=-(N-1)}^{N-1} \hat{R}(k)e^{-j\omega k} \\
&= \hat{S}_c(\omega)
\end{aligned} \tag{3.18}$$

A measure of the performance of the periodogram can be found in the bias and variance, which are both related to the MSE, defined as

$$\begin{aligned}
\text{MSE} &= E\left\{|\hat{g}-g|^2\right\} \\
&= E\left\{|\hat{g}-E\{\hat{g}\}+E\{\hat{g}\}-g|^2\right\} \\
&= E\left\{|\hat{g}-E\{\hat{g}\}|^2\right\}+|E\{\hat{g}-g\}|^2 \\
&\qquad +2\text{Re}\left[\left(E\{\hat{g}-E\{\hat{g}\}\}\right)^*\left(E\{\hat{g}-g\}\right)\right] \\
&= \text{var}\{\hat{g}\}+|\text{bias}\{\hat{g}\}|^2
\end{aligned} \tag{3.19}$$

As mentioned previously, the bias of the periodogram method is physically visible through the *leakage* into sidelobes, though the estimate is unbiased at the frequency of interest. It is also interesting to note that the periodogram is

unbiased in the case of white noise. Variance manifests as erratic values in the PSD estimator. As the periodogram is an *inconsistent estimator*, the estimated PSD values may fluctuate around the true PSD, but the mean and variance of said values are equivalent to the true PSD. One common method to reduce the bias of the periodogram estimator is to apply a weighting scheme over the finite length data sequence, known as a *window*, which will be described in the next section.

3.1.2.2 Window Functions

Various window functions have been developed that act to reduce spectral leakage and improve performance of the periodogram method by reducing the variance through local weighted averaging. One caveat of the window method is the simple fact that a window cannot be both time and band limited (Stoica and Moses 2005; Mitra 2006). In other words, the frequency resolution of the estimator cannot be infinitely small with a finite set of data samples. Thus, there exists a tradeoff between the resolution that can be achieved and the improvement in variance. As a general rule of thumb, the length of the lag window should be chosen as $M \leq N/10$, which reduces the variance of the estimated PSD by a factor of nine when compared with the periodogram (Stoica and Moses 2005).

Some commonly used window functions are listed in Table 3.1 along with the equations, main lobe width and sidelobe level (Stoica and Moses 2005). Temporal and spectral shapes of the window functions in Table 3.1 are given in Figure 3.1. The temporal/sample domain is shown on the left side of the figure while the discrete Fourier transform (DFT)/frequency response is shown on the right. Each window has a length of $M = 30$ and the DFT is calculated utilizing zero padding. Zero padding appends a set of zeros to a data sequence, causing the DFT to be calculated at additional points in the frequency domain. This action does *not*

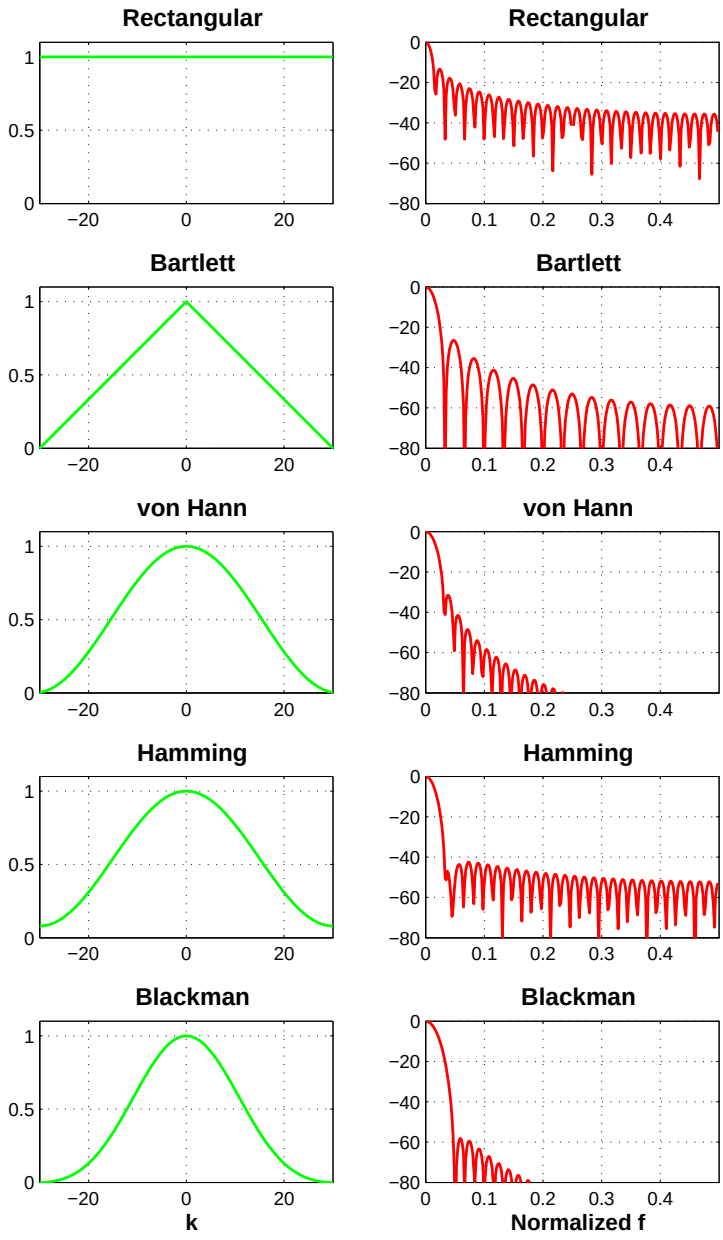

Figure 3.1: Examples of five window functions and their DFTs. Parameters specific to each window function are given in Table 3.1. For each figure, $M = 30$, and the DFTs were zero padded to 512 points.

Table 3.1: Common Window Functions

Window Function	**Equation**	**Main Lobe Width (radians)**	**Sidelobe Level (dB)**
Rectangular	$w(k) = 1$	$2\pi/M$	-13
Bartlett	$w(k) = \frac{M-k}{M}$	$4\pi/M$	-25
von Hann	$w(k) = 0.5 + 0.5\cos\left(\frac{\pi k}{M}\right)$	$4\pi/M$	-31
Hamming	$w(k) = 0.54 + 0.46\cos\left(\frac{\pi k}{M-1}\right)$	$4\pi/M$	-41
Blackman	$w(k) = 0.42 + 0.5\cos\left(\frac{\pi k}{M-1}\right)$ $+0.08\cos\left(\frac{\pi k}{M-1}\right)$	$6\pi/M$	-57

improve the spectral resolution, however, it does provide an interpolated estimate of the additional points in the spectrum.

Window functions are but one variation of the periodogram estimator that provides improvement in the assessment parameters of bias and variance.

3.1.2.3 Welch Method

Often, when making measurements, it is beneficial to make multiple estimates and average the results, which ultimately leads to more accurate estimates of the parameter due to the fact that the mean is an unbiased estimator (Shanmugan and Breipohl 1988). In a similar fashion, the periodogram estimator variance can be improved by averaging the results of several estimates at the expense of resolution (Stoica and Moses 2005). The Welch method allows the periodogram to be calculated for several subsets of the data, which can also be windowed, if desired. Let

$$y_j(t) = y((j-1)K + t), \qquad \begin{aligned} t &= 1, \ldots, M \\ j &= 1, \ldots, S \end{aligned} \tag{3.20}$$

where y_j is the $j$the subset within the data. Depending on the value of K, the subsets can be overlapping, if needed. In the event that $K = M$, a special case is generated called the Bartlett method (Stoica and Moses 2005). A recommended value for K is $M/2$, which results in half of the current subset being used as half of the next spectrum estimate and is given as:

$$\hat{S}_j(\omega) = \frac{1}{MP_{\text{win}}} \left| \sum_{t=1}^{M} \nu(t) y_j(t) e^{-j\omega t} \right|^2 , \tag{3.21}$$

where the windowed periodogram is normalized by the power of the window function $\nu(t)$, which is calculated as

$$P_{\text{win}} = \frac{1}{M} \sum_{t=1}^{M} |\nu(t)|^2 . \tag{3.22}$$

Then, by averaging the subset periodograms, the Welch estimator provides an estimate for the power spectrum of the signal

$$\hat{S}_W(\omega) = \frac{1}{L} \sum_{l=1}^{L} \hat{S}_j(\omega) . \tag{3.23}$$

As an example of the Welch method, Figure 3.2 illustrates how the periodograms of subsets within the data are combined to form the power spectrum estimate. Time series data representing simulated weather signals collected with a radar are presented at the top of the figure. Green and blue sinusoidal plots are the real and imaginary parts of the signal, respectively. The data are produced via the Gaussian model for weather signals and are adapted from Zrnić (1975), which is also discussed in Chapter 2. The simulated spectrum is generated with the parameters listed in Table 3.2. Each Welch subset within the time series is used to calculate a separate windowed periodogram. It is the additional subsets, which are gained by allowing overlapping samples, that account for the increased accuracy of the Welch method over the Bartlett or periodogram techniques. Further, the temporal windowing reduces the correlation between subsets by reducing

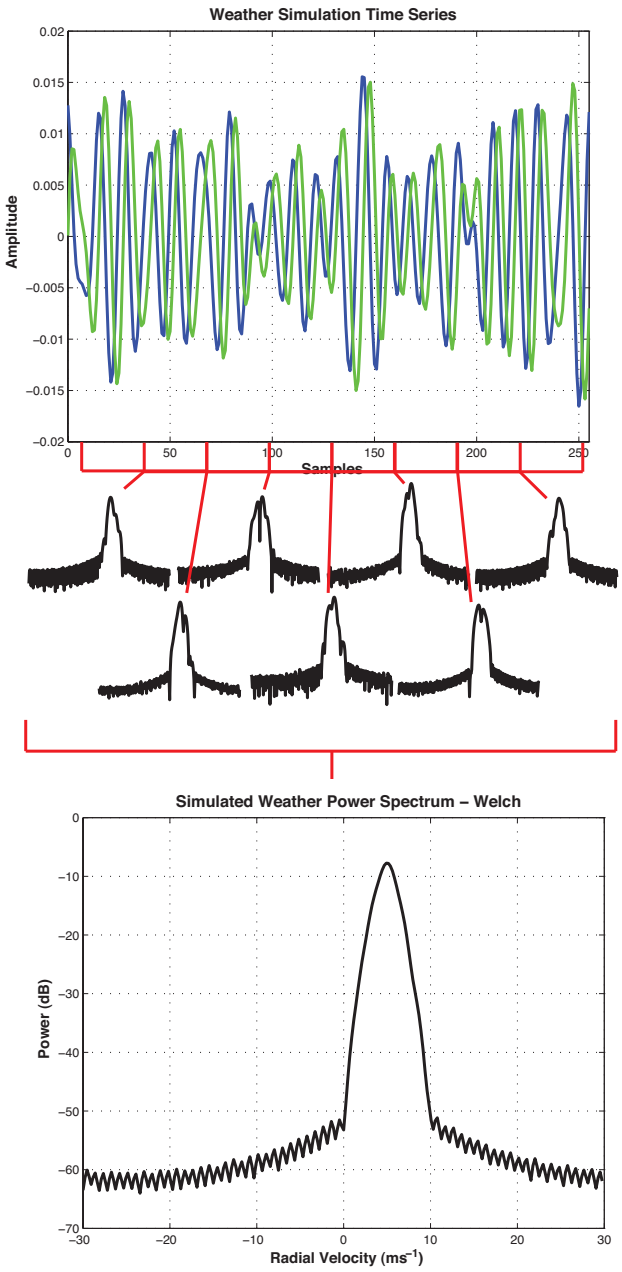

Figure 3.2: An example of the Welch method. Blue and green lines in the top figure represent the real and imaginary parts of a time-series signal, respectively. Periodograms from each subset of data are given and the final average value is presented in the bottom figure. The overlapping subsets allow for half of the previous set and half of the subsequent subset to comprise each individual subset ($K = M/2$).

Table 3.2: Weather Signal Simulator Parameters

Parameter	**Value**
SNR	55 dB
N	256 samples
$\bar{v}_{\mathrm{r}}$	5 $\mathrm{m\,s^{-1}}$
v_{a}	30 $\mathrm{m\,s^{-1}}$
σ_{v}	1 $\mathrm{m\,s^{-1}}$
P_{peak}	1.0
M	64
K	32
Window	Hamming

the effect of the subset edges on the spectra, thus reducing the variance of the estimator (Stoica and Moses 2005).

To compare the non-parametric power spectrum estimator techniques discussed in this section, 100 weather simulations, like the one discussed for the Welch technique, were run and the bias and variance of each velocity bin was calculated. The results of the simulation are presented in Figure 3.3. The bias measurements are the mean value of the 100 runs and are given in Figure 3.3(a). The model spectrum is given as well as one example of the model with noise. The periodogram, Bartlett and Welch estimators are shown. Note that the periodogram is the least biased. The Welch is next followed by the Bartlett method. The variance of the estimators is given in Figure 3.3(b). As expected, the Welch method has the lowest variance for the 100 runs. The high leakage associated with both the Bartlett and Welch techniques is evident in the noise regions of the spectrum. As the Bartlett method does not use a temporal window function, it

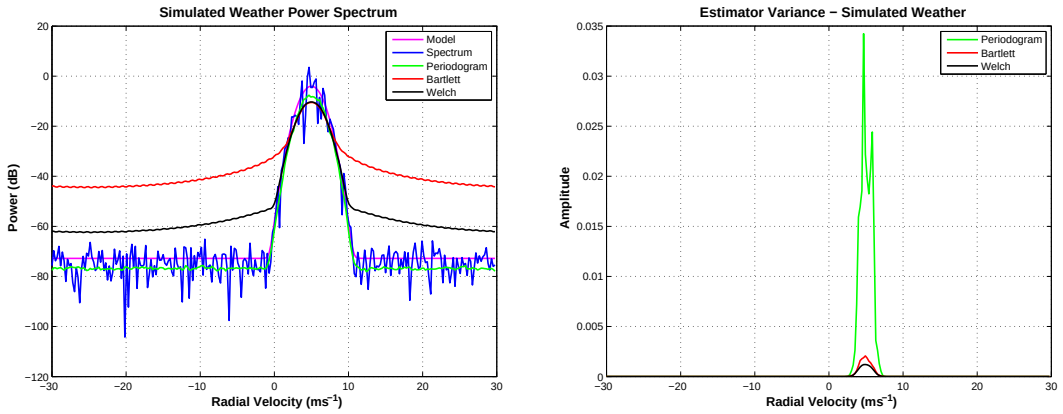

(a) (b)

Figure 3.3: A comparison of spectral processing algorithms. Values from Table 3.2 are used to simulate time-series weather data. The resulting bias from 100 simulations for the periodogram, Bartlett and Welch techniques are given in (a). The associated variance for the three methods is given in (b). Note that the periodogram has the lowest bias but the highest variance. The Bartlett and Welch techniques both act to reduce the variance in the spectrum estimation.

is expected that the leakage is greater than the Welch method, and this is indeed the case.

A review of the basic non-parametric spectral estimation techniques as well as a definition of the classical approach to spectral analysis has been presented. Spectral resolution was not examined at this point in the study, but will be included in subsequent tests. From here, adaptive techniques will be discussed that attempt to make the most of a finite sample set with the goal of estimating a continuous spectrum.

3.1.3 Adaptive Spectral Estimation

One of two paths can be utilized in the attempt to gain spectral information from a process. The first involves making assumptions about a signal in the form of a model. With this path, one first defines a set of parameters known to belong to the signal of interest and then attempts to calculate the value of these parameters. The second path involves no assumptions regarding the signal, other than stationarity. It is necessary, however, for finite samples estimating a continuous process, to assume that the the signal is constant over a particular bandwidth. This leads to the classic tradeoff between bandwidth/resolution and statistical stability (Stoica and Moses 2005).

In an effort to obtain better resolution and statistical stability, the classical techniques described in the previous section represent data-independent methods of spectral estimation. While no attempt to define a model for weather data spectral estimation is made, the data itself can be used to help improve statistical stability and, in some cases, resolution. The techniques described in this section will utilize the data itself in the production of PSD estimation.

3.1.3.1 Spectral Estimation: Revisited

To explore many of the adaptive spectral estimation techniques, it is beneficial to imagine the spectral estimation problem as a series of estimates over narrow frequency bands, or bandpass filters (Stoica and Moses 2005). Some stipulations of the estimation are listed here:

(i) $S(\omega)$ is nearly constant over the filter passband

(ii) The filter gain is unity over the passband, zero elsewhere

(iii) Power of the filtered signal is consistent with the true signal power

As an example, the familiar periodogram technique will be redefined through this new approach.

At a particular frequency ($\tilde{\omega}$), the periodogram estimator is

$$\begin{aligned} \hat{S}_p(\tilde{\omega}) &= \frac{1}{N}\left|\sum_{t=1}^{N} y(t)e^{-i\tilde{\omega}t}\right|^2 \\ &= \frac{1}{\beta}\left|\sum_{k=0}^{N-1} h_k y(N-k)\right|^2 , \end{aligned} \tag{3.24}$$

where β is the filter bandwidth. This translates directly to a convolution sum with infinite zeros appended.

$$y_F(N) = \sum_{k=0}^{\infty} h_k y(N-k) \tag{3.25}$$

$$h_k = \begin{cases} e^{i\tilde{\omega}k}/N & \text{for } k = 0,\ldots,N-1 \\ 0 & \text{otherwise} \end{cases} \tag{3.26}$$

This results in the realization that

$$\begin{aligned} H(\omega) &= \sum_{k=0}^{\infty} h_k e^{-i\omega k} \\ &= \frac{1}{N}\frac{e^{iN(\tilde{\omega}-\omega)}-1}{e^{i(\tilde{\omega}-\omega)}-1} \\ &= \frac{1}{N}\frac{\sin[N\tilde{\omega}-\omega)/2]}{\sin[(\tilde{\omega}-\omega)/2]}e^{i(N-1)(\tilde{\omega}-\omega)/2} \end{aligned} \tag{3.27}$$

which is exactly the Fourier transform of a rectangular window centered at $\tilde{\omega}$ over the range of $\Delta\omega = [-\pi, \pi]$. While the response of the filter does meet the criteria laid out earlier, it results in poor resolution and spectral leakage values (Stoica and Moses 2005). From here, other techniques will be defined that improve upon this basic method.

3.1.3.2 Capon Method

In the periodogram approach, no effort was made to alter the bandpass filter for enhanced performance. The Capon method does try to alter the filter by making use of one major piece of information: the data itself (Stoica et al. 1999; Stoica and Moses 2005). We begin with a filter of length $m + 1$ and response

$$h = [h_0, h_1, \ldots h_m]^*. \tag{3.28}$$

The output of the filter at time t is

$$y_F(t) = \sum_{k=0}^{m} h_k y(t-k) = h^* y(t) \tag{3.29}$$

The power of the output is then

$$E\{|y_F(t)|^2\} = h^* R h \tag{3.30}$$

where R is the covariance matrix of the filter output. The filter response at a given frequency ω is given by

$$H(\omega) = \sum_{k=0}^{m} h_k e^{-i\omega k} = h^* a(\omega) \tag{3.31}$$

$$a(\omega) = [1 \; e^{-i\omega} \ldots e^{-im\omega}]^T \tag{3.32}$$

Thus, for the filter to satisfy criteria (i), (ii), and (iii) laid out in Section 3.1.3.1, it is reasonable to minimize the total power of the output while constraining the center frequency to be unchanged. Mathematically, the problem is states as

$$\min_h h^* R h \quad \text{subject to } h^* a(\omega) = 1 \tag{3.33}$$

The solution is obtained using a Lagrange multiplier, γ,

$$\begin{aligned} L(h,\gamma) &= h^*Rh + \gamma[h^*a(\omega) - 1] && (3.34) \\ &= h^*Rh + \gamma h^*a(\omega) - \gamma && (3.35) \end{aligned}$$

Taking the partial derivative with respect to h and setting the result equal to zero locates a local minimum and provides a solution for $h(\gamma)$.

$$\begin{aligned} \frac{\partial L}{\partial h} &= 2Rh + \gamma a(\omega) = 0 \\ h &= -\frac{\gamma}{2}R^{-1}a(\omega) && (3.36) \end{aligned}$$

Finally, the constraint equation is used to solve for γ, providing a final solution for h

$$\begin{aligned} h^*a(\omega) &= -\frac{\gamma}{2}a^*(\omega)R^{-1}a(\omega) = 1 \\ -\frac{\gamma}{2} &= \frac{1}{a^*(\omega)R^{-1}a(\omega)} \\ h &= \frac{R^{-1}a(\omega)}{a^*(\omega)R^{-1}a(\omega)} && (3.37) \end{aligned}$$

The power of the signal is now defined as

$$E\{|y_F(t)|^2\} = \frac{1}{a^*(\omega)R^{-1}a(\omega)} \tag{3.38}$$

and the power spectral density as

$$S_{\mathrm{C}}(\omega) \simeq \frac{1}{a^*(\omega)R^{-1}a(\omega)} \tag{3.39}$$

In general, R is replaced with the estimate

$$\hat{R} = \frac{1}{N-m}\sum_{t=m+1}^{N} y(t)y^*(t) \tag{3.40}$$

Several studies have shown that the resolution and frequency accuracy of the Capon method outperforms non-adaptive techniques (Capon 1969; Li and Stoica 1996; Stoica and Moses 2005). A simulation comparing results will be given at the end of this section.

3.1.3.3 APES Method

If the Capon method is applied to a signal that is assumed to be a sinusoid, $\alpha e^{i\omega t}$, then the following statement can be derived (in a forward sense):

$$H(\omega) = h^*[e^{i\omega t}\ e^{i\omega(t-1)} \dots e^{i\omega(t-m)}]^T\alpha = h^*[1\ e^{i\omega} \dots e^{i\omega m}]^T\alpha e^{i\omega t} = h^*a(\omega)[\alpha e^{i\omega t}]\ , \tag{3.41}$$

and is the output of the filter (Stoica and Moses 2005). The constraint that the signal be unchanged at the passband can be given in the same way as Capon:

$$h^*a(\omega) = 1\ . \tag{3.42}$$

Now it is desired to have the output of the filter (when fed with the data) to be as close to (in a least-squares sense) the sinusoid with frequency ω. In mathematical terms this is expressed as

$$\min_{h,\alpha} \frac{1}{N-m} \sum_{t=m+1}^{N} |h^*\tilde{y}(t) - \alpha e^{i\omega t}|^2 \tag{3.43}$$

where $\tilde{y}(t) = [y(t), y(t-1), \dots, y(t-m)]^T$. Fortunately, this equation can be solved in a closed form. If

$$g(\omega) = \frac{1}{N-m} \sum_{t=m+1}^{N} \tilde{y}(t)e^{-i\omega t} \tag{3.44}$$

then

$$\begin{aligned} & \frac{1}{N-m} \sum_{t=m+1}^{N} |h^*\tilde{y}(t) - \alpha e^{i\omega t}|^2 \\ = \ & h^*\hat{R}h - \alpha^* h^* g(\omega) - \alpha g^*(\omega)h + |\alpha|^2 \\ = \ & |\alpha - h^*g(\omega)|^2 + h^*[\hat{R} - g(\omega)g^*(\omega)]h \end{aligned} \tag{3.45}$$

where

$$\hat{R} = \frac{1}{N-m} \sum_{t=m+1}^{N} \tilde{y}(t)\tilde{y}^*(t) \tag{3.46}$$

The minimization of Equation (3.45) with respect to α is apparent in that the first term on the right hand side (RHS) of Equation (3.45) can be set equal to zero ($\alpha(\omega) = h^* g(\omega)$) (Stoica and Moses 2005). The remaining problem is to minimize the second term of the RHS of Equation (3.45), which is the exact derivation of the Capon method performed previously. Thus

$$\min_h h^* \hat{Q}(\omega) h \quad \text{subject to } h^* a(\omega) = 1 \tag{3.47}$$

where

$$\hat{Q}(\omega) = \hat{R} - g(\omega) g^*(\omega) \tag{3.48}$$

and

$$h(\omega) = \frac{\hat{Q}^{-1}(\omega) a(\omega)}{a^*(\omega) \hat{Q}^{-1}(\omega) a(\omega)} \tag{3.49}$$

The amplitude for frequency ω can be found by

$$\alpha(\omega) = h(\omega)^* g(\omega) \ . \tag{3.50}$$

It is interesting to note that in the solution for $h(\omega)$, if the $\hat{Q}^{-1}(\omega)$ is replaced with I, then the Welch approach results with the maximum overlap between subvectors. Also, if $\hat{Q}^{-1}(\omega)$ is replaced with $\hat{R}^{-1}$, the equation represents the Capon method. The literature states that the Amplitude and Phase Estimation (APES) method, while having lower resolution than Capon, has higher accuracy in amplitude estimation in areas near or at the true spectral frequencies (Li and Stoica 1996; Stoica and Moses 2005). Simulated results will be presented later.

3.1.3.4 CAPES Method

Another method that incorporates the dataset into its filter coefficient calculation combines the strengths of two algorithms, namely the frequency accuracy of Capon and the amplitude accuracy of APES (CAPES) (Jakobsson and Stoica

2000; Stoica and Moses 2005). By first locating the n highest peaks with the Capon method and then evaluating APES at those frequencies, statistical accuracy can be improved. It must be noted however that, as in APES, the signals are assumed to be sinusoids.

To test the adaptive spectral estimation techniques, another simulator was created. In this case, 100 runs were used to evaluate the bias and variance of each estimation technique. A signal was generated with four peaks located at $f = \begin{bmatrix} 0.08 & 0.1 & 0.16 & 0.18 \end{bmatrix}$ and amplitudes of $\begin{bmatrix} 10 & 10 & 10 & 2 \end{bmatrix}$. White noise was added at various power levels to allow for the signal-to-noise ratio (SNR) to vary. Examining the performance at several SNR values identifies algorithm stability for a variety of signal strengths and is an indicator of the algorithm's robustness. For this test, 100 temporal samples are used and zero padding is applied to increase the DTFT frequency estimates to 5000 points. Again, this does not improve the resolution of the signal but simply provides additional points of reference in the spectra. The window length for the Welch, Capon and APES methods were set to $m = N/2 - 1$. Spectral bias for the 100 runs for an SNR of 30 dB for the periodogram, Welch, Capon and APES algorithms are shown in Figure 3.4. Vertical black lines indicate the true frequency of the peaks.

As expected, the periodogram has the highest spectral leakage due to the sidelobes of the rectangular window. Amplitude and frequency estimates are near the true values, however, it is apparent that the spectral leakage has biased the peak located at $f = 0.08$. Resolution is good as three of the peaks are easily identified despite their proximity while the fourth peak could easily be confused with a sidelobe.

Utilizing overlapping data subsets, the Welch method suffers from a loss of resolution, as expected. In fact, the loss of resolution is so great that the fourth

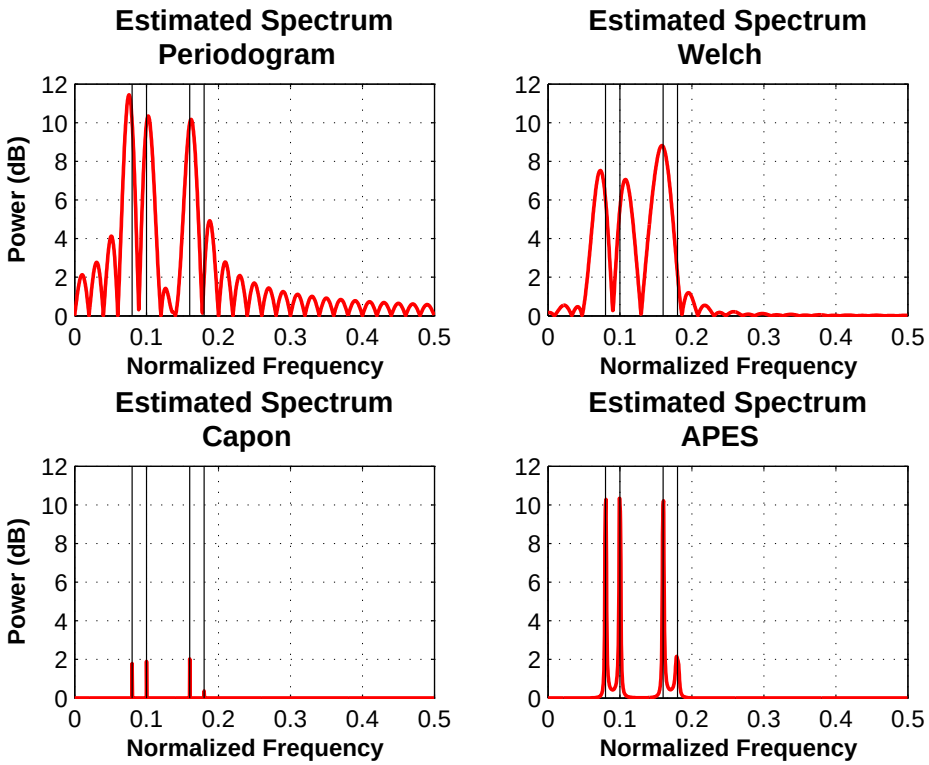

Figure 3.4: Simulated results for non-parametric and adaptive spectral processing. Four tones were generated with random noise with a SNR of 30 dB and are denoted by the vertical black lines. The periodogram and Welch techniques are shown in the top left and right plots, respectively, while the adaptive Capon and APES techniques are represented in the bottom two. Capon and APES are able to resolve the four peaks with a high degree of accuracy, although the Capon algorithm fails to accurately determine the signal amplitudes. The APES algorithm correctly resolves the tone amplitudes.

peak is obscured by the main lobe of the third peak. Though no window function is used on the data subsets, the amplitude estimates are negatively biased.

Though hard to observe, the Capon estimates are highly accurate in frequency. Amplitude estimates are considerably biased, however, and the relative strength of signals is preserved. If only accurate frequency estimates are of importance, Capon would suffice. Some possible scenarios for which high resolution frequency estimates would be more important than accurate amplitudes include commercial or tactical electromagnetic spectrum usage, chord structures in music, color content of images, among others. The Capon technique is able to resolve the four peaks with high accuracy.

Contrary to the Capon technique, APES is highly accurate in amplitude estimation but is not necessarily accurate in frequency. In this example though, the frequency estimations are highly accurate as well due to the high SNR. The MSE of the four techniques plotted with SNR as the abscissa is given in Figure 3.5. Combining APES's amplitude accuracy with Capon's frequency resolution and accuracy through the CAPES algorithm is also performed and the MSE results are given in the figure as well.

Periodogram and Welch plateau at relatively low amplitude and frequency error values with the periodogram outperforming Welch. The Capon technique also plateaus in amplitude but at a much higher MSE value when compared to the non-parametric methods. In frequency accuracy, however, Capon is unmatched, despite the periodogram being the maximum likelihood estimator. It is postulated that this is a result of the periodogram being a better biased-based estimator with low statistical accuracy (high variance) as opposed to the Capon method, which has improved variance performance (Stoica and Moses 2005). APES trends toward high MSE with low SNR values, but eventually overtakes the other techniques. With the aid of the Capon algorithm to first estimate frequency content,

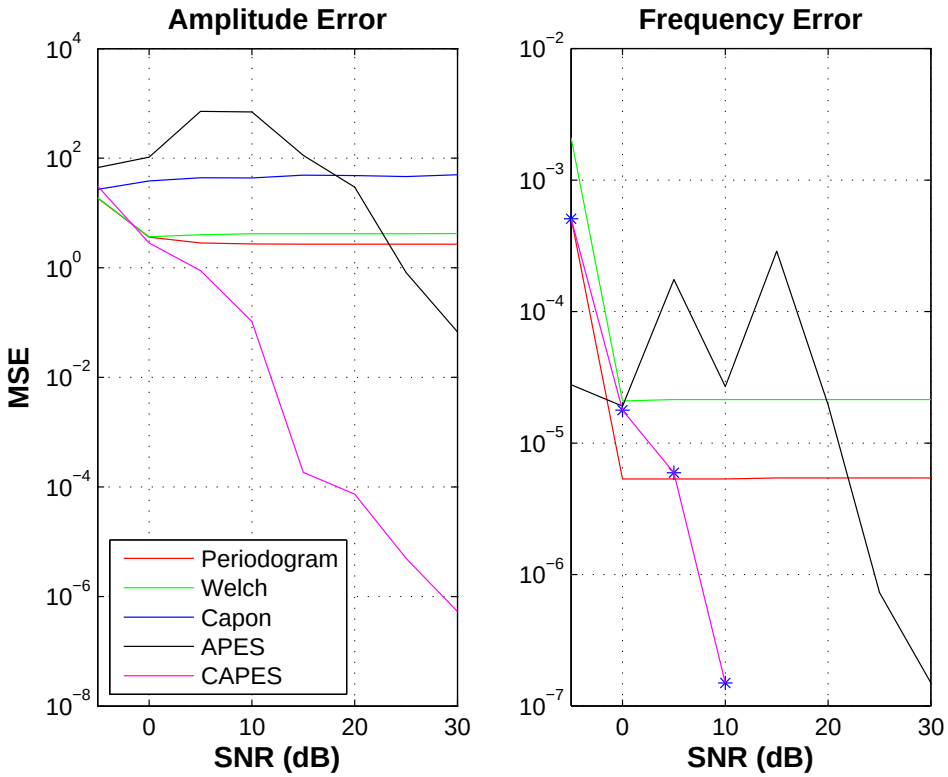

Figure 3.5: A comparison of the results of a spectral processing algorithms simulation. Shown in the left figure are the amplitude errors for different levels of SNR. Note that the non-parametric methods reach an asymptotic value rather quickly, as does the Capon algorithm. APES and its close relative, CAPES, show improvement in amplitude estimation as the SNR is increased. The figure on the right displays the error in frequency for different SNR values. Again, APES and CAPES outperform the non-parametric techniques for higher SNR values.

the CAPES amplitude estimates are far and away the best except perhaps for the lowest SNR=-5 dB. Note that for high SNR values, the APES algorithm performance begins to approach that of Capon, relative to the non-parametric techniques.

3.1.4 Waveform Design

In the previous section, an exploration of regularly sampled temporal data analysis in the frequency domain was produced. By no means is this the extent of possibilities for the temporal domain. Adjustments to the way the data are collected, or predetermined alterations to the phase or frequency can relax constraints placed on measurements. Several techniques will now be presented that improve velocity ambiguities, radar sensitivity and range resolution.

3.1.4.1 Staggered Pulse Repetition Time

A review of the Doppler dilemma in Chapter 2 indicates that the maximum measurable radial velocity for a pulsed radar is determined, through the Nyquist theory, to be

$$v_{\mathrm{a}} = \frac{\lambda}{4T_s} \ . \tag{3.51}$$

One method to remove this ambiguity is to utilize two sampling intervals that produce an ambiguity function that allows for a wider range of unambiguous velocities (Doviak and Zrnić 1993). An example of a staggered pulse repetition pattern (known as a staggered PRT) is given in Figure 3.6 and the associated ambiguity waveform is presented in Figure 3.7. The PRTs chosen for this example maintain a ratio of $\kappa = n/m = 2/3$, or $T_{s2} = 3T_{s1}/2$ with a wavelength of 3 cm. As a result, the new maximum unambiguous velocity is

$$v_{\mathrm{a}}^{\mathrm{SPRT}} = \frac{\lambda}{4(T_{s2} - T_{s1})} \ , \tag{3.52}$$

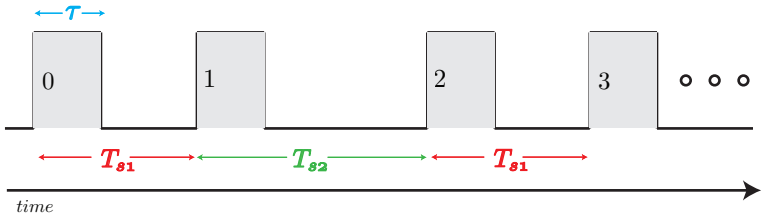

Figure 3.6: An illustration of a staggered PRT waveform. The general idea of a staggered PRT is that two pulse repetition times are interleaved, creating a short-long-short repeating pattern. In this example, the pulse width is held constant for each pulse.

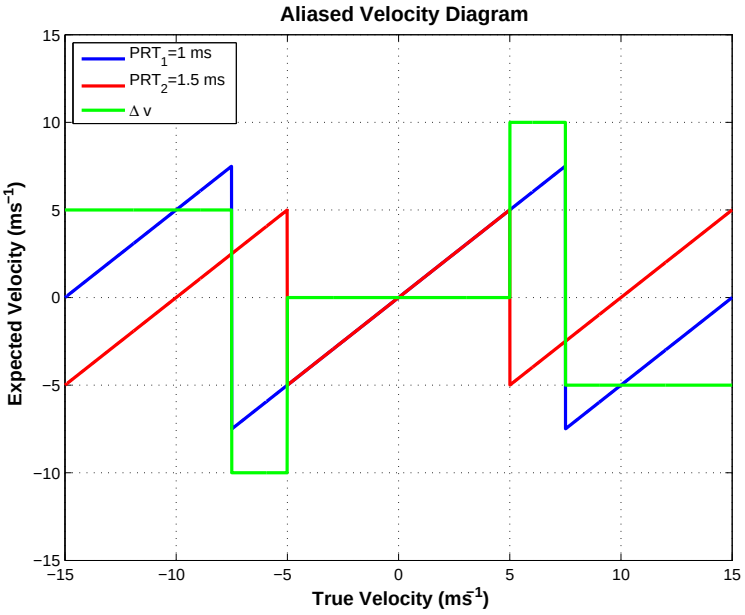

Figure 3.7: An ambiguity waveform for a staggered PRT pattern with $T_{s1} = 1$ ms and $\lambda = 3$ cm. In this case, the ratio between the two PRTs is 2/3. Utilizing this chart with individual velocity estimates found from long and short pulse pairs provides a dealiased velocity estimate with an extended unambiguous velocity range.

and, if $T_{s1} = 1$ ms, is found to be 15 $\mathrm{m\,s^{-1}}$. Early techniques called for the estimated velocity to be directly calculated from a modified version of the pulse-pair processor velocity calculation (Doviak and Zrnić 1993), namely

$$\hat{v} = \frac{\lambda}{4\pi(T_{s2} - T_{s1})} \arg\left(\frac{\hat{R}_{1,1}}{\hat{R}_{1,2}}\right) . \tag{3.53}$$

Only PRT ratios of the form $\zeta = m/(m+1)$ extend the unambiguous velocity to the theoretical maximum through this technique due to the loss of individual arguments of $\hat{R}_{1,1}$ and $\hat{R}_{1,2}$ when combined in the ratio (Torres et al. 2004).

Later methods made use of a graphical approach through dealiasing rules to include additional PRT ratios (Torres et al. 2004). The rules are based on the Δv function depicted as the green line in Figure 3.7. Depending on the values of the individually calculated velocity estimates, a unique dealiased value can be determined. Example pseudocode illustrating the dealiasing procedure is given here:

1. Create velocity ambiguity and difference waveforms with associated aliasing velocities: v_1, v_2, Δv, v_{a1}, v_{a2}

2. Calculate the difference between the two velocities individually estimated from two different PRTs $\Delta\hat{v} = \hat{v}_{f1} - \hat{v}_{f2}$

3. Determine the position of the closest match to the waveform $[v, idx] = find(\min[abs\{\Delta\hat{v} - \Delta v\}])$

4. Follow the rules to identify the new $\hat{v}_{\mathrm{SPRT}}$:

$$\hat{v}_{\mathrm{SPRT}} = \begin{cases} \hat{v}_{f1} - 2v_{a1} & \text{if } v(idx) < -v_{a1} \\ \hat{v}_{f1} + 2v_{a1} & \text{if } v(idx) > v_{a1} \\ \hat{v}_{f1} & \text{else} \end{cases}$$

Since the ambiguous velocity is proportional to the wavelength of the carrier signal, and due to the Doppler dilemma (see Chapter 2), staggered PRT

algorithms are used frequently for shorter wavelength systems, such as X and Ka-bands. With the increasing utilization of dual-polarization in weather radars, special considerations for the calculation of the polarimetric variables when staggered PRTs are used. For instance, ground clutter mitigation, while simple when uniform sampling is used, becomes difficult with staggered PRTs. Warde et al. (2011) have explored the issue and developed an algorithm, Clutter Environment Analysis using Adaptive Processing (CLEAN-AP), which accounts for the nonuniform sampling and allows for the removal of clutter in both single and dual-polarization modes.

Also a concern at shorter wavelengths is attenuation due to the atmosphere and precipitation. Maintaining sensitivity at large distances from the radar becomes difficult and is generally corrected by increasing the power of the transmitter. Sometimes this option is not ideal due to cost or size considerations. However, additional techniques exist which allow radars to achieve comparable sensitivity without increasing the transmitter size. One such technique, pulse compression, will be discussed in the next section.

3.1.5 Pulse Compression

Sensitivity is quantified by the minimum detectable signal (MDS) of a radar. Often this parameter is defined by a minimum Reflectivity value that can be detected at a particular range with a specific SNR. For example, the WSR-88D radar can detect precipitation with -7.5 dBZ at 50 km with an SNR>0 dB (Doviak and Zrnić 1993). As radar frequency increases, the sensitivity of the system increases as well, allowing for lower power transmitters to be utilized. However, the attenuation that occurs when electromagnetic waves travel through rainfall increases with higher frequency systems, reducing sensitivity at longer ranges.

Increasing the average power helps to restore the sensitivity and can be accomplished in one of two ways: increase the peak power or increase the duty cycle. As previously mentioned, increasing the peak transmit power is not often a desirable solution due to cost or size considerations. Since reducing the PRT is also disadvantageous due to decreased unambiguous ranges, a common technique is to increase the width of the transmit pulse. Of course, increasing the transmit pulse produces larger sampling volumes in range, which is also an unacceptable drawback. Fortunately methods exist that can regain the desired range resolution while maintaining the sensitivity necessary for meaningful observations. One such technique is pulse compression.

Pulse compression refers to the idea that a pulsed waveform of length τ, which has an associated bandwidth, β, passes through a matched filter that compresses the pulse to an effective length $\tau_c = 1/\beta$. The pulse compression ratio refers to the ratio between the long pulse length, τ, and the compressed pulse length, τ_c. The time-bandwidth product is equal to the pulse compression ratio via $\beta\tau = \tau/\tau_c$. Typically the pulse compression technique of choice is evaluated by observing the ambiguity function (Skolnik 2001; Sinsky and Wang 1974), which is now described.

3.1.5.1 Ambiguity Function

Typically radar waveforms are explored through the use of the ambiguity function, which is a product of the matched filter found in all radar systems. A matched filter is used to maximize the peak signal to mean noise ratio (Skolnik 2001). It can be shown that the frequency response of the matched filter that maximizes this ratio with the application of white noise is

$$H(f) = G_a S_r^*(f) e^{-j2\pi f\tau} \tag{3.54}$$

where G_a is a constant, $S_r(f)$ is the PSD of the received input signal, and τ is the pulse width. A proof is given in the following passage.

A matched filter maximizes the ratio

$$\Upsilon = \frac{|s_m(t)|^2_{\max}}{\tilde{N}} \tag{3.55}$$

where the magnitude of the output of the matched filter is

$$|s_m(t)| = \left| \int_{-\infty}^{\infty} S(f)H(f)e^{j2\pi ft}\ df \ \right| \tag{3.56}$$

and the mean noise power is

$$\tilde{N} = \frac{\tilde{N}_0}{2} \int_{-\infty}^{\infty} |H(f)|^2\ df\ . \tag{3.57}$$

Thus,

$$\Upsilon = \frac{\left| \int_{-\infty}^{\infty} S(f)H(f)e^{j2\pi f\tau}\ df\ \right|^2}{\frac{\tilde{N}_0}{2} \int_{-\infty}^{\infty} |H(f)|^2\ df}\ . \tag{3.58}$$

From here, Schwartz's inequality is used to simplify the equation. The inequality states that for two complex functions P and Q,

$$\int P^*P\ dx\ \int Q^*Q\ dx\ \geq \left| \int P^*Q\ dx \right|^2 \tag{3.59}$$

where, in this case, $P^* = S(f)exp[j2\pi f\tau]$ and $Q = H(f)$ and the equality applies when $P = kQ$ (Skolnik 2001; Shanmugan and Breipohl 1988). Thus,

$$\begin{aligned}
\Upsilon &= \frac{\left| \int_{-\infty}^{\infty} S(f)H(f)e^{j2\pi f\tau}\ df\ \right|^2}{\frac{\tilde{N}_0}{2} \int_{-\infty}^{\infty} |H(f)|^2\ df} \\
&\leq \frac{\int_{-\infty}^{\infty} S(f)S^*(f)e^{j2\pi f\tau}e^{-j2\pi f\tau}\ df\ \int_{-\infty}^{\infty} H(f)H^*(f)\ df}{\frac{\tilde{N}_0}{2} \int_{-\infty}^{\infty} |H(f)|^2\ df} \\
&\leq \frac{\int_{-\infty}^{\infty}\ |S(f)|^2\ df\ \int_{-\infty}^{\infty} |H(f)|^2\ df}{\frac{\tilde{N}_0}{2} \int_{-\infty}^{\infty} |H(f)|^2\ df} \\
&\leq \frac{\int_{-\infty}^{\infty}\ |S(f)|^2\ df}{\frac{\tilde{N}_0}{2}}\ .
\end{aligned} \tag{3.60}$$

From Parceval's theorem, it is known that $\int_{-\infty}^{\infty} |S(f)|^2 \, df = \mathsf{E}$, where E is simply the energy of the signal. Finally, the peak signal to mean noise ratio at the output of the matched filter is given by

$$\Upsilon \leq \frac{2\mathsf{E}}{\tilde{N}_0} \tag{3.61}$$

and has no dependence on the transmitted signal parameters such as bandwidth, shape or duration (Skolnik 2001). With the knowledge that the matched filter is simply a copy of the transmitted pulse delayed in time, the discussion of the ambiguity function can continue.

If it assumed that the transmitted radar signal is of the form $s(t) = u(t)\exp[j2\pi f_0 t]$ with $u(t)$ as the complex modulation function and f_0 as the carrier frequency (Skolnik 2001). It is assumed that return echo from a target (or distribution of targets) will be the transmitted signal shifted in frequency by f_d, the Doppler shift, and delayed in time by t_0. Thus, the returned signal is of the form $s_r(t) = u(t - t_0)\exp[j2\pi(f_0 + f_d)(t - t_0)]$. Finally, the output of the matched filter is simply the correlation between the transmitted and received pulse

$$s_m(t) = \int_{-\infty}^{\infty} u(t - t_0)u^*(t - t_r)e^{j2\pi(f_0+f_d)(t-t_0)}e^{-j2\pi f_0(t-t_r)} \, dt \; . \tag{3.62}$$

Traditionally, $t_0 = f_0 = 0$, thus creating the well known *ambiguity function*

$$\chi(t_r, f_d) = \int_{-\infty}^{\infty} u(t)u^*(t + t_r)e^{j2\pi f_d t_r} \, dt \tag{3.63}$$

where the magnitude or magnitude squared is typically plotted and examined for radar performance parameters (Skolnik 2001; Sinsky and Wang 1974; Mahafza 2000)

Several examples of pulsed waveforms will be presented in the following sections. In each method, the goal is to achieve good *resolution* by having a sharp, narrow peak at the origin of the diagram. By examining Equation (3.63), it is observed that the time delay axis can be converted to units of meters by $r = (t_r c)/2$.

Similarly, Doppler frequency can be converted to radial velocity via $v_r = (f_d\lambda)/2$. In this way, the ambiguity is directly related to the range and radial velocity resolution of the system by examining the pulsed waveform.

For a simple first case, a 1-μs rectangular pulse is transmitted at a constant frequency, or $s_{\text{rect}}(t) = u(t)exp[j2\pi ft]$ with $f = 10$ GHz. The associated ambiguity function is given in Figure 3.8. As expected, the pulse has good range

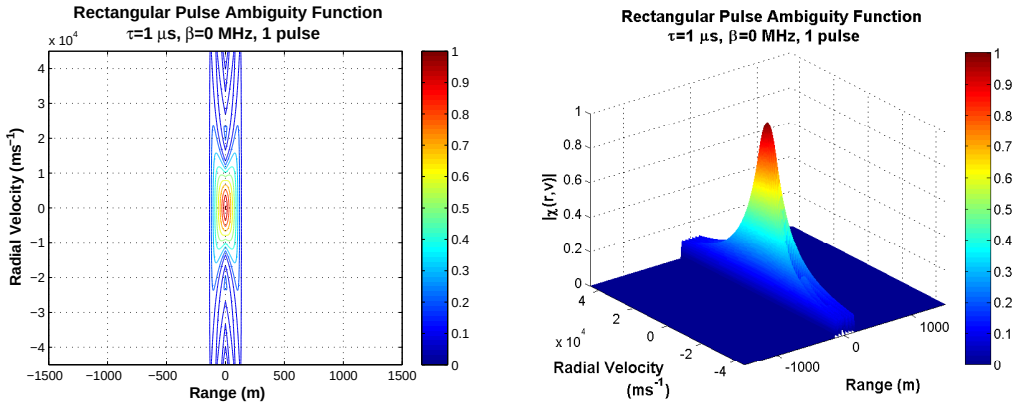

(a) (b)

Figure 3.8: An ambiguity function for a 1-μs rectangular pulse. A two-dimensional view is given in (a) while a three dimensional view is presented in (b). Note that the pulse produces good range accuracy.

resolution (approximately 150 m) and for a single pulse, appropriate radial velocity ambiguity. Changing the pulse width to 8 μs provides a different ambiguity function, which is presented in Figure 3.9. Intuitively, a longer pulse width should produce larger range resolution and it is seen to be the case. By the same token, the frequency resolution is improved with a longer pulse when compared to a shorter one.

While examining single pulses is beneficial for understanding and interpreting the ambiguity function, calculating the ambiguity function for a series of pulses,

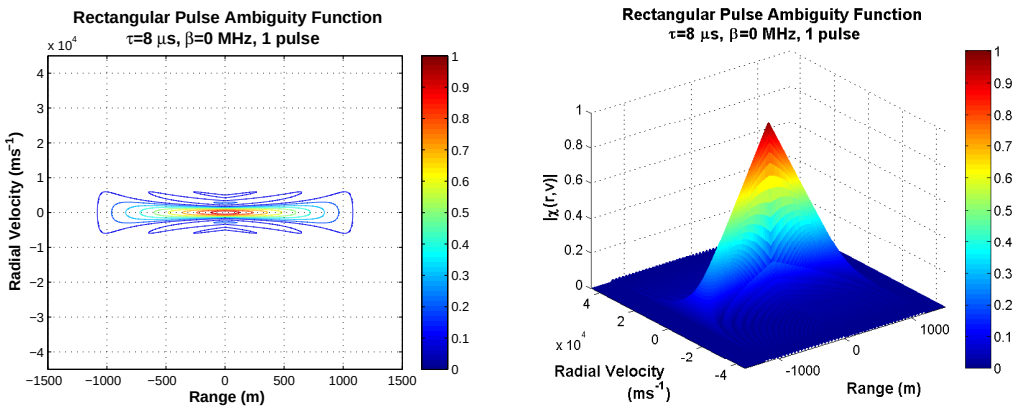

(a) (b)

Figure 3.9: Similar to Figure 3.8, except for an 8-μs pulse. In this case, the diagram indicates that the waveform provides less range accuracy than the 1-μs pulse. Note that the range axis at the zero-Doppler cut exhibits a triangular shape, which is expected due to the rectangular pulse envelope.

or a pulse train, highlights some other aspects of radar design such as the ambiguous velocity and range. Two examples of pulse trains are given in Figure 3.10. In Figure 3.10(a), five 50 μs pulses are transmitted with a PRF of 8000 Hz. While slightly unrealistic for traditional radar systems, the parameters were chosen both to allow for quick calculation and ease of interpretation. It is, however, not unlikely that relatively long pulses with high PRFs will become more prevalent in the future with the increase of solid state amplifier transmitter systems. Given a PRF of 8000 Hz, it is expected that the ambiguous range of 18.75 km and an aliasing velocity of 60 m s^{-1}. This is indeed the observed in Figure 3.10(a), though it is important to note that the velocity *ambiguity* occurs at $2v_{\mathrm{a}}$. For example, a target moving at 120 m s^{-1} will be confused with a target that is stationary, e.g., 0 m s^{-1}. A 6-pulse, 2/3 ratio staggered PRT ambiguity function is presented in Figure 3.10(b). Note that the effect of the alternating pulses defocuses the

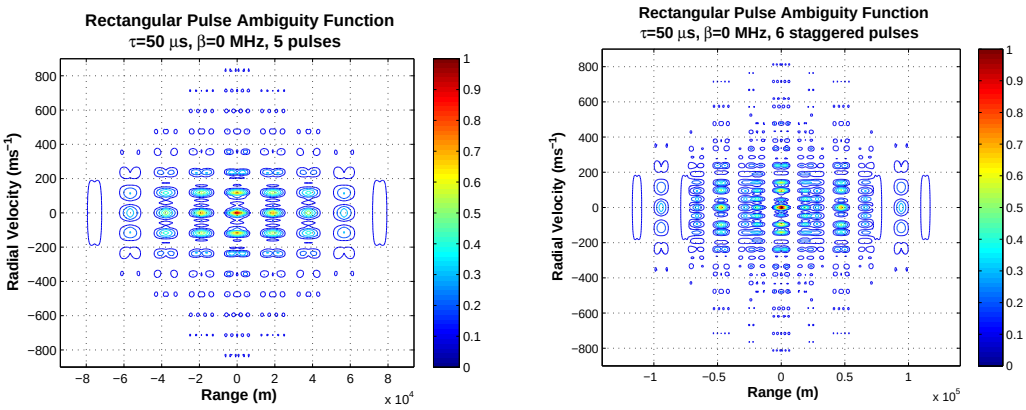

(a) (b)

Figure 3.10: A multiple pulse ambiguity function for a 50-μs pulse for (a) five uniformly sampled pulses and (b) six staggered PRTs. The processing of multiple pulses generates additional points of ambiguity in both range and frequency due to the Doppler dilemma at locations known as the unambiguous range and velocity. Utilizing staggered PRTs allows for the ambiguity points to defocus, providing a method for dealiasing velocity estimates.

ambiguity lobes, allowing for the technique described in Section 3.1.4.1 to be employed. Further exploration of how the staggered algorithm aids in the dealiasing will be explained in a later section.

3.1.5.2 Linear Frequency Modulation

As previously discussed, improving radar sensitivity or range resolution is often a goal in radar systems. One method to achieve both of these goals is to modulate the frequency of the pulsed waveform instead of utilizing a single tone. Thus, the transmitted waveform takes the form of $s_{\text{LFM}}(t) = s_{\text{rect}}(t)\exp[\phi(t)] = u(t)\exp[j2\pi ft]\exp[j2\pi\beta t^2/\tau]$ where $\phi(t)$ is the frequency modulation function, β is the bandwidth of the frequency *chirp* and τ is the actual duration of the pulsed signal. Further examination of the signal reveals that the instantaneous frequency of the modulated signal is

$$\frac{d\phi(t)}{dt} = \frac{2\pi\beta}{\tau}t \tag{3.64}$$

and is linear with respect to t, thus the term Linear Frequency Modulation (LFM) is appropriate.

A first example of the LFM technique is generated using a single 1-μs pulse with β =5 MHz. The resulting ambiguity function is given in Figure 3.11. Note the linear slope in the primary ambiguity peak, which is proportional to the time-bandwidth product of $\beta\tau = 5$. A somewhat more realistic example achieves both goals of improved sensitivity and range resolution by transmitting an 8-μs pulse with the same 5 MHz bandwidth and the results are given in Figure 3.12. In this example, the time-bandwidth product is 40 and is observed in the steeper slope of the ambiguity peak. From Figure 3.9, it is known that the zero-Doppler cut of the single rectangular pulse ambiguity function is a triangle function. The LFM waveform claims to improve range resolution and the proof is found by examining

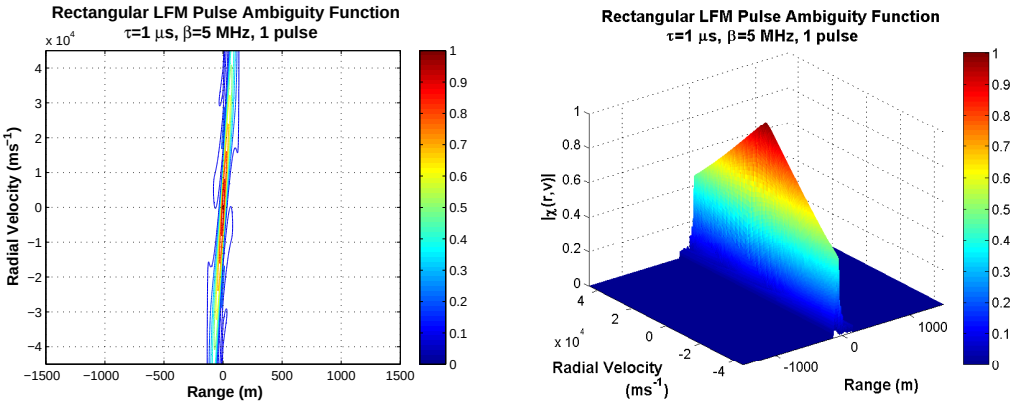

(a) (b)

Figure 3.11: Similar to Figure 3.8, except the bandwidth of the pulse is allowed to span 5 MHz. The result is a pulse that has a much improved range accuracy. The slope of the ambiguity function is related to the time-bandwidth product, in this case, 5.

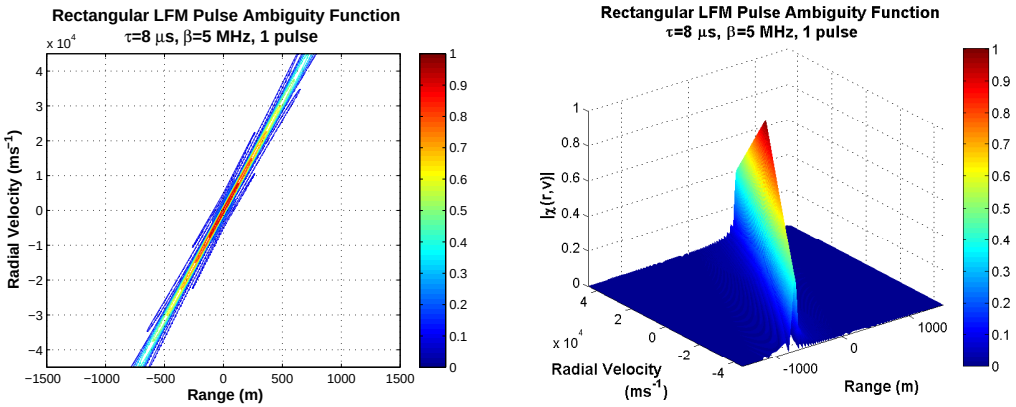

(a) (b)

Figure 3.12: Similar to Figure 3.9, except the bandwidth is 5 MHz. The range accuracy is enhanced when a LFM waveform is utilized. The benefit of the longer pulse width is the increase in radar sensitivity as compared to a shorter pulse wi the same bandwidth.

the zero-Doppler cut for the LFM chirp signal presented in Figure 3.13. Note

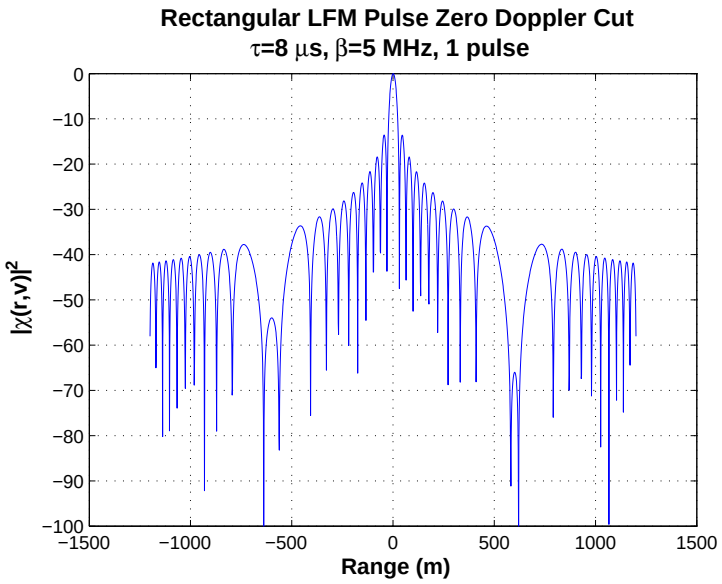

Figure 3.13: A display of the zero-Doppler cut of the ambiguity function presented in Figure 3.12. Note the familiar *sinc* function appearance. The shape of the range ambiguity pattern is directly related to the Fourier transform of the second derivative of the frequency modulation function.

that the range resolution is significantly improved from the original 1.2 km to the new 30 m. Also, the zero-Doppler response is a familiar *sinc* function, commonly found in signal processing.

For completeness, a multiple pulse ambiguity diagram is presented in Figure 3.14 for a LFM case with five, 50-μs pulses and a bandwidth of 5 MHz. Note the different range scale on the abscissa, which accounts for the large time-bandwidth product but shallow appearance of the slope of the diagram.

As is typical whenever a *sinc* function is encountered, it is desirable to reduce the leakage caused by the range sidelobes through traditional signal processing techniques.

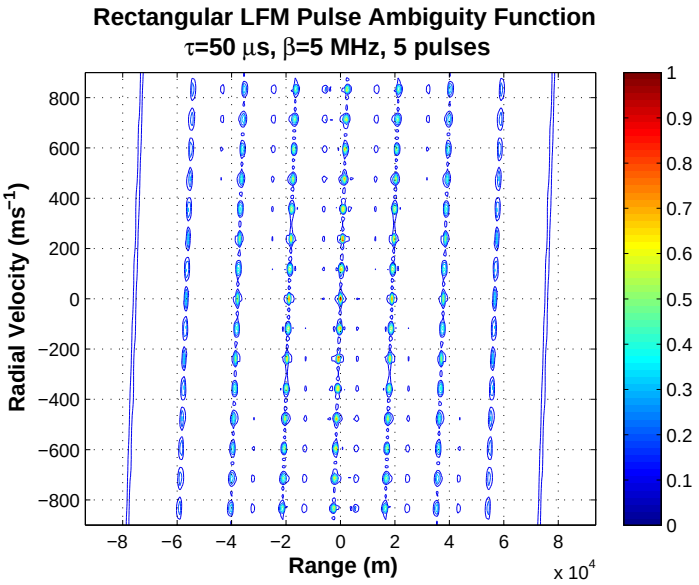

Figure 3.14: Similar to Figure 3.10, except for a LFM waveform with a bandwidth of 5 MHz. Five equally spaced pulses of length 50 μs are used to produce this ambiguity function.

3.1.5.3 Pulse Tapering

Similar to applying a window function to time series data discussed in Section 3.1.2.2, pulse tapering refers to modulating the amplitude of the waveform during the pulsed output (Skolnik 2001). For this scenario, the waveform takes the form $s_{\text{taper}}(t) = a(t)s_{\text{LFM}}(t)$, where $s_{\text{LFM}}(t)$ is the LFM signal defined in the previous section and $a(t)$ is the amplitude modulation function. Typical functions include the familiar Hamming window, Blackman, etc. For an initial test, it is assumed that the amplifier circuit for the transmitted waveform operates well within the linear region, thus allowing for the tapered waveform to be transmitted (Skolnik 2001). As a result, the waveform is tapered again on receive and will be referred to a matched taper LFM waveform. The results of a 8-μs pulse with a 5-MHz bandwidth and a Hamming taper are given in Figure 3.15. The

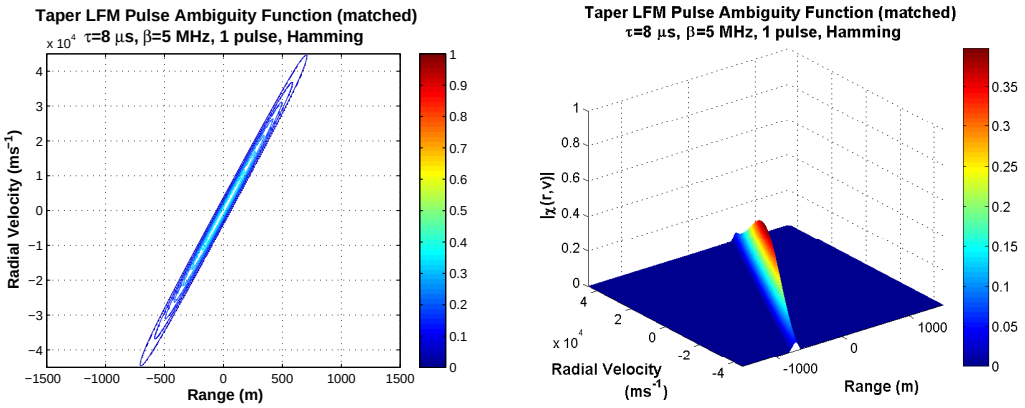

(a) (b)

Figure 3.15: Similar to Figure 3.12, except with a Hamming window applied to both the transmitted waveform as well as the matched filter. The weighting results in a loss of amplitude and, subsequently, radar sensitivity. However, the leakage from the range sidelobes is substantially reduced.

same sloped response is viewed due to the time-bandwidth product, however, the amplitude is normalized to an untapered LFM pulse and the side effects of the taper are apparent. First, the magnitude of the ambiguity function is reduced, indicating a loss of sensitivity. Further evidence of this fact can be seen in the zero-Doppler cut of the ambiguity function shown in Figure 3.16. Note that a loss in sensitivity of approximately 8 dB is observed in the main lobe. Additionally, the main lobe has increased in width to approximately 54 m, almost twice as large as the non-tapered case. More significantly though, the sidelobe levels have decreased from -13 dB to -49 dB, a significant change. Unfortunately, losing more than six times the original signal power is unacceptable, especially since increased sensitivity is one of the primary goals of pulse compression.

An alternative to the matched taper LFM waveform is the *mismatched* taper LFM waveform (Skolnik 2001). If, as is common, the transmitting amplifier is

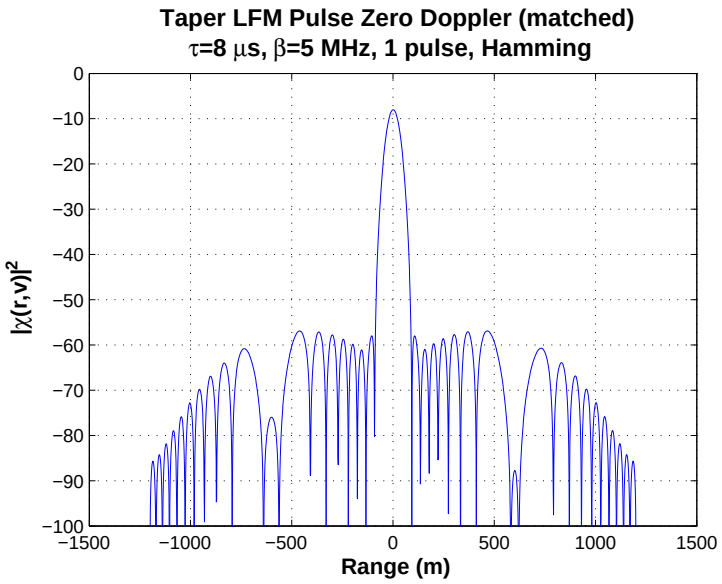

Figure 3.16: Similar to Figure 3.13, except with a Hamming window applied to both the transmitted waveform as well as the matched filter. Note the significant reduction in the range sidelobe amplitude. However, the mainlobe amplitude is reduced by approximately 8 dB and may be an unacceptable tradeoff for the improved sidelobe performance.

saturated in normal operating mode, or if sensitivity degradation of the matched case is unacceptable, the taper can be applied only in the matched filter, generating a mismatch between the transmitted and received signals. Despite this mismatch, significant reduction of the range sidelobes can be achieved. Results from a mismatched taper LFM waveform simulation are given in Figure 3.17. Effects similar to those due to the taper are seen in this case as well. A general

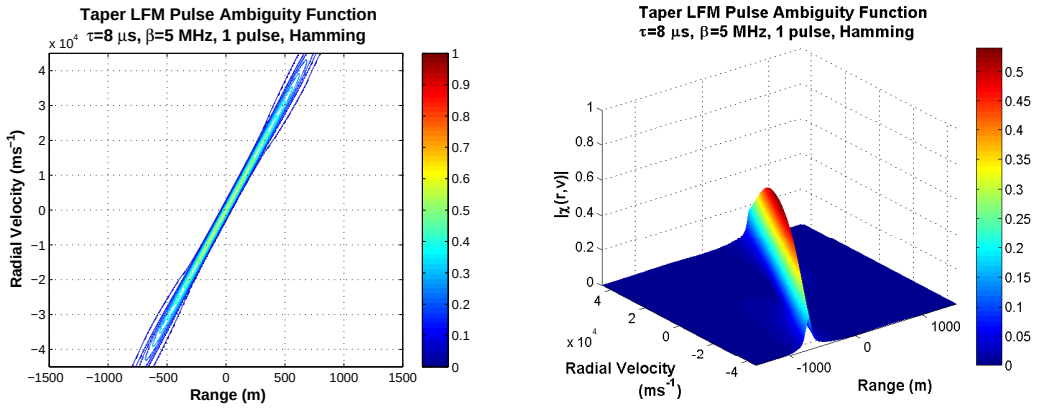

Figure 3.17: Similar to Figure 3.15, except the Hamming window is only applied at the matched filter, thus creating a mismatched waveform. By only applying the window function once, some of the radar sensitivity is retained while still reducing the leakage caused by sidelobes.

loss of sensitivity is observed and an examination of the zero-Doppler cut presented in Figure 3.18 illuminates the parameters of interest. A loss in sensitivity is observed, however, the main lobe level is only 5.4 dB below an untapered LFM pulse. Sidelobe levels peak at approximately -34.6 dB below the main lobe, offering a significant reduction in range leakage. The main lobe width is increased from 30 m to 42 m, but again, the loss of sensitivity and the reduction in range sidelobe levels must be weighed for each application.

While tapering is a fairly straightforward solution to high range sidelobe levels, the loss of sensitivity is unacceptable in many scenarios. Thus, additional

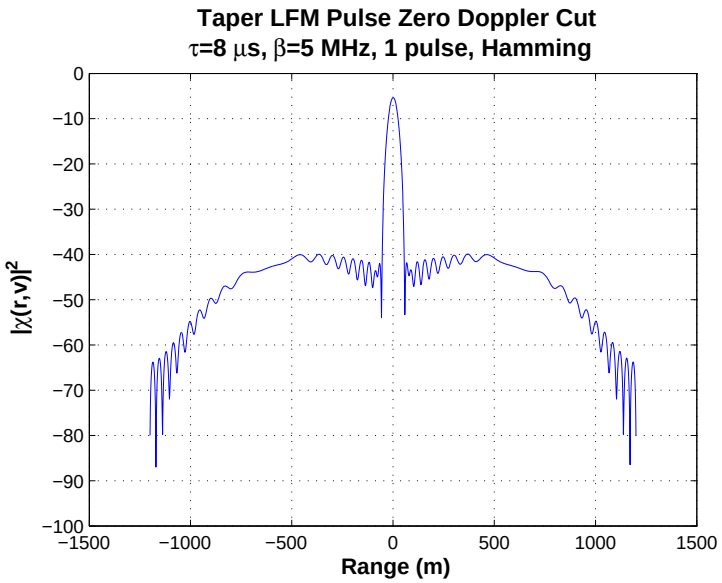

Figure 3.18: Similar to Figure 3.16 except the Hamming window is only applied at the matched filter. Note that the range sidelobes are somewhat higher than the matched tapering case, but the loss of sensitivity is reduced to approximately 5.4 dB.

techniques have been explored to reduce sidelobe levels without the sacrifice of radar sensitivity.

3.1.5.4 Nonlinear Frequency Modulation

Significant efforts have been made from the earliest attempts at pulse compression to reduce the range sidelobes without significantly impacting sensitivity through the use of nonlinear LFM (NLFM) signals (Cook 1964; Fowle 1964; Millett 1970). Early studies focused mainly on sinusoidal frequency modulation functions. More recent developments examine the use of polynomial functions and utilize modern computing and optimization to improve sidelobe performance (Doerry 2006; Chan et al. 2009). For this work, the author will utilize a simple sinusoidal chirp signal defined in Cook (1964). The transmitted signal is again of the form $s_{\text{NLFM}}(t) = s_{\text{rect}}(t)\exp[\phi(t)]$. This time, the instantaneous frequency is defined as

$$\frac{d\phi(t)}{dt} = 2\beta \sin^{-1}\frac{2t}{\tau} + \frac{2\pi\beta}{\tau}t \ , \tag{3.65}$$

and is presented in Figure 3.19. Note that the NLFM instantaneous frequency quickly leaves the boundary of the chirp bandwidth and slowly moves across the center frequency (0 Hz). The waveform will be scaled by the true center frequency of the application. An analogous action is to reduce the amplitude of the samples found at the edges of a discrete dataset through a window function. The results of the NLFM chirp signal on the standard 8 μs, 5 MHz rectangular pulse are presented in Figure 3.20. Note the somewhat sinusoidal shape to the ambiguity function as a result of the frequency modulation. It is difficult to judge the effectiveness of the modulation by looking at the full ambiguity function. Thus the zero-Doppler cut is shown in Figure 3.21. Not only have the sidelobes been reduced to less than 50 dB below the main lobe, no sensitivity degradation is observed. Further, the width of the primary lobe is reduced to 15 m, one half of

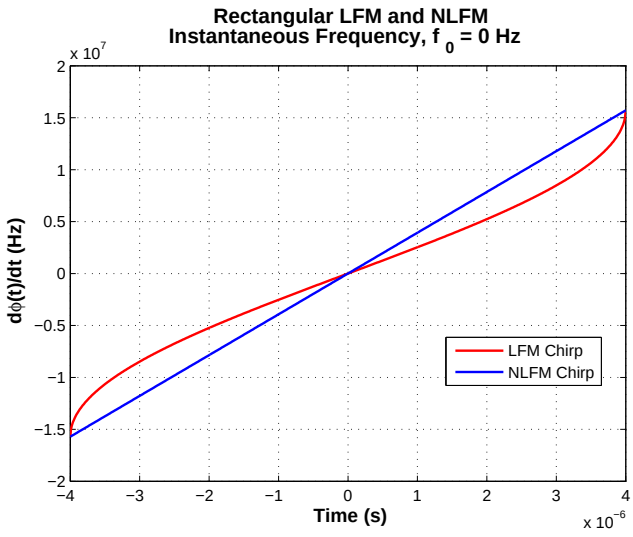

Figure 3.19: A depiction of the instantaneous frequency for a LFM (blue) and a NLFM (red) waveform. The NLFM waveform quickly visits the extreme ends of the signal bandwidth but spends a larger quantity of time near the center frequency (0 Hz in the figure). Window functions can be thought of in a similar way as they attenuate samples near the edges of the dataset while existing near identity for the central data points.

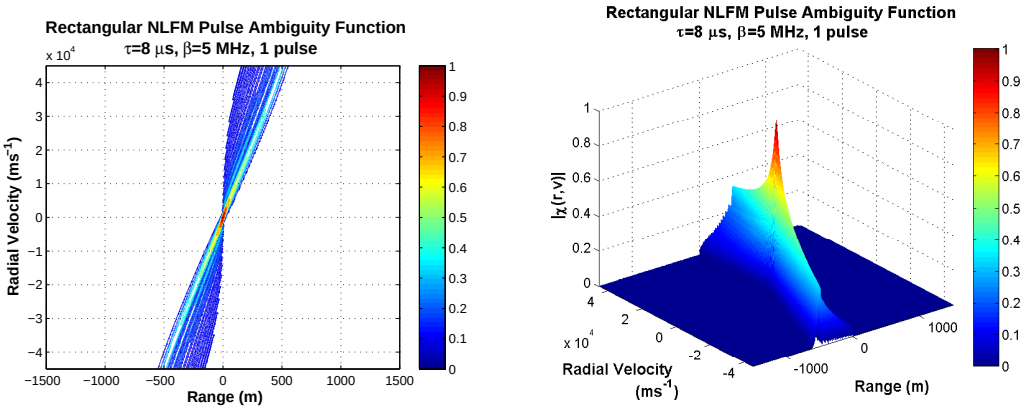

Figure 3.20: Similar to Figure 3.12 except for a NLFM waveform. Note the sinusoidal shape of the ambiguity function. A sinusoidal frequency modulation pattern was selected for the NLFM waveform.

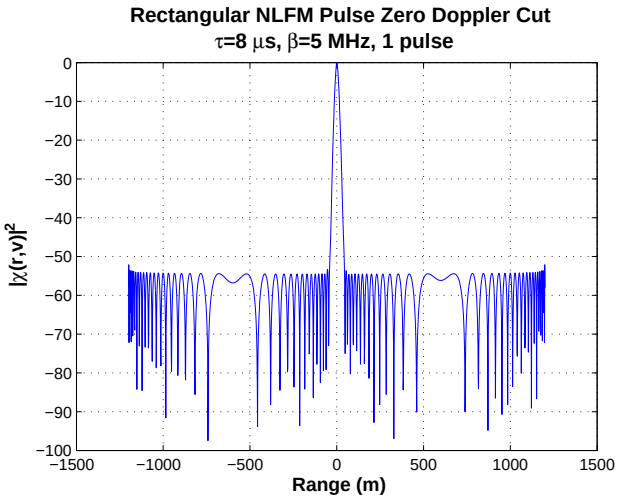

Figure 3.21: Similar to Figure 3.13 except for a NLFM waveform. The waveform produces an improved range resolution as well as reducing the range sidelobe levels without sacrificing radar sensitivity.

the LFM main lobe width. It is expected that the overall bandwidth of the signal could be reduced to achieve the same range resolution as the LFM waveform, but with reduced sidelobes.

The discussion thus far is the extent to which pulse compression will be explored through this work. Many other chirp function exist and optimization algorithms are employed to satisfy cost functions designed to minimize sidelobes or derive specific beam shapes. In the next section, the discussion will shift toward array processing where the techniques described thus far will be applied to spatial sampling networks.

3.2 Radar Array Processing

3.2.1 Signal Model

Though not immediately apparent, there exists an intuitive similarity between the temporal techniques discussed thus far and those used for a uniform linear array (ULA) of radar antennas. These techniques are used in the weather radar community through profiling and precipitation radars (see Chapter 1). To understand the similarity, a proper spatial model must be created, referred to as the *array model*. Instead of searching for specific frequencies within a set of temporal data, the direction of arrival (DOA), $\theta = [-90°, 90°]$, will be estimated based on signals from a set of m sensors, $y(t) = \begin{bmatrix} y_1(t) & \dots & y_m(t) \end{bmatrix}$. This direction can be determined directly from the time delay (τ) between the sensor signals represented in the phase of $a(\theta) = \begin{bmatrix} 1 & e^{-i\omega_c \tau_2} & \dots & e^{-i\omega_c \tau_m} \end{bmatrix}^T$ (Stoica and Moses 2005). An illustration in Figure 3.22 helps to define the physical time delay for different DOAs. For this model, it is assumed that there are a finite number of sensors that emit a signal ($s_k(t)$). As such, the array model is described as

$$\begin{aligned} y(t) &= [a(\theta_1) \dots a(\theta_n)][s_1(t) \dots s_n(t)]^T + e(t) \\ \theta_k &= \text{the DOA of the } k\text{th source} \\ e(t) &= \text{noise associated with each sensor} \\ s_k(t) &= \text{signal corresponding to the } k\text{th source} \end{aligned} \tag{3.66}$$

In the case of a ULA, the time delay can be expressed as

$$\tau_k = (k-1)\frac{d \sin\theta}{c} \quad \text{for } \theta \in [-90°, 90°] \tag{3.67}$$

It is possible to then replace the $a(\theta)$ vector with

$$\begin{aligned} a(\theta) &= [1, e^{-i\omega_c d \sin\theta/c}, \dots, e^{-i(m-1)\omega_c d \sin\theta/c}]^T \\ &= [1, e^{-i\omega_s}, \dots, e^{-i(m-1)\omega_s}]^T \end{aligned} \tag{3.68}$$

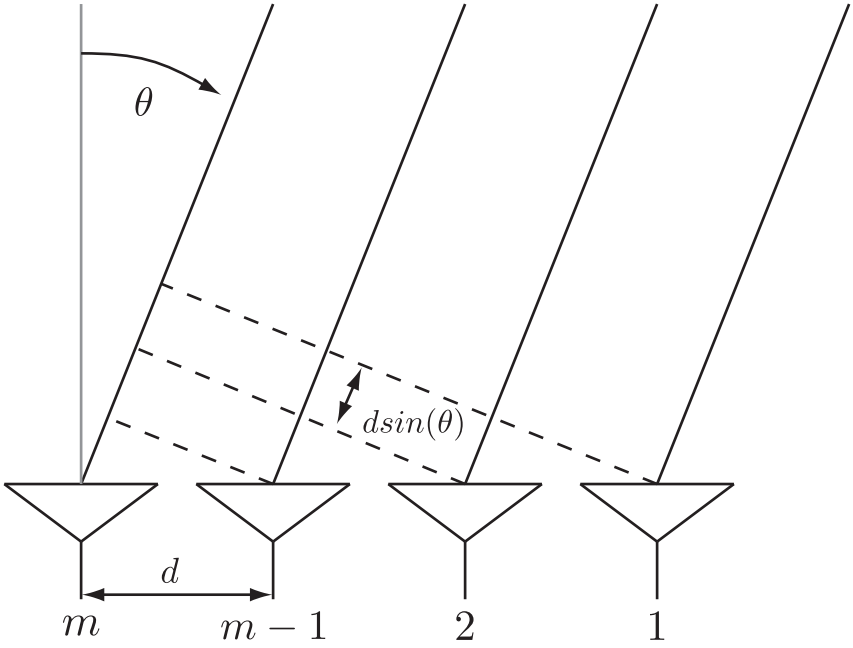

Figure 3.22: An illustration of a linear array of radar elements. Given a source in the far field at an angle θ relative to a vector normal to the array baseline, the time delay between adjacent elements is related to $\tau \propto d \sin\theta$, where d is the distance between elements.

if $\omega_c = 2\pi f_c = 2\pi c/\lambda$ (Stoica and Moses 2005).

It remains to formulate methods for DOA estimation from signals produced at the output of an array of sensors. The algorithms described through the remainder of this section are called *beamforming techniques*.

3.2.2 Fourier Beamforming

The first technique to be explored is Fourier beamforming, which is analogous to the periodogram approach used in the spectral processing of temporal data. Standard Fourier beamforming is used as a baseline and forms the model for subsequent beamforming tests. Utilizing notation similar to Palmer et al. (1998) and Cheong et al. (2004), let $\mathbf{x}(t)$ be a vector of received signals from M array elements. Combining these signals through a carefully selected weighting vector, $\boldsymbol{w}$, gives a complex voltage corresponding to the desired direction controlled by $\boldsymbol{w}$

$$y(t) = \boldsymbol{w}^* \mathbf{x}(t) \ . \tag{3.69}$$

By selecting different weight vectors, the array essentially scans across a defined set of angles, sampling different points in angular space. As with traditional weather radars, multiple samples are utilized to improve power and velocity estimates. Thus, N temporal samples are gathered from each array element and the vector $\mathbf{x}(t)$ becomes an $M \times N$ matrix, $\mathbf{X}$. Likewise, a set of pointing vectors is developed for each of L desired sampling angles, creating a matrix $\mathbf{W}$, which is $M \times L$. Power and velocity can then be estimated utilizing a variation of the pulse pair processing technique discussed in Doviak and Zrnić (1993) and derived

in Cheong et al. (2004) through the calculation of the autocovariance of the array output signals

$$\begin{aligned} R_{\mathrm{yy}}(\tau) &= E\left\{y(t)y^*(t-\tau)\right\} \\ &= E\left\{\mathbf{W}_l^*\mathbf{X}\mathbf{X}^*\mathbf{W}_l\right\} \\ &= \mathbf{W}_l^*\mathbf{R}_{\mathbf{xx}}(\tau)\mathbf{W}_l \end{aligned} \tag{3.70}$$

where $\mathbf{W}_l$ represents the lth column of the steering vector matrix. Thus, $R_{yy}(\tau)$ is a scalar value and $\mathbf{R}_{\mathbf{xx}}(\tau)$ is an $M \times M$ matrix at lag τ. Typically, the weight matrix is given by:

$$\mathbf{W} = \frac{1}{\sqrt{M}} \begin{bmatrix} e^{j\frac{2\pi}{\lambda}\sin\theta_1 \cdot d_1} & e^{j\frac{2\pi}{\lambda}\sin\theta_2 \cdot d_1} & \dots & e^{j\frac{2\pi}{\lambda}\sin\theta_L \cdot d_1} \\ e^{j\frac{2\pi}{\lambda}\sin\theta_1 \cdot d_2} & e^{j\frac{2\pi}{\lambda}\sin\theta_2 \cdot d_2} & \dots & e^{j\frac{2\pi}{\lambda}\sin\theta_L \cdot d_2} \\ \vdots & \vdots & \ddots & \vdots \\ e^{j\frac{2\pi}{\lambda}\sin\theta_1 \cdot d_M} & e^{j\frac{2\pi}{\lambda}\sin\theta_2 \cdot d_M} & \dots & e^{j\frac{2\pi}{\lambda}\sin\theta_L \cdot d_M} \end{bmatrix} \tag{3.71}$$

where θ_l is one within a vector containing the set of $l = [1, 2, \cdots L]$ desired sampling angles, λ is the radar operating wavelength and $d_{\mathbf{m}}$ is the position of the mth radar element from the phase center of the array. Utilizing the pulse pair processor concept (Cheong et al. 2004), power and radial velocity can be obtained via

$$P(\theta_l) = R_{yy}(0) = \mathbf{W}_l^*\mathbf{R}_{\mathbf{xx}}(0)\mathbf{W}_l \tag{3.72}$$

$$v_{\mathrm{r}}(\theta_l) = -\frac{\lambda}{4\pi T_{\mathrm{s}}}\arg\left[R_{\mathrm{yy}}(T_{\mathrm{s}})\right] \tag{3.73}$$

where T_{s} is the pulse repetition time (PRT).

3.2.3 Non-Parametric Beamforming

3.2.3.1 Window Functions

Variations of the pulse pair beamforming technique are explored with the goal of improving the accuracy and performance of the radar. The first and most

straightforward variation is to perform a weighted Fourier beamforming by simply augmenting the weight matrix through a Hadamard product with a matrix of scalar values, $\mathbf{A}_{\text{win}}$,

$$\begin{aligned} \mathbf{W}_{\text{win}} &= \mathbf{W} \circ \mathbf{A}_{\text{win}} \\ &= \mathbf{W} \circ \left(\begin{bmatrix} a_1 & a_2 & \dots & a_M \end{bmatrix}^{\text{T}} \begin{bmatrix} 1 & 1 & \dots & 1 \end{bmatrix} \right) \end{aligned} \tag{3.74}$$

where a_m is the mth value of any window function (Hamming, Hann, etc.) arranged in a column vector, which is then multiplied by an L-length row vector of ones. This is analogous to the window method applied in the spectral processing techniques described earlier. The columns of $\mathbf{A}_{\text{win}}$ are selected such that the amplitude of each array element is weighted by a value a_m, thus reducing the impact of sidelobes in the beamforming dimension at the expense of angular resolution and gain.

3.2.4 Adaptive Beamforming

While variations on Fourier beamforming algorithms are simple to implement, adaptive algorithms provide unmatched performance regarding sidelobe mitigation and angular resolution. In the subsequent sections, adaptive techniques described in a temporal sense earlier in the chapter will be presented and applied to spatially sampled data.

3.2.4.1 Capon Method

Data-dependent techniques alter the weighting function adaptively with respect to the received data and are able to minimize the impact of sidelobes while improving angular resolution. One such technique, known as Capon's method or the Minimum Variance method, attempts to minimize the power output of the

beamformer while maintaining unity gain in the desired pointing direction (Capon 1969). The resulting beampattern attempts to place nulls over points of strong interference or clutter. Expressed mathematically,

$$\min_{\boldsymbol{w}} \; P(\theta_l) \quad \text{subject to } \boldsymbol{e}_l^* \boldsymbol{w} = 1 \tag{3.75}$$

where $\boldsymbol{e}_l = \left[e^{j\frac{2\pi}{\lambda}\sin\theta_l \cdot d_1} \quad e^{j\frac{2\pi}{\lambda}\sin\theta_l \cdot d_2} \quad \dots \quad e^{j\frac{2\pi}{\lambda}\sin\theta_l \cdot d_M} \right]^{\mathrm{T}}$.

By examining the mathematical statement of Capon's method, it is apparent that little control of the beam pattern is maintained at angles other than the direction of interest. It is possible that, for areas other than the pointing direction with low signal strength, high gain values can result. Of course, the impact should be minimal since the signal strength is low.

Lagrangian methods are used to solve the well-known minimization problem and a solution for the Capon weight vector follows:

$$\boldsymbol{w}_{\mathrm{C}} = \frac{\mathbf{R_{xx}}^{-1}(0)\boldsymbol{e}_l}{\boldsymbol{e}_l^* \mathbf{R_{xx}}^{-1}(0)\boldsymbol{e}_l}. \tag{3.76}$$

The Capon weight vector is then substituted for $\mathbf{W}_l$ in both Equations (3.72) and (3.73) for high-resolution estimates of power and radial velocity.

While the angular accuracy of Capon's method is often superior to that of Fourier beamforming, small errors present in the steering vector, $\boldsymbol{e}_l$, can reduce the accuracy of amplitude estimations. Small errors can arise due to uncertainties in the array element positions, which result in an offset between the point of interest and the unity constraint location, thus allowing Capon's method to attenuate or skew the power measurement at the desired angle. A robust version of Capon's method exists that makes assumptions regarding the uncertain weighting vector and iteratively converges toward an optimal solution (Li et al. 2003; Li and Stoica 2006; Stoica and Moses 2005).

3.2.4.2 Robust Capon Method

As previously mentioned, robust Capon beamforming (RCB) makes an assumption that the true steering vector, $\boldsymbol{e}_0$, lies within an uncertainty set of ellipsoidal shape, or

$$[\boldsymbol{e}_0 - \bar{\boldsymbol{e}}]^* \mathbf{C}^{-1} [\boldsymbol{e}_0 - \bar{\boldsymbol{e}}] \leq 1 \tag{3.77}$$

where $\bar{\boldsymbol{e}}$ and $\mathbf{C}$ are given. Note that the l parameter from Equation (3.76) is dropped for simplicity. In the previous subsection, the Capon beamformer was viewed as a spatial filtering problem. For the robust Capon beamformer, the same problem is viewed from a covariance fitting standpoint and attempts to find the largest possible power at the signal of interest while keeping the residual covariance matrix positive semidefinite. At the same time, only steering vectors within the previously defined uncertainty ellipsoid are considered. Thus, the beamforming optimization is formulated as

$$\begin{aligned} \max_{\sigma^2, \boldsymbol{e}} \sigma^2 \qquad & \text{subject to } \mathbf{R_{xx}} - \sigma^2 \mathbf{e}\mathbf{e}^* \geq 0 \\ & \text{for any } \boldsymbol{e} \text{ satisfying } [\boldsymbol{e} - \bar{\boldsymbol{e}}]^* \mathbf{C}^{-1} [\boldsymbol{e} - \bar{\boldsymbol{e}}] \leq 1 \end{aligned} \tag{3.78}$$

where σ^2 is the power in the direction of interest. A complete and thorough derivation of the solution to the above formula can be found in Li et al. (2003). However, a summary of the steps involved is given in pseudocode format below:

1. Select a value for ϵ (related to the ellipsoidal search space)
2. Perform the eigendecomposition of $\mathbf{R_{xx}}$ and find $\mathbf{U}, \mathbf{\Gamma}$, where $\mathbf{U}$ is the set of eigenvectors and $\mathbf{\Gamma}$ is a diagonal matrix containing the corresponding eigenvalues, γ_m, with $m = 1 \ldots M$
3. Set a new vector $\boldsymbol{z} = \mathbf{U}^H \bar{\boldsymbol{e}}$

4. Solve $g(\lambda) = \sum_{m=1}^{M} \frac{|z_m|^2}{(1+\lambda\gamma_m)^2} = \epsilon$ for λ using Newton's method knowing the solution is unique and lies in the range
$\frac{||\bar{\boldsymbol{e}}||-\sqrt{\epsilon}}{\gamma_1\sqrt{\epsilon}} \leq \lambda \leq \min\left\{\left(\frac{1}{\epsilon}\sum_{m=1}^{M}\frac{|z_m|^2}{\gamma_m^2}\right)^{1/2}, \frac{||\bar{\boldsymbol{e}}||-\sqrt{\epsilon}}{\gamma_M\sqrt{\epsilon}}\right\}$

5. Use the determined value of λ to find $\hat{\boldsymbol{e}}_0 = \bar{\boldsymbol{e}} - \mathbf{U}(\mathbf{I}+\lambda\boldsymbol{\Gamma})^{-1}\mathbf{U}^H\bar{\boldsymbol{e}}$

6. Compute the estimated signal power from
$\hat{\sigma}^2 = \frac{||\hat{\boldsymbol{e}}_0||^2}{M}\frac{1}{\bar{\boldsymbol{e}}^H\mathbf{U}\boldsymbol{\Gamma}(\lambda^{-2}\boldsymbol{I}+2\lambda^{-1}\boldsymbol{\Gamma}+\boldsymbol{\Gamma}^2)^{-1}\mathbf{U}^H\bar{\boldsymbol{e}}}$

7. Calculate the new RCB weights $\boldsymbol{w}_{\text{RCB}} = \frac{(\mathbf{R_{xx}}+\frac{1}{\lambda}\mathbf{I})^{-1}\bar{\boldsymbol{e}}}{\bar{\boldsymbol{e}}^H(\mathbf{R_{xx}}+\frac{1}{\lambda}\mathbf{I})^{-1}\mathbf{R_{xx}}(\mathbf{R_{xx}}+\frac{1}{\lambda}\mathbf{I})^{-1}\bar{\boldsymbol{e}}}$

8. Use $\boldsymbol{w}_{\text{RCB}}$ for $\mathbf{W}_l$ in Equations (3.72) and (3.73).

The result of the algorithm is high angular resolution with estimates that do not suffer from uncertainties in the steering vector. While computational costs are significantly higher than those of the non-parametric or Capon methods, the benefits are significant and should be considered when weighing the different algorithms.

Another consideration is the choice of the user parameter, ϵ. A value must be chosen that is just large enough to produce accurate power estimates. Typically, a comparison with Fourier beamforming results can lead to an appropriate value. As ϵ decreases, the performance of RCB approaches that of Capon. Values of ϵ that are too large significantly degrade the performance of the algorithm and produce unusable results. Thus, this added level of complexity must be considered.

3.2.4.3 APES Method

The main difference between the APES counterpart for the spatial model is the fact that in the temporal case, the signal is assumed to be a sinusoid or a function of the form $\alpha e^{j\omega t}$. The spatial model makes no assumption regarding the type of signal, however, the system must be a ULA. There is some conjecture as to

weather APES can be extended to irregular array arrangements, however Stoica and Moses (2005) indicates that the difference between the interference and steering vectors used to determine h and the signal itself, respectively, are not proportional to each other thus removing the ability to attenuate the interference terms. Steering vector and calibration errors are better handled by APES than with Capon, though the same patterns of undesired attenuation are incurred.

Through the new model, Equation (3.43) becomes

$$\min_{h,s(t)} \sum_{t=1}^{N} \sum_{k=1}^{L} |h^* \bar{y}_k(t) e^{j(k-1)\omega_s} - s(t)|^2 \quad \text{subject to} \quad h^* \bar{a}_1 = 1 \tag{3.79}$$

where

$$\begin{aligned} \bar{a}_k &= \left[e^{-j(k-1)\omega_s}, e^{-j(k)\omega_s}, \ldots, e^{-j(k+\bar{m}-2)\omega_s}\right]^T \\ \bar{y}_k &= \left[y_k(t), y_{k+1}(t), \ldots, y_{k+\bar{m}-1}(t)\right]^T \ , \end{aligned} \tag{3.80}$$

with $k = 1, \ldots, L$, $L = m - \bar{m} + 1$, and $\bar{m} < m$ (Stoica and Moses 2005). Typically, a value of $L = 2$ is chosen, dividing the array into two, highly overlapping subsets. From here, it is relatively straightforward to derive the solution to the minimization problem by extending the derivation in Section 3.1.3.3 with the definitions above.

Specifically, $\hat{s}(t) = h^* g(t)$ where

$$g(t) = \frac{1}{L} \sum_{k=1}^{L} \bar{y}_k(t) e^{j(k-1)\omega_s} \ . \tag{3.81}$$

Thus, the minimization problem is reduced to

$$\min_{h} h^* \hat{Q} h \quad \text{subject to } h^* \bar{a}_1 = 1 \tag{3.82}$$

with

$$\begin{aligned}\hat{Q} &= \hat{R} - \hat{G} \\ \hat{R} &= \frac{1}{NL}\sum_{t=1}^{N}\sum_{k=1}^{L}\bar{y}_k(t)\bar{y}_k^*(t) \\ \hat{G} &= \frac{1}{N}\sum_{t=1}^{N} g(t)g^*(t)\ .\end{aligned} \tag{3.83}$$

Much like the temporal case, the filter coefficients become

$$\hat{h} = \frac{\hat{Q}^{-1}\bar{a}_1}{\bar{a}_1^*\hat{Q}^{-1}\bar{a}_1} \tag{3.84}$$

with the spatial spectrum given as

$$\hat{\sigma}_s^2 = \frac{1}{N}\sum_{t=1}^{N}|\hat{s}(t)|^2 = \hat{h}^*\hat{G}\hat{h}\ . \tag{3.85}$$

As a test of the array processing techniques, the periodogram, Capon, robust Capon, and APES methods were tested in a simulator similar to that used in Stoica and Moses (2005). Signal vectors were generated for a ULA consisting of 32 elements with a SNR of 10 dB and 100 temporal samples. Targets were positioned at 7.2, 9, 14.4, and 16.2 degrees with unity amplitudes. The results of the test are given in Figure 3.23

The actual position of the targets is indicated by the black vertical lines. Again, the periodogram has the lowest resolution and is not able to discern the closely spaced targets. The Capon method is able to resolve all four targets and again suffers from poor amplitude estimation. Some amplitude accuracy is recovered with the use of the robust Capon technique. Though three of the four target amplitudes are overestimated, overall, the bias is smaller than that of Capon. The APES technique also resolves the four targets, however the amplitude estimates are all higher than the true values. A possible justification for this is, again, the angle estimation is slightly off, resulting in inaccurate amplitude estimates.

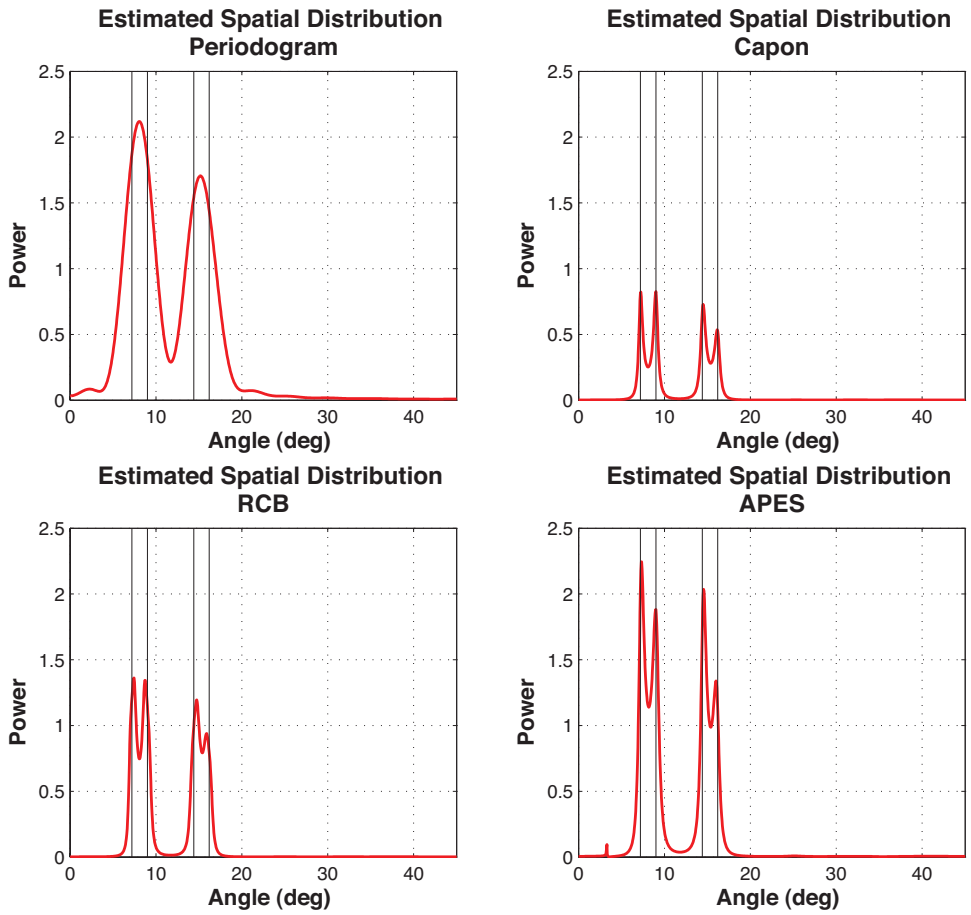

Figure 3.23: Results from an array processing simulator testing the periodogram, Capon, RCB and APES beamforming algorithms. Four targets were placed in the far field and their location are indicated by the black vertical lines. The three adaptive algorithms provide the best target location identification. $\epsilon = 0.05$ is used in the RCB computation.

It is difficult to define resolution for beamforming algorithms. Typically, a metric is utilized to quantify the ability of the algorithm to separate two closely-spaced targets. For instance, Palmer et al. (1999) discuss the peak-to-valley brightness (PVB), which is defined as the normalized difference between the peak of the highest point source and the minimum value laying between the two points. Thus, PVB provides a metric through which the resolution, or *resolvability*, of algorithms can be compared. It is known and understood that lower SNR will result in lower PVB scores and simulations can be performed to confirm this relation. From theory, it is also determined that as the SNR approaches zero, the performance of the Capon technique approaches that of Fourier beamforming, which is known to have a deterministic resolution.

For practical reasons, including computational complexity and accuracy, it is prudent to select a flagship algorithm by which real data analysis will be performed. Although RCB is more computationally expensive than APES or Capon, there are other advantages that overshadow this slight increase of computational complexity. It is known that with real phased array data, steering and calibration errors will be present, no matter how small. Due to this fact, RCB is the technique of choice as APES and Capon are not known for their good handling of these errors. Thus, ultimately, data collected by the radar system described in the next chapter will be processed using the RCB algorithm.

Further, additional techniques are available that choose to minimize the MSE of the estimated parameters as opposed to the maximizing of the signal-to-interference-plust-noise ratio, as the techniques described so far attempt to do (Li and Stoica 2006). Minimum MSE (MMSE) techniques are equipped to handle steering vector error, like RCB, in a fundamentally different manner. MMSE algorithms are, unfortunately, beyond the It is beyond the scope of this study and will not be explored.

3.2.5 Array Design

Typically, array element layouts are dependent upon interrelated items such as the size of the individual elements, the number of channels that is manageable for the system, the grating lobe location, the sidelobe performance, and the wavelength of transmission. Often times, sacrifices must be made to create a sustainable system. For instance, given a particular carrier frequency, the beamwidth of an array is determined by an empirical equation

$$\theta_{3\text{dB}} = \frac{51\lambda}{A} \tag{3.86}$$

where A is the aperture of the full array in the dimension of interest and is calculated by the interelement spacing, for a uniform array, via $A = dn$, with $n = [0, 1, \ldots, N-1]$, N being the total number of elements (Skolnik 2001). By defining the required aperture, the number of elements can be chosen to match the capabilities of the system or based on budgetary constraints. Once the number of elements is selected, the interelement spacing is known, thus determining another product of array theory, the grating lobe.

Grating lobes are ambiguities that appear at particular angles when the spacing between adjacent elements is larger than a specific value and is governed by the equation (Skolnik 2001)

$$\theta_{\text{gl}} = \sin^{-1} \lambda/d \ . \tag{3.87}$$

No grating lobes are present when $d \leq \lambda/2$ and this is similar to the Nyquist sampling theory presented in Chapter 2, meaning, the ambiguities will be present when spatial sampling is not performed at a sufficient rate.

To examine the effects of grating lobes on the radar parameters, a modification to the ambiguity function presented in Section 3.1.5.1 is performed. Details presented in Brookner (1964) define the ambiguity function for a linear array as

$$\chi(t_r, f_d, \theta) = \chi(t_r, f_d, 0) \left(\sum_{n=1}^{N} g_n e^{j2\pi d \sin(\theta)/\lambda} \right) . \tag{3.88}$$

Thus, at $\theta = 0$, the ambiguity function matches that of a single, monostatic radar with the same pulsed waveform pattern. Example ambiguity diagrams for the new multidimensional definition are presented in Figure 3.24. Both the zero-

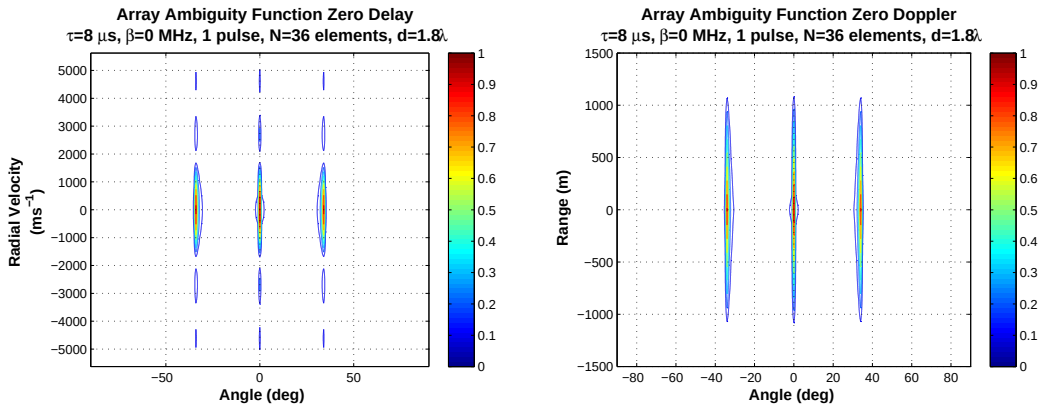

(a) (b)

Figure 3.24: Ambiguity functions for a uniformly spaced array. The actual ambiguity function is three dimensional so cross sections of the radial velocity and range planes are displayed in (a) and (b), respectively. Note the appearance of the grating lobes at $\pm 33°$.

Doppler and zero-Delay cuts are presented with the angle as the abscissa. Note the spacing of the elements of the ULA is $d = 1.8\lambda$, ensuring that grating lobes are present at approximately 33°.

A second example of the multidimensional ambiguity function is presented in Figure 3.25. In this case, the bandwidth of the transmitted pulse was increased to 5 MHz. As expected, the range resolution improved, however, the grating lobes

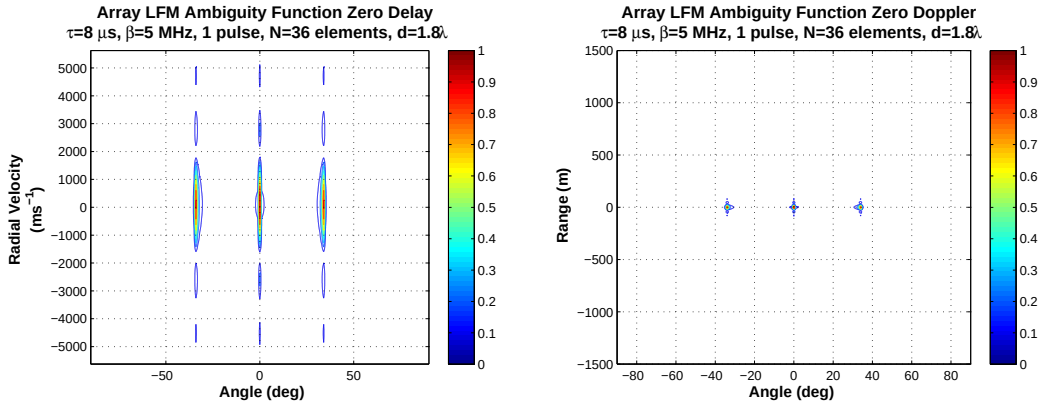

(a) (b)

Figure 3.25: Similar to Figure 3.24 except for a LFM waveform. Note the improved range resolution apparent in (b). The LFM waveform does not reduce the impact of the grating lobes.

still pose a problem for the system. Some techniques designed to mitigate the impact of grating lobes are presented in the subsequent sections.

3.2.5.1 Irregular Spacing

Grating lobe interference is a significant problem that is common for phased array systems. One technique for mitigating grating lobes and sidelobe interference is to employ irregular or nonuniform element spacing (Jarske et al. 1988). Often, array element locations are selected through optimization, which is performed to minimize the impact of these undesirable array artifacts (Kumar and Branner 1999, 2005). Irregular array spacing also changes the shape of the beam pattern such that the grating lobes split and are attenuated. Due to this affect, the lobes cease to behave like grating lobes and take on the qualities of strong sidelobes. Recall from the array processing discussion in Section 3.2.4 that adaptive beamforming techniques are able to minimize the impacts of sidelobes. Careful

selection of interelement spacing for spatial arrays can significantly reduce the impact of grating lobes. Cheong et al. (2006) explored the use of irregular spacing to remove interference from biological clutter in the grating lobes on the TEP radar system and a similar technique will be used here.

A simple test was performed to examine the effectiveness of irregular spacing on grating lobe reduction using radar simulator code modified from Stoica and Moses (2005). A 36 element ULA was simulated with a target positioned at 0° and an SNR of 30 dB. The array was separated into 6 subarrays with 6 elements each, and the space between each subarray was allowed to change via a systematic search through a set of possible values. An optimum value of 0.955λ was chosen as the space between adjacent subarrays. The resulting returns from a target located at 0° are given in Figure 3.26. The red line indicates the return from a standard ULA with the prominent grating lobes present at ±33°. The blue line represents the irregularly spaced array. Note that the grating lobes are now split and reduced in magnitude. Nulls present in the six element array factor created by separating the subarrays overlap the grating lobes present in the subarray patterns. It is expected that the application of an adaptive algorithm, such as Capon or RCB, will minimize the impact of the grating lobes.

A second simulation was performed with a target at 20° and Fourier beamforming as well as Capon and RCB were implemented. The results are presented in Figure 3.27(b), with the ULA response shown in (a) for comparison. Grating lobes, which are sidelobes in (b), are visible in the blue return pattern associated with the Fourier beamforming. The red line, calculated from the adaptive Capon beamforming algorithm, shows significantly reduced power received at the grating lobe locations for the irregular case. As expected, the power estimate from the Capon algorithm is lower than the actual value, a discrepancy that is corrected through the use of RCB.

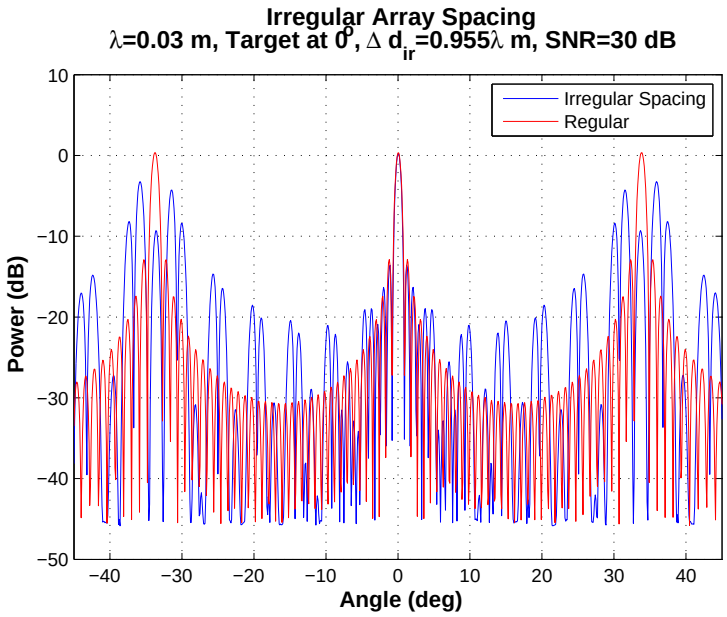

Figure 3.26: Example beam patterns of a ULA and an array with irregular interelement spacing. The ULA has 36 elements with $d = 1.8\lambda$. The irregular array is subdivided into six subarrays comprised of six elements each, with the intersubarray spacing defined as 0.955λ. Note the grating lobes present in the ULA are defocused and reduced in magnitude for the irregular spacing case.

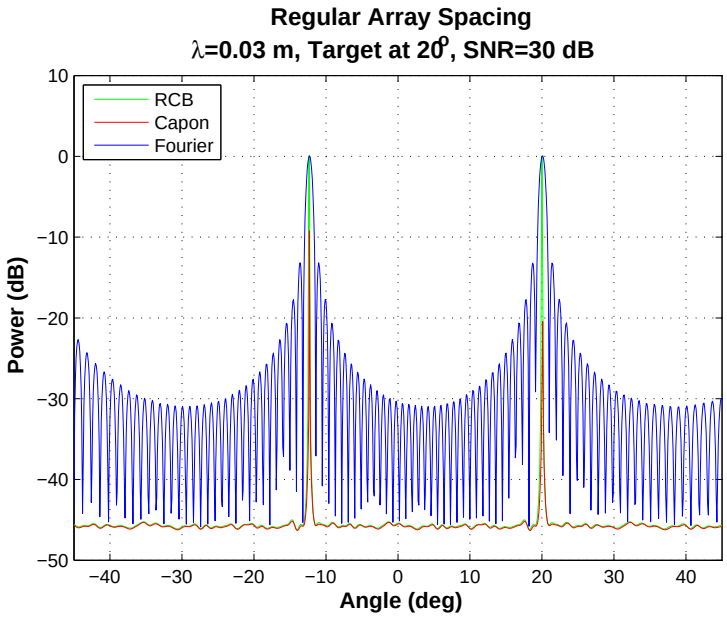

(a)

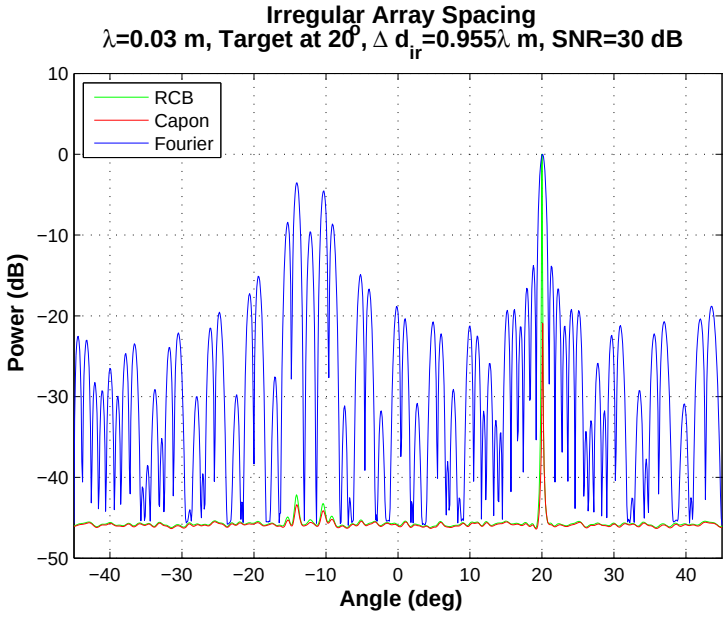

(b)

Figure 3.27: Simulation results for a regular (a) and irregular (b) array spacing. The ULA case shown in (a) suffers from ambiguities generated by the grating lobes. Once the irregular spacing has deformed the grating lobes into large side-lobes in (b), adaptive algorithms such as Capon or RCB are able to minimize the impact of the grating lobes.

As an exploratory exercise, a specific pattern of irregular spacing is explored, inspired by the staggered PRT algorithm described earlier.

3.2.5.2 Staggered Array Sampling

Since uniform arrays can be thought of as spatial sampling, often times temporal techniques that are effective in traditional signal processing algorithms can also be applied to array systems. Removing frequency ambiguities in the temporal domain was accomplished by utilizing a staggered PRT algorithm. A staggered spatial sampling technique will be described here that yields surprising results.

Grating lobes are ambiguities that cast doubt on the true angle of arrival for a phased array output. Another way to view the problem is to think of the main lobe as having a positive and negative steerable angular region in which it can discern targets at their true positions. This region is $\pm\theta_{\text{gl}}/2$. As the mainlobe arrives at $+\theta_{\text{gl}}/2$, the grating lobe originating at $-\theta_{\text{gl}}$ has now shifted to $-\theta_{\text{gl}}/2$. This is similar to the wrapping effect seen in radial velocity measurements for Doppler radars. In a manner similar to the technique presented in Section 3.1.4.1, the observable region of the radar can be increased by utilizing staggered spacing. An ambiguity waveform can be established in which the wrapping angles are

$$\theta_{\text{gl}}^1 = 0.5 \sin^{-1} \lambda/d_1 \tag{3.89}$$

$$\theta_{\text{gl}}^2 = 0.5 \sin^{-1} \lambda/d_2 \tag{3.90}$$

resulting in an effective increase in the viewing region, or shifting of the grating lobes, to $\theta_{\text{gl}}^{\text{s}} = m\theta_{\text{gl}}^2 = n\theta_{\text{gl}}^1$, giving a staggered spatial ratio of $\kappa = n/m$.

With staggered array spacing, the shape of the radar beam is altered in a manner that is similar to the staggered PRT ambiguity function. Recall that in Figure 3.10, the ambiguity peaks along the Doppler axis were defocused and the amplitude was reduced. A similar effect can be seen in Figure 3.28. The green

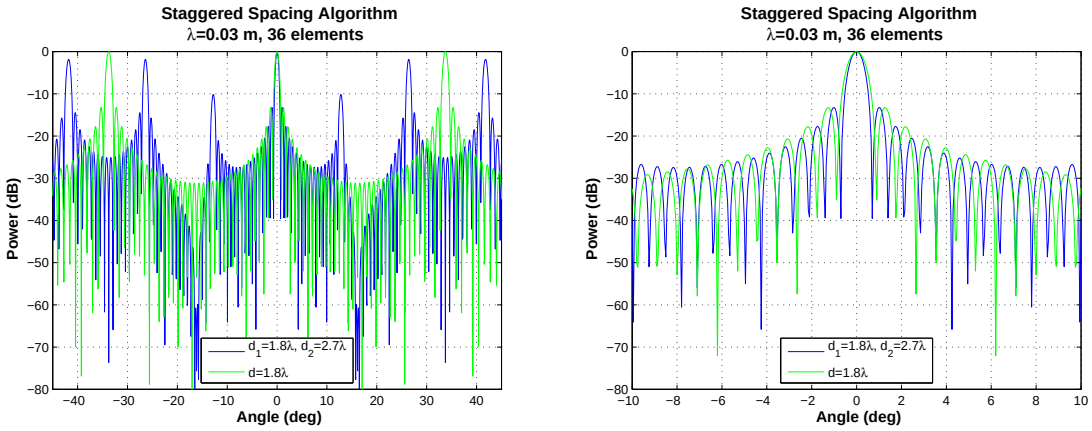

(a) (b)

Figure 3.28: Simulated beam pattern for a ULA (green) and a staggered spacing (blue) case. Much like the irregular spacing scenario explored earlier, the staggered array deforms the grating lobes allowing a dealiasing algorithm to increase the array field-of-view. A closer view of the main lobe and near-in sidelobes is given in (b).

line represents the ULA with $d = 1.8\lambda$ where the blue line represents a staggered array with $d_1 = 1.8\lambda$ and $d_2 = 2.7\lambda$, giving a staggered ratio of 2/3. Note the presence of the grating lobes in the ULA case. The grating lobes split and reduce in amplitude after the staggered spacing is implemented. A closer view of the mainlobe and near sidelobes is given in (b). It is the splitting of the grating lobes that will ultimately be exploited for the dealiasing procedure.

To perform angular dealiasing, an ambiguity waveform must be generated. An example ambiguity waveform is presented in Figure 3.29. The same temporal rules

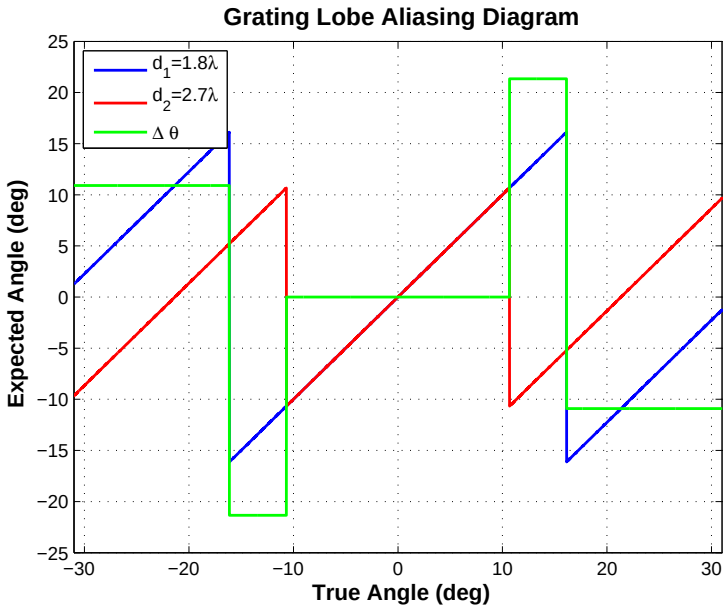

Figure 3.29: An illustration of the spatial ambiguity waveform derived from the staggered spacing algorithm. The blue line represents the ambiguity waveform for the elements with $d_1 = 1.8\lambda$ spacing, while the red line represents the elements with $d_2 = 2.7\lambda$. The resulting staggered ratio is $\kappa = 2/3$. The difference between the two ambiguity waveforms is plotted as the green line and will help dealias the estimated DOAs.

for dealiasing apply here. One caveat of the staggered array spacing technique

is the data processing procedure. For temporal cases, the short pulse pairs are processed individually and an average $\hat{R}(T_s)$ value is computed. It is this value that is used in Equation (2.64). Likewise, the same is repeated for the long pulse pairs and the resulting velocity estimates are used with the dealiasing rules to produce a new velocity estimate.

In the spatial case, the processing is carried out in a similar fashion: pairs of elements are processed and an average value is used to determine an angle of arrival for both the short and long spacing. To test the theory, a simulation was created using modified code from Stoica and Moses (2005). A single source is placed in the far field with unity power. Noise was removed from the simulation by setting $\sigma_{\mathrm{N}}^2 = 0$ and only one pulse is utilized. 36 equally spaced elements are used as a baseline for comparison while the staggered setup utilizes 30 elements, approximately matching the aperture size of the ULA. As a result, there are 15 short space pairs and 14 long space pairs. Angular aliasing occurs at approximately $\pm 16.12^\circ$ for the short pairs and at $\pm 10.87^\circ$ for the long pairs.

Results from the simulation with a target positioned at -3.2° are presented in Figure 3.30. The black line represents the return from the single target as seen from a ULA. Note that the ambiguity generated by the grating lobes is not a concern in this case because the target is within the vertical blue dashed lines, which denote the unaliased angular region. Once the target leaves this region, the grating lobes will produce false readings within the angular field-of-view. The blue and red lines represent the short and long element pairs, respectively. The angle of arrival is selected as the maximum power point for the average pattern that lies within the respective unaliased region, denoted by the vertical dashed lines. The maximum position is indicated with a star in the corresponding color. As can be seen, the maximum values match with the true position of the target, -3.2°. The maximum values are then used in conjunction with the chart in Figure 3.29 to

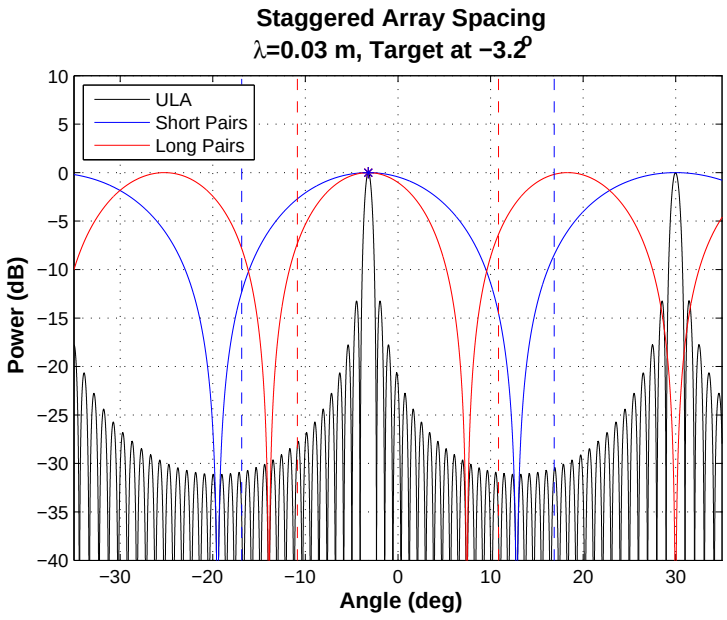

Figure 3.30: Simulated results from a staggered array. The black line represents the angular power distribution from a ULA for a target located at -3.2° and a power of unity. No noise was added to the signal for this simulation. The blue and red lines represent the power distribution from processing the short and long pairs of elements, respectively. The dashed vertical lines correspond to the angular ambiguity points and define the field-of-view for the element pairs. The $*$ points represent the maximum value within the pair field-of-view. The maximum points are the estimates used in conjunction with Figure 3.29 to produce the accurate dealiased DOA of -3.2°.

produce the angle of arrival estimate, $\hat{\theta}$. In this example, the dealiasing rules indicate that the estimated angle is $\hat{\theta} = \hat{\theta}_1$ since the target is not outside of either unaliased boundary.

A second simulation tests the effectiveness of the algorithm with a target well outside the unaliased regions. The results of the test for a target placed at 30° are presented in Figure 3.31. The three lines show a maximum value at

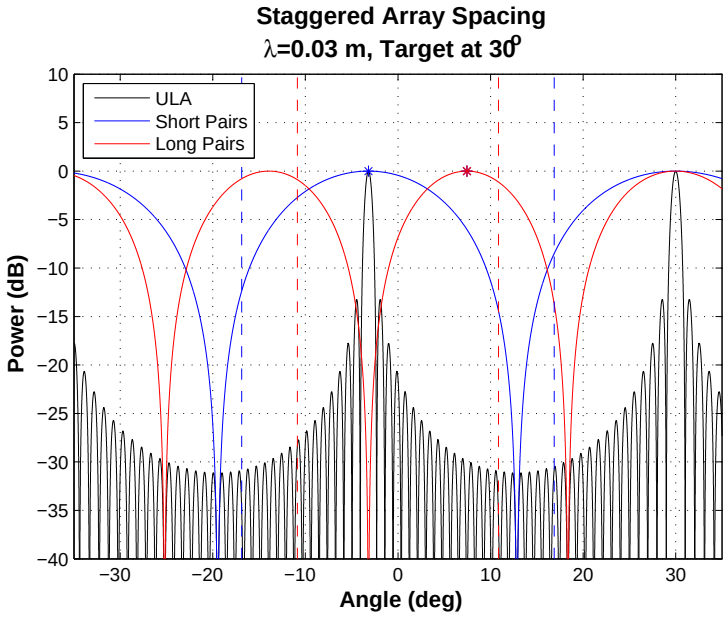

Figure 3.31: Similar to Figure 3.30 except for a target located at 30°. Note the short pair peak coincides with the ULA due to the spacing of 1.8λ. The offset peak found through the long pair processing facilitates the accurate DOA estimate of 30° via the chart in Figure 3.29.

30°, which is where the target is actually located. However, within the unaliased boundary, the ULA shows a target at approximately -3.2°. The staggered array spacing algorithm will provide a method for resolving the ambiguity generated by the grating lobe. Since the short space pairs are separated by a distance that matches the ULA, the blue line shows a peak that coincides with the ULA grating

lobe. However, the long space pairs produce a peak that is offset from the ULA grating lobe, at 7.5°. The combination of the two peak values with the dealiasing rules produce an angle estimate of $\hat{\theta} = 30°$, the actual target angle value.

While in theory the staggered array spacing technique is shown to work, there are concerns with some artifacts of the processing that must be addressed. Due to the pair processing, the beamwidth of the individual pairs is extremely large, on the order of 9.4° and 4° for the short and long pairs, respectively. Resolving a single target in the absence of noise proves the methodology and theory, however, in practice the technique may not be achievable. In the case of multiple or distributed targets, an average position of all scatterers would be produced as the peak value for each set of pairs. Thus, it is likely that a nearly flat angular spectrum would be produced, causing the dealiasing algorithm to fail. More work in studying the effects of the staggered array spacing is required to identify potential applications and implementations.

3.2.6 Generalization to Conformal/Non-Planar Arrays

For the purpose of this discussion, linear arrays were utilized for their simplicity as well as for the applicability to the instrument discussed in the following two chapters. However, all of the work can be translated to planar and conformal arrays. A simple extension of the spatial model is all that is needed to produce solutions for a number of element configurations. There are two extensions that must be made to apply the array theory discussed thus far to three dimensions.

First, the element position vector, $\mathbf{d} = \begin{bmatrix} d_1 & d_2 & \dots & d_m \end{bmatrix}^T$ $(m \times 1)$ becomes a $(m \times 3)$ matrix, namely

$$\mathbf{d} = \begin{bmatrix} d_{x1} & d_{y1} & d_{z1} \\ d_{x2} & d_{y2} & d_{z2} \\ & \vdots & \\ d_{xm} & d_{ym} & d_{zm} \end{bmatrix} . \tag{3.91}$$

Next, the angle of arrival is no longer simply dependent upon θ. Instead, spherical coordinate angles θ and ϕ must be utilized. An illustration helps define the new three-dimensional coordinate system and is given in Figure 3.32. Typically, the

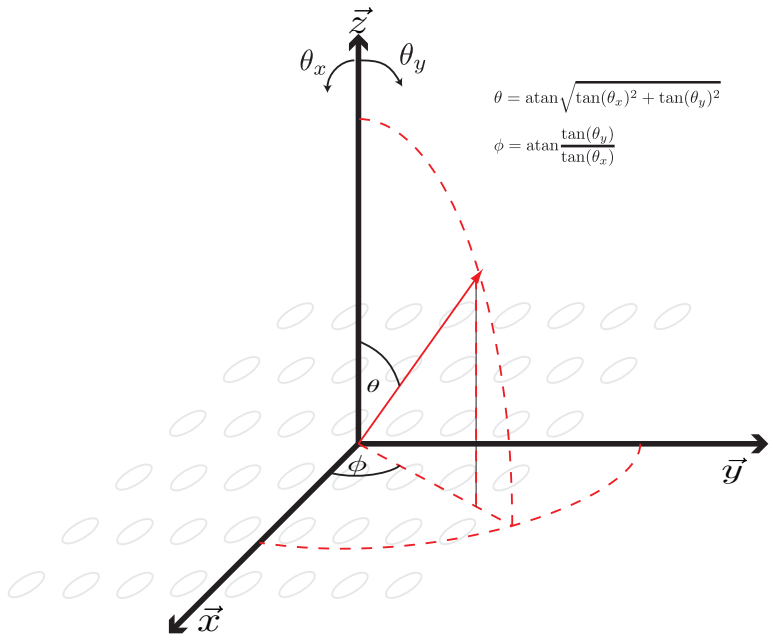

Figure 3.32: A diagram representing the change from a linear array to a planar or conformal array. The transition from a single axis of coordinates to three dimensions is relatively straightforward through simple change-of-variable equations. A simple planar array of elements is shown in the diagram for reference.

grid of angles selected for observation is defined by θ_x and θ_y because they are more intuitively traversed. θ_x is defined as the angle made from the $\vec{z}$ axis to

a point in the xz plane. Similarly, θ_y is defined as the angle from $\vec{z}$ to a point in the yz plane. To convert these values to the appropriate coordinate system, a change of variables must be employed. The following equations transfer the desired observation angles to spherical coordinates.

$$\theta = \text{atan}\sqrt{\tan(\theta_x)^2 + \tan(\theta_y)^2} \tag{3.92}$$

$$\phi = \text{atan}\left(\frac{\tan(\theta_y)}{\tan(\theta_x)}\right) . \tag{3.93}$$

From here, it is simple to change the $\sin\theta$ term in the beamforming model to the three-dimensional vector, $\begin{bmatrix}\sin\theta\cos\phi & \sin\theta\sin\phi & \cos\theta\end{bmatrix}$.

One interesting array design that is currently under consideration by the University of Oklahoma and NSSL utilizes a non-planar design. With maturation of polarimetric radars, scientists and researchers now demand dual-polarization radar parameters for modern radar systems. Polarimetric planar arrays suffer from cross-polarization squinting when the beam is steered off broadside, specifically at angles non-orthogonal to the primary array axes. Zhang et al. (2011) are currently exploring a cylindrical design that would reduce the degradation of polarimetric products, while maintaining the benefits of a phased array, such as electronic steering and multi-function capability. An illustration of a cylindrical array and the corresponding coordinate axes are given in Figure 3.33. As the array depicted is round in shape, particular elements cannot be used to observe some regions of space. It is proposed that the array be subdivided into overlapping subarray sets that will be used to observe designated azimuth angles. Given this arrangement, it is a simple task to utilize the three-dimensional model described above to perform array processing on even a complex geometric structure such as a cylinder.

Leveraging the resources available at the University of Oklahoma as well as the knowledge summarized in this chapter, the author and a team of students, faculty

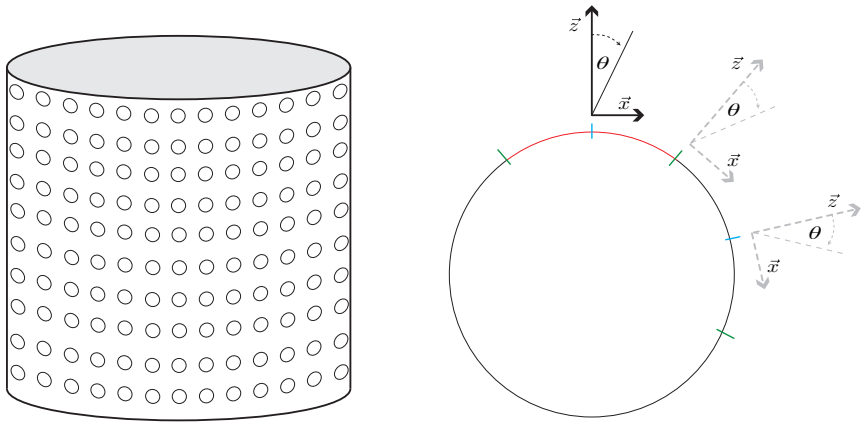

Figure 3.33: A depiction of a cylindrical system (a) and a suggested coordinate system for array processing (b). Cylindrical arrays are being explored by Zhang et al. (2011) as a viable replacement for planar arrays that suffer from polarimetric parameter degradation when steered to particular angles.

and staff proceeded to design and build an innovative radar system exploiting the latest beamforming techniques. The Atmospheric Imaging Radar (AIR) system will be presented in detail in the subsequent chapter.

Chapter 4

The Atmospheric Imaging Radar

4.1 System Design

A brief description of the AIR was given in Chapter 1 while a significant review of relevant background material was presented in Chapters 2 and 3. As previously discussed, the AIR is an imaging radar and exhibits many improvements over conventional radar systems, particularly dish radars. Temporal resolution and algorithmic versatility are the primary benefits of the AIR. A detailed system description will now be presented in this chapter.

4.1.1 Full System Overview

The AIR is a mobile imaging system that operates at X-band meant to observe radiation scattering primarily from rain and other hydrometeors. A photograph of the AIR is presented in Figure 4.1. As an imaging radar, the AIR transmits a broad beam, which determines the FOV or observable region in which beamforming is performed and is determined by the transmit horn at the top of the array structure. Thirty-six receive channels collect the return signals from the scattered transmit pulse, and I and Q values are recorded via five, eight-channel software-defined radio digital receivers and a computer system, which are housed within the truck cab.

Figure 4.1: An image of the AIR mobile radar. The completed system is comprised of multiple subsystems divided into the pedestal, array, transmit, receive, and digital storage assemblies. Each subsystem will be discussed in detail and results from subsystem tests are presented.

Beamforming is accomplished using a ULA, meaning, the pedestal must rotate in azimuth to gather a horizontal sector of data. Each subarray has a digital down conversion unit attached to the back of the assembly. A climate controlled enclosure is mounted behind the array support structure on the radar pedestal. Housed within the enclosure are the waveform generator, TWT, and analog up conversion components. A block diagram showing the signal paths within the radar system is presented in Figure 4.2. The radar is tethered, meaning it cannot

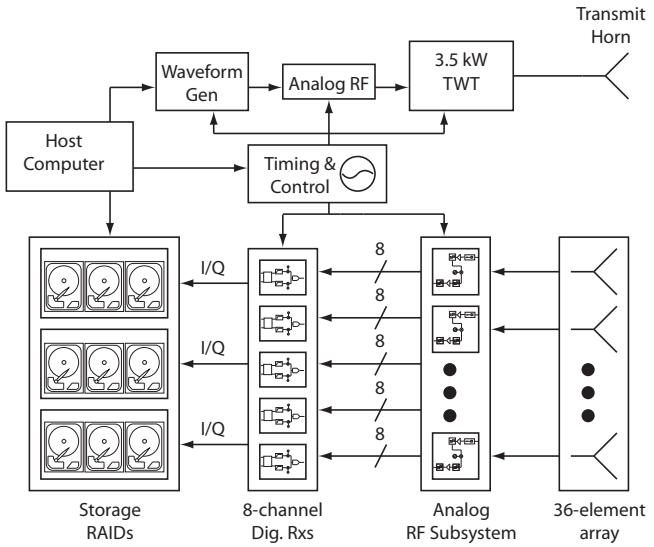

Figure 4.2: A block diagram displaying the signal flow through the AIR system. Note the transmit and receive chains are kept coherent by a master oscillator that distributes a 80-MHz clock signal. The individual components are discussed in detail in this chapter.

rotate a full 360°. However, a 270° range of motion can be achieved before mechanical stops are engaged. A large, 20-kW diesel generator provides power for the radar system. Clutter mitigation and other data quality improvements are achieved through the use of digital beamforming algorithms. Overall, the AIR provides a significant improvement over traditional systems due to the versatility of its design.

Remarkable temporal resolution can be achieved with the AIR. While mechanical rotation limitations remain, infinite elevation angles can be collected at each azimuth angle. While elevation beam positions existing within the 3-dB beamwidth will not be independent and therefore are consolidated to one sample, the fact remains that multiple elevations angles are collected and overall scan times are reduced when compared with traditional parabolic dish systems. Typically, the elevation extent is defined by the transmit 3-dB beamwidth, in this case approximately 20°. Thus the AIR reduces the data acquisition time by a factor of 20 when compared to a pencil-beam radar.

System parameters for the AIR system are given in Table 4.1. One notable feature of the AIR is the use of a TWT amplifier. The advantages of the TWT are an increased maximum duty cycle. A typical magnetron system has a maximum duty cycle of 0.1% compared to the 2% maximum for the TWT, in our case. A longer duty cycle allows for a low power, relatively long pulse to be utilized, reducing the need for high power switching hardware and allowing for diverse waveforms to be utilized for pulse compression.

One of the disadvantages of an imaging radar system is the necessary wide transmit beam. Sensitivity is sacrificed in exchange for the rapid volumetric updates. Of course, the longer pulses facilitated by the TWT help to recover some of the lost sensitivity of the AIR. To quantify the loss of sensitivity and ascertain the feasibility of recovery through pulse compression, a sensitivity calculation was performed and a discussion of the technique and results is given next.

Table 4.1: System Characteristics of the AIR

System		**Subarrays**	
Frequency	9.55 GHz	3-dB Beamwidth	1°×20°(FOV)
Power	3.5 kW TWT	Gain	27 dBi
Duty Cycle (Max)	2%	VSWR	2:1
Sensitivity	<10 dBZ @10 km 0 SNR	Polarization	Horizontal (RHI Mode)
Range Resolution	30 m (pulse compression)	Size	1.2×0.05 m
Array		**Pedestal**	
Beamwidth	1°×1°	Rotation Rate	40° s^{-1}
Number of Subarrays	36	Controller	PID
Aperture	1.2×1.8 m	Gear Ratio	100:1
Configurable Array			
Linear			
Transmit Horn		**Receiver**	
Beamwidth	1°×20°	Type	Digital
Gain	28.5 dBi	ADC	14−bits
Size	1.5×0.12 m	Sampling Rate	40 MHz
Slotted Waveguide Array			

4.1.2 Sensitivity Calculation

It is relatively straightforward to determine the MDS of a radar system with some minor assumptions by making use of the weather radar equation derived in Chapter 2. For convenience the weather radar equation is repeated here:

$$\bar{P} = \frac{P_t g_t g_r c\tau \theta_{3\text{dB}}^2 \pi^3 |K_m|^2 Z_e}{2^{10} r^2 \mathrm{l}^2 \ln 2 \lambda^2} \ . \tag{4.1}$$

As the weather radar equation shown above assumes a circularly symmetric beam, a slight modification is required in which the $\theta_{3\text{dB}}^2$ term is replaced with a $\phi_{3\text{dB}}$ and $\theta_{3\text{dB}}$. The MDS for weather radars is denoted in dBZ at a particular range, for a specific SNR. In this case, 0 dB SNR= 0 dB and a range of 10 km is chosen. Specific parameter values are presented in Table 4.2 and the weather radar equation is solved for equivalent reflectivity, Z_e.

Table 4.2: Weather Radar Equation Parameters: AIR

P_t	3.5 kW	τ	1.0 μs
g_t	28.5 dBi	g_r	27 dBi
$\theta_{3\text{dB}}$	1°	$\phi_{3\text{dB}}$	20°
$\lvert K_m \rvert^2$	0.9275	r	10 km
l^2	0.45 dB	λ	3.14 cm
$\bar{P}$	-100 dBm	c	3×10^8 m s^{-1}

Many of the values are specific to components listed in Table 4.1. Others, such as the complex refractive index and two-way losses, were calculated from theoretical and empirical data (Doviak and Zrnić 1993). The values must be converted to linear and radian units prior to the calculation of the Z_e parameter, which must be normalized by a factor of 1 mm^{6}m^{-3}. The return power parameter

is determined by the noise floor of the down conversion unit. The resulting reflectivity value indicates the MDS for a single subarray within the AIR system for a single radar pulse. Ideally, the system noise is independent between subarrays and the signal of interest is coherent. Thus, the array gain can be exploited, in an ideal case, to be a factor of $10 \log_{10} M$, where M is the number of elements in the array.

Results from the sensitivity calculation are presented in Table 4.3. The advantages of the TWT become apparent by the significant improvement of the MDS with the transmission of a longer, 8-μs pulse. Still, with a simple 1-μs pulse, signals associated with light drizzle are theoretically detected with a single subarray (Doviak and Zrnić 1993). For comparison, the MDS for a dish radar with a 1.2-m parabolic reflector with a 44-dBi gain and a transmit power of 25-kW is given. Of course, a 25-kW transmitter would likely be a magnetron and an 8-μs pulse is unrealistic. Nevertheless, the results are merely presented for comparison. While the sensitivity values exceed that of the AIR, the calculated MDS values were deemed adequate for severe storms. It was by this manner that the sensitivity requirement was met during the design of the AIR.

Table 4.3: AIR Minimum Detectable Signal at 10 km

Unit	**1 μs MDS**	**8 μs MDS**
Subarray	20.75 dBZ	11.72 dBZ
Array	5.19 dBZ	-3.84 dBZ
Dish	-7.28 dBZ	-16.31 dBZ

Mobile radars are ideal instruments for recording rapidly evolving phenomena due to the ability to gather data at a close proximity, improving spatial resolution. The AIR was intended to at least match the spatial resolution of existing systems.

To do so, special care was given to the array structure. In the next section, a description of the AIR subarray arrangement and the design process will be presented.

4.1.3 Array Design and Aperture Evaluations

Limits, with regard to finances and data bandwidth, had a major impact on the maximum number of elements for the array. Ideally, a ULA could be constructed from patch antennas spaced no further than 0.5λ, occuping an aperture of 1.6 m, giving a beamwidth of 1° with no grating lobes. However, such an array would require over 100 channels, in the case of the AIR. From Table 4.1 and discussed in detail in a later section, the digital receiver is capable of 14-bit resolution. For I and Q sampling at 40 MSs^{-1}, over 14 GBs^{-1} of data would need to be stored. Further, 100 channels require an equal number of expensive components such as low-noise amplifiers (LNAs), RF filters, reference oscillators, and enclosures.

Rather than attempt a project with such high uncertainty, a more practical design was created. Instead of single patch elements comprising the baseline dimension of the array, subarrays incorporating pairs of patch antennas were selected. Due to the limitations of the physical structure of the subarray, the patch antennas are separated by 0.7λ, and the subarray dimension along the baseline is 0.057 m. The inter-subarray spacing is primarily a factor of the subarray radome, which encloses the entire patch antenna structure. Due to these limitations, grating lobes became an issue and mitigation strategies to this dilemma were explored.

While the physical dimension of the subarrays was less than ideal, an opportunity to attempt grating lobe mitigation techniques resulted. By design, individual

subarray locations on the array can be altered, allowing for exploration of alternative array spacings, like the techniques discussed in Chapter 3. Before committing to a design, simulations were performed to ascertain the ideal beam patterns and the effectiveness of the irregular array spacing. While many of the results of such an analysis were given in the previous chapter, additional figures are presented here which illuminate the design process specifically for the AIR.

First, a simulation of the full two-way antenna pattern was developed for understanding the interaction between the transmit and receive beams. It is anticipated that grating lobes should be attenuated by the shape of the transmit beam. The two-way antenna pattern for the ideal 100 element array with λ inter-subarray spacing is given in Figure 4.3. Shown are the estimated element pattern,

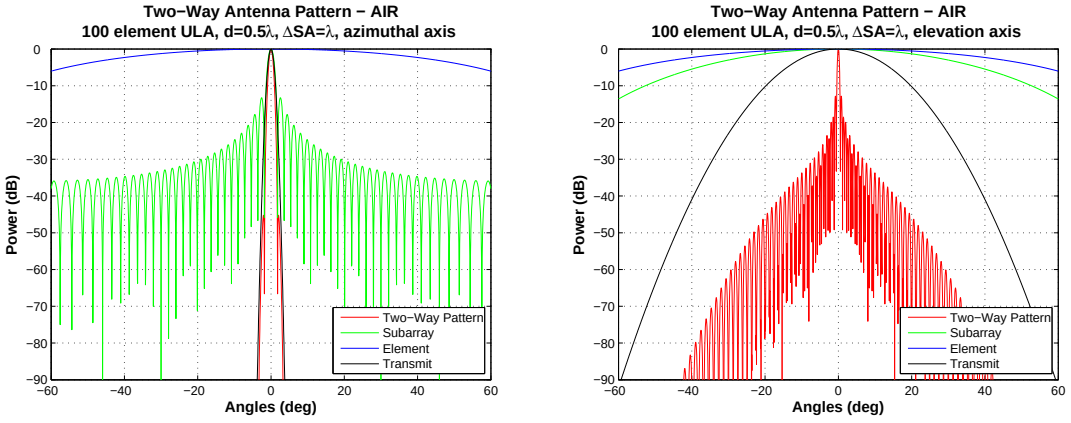

(a) (b)

Figure 4.3: A two-way antenna pattern in both (a) azimuthal and (b) elevation planes for a 100 element, λ spaced array. Patch element (blue), subarray (green), transmit (black) and full array patterns are included in the simulation of the two-way pattern (red). The transmit pattern has a dramatic effect on the overall shape of the beam. No tapering is available in the azimuthal dimension and no weights were applied to the ULA.

Gaussian approximation for the transmit pattern, subarray factor, and the two-way pattern. The azimuthal cut of the respective antenna patterns is shown in Figure 4.3(a) while the elevation, beamformed cut is shown in Figure 4.3(b). Note the influence of the transmit beam on the receive pattern in both horizontal and vertical dimensions and how the FOV is determined by the characteristics of the transmit pattern. It should be mentioned that the Gaussian approximation for the transmit beam is somewhat unrealistic in that the measured patterns plateau at -40 dB at approximately $\pm 45^{\circ}$ for both azimuthal and elevation axes. Additionally, the azimuthal pattern has some sidelobes present, none exceeding -23 dB, between 2°and 45°(see Figure 4.28). Thus, the azimuthal pattern will still act to reduce the impact of the subarray sidelobes, though not to the degree indicated in the simulation. For completeness and clarity, the two dimensional pattern is presented in Figure 4.4. The majority of the energy is focused in a small region though sidelobes from the Fourier beamforming algorithm are present and indicate angular leakage.

Incorporating the actual physical dimensions and characteristics of the 36 receive channels into the simulations provided a detailed view of the array performance before any fabrication was initiated. The actual size of the subarray elements in the beamforming dimension is 0.05715 m, or roughly 1.8λ. To further enhance the simulations and provide more realistic representation, a spacing of 0.7λ was used between the patch antennas that comprise each subarray. Again, many simulation results based on this element spacing were presented in Chapter 3, however, the full two-way pattern was not examined. Now the results of the two-way pattern simulations will be presented and the results are shown in Figure 4.5. It is with the inclusion of the realistic array spacing that the grating lobes appear. Additionally, the subarray pattern, having increased in the elevation dimension, becomes more narrow with nulls appearing at approximately

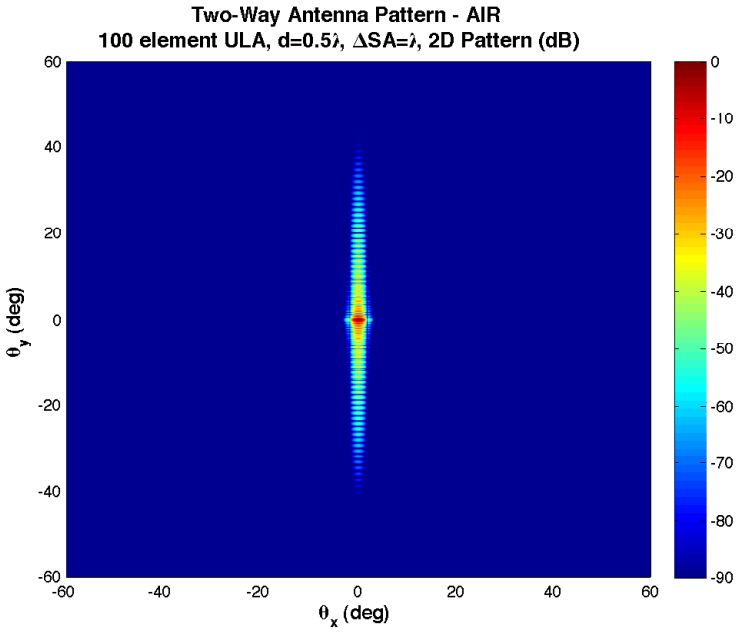

Figure 4.4: A two-dimensional representation of an ideal 100 element ULA with 0.5λ spacing. The two-way pattern is shown as a narrow band oriented in the vertical dimension. Note that the actual 3 dB beamwidth of the beam is quite narrow.

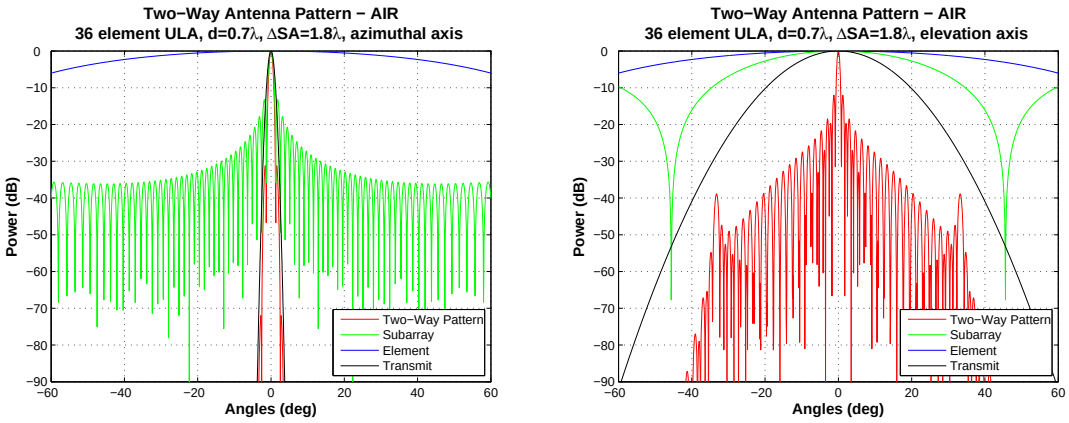

(a) (b)

Figure 4.5: As in Figure 4.3, except for a 36 element array with 1.8λ subarray spacing. Each patch array is separated by 0.7λ due to the actual constraints in array fabrication. Note the emergence of the sidelobes in the elevation pattern (b). The magnitude of the grating lobes is approximately accurate despite the Gaussian approximation for the transmit beam.

±45°. The transmit beam again has a significant effect on the grating lobe magnitudes. Again, the transmit beam is an approximation, however, the effect is representative of the true two-way pattern. The two-dimensional pattern is given in Figure 4.6. Observe the grating lobes at approximately ±38° in the elevation

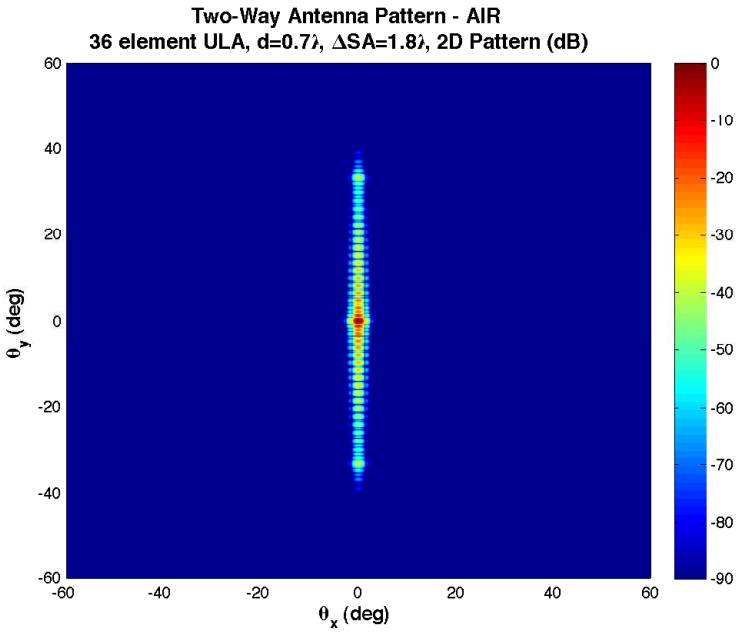

Figure 4.6: As in Figure 4.4, except for the realistic 36 element, 1.8λ spaced array. Note the appearance of the grating lobes in the vertical dimension. Techniques to mitigate the effects of grating lobes were presented in Chapter 3.

dimension.

Grating lobe ambiguities are a concern when observing at the array broadside, but can have an even greater impact when steering off-broadside. For instance, at the limits of the FOV, one of the grating lobes will move closer to the broadside position, reducing the attenuation caused by the transmit beam. A simulation with the main beam steered to -10° was performed and the results are given in Figure 4.7. The negative-side grating lobe has all but disappeared from the

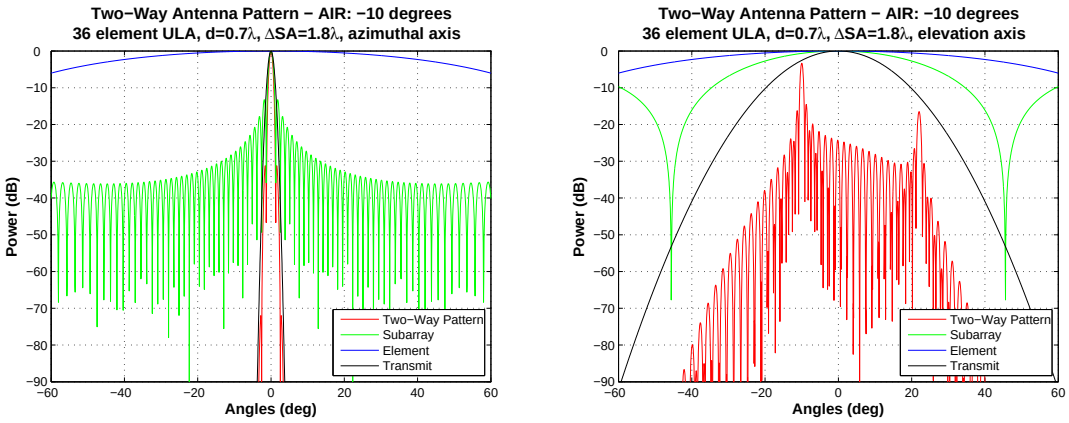

(a) (b)

Figure 4.7: As in Figure 4.5, except the beam is steered to -10° in elevation. Note the increase in the grating lobe magnitude due to the reduction in transmit beam attenuation at the shifted location. Also, note the reduction in the main lobe magnitude resulting from a similar effect. The azimuthal axis is normalized to the peak of the main lobe, but the pattern remains unchanged.

vertical axis image while the positive-side grating lobe has increased in magnitude by more than 20 dB. The two-dimensional pattern is presented in Figure 4.8.

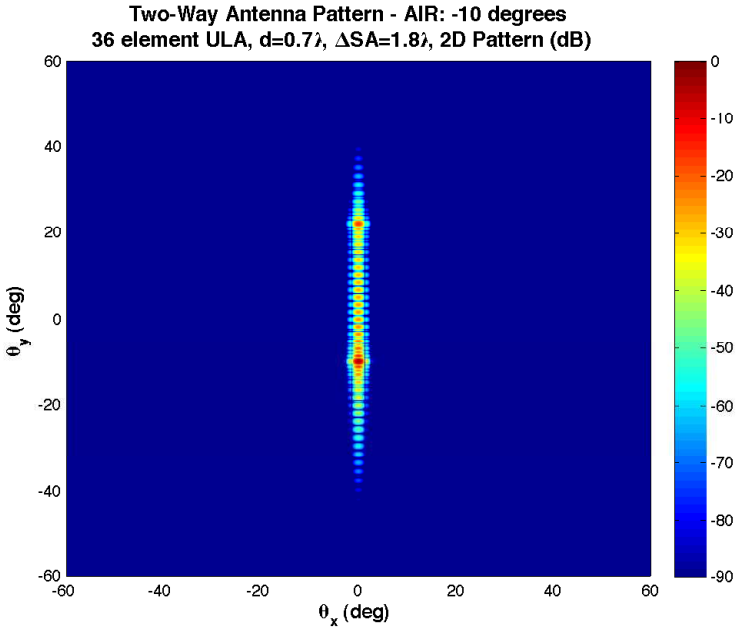

Figure 4.8: As in Figure 4.6, except the beam is steered to -10°. Note the increase in the grating lobe level on the upper portion of the vertical axis.

As discussed in Chapter 3, traditional amplitude tapering (windowing) and adaptive techniques will not reduce the impact of the grating lobe. Instead, staggered spacing or some form of irregular spatial arrangement is required, thus inducing a sidelobe-like behavior in the grating lobes, allowing Capon or RCB algorithms to reduce the interference/ambiguities.

A simulation of the irregular spacing arrangement discussed in Chapter 3 was performed, with the six-element subarray arrangements, each separated by 0.995λ. The results are displayed in Figure 4.9. As expected, the grating lobes have been deformed and will now behave like sidelobes after the application of an adaptive beamforming algorithm. The two-dimensional pattern is given in Figure 4.10. For completeness, the single and dual-axis images for the irregularly

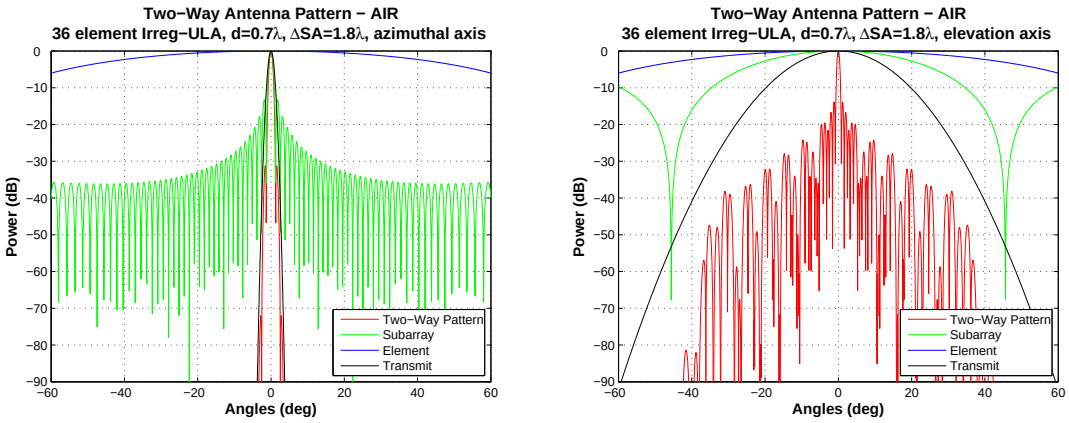

(a) (b)

Figure 4.9: As in Figure 4.5, except an irregular array spacing is implemented. The irregular pattern is described in Chapter 3 and is composed of six-element subarray arrangements. The spacing between each six-element group is 0.995λ. The deformed grating lobes are now treated as sidelobes in adaptive beamforming algorithms such as Capon or RCB.

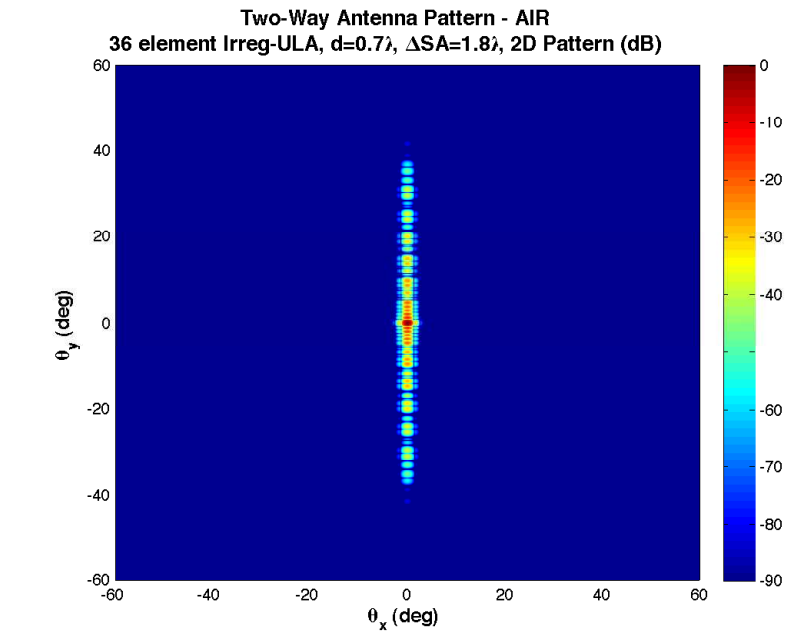

Figure 4.10: As in Figure 4.6, except for an array of irregular spacing. Note the deformation of the grating lobes in the elevation axis.

spaced array are given in Figures 4.11 and 4.12 with the main beam steered to -10°. Note that the peak of the now deformed grating lobe is lower than that of the ULA case when the main beam is steered to -10°.

To facilitate exploration of spatial arrangements, the array supporting frame for the AIR is larger than the space occupied by the 36 subarrays when positioned side-by-side. By providing the additional space, irregular arrangements can be explored, though none were completed for this dissertation.

What follows is a subsystem-level description of the AIR. Each subsystem is defined in its role in the overall system, construction and operation. Also included are any subsystem testing and validation results.

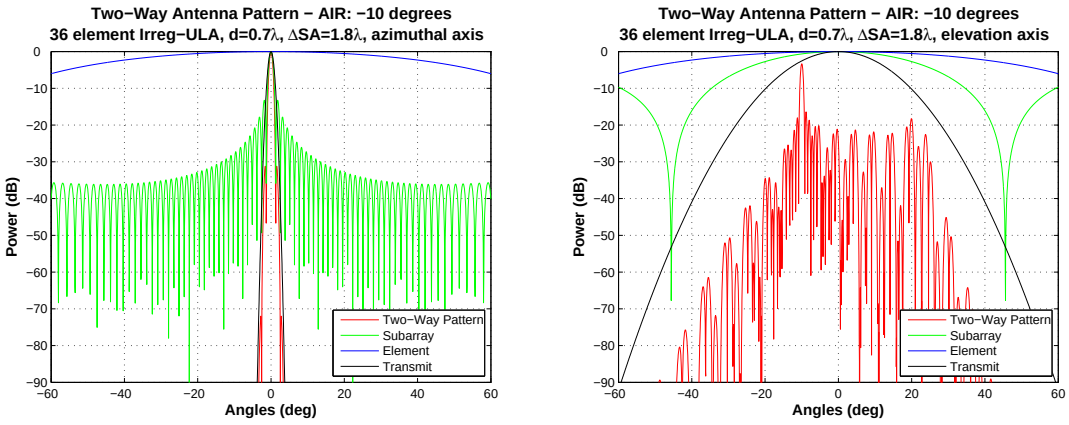

(a) (b)

Figure 4.11: As in Figure 4.7, except for an irregularly spaced array. Though the deformed grating lobes increase in magnitude as the beam steers away from broadside, adaptive beamforming algorithms will significantly reduce the impact of any leakage cased by their presence.

4.2 Subsystem Description, Design and Evaluation

4.2.1 Overall Structure and Common Signals

4.2.1.1 Truck and Pedestal

Integral to the mobile aspect of the design, the vehicle serves not only as the platform for the array and all of the control and processing equipment, but must be capable of transporting the entire system to remote locations at relatively high speeds. As the phenomena of interest are quickly evolving, observation scenarios can rapidly change and high mobility is necessary for the safety of the equipment and the operating personnel. As such, a powerful vehicle was required to carry several thousand pounds of equipment through potentially rough terrain. A Cheverolet C5500 medium duty commercial diesel truck was selected

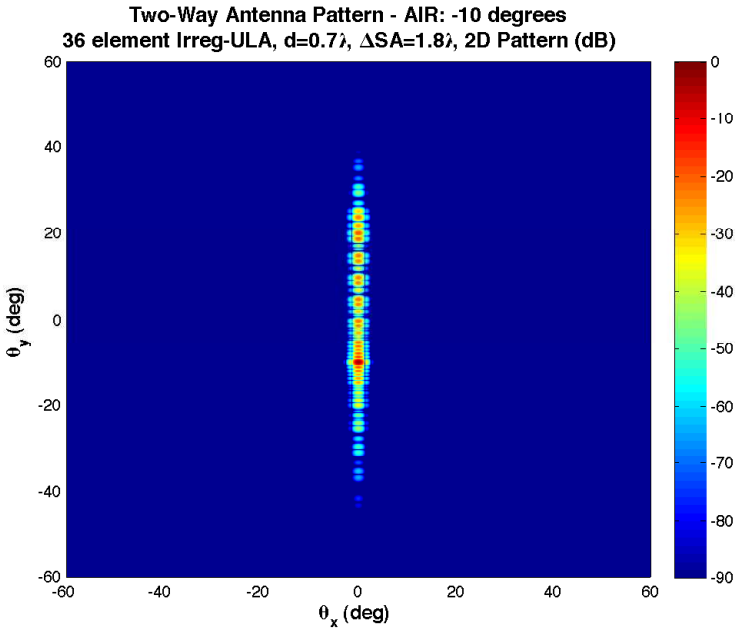

Figure 4.12: As in Figure 4.8, except for an irregularly spaced array. Note the deformation of the grating lobes, which allows for the application of adaptive sidelobe reduction.

as the platform for the AIR. An image of the bare chassis prior to any modifications is presented in Figure 4.13(a). The 6.6 liter diesel engine provided 330

(a)

(b)

Figure 4.13: The AIR truck chassis (a) before and (b) after the installation of the truck bed. A Chevy C5500 was selected because of its powerful engine and four-wheel drive capability. A high towing capacity allows the AIR to carry its own radar system as well as transport other, trailer mounted systems as well.

horsepower, which is sufficient to quickly move the radar and equipment between observation points. Further, the truck originally had a gross vehicle weight rating (GVWR) of 17,500 pounds, but an upgrade was purchased increasing the GVWR to 19,000 pounds. Additionally, the four-wheel drive allows the radar to maneuver through mud and primitive roadways.

Following the acquisition of the truck, an appropriate truck bed was selected. The steel comprising the bed must be robust so as to facilitate the mounting of an extremely heavy radar pedestal and generator without compromising the stability of the vehicle by overburdening the suspension system. A CM SS 84" truck bed was determined to be an ideal fit for the application. While the 1/8" steel skin was too thin to mount the pedestal directly, a supplemental 1/2" steel plate was added to give additional rigidity to the structure. A photograph of the AIR truck complete with truck bed is given in Figure 4.13(b).

After the truck bed was installed, computer racks were constructed and mounted inside the truck cab. A photograph of the completed rack is given in Figure 4.14. Three hydraulic booms were also installed, which can be lowered to stabilize the

Figure 4.14: A complete computer rack within the AIR truck cab. The metal cylinder at the base of the rack is a shock absorber designed to minimize vibrations on sensitive computer equipment.

truck in high winds as well as level the bed of the truck to ensure accurate elevation angle readings while scanning. The booms are controlled from within the truck cab with a set of four switches.

The pedestal design was of particular importance for the AIR given the unique nature of the radar. An array support structure would be required as well as a mechanism to rotate at a specified $30°s^{-1}$ and accelerate at $10°s^{-2}$. In addition to the array, several of the transmit subsystem components would be mounted

inside an enclosure that would reside behind the array panel, including the TWT, up converter, waveform generator, and waveguide pressurization device. Further requirements stated that the array panel was to rotate in the elevation plane, allowing a full 90° of motion, including a stow position that would minimize wind drag when the platform was in transit. Additionally, the stow position would allow the truck to pass safely under standard bridge and overpass heights. Finally, the pedestal must be able to withstand 44 $\mathrm{m\,s^{-1}}$ winds.

The task of designing and constructing the pedestal was given to a team of mechanical engineering students in the School of Aerospace and Mechanical Engineering (AME) at OU. The team was comprised of one AME professor, Dr. K. H. Chang, and four students: Joshua Davis, Derek Geyer, Jonathan Giuliano, and Ryan Johnson. Over several months, the pedestal design was derived and construction was completed in the spring of 2009. The final drawing of the pedestal is presented in Figure 4.15. The overall weight of the pedestal itself is approximately 1,800 pounds. Significant effort was put into the design of the aluminum array structure and the steel support system for the pedestal. Finite element analysis was performed for several wind load, road vibration, and automobile collision scenarios. In many cases, the design was altered to enhance performance and achieve a minimum safety factor of two.

To facilitate the rotational requirements, a Parker MPP115 motor was utilized to drive a 100:1 ratio, right-angle gear head which rotated a platform resting on a wind-turbine-grade bearing. Controlling the motor is a servo amplifier and controller unit, also produced by Parker, the Gemini GV6K. The controller is controlled via an Ethernet connection and has the capability of performing position control and monitoring, thus creating a closed loop system. Overall, the system more than meets the $30^{\circ}\mathrm{s^{-1}}$ and $10^{\circ}\mathrm{s^{-2}}$ angular velocity and acceleration requirements, respectively.

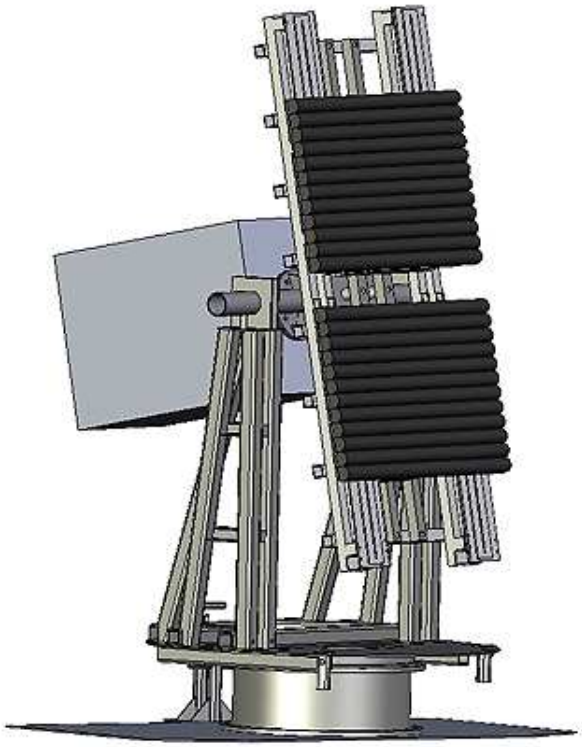

Figure 4.15: An illustration of the AIR pedestal. The array panel has additional space at both ends allowing for the subarrays to be shifted in position, enabling irregular spacings to be tested. The transmit enclosure is shown mounted behind the array panel.

Elevation axis motion and control was facilitated through the use of a Washdown Electric 1,798 pound push/1,348 pound pull Force Actuator with an 18" stroke. The actuator attached to an arm that rotated the elevation axis directly. The actuator is fully capable of quickly increasing or decreasing the elevation angle of the array with the use of a weather-sealed controller located near the pedestal base. A locking pin is used to secure the array in the stow position and four tension arms prevent the array from rocking during travel.

Maintenance of the pedestal is somewhat minimal. As much of the structure is steel, paint must be monitored and reapplied frequently. Rust is a substantial threat to the integrity of the system and paint is the best mitigator of its propagation. The bearing is another potential point of failure and grease must be added approximately every 100 hours of operation. An access port on the side of the bearing allows the application of grease with an appropriate grease gun.

4.2.1.2 Power, Clock, and Trigger Distribution

On a mobile platform, electrical power is provided through the use of a generator. For the case of the AIR, an Ampere budget was developed and, in a worst case scenario, nearly 80 A would be required to power the AIR. Thus, a MQ Power 20-kW diesel powered generator was installed. A picture of the generator is presented in Figure 4.16.

The generator produces a single-phase 240 VAC output, which is passed through a power transfer switch. A power transfer switch allows the radar to acquire alternating current (AC) power from either the generator or, if it is available, a 240 VAC wall outlet. The AC power is then distributed to all the relevant equipment. A block diagram of the transfer switch wiring is given in Figure 4.17, while a diagram of the overall AC power distribution is presented in Figure 4.18. A breaker box is essential to the operation of the radar for two reasons. First,

Figure 4.16: An image of the 20-kW diesel generator that provides electrical power to the AIR. Power output is 240 VAC single phase and passes through a transfer switch prior to entering the main breaker box, which distributes power to the subsystems.

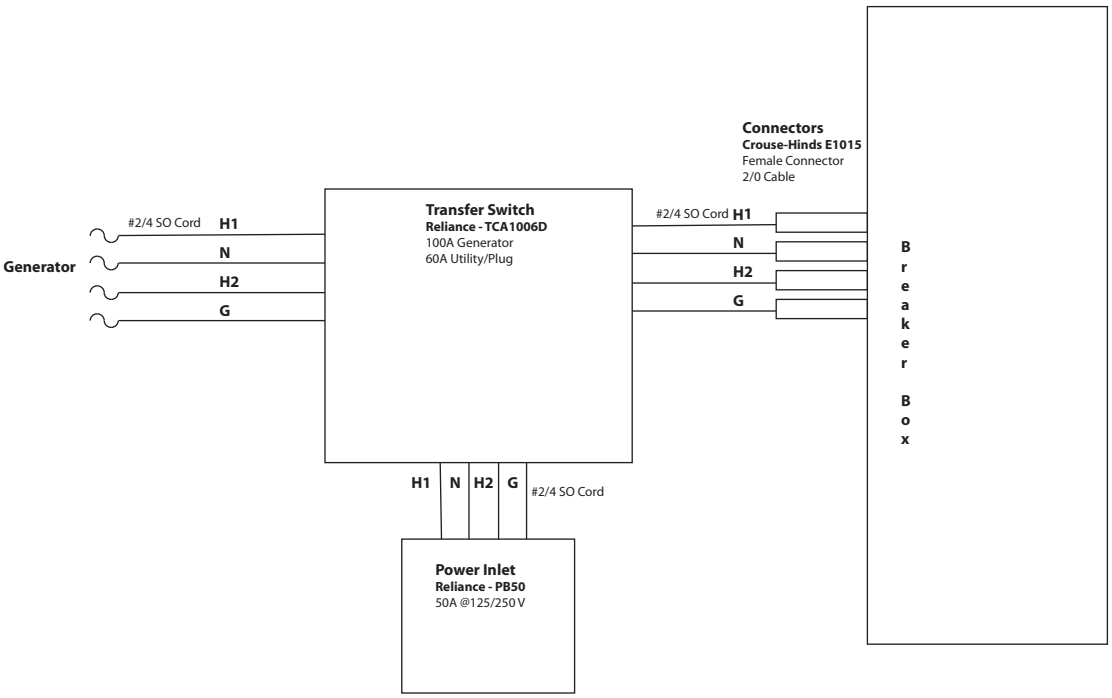

Figure 4.17: An illustration of the AC power transfer switch wiring. The AIR can be powered by either the diesel generator or a 240 VAC wall outlet. The transfer switch allows the user to determine which source is used. Regardless of the source, power is delivered to a breaker box, which protects the subsystems from short circuits and allows for quick identification of device failures.

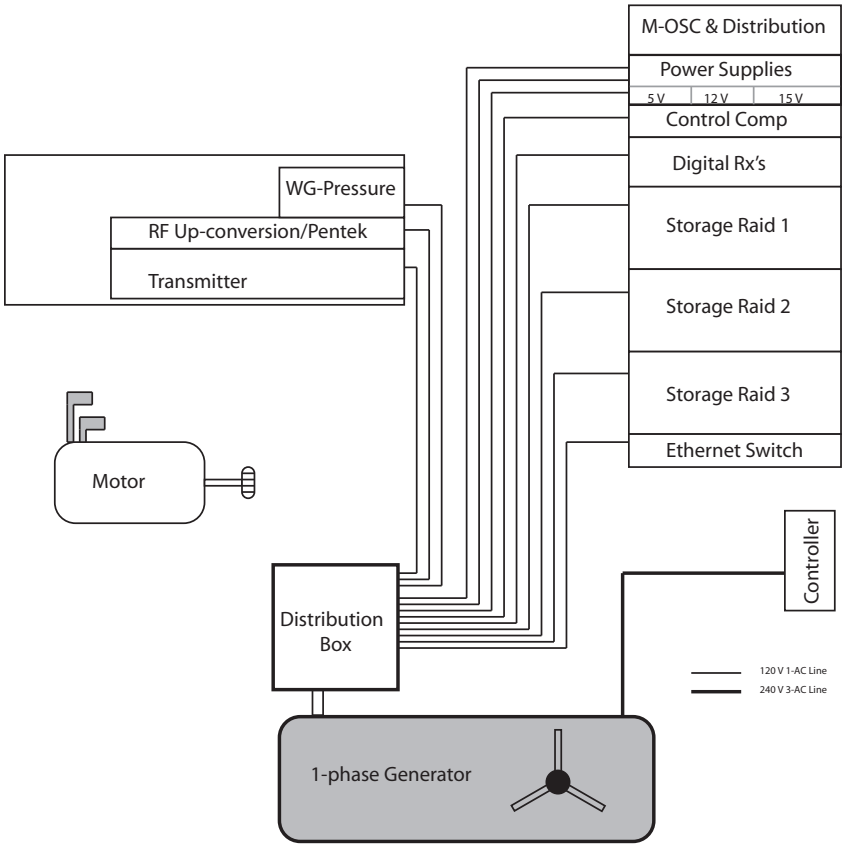

Figure 4.18: A block diagram of the AC power distribution within the AIR. Note the many pieces of equipment that require AC power. Subsystems are isolated to particular breakers so as to allow for easy identification of device failure.

the distribution box contains circuit breakers that will disconnect a link should a short circuit occur downstream, which protects the equipment and prevents shock or fire from occurring. Second, the breakers can provide subsystem isolation that allows some systems to continue running if another system shorts or fails. Also, it is easier to identify offending equipment when only a few components are associated with a specific breaker.

While many of the components within the system require AC power, a great many also need direct current (DC) power to operate. As such, three large DC power supplies were installed that distribute power to many of the digital and analog components. In this case two 5 and one 12 and 15-VDC power supplies were used with current ratings of 16, 6, 13, 5.5 A, respectively. The 16-A power supply is solely for the digital receivers and trigger board. A table indicating the major components requiring DC power and the current drawn by each is presented in Table 4.4. As can be seen, a large amount of the DC power was required for the

Table 4.4: Major DC Components and Required Current

Component	**Voltage (V)**	**Current (A)**	**Number**	**Total Current (A)**
Trigger Board	5	1	1	1
Digital Receiver	5	1.5	5	7.5
RF Amp (RFDC)	15	0.08	36	2.88
IF Amp (RFDC)	5	0.08	36	2.88
Oscillator (RFDC)	12	0.25	36	9

RF down conversion units located behind each subarray. The voltage was sent along two large cables capable of transferring high current without appreciable

loss over a distance of approximately 30 feet. A diagram of the cable wire colors and pin placement on the connectors is given in Figure 4.19. Due to the large

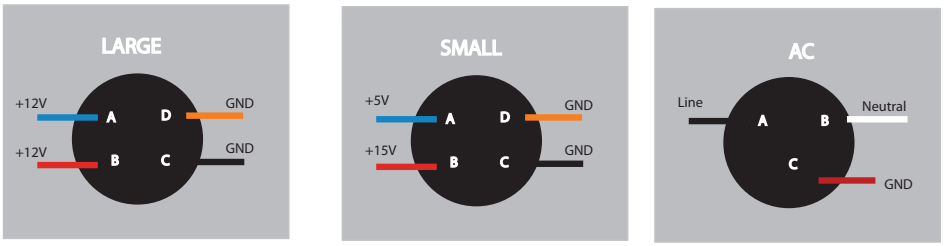

Figure 4.19: A diagram of wire colors and pin placement for the AC and high-current DC cables. Due to the large amount of current drawn by the 12-VDC devices, two pairs of wires were utilized in one large cable.

number of components behind the array that required DC voltage, a distribution box was constructed. The purpose of the distribution box was to allow a handful of cables to power and synchronize a large number of components. The distribution box simply accepts the high current DC lines from the cab and distributes the appropriate voltages to the individual down conversion units via an arrangement of terminal boards. An image showing the exterior of the distribution box is given in Figure 4.20. The connectors on the right are attached to the DC ports on each of the 36 down conversion units. On the left, 36 threaded Neill-Concelman (TNC) connectors distribute the 80-MHz clock signal to each phase-locked oscillator (PLO) housed within the down conversion units. The clock signal maintains coherence between the transmit and receive subsystems. The distribution of this signal will be discussed next.

The clock signal is generated by a Rhode and Schwartz SML01 with an option that raises the output power capabilities. The output signal is generated at +23 dBm so that the appropriate power level arrives at each component following the splitting network housed within the clock distribution box. A diagram

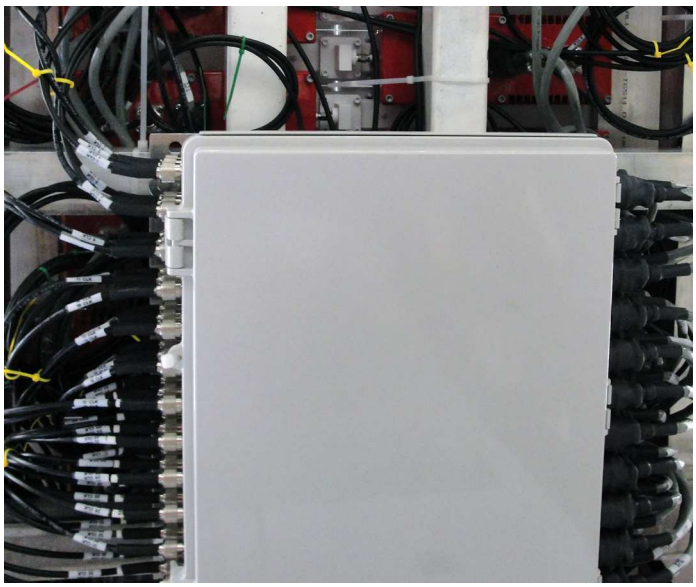

Figure 4.20: An photograph of the clock and DC power distribution box located on the back of the array panel. The DC cables are shown on the right side of the box while the 80-MHz clock lines are on the left. Several terminal boards and power splitters were used inside the box to split the incoming signals and disseminate to each down conversion unit.

illustrating the signal splitting that occurs to the clock signal path is given in Figure 4.21.

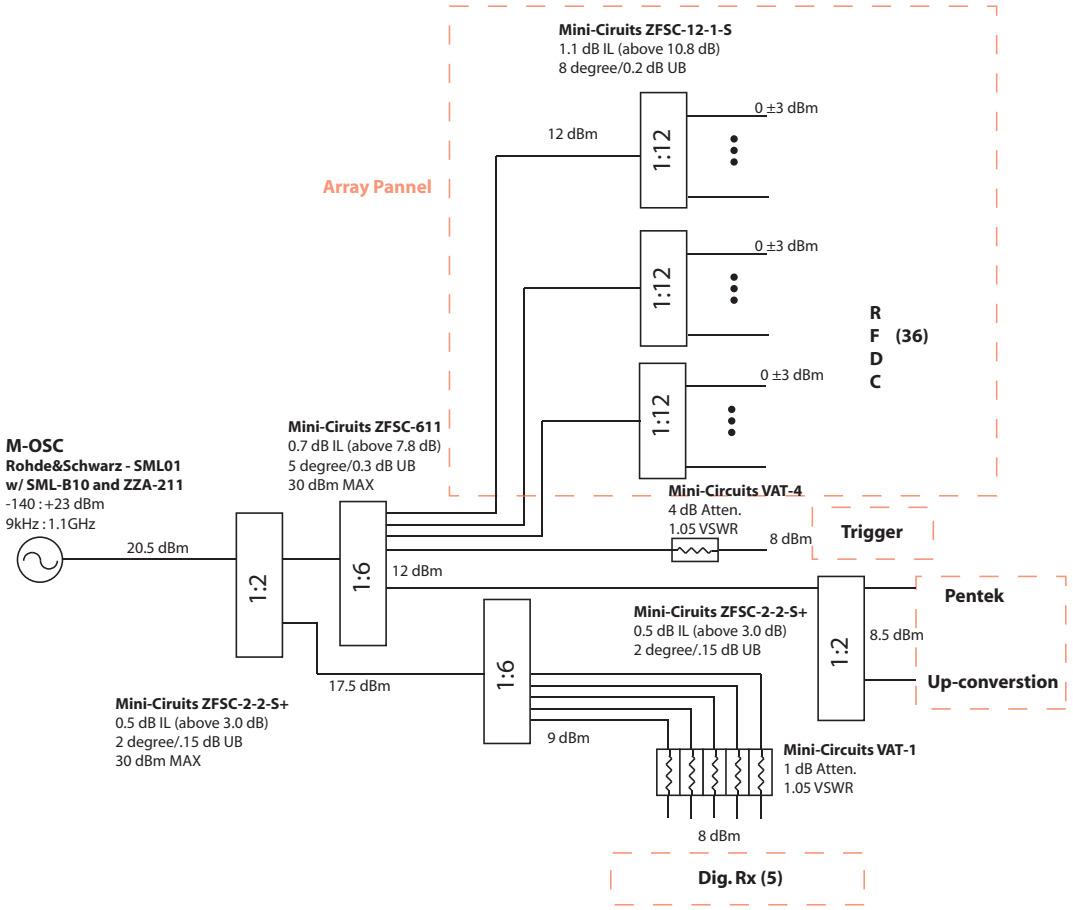

Figure 4.21: A diagram illustrating the clock signal path within the AIR system. Many coaxial power splitters are utilized to distribute the 80-MHz clock signal to the many dependent subsystems. The initial power of the clock produced by the master oscillator must be sufficiently high to ensure proper coherence downstream.

In addition to the clock signal, many of the components require a trigger to synchronize the timing between the transmit and receive subsystems. A field programmable gate array (FPGA)-based board designed in-house at OU is utilized to generate and distribute the trigger signals to the appropriate components. The trigger board itself has seven SubMiniature version A (SMA) outputs, two

clock input lines, +5 VDC input connector and an RS-232 (serial) connection for control. The five digital receivers as well as the TWT and waveform generator all require a trigger signal before they begin their designated task. Several tests were performed to ascertain the appropriate timing required for the transmission of the selected waveform due to a nominal delay in the reception of the trigger signal and the transmission of the amplified RF signal by the TWT.

An example of the results of a particular trigger signal delay are presented in Figure 4.22. The purple signal is the output of a crystal detector placed at

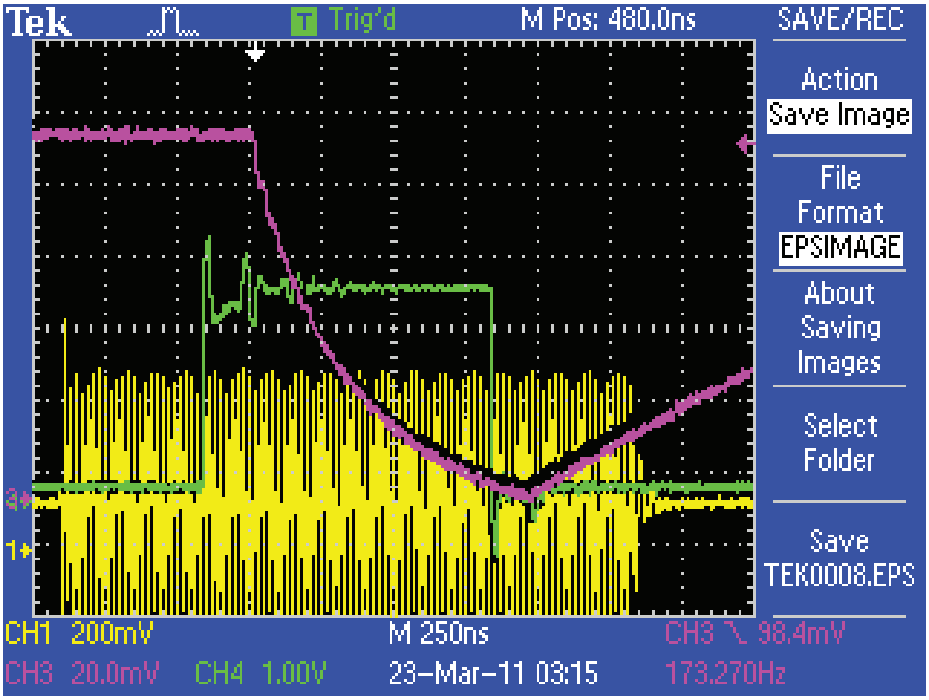

Figure 4.22: Results of the trigger timing test performed with the trigger board (green), waveform generator (yellow) and TWT (purple). TWT RF output was sampled at the waveguide output with a crystal detector. Note the delay between the rising edge of the trigger pulse and the TWT output. A similar effect is observed on the falling edge. Delays are added to the trigger signals to synchronize the transmit and receive tasks.

the waveguide port of the TWT. The yellow and green signals are the output of the waveform generator and TWT trigger signal, respectively. The waveform generator produces an IF waveform that is longer than the intended pulse width so that the signal is available to the TWT when the tube begins to fire. Note the 170 ns delay between the trigger signal and the actual output of the TWT. Additional timing assessments must be completed in the case of LFM waveforms due to the tight requirements for bandwidth and a priori knowledge of the transmitted waveform for matched filtering. The measured delays between the waveform generator and trigger signal and the TWT output are presented in Table 4.5.

Table 4.5: TWT Timing Delays

	Trigger to TWT	**Wave Gen to TWT**
Rising Edge	170 ns	80 ns
Falling Edge	105 ns	320 ns

The following section will describe the transmit chain in detail and provide information regarding the components that comprise it.

4.2.2 Transmit Chain

4.2.2.1 Transmit Enclosure

Many of the components that comprise the transmit chain are housed within the weather sealed, climate controlled enclosure mounted behind the array structure designed and built by EIC. Controlling the temperature of the interior is a 2,500 British thermal unit (BTU) thermoelectric solid state air conditioner. The interior walls are lined with insulating foam and a standard 19" computer rack is included inside. Three doors provide access to the equipment: one in front to

slide the equipment in on traditional computer rack rails, and two on the side to allow access to the input and output ports for each piece of equipment. An illustration indicating the equipment housed within the enclosure is given in Figure 4.23. On the bottom is the TWT, with the waveform generator computer

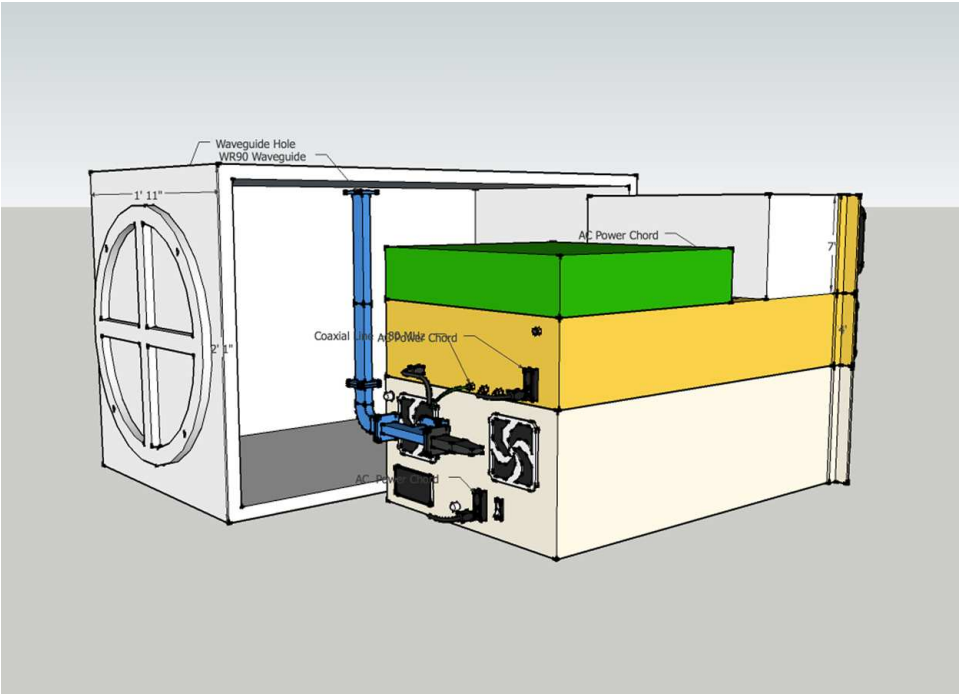

Figure 4.23: An illustration of the equipment housed within the weather sealed enclosure. The TWT is the large unit on the bottom of the equipment stack with the waveform generator computer resting on top. The green box is the analog up converter and the shorter case behind the up converter is the waveguide pressurization unit.

positioned just above. Continuing upward, the green box represents the analog up conversion network and positioned toward the front of the enclosure at the top is the waveguide pressurization unit.

To pressurize the waveguide exiting the back of the TWT, an Andrew MR050-81045 high-pressure desiccant dehydrator is used. Waveguide windows at the

transmit horn and the TWT seal the ends while alternating cover/choke flanges provide o-ring seals to prevent leaks. Positive 5 pounds-per-square inch (PSI) pressure is maintained within the waveguide to prevent moisture from entering and a desiccant chamber removes any condensation that forms with temperature changes.

4.2.2.2 Waveform Generation

At the heart of the transmit subsystem is the arbitrary waveform generator. Chapter 3 discussed many of the advantages and disadvantages of utilizing different waveforms to achieve improved sensitivity and/or improve range resolution. It is the waveform generator that facilitates this process. For the AIR, a Pentek 7140 was selected to perform the task of generating the waveforms required to achieve specific performance requirements.

While the 7140 is capable of performing digital up conversion as well as down converting four channels, only a single up conversion channel is used and passes the 50-MHz IF waveform to the analog up converter discussed in the next section. The waveform is kept coherent with the up converter stage as well as the receive subsystem by accepting a 240-MHz clock signal generated by a 3× multiplier from the 80-MHz clock signal within the up converter. The Pentek board is housed inside a computer running a version of Red Hat.

4.2.2.3 Up Converter

The up converter is an analog system that transfers the IF waveform to the RF transmit frequency. A two-stage superheterodyne network was constructed and a block diagram of the components is given in Figure 4.24. An IF signal at 50 MHz enters the up converter and is mixed with an 800-MHz signal generated by a PLO,

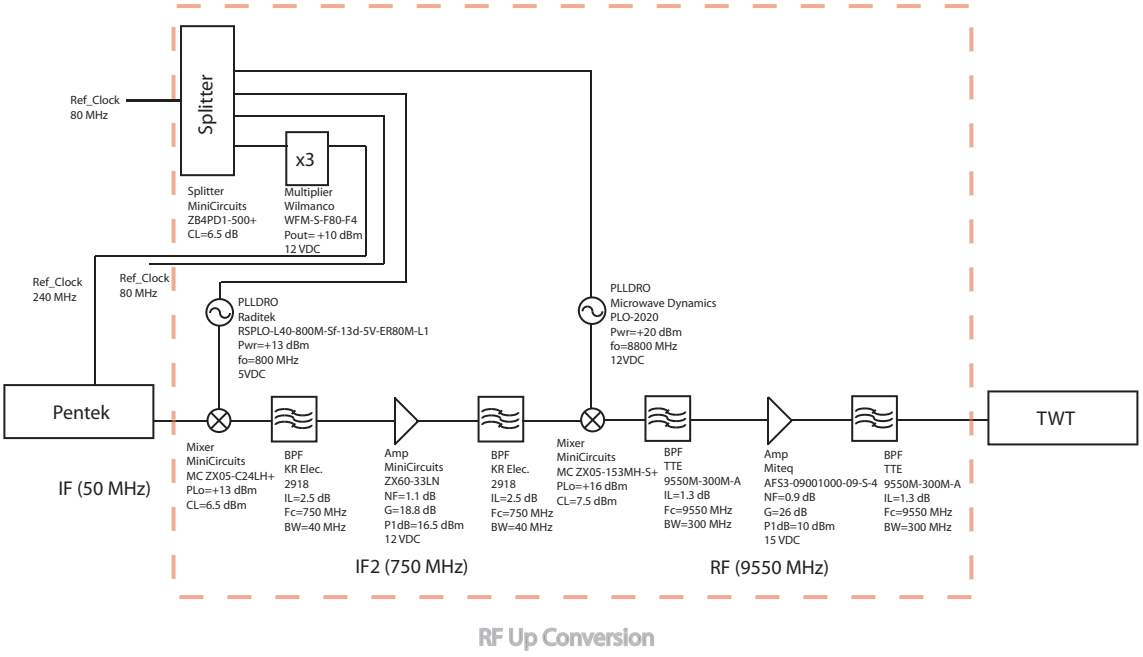

Figure 4.24: A block diagram of the analog up converter network. The 50 MHz IF signal from the Pentek board is mixed to an secondary IF of 750 MHz, filtered and then mixed to the final RF frequency of 9550 MHz. Within the up converter, a 240-MHz clock signal is generated for use by the waveform generator. The RF output signal is passed to the TWT for amplification.

which is coherent with the rest of the radar by the 80-MHz clock signal. Thus a 750-MHz second IF signal is generated. After filtering and amplification, the signal is mixed again, this time with a 8800-MHz local oscillator (also coherent) to produce the desired RF frequency of 9550 MHz. After more filtering and amplification, the RF signal is passed to the TWT where it is amplified before transmission. A photograph of the completed up conversion system is presented in Figure 4.25. Note that the up converter has its own power supplies and only

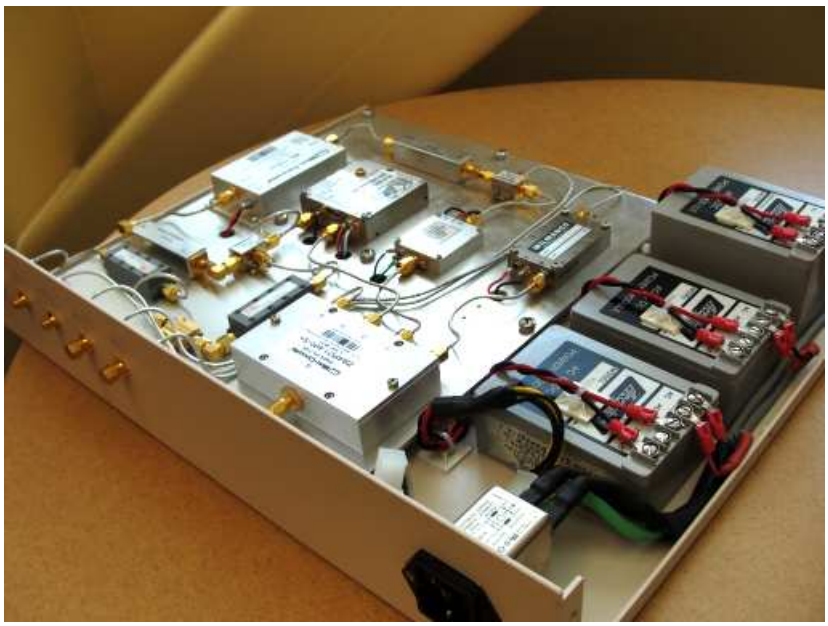

Figure 4.25: A photograph of the completed up conversion unit. DC voltage is distributed by three, on-board power supplies. The inputs, located on the front panel, are a 80-MHz clock input, 50-MHz IF input, 9550-MHz RF output, 240-MHz clock output, and an 80-MHz clock output.

requires an AC power connection. Also, a frequency multiplier within the system produces the 240-MHz clock signal utilized by the Pentek waveform generator.

After completion, tests were performed to confirm the functionality of the unit, with results presented in Table 4.6. Attenuation was required at the up

Table 4.6: RF Up Conversion

Specification	Value	Units
Gain	35	dB
Input P1dB	-24	dBm
Output P1dB	10	dBm
Max P_{IF}	-15	dBm
Noise Figure	10.74	dB
Weight	13.4	pounds

conversion IF input to match the RF output to the required TWT RF input. Matching the outputs is necessary so that nonlinearities that occur during the IF stage amplifier saturation did not propagate through the TWT.

4.2.2.4 Transmitter

After the prescribed waveform has been converted to the RF frequency of 9.55 GHz, a TWT amplifier increases the energy of the signal for transmission through the antenna. In this case, an 3.5-kW Applied Systems 174X TWT was selected. A photograph of the amplifier prior to installation is given in Figure 4.26. The X-band transmitter operates between 8.8 to 10.5 GHz and produces a 65.57-dBm output with -1.5-dBm input. A maximum duty cycle of 2% is specified with a maximum PRF of 410 KHz and maximum pulse width of 16 μs. The WR-90 waveguide output on the back of the TWT has an attached waveguide switch that is capable of directing the RF output either to the transmit antenna or to a matched load. This allows testing to be performed without fear of radiating

Figure 4.26: A photograph of the TWT amplifier prior to installation. The forward and reverse sample ports are located on the front of the device while the waveguide output and RF and trigger inputs are on the back. A control interface is also located on the front panel with a display indicating the amplifier status.

unnecessarily. Further, the switch provides the capability to transmit a low power calibration signal through the transmit antenna, if desired.

Communication is handled over a serial line connected to the waveform generator computer. A nominal warmup time is required for the tube and the countdown is displayed on the front panel. Forward and reverse power sample ports are available on the front plate of the TWT for trouble shooting and testing. The amplifier is listed as weighting 100 pounds.

4.2.2.5 Transmit Antenna

The final component in the transmit chain is the slotted waveguide array antenna. Seavey Engineering produced the antenna and a photograph is given in Figure 4.27. The antenna is mounted at the top of the array supporting structure.

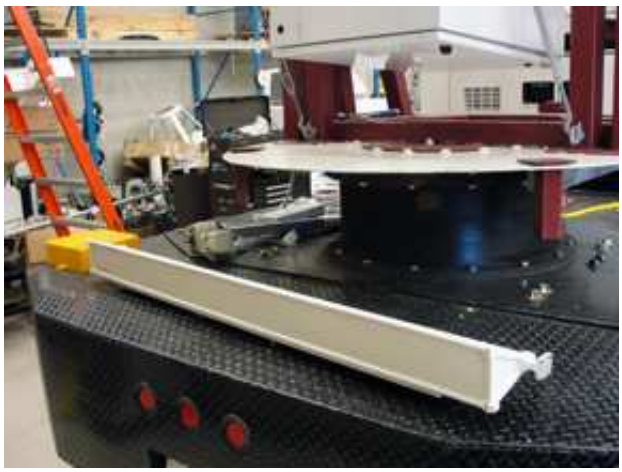

Figure 4.27: A photograph of the transmit horn. The slotted waveguide array has a peak output of 6 kW and is mounted at the top of the array support structure.

The antenna is rated to operate between 9.4 and 9.6 GHz and is comprised of a WR-90 with 64 carved slots. An external trough with a foam radome and lexan window surround the waveguide. The maximum output power is 6 kW. Beam patterns produced by Seavey during the validation of the antenna are provided

in Figure 4.28. As indicated in the patterns, there exists a shift in the peak-of-

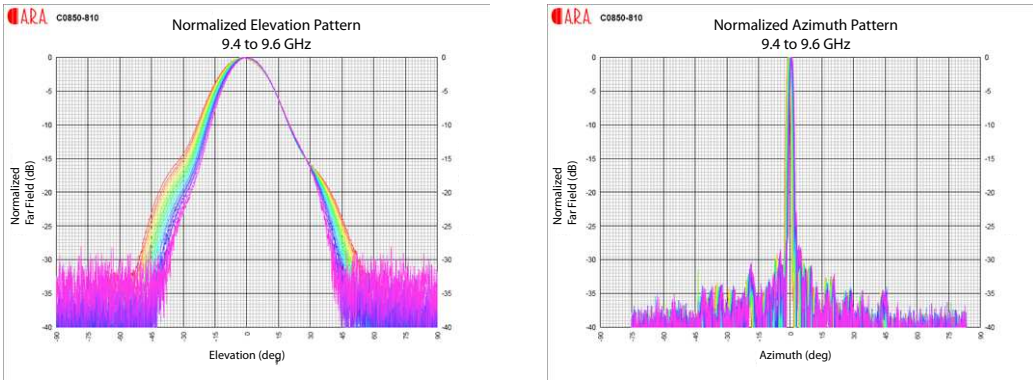

(a) (b)

Figure 4.28: The elevation and azimuthal beam patterns for the slotted waveguide array. Note that several frequencies are given for each pattern and that a change in frequency results in an angular shift in the beam peak and must be accounted for when utilizing the antenna.

beam as the transmit center frequency is changed. The patterns shown display a Δf of 200 MHz, well above any LFM waveform bandwidth and thus, significant degradation of the transmit and return signals due to the beam motion is not a concern.

The antenna used on the AIR was originally designed to work at marine frequencies of 9.41 GHz. Since the AIR operates at 9.55 GHz, a nominal shift in both the elevation and azimuth peak-of-beam occurs. According to the patterns and confirmed by Seavey, the skew in azimuth angle is 3° while the skew in elevation is 0.97°. It is important to know that the angle of the transmit antenna must be adjusted to account for this fact if it is ever removed or maintenance or testing.

Now that a complete description of the transmit subsystem has been presented, a detailed review of the receive chain is given in the next section.

4.2.3 Receive Chain

4.2.3.1 Subarrays

While simple in overall concept with regard to the desired beam pattern, the design and construction of the subarray antennas was a difficult undertaking. A suitable solution was found with Micro-Ant, a company that specializes in patch array antennas. Instead of utilizing a corporate feed network, meaning a multi-layer circuit board would be required to combine all elements, Micro-Ant was able to develop a design that utilized network that combined the signals from each element in series. As such, a much more desirable physical shape could be obtained by way of a structure that was much thinner than a corporate counterpart.

For ease of construction due to milling/etching constraints, the subarray design was separated in half along the azimuthal axis so that two, smaller identical arrays would comprise a single subarray unit. The two arrays are then combined and the output signal is delivered to the down conversion units by a waveguide to SMA adapter on the back side of the subarray. Mounting schemes were specified such that the subarrays would mount to the existing array structure on the pedestal. Further, radomes would be part of the subarray structure itself and no additional considerations would have to be applied to meet the environmental condition requirements.

A photograph of the two subarray prototype antennas is presented in Figure 4.29. The prototypes were an excellent representation of the final product and provided valuable means of testing the performance. The final production models were released to OU with an enhanced structure, making the units more rigid and robust. Further, the ultraviolet (UV) protective paint on the radome

Figure 4.29: A photograph of the two prototype subarray assemblies. The subarrays themselves are comprised of an array of patch antennas combined in series. Identical 2×36 element arrays are combined in the center to form the full subarray. A waveguide to SMA adapter serves as the output port.

was added to facilitate prolong the lifetime of the antennas.The final subarray units were delivered and a photograph of the shipment is given in Figure 4.30.

Figure 4.30: A photograph of the 36 production subarrays. The final design had an upgraded structure for added stability and a painted radome for UV and weather protection. The down conversion units attach to the back of the subarray assemblies.

Following the receipt of the subarray units, testing was performed to ascertain the uniformity with which the components adhered to the frequency requirement. Each subarray was tested in the ARRC anechoic chamber and the S11 parameter was measured with an Agilent Network Analyzer. The results are presented in Figure 4.31. The span of the plot is 1 GHz with each subdivision measuring 100 MHz. Based on these measurements, it was determined that the voltage standing wave ratio (VSWR) specification was met by utilizing the relationships

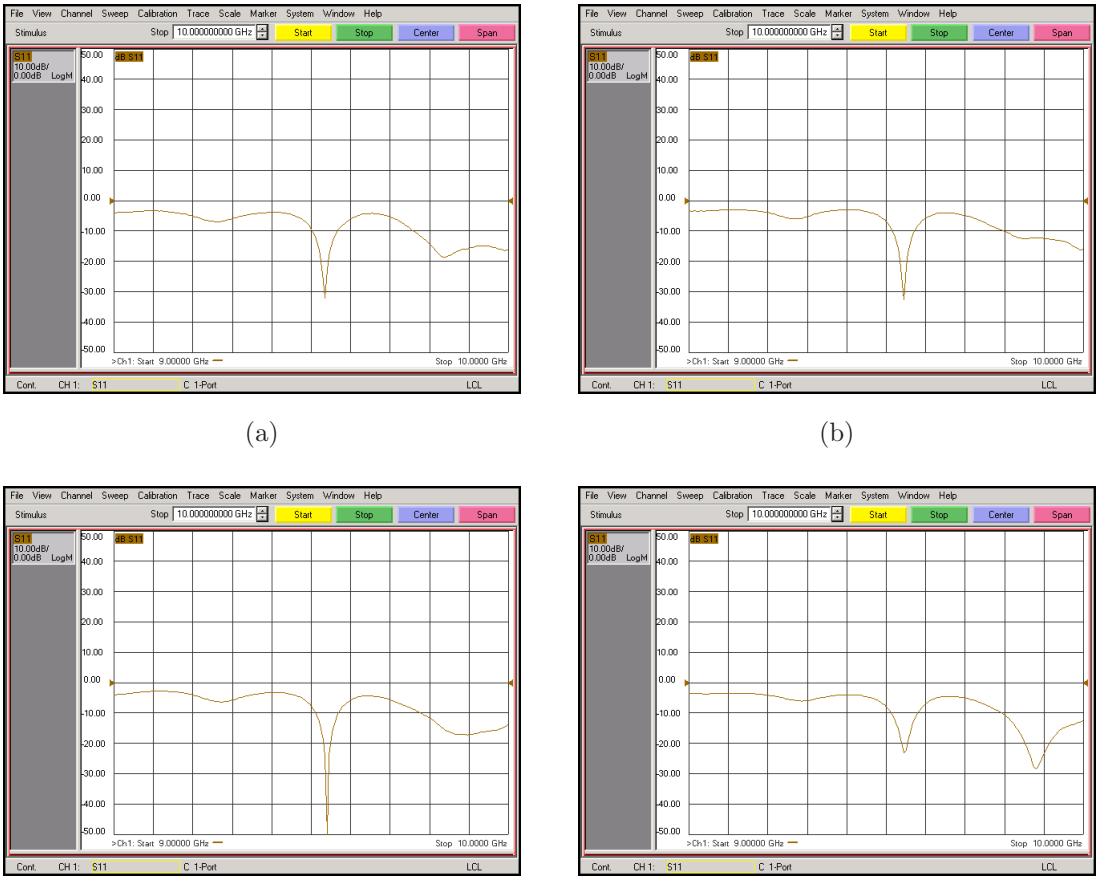

Figure 4.31: Example S11 readings from four of the 36 subarrays. Testing of the subarray units was conducted to ensure proper tuning and uniformity among the receive channels. The vertical axis has 10 dB divisions while the horizontal axis has 100 MHz divisions.

between the S11 parameter and the magnitude of the reflection coefficient (Pozar 2005).

$$VSWR = \frac{1+|\Gamma|}{1-|\Gamma|} \tag{4.2}$$

$$|\Gamma| = 10^{\frac{S11_{\mathrm{dB}}}{20}} \tag{4.3}$$

By examining Figure 4.31 and focusing on the passband of the radar (9545 to 9555 MHz), the notch is well below the necessary -9.54 dB required to meet the VSWR value of two. Additionally, the deviation from subarray to subarray was considered acceptable for the application.

Part of the design specification required threaded bolts to be positioned such that the down conversion units could be attached to the back of each subarray. Images of the final down conversion unit mounted to the back of the final subarray assembly is presented in Figure 4.32. The output of each waveguide adapter would have a diode limiter attached to the SMA port, protecting downstream equipment. The addition of the limiter increases the noise figure of the down converter, but was deemed necessary for protection.

4.2.3.2 Down Converters

The design of the down converter subsystem was a particular challenge due to constraints placed both on the cost and size of each unit. In order for each subarray to fit precisely next to the neighboring subarray, the down conversion box had to be sized to not interfere with the ULA alignment. Also, the design must be large enough to allow assembly and population of the interior components. A design was reached where adjacent down conversion units would alternate about the horizontal axis behind each subarray. This was possible due to the symmetry of the subarray design mentioned earlier.

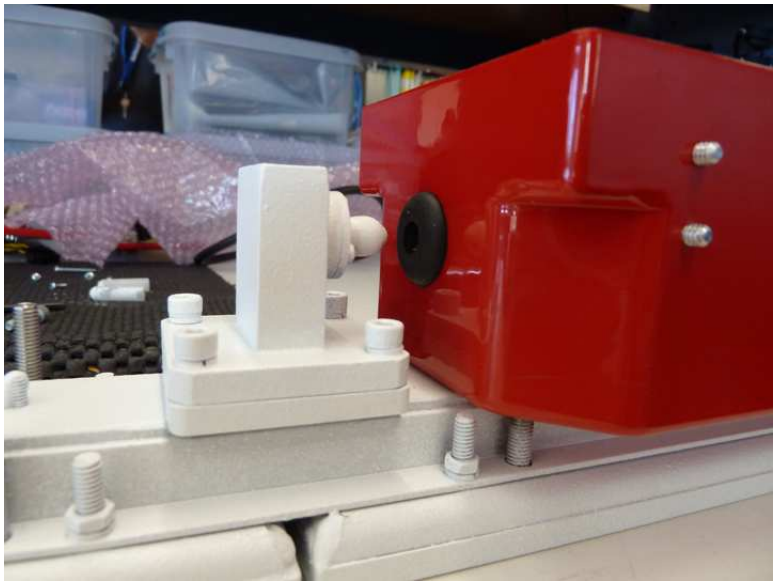

Figure 4.32: An image of a down conversion enclosure mounted on a subarray. The waveguide to SMA adapter port aligns with the input grommet on the enclosure. A diode limiter attaches to the SMA port and enters the box through the grommet.

Several iterations of the down conversion enclosures were fabricated, with each increasingly reducing the weight of the enclosure. Initial designs produced aluminum boxes weighting over 5 pounds, while the final design weighed less than 2 pounds. Environmental sealing was achieved through liberal use of silicone sealant and a rubber gasket between the lid and the main body of the enclosure. A package of desiccant also serve to remove any moisture within the enclosure. Fabrication of the enclosure was completed by Skovira. A photograph of an unpainted prototype enclosure is presented in Figure 4.33. Note that the clock, IF signal, and DC power cables connect through the lid of the enclosure.

The design of the analog system housed within the enclosures was the driving factor for cost. With 36 subarrays, the cost of a single component in the down conversion chain was important. Due to this and the size constraints, a single stage down conversion network was selected. A block diagram depicting the analog down conversion stage is presented in Figure 4.34. One of the difficulties of a single stage down conversion network is producing an RF bandpass filter with sufficiently narrow bandwidth to remove the image frequency (9.65 GHz) during the single mixing stage. Additionally, it is necessary to ensure that neighboring frequency channels to not propagate through the network.

Stepping through the components on the block diagram begins with a limiter that protects all of the components downstream, including the digital receivers. The limiter increases the noise figure of the down converter but is considered necessary for protection. Following the amplification by a LNA, the RF bandpass filter with a 100-MHz bandwidth removes unwanted signals from the subsequent mixing stage. The LO frequency is produced by a PLO located inside the enclosure and is coherent with the rest of the system via the 80-MHz clock signal. The IF filter and amplification stage is contained on a single PCB board and was

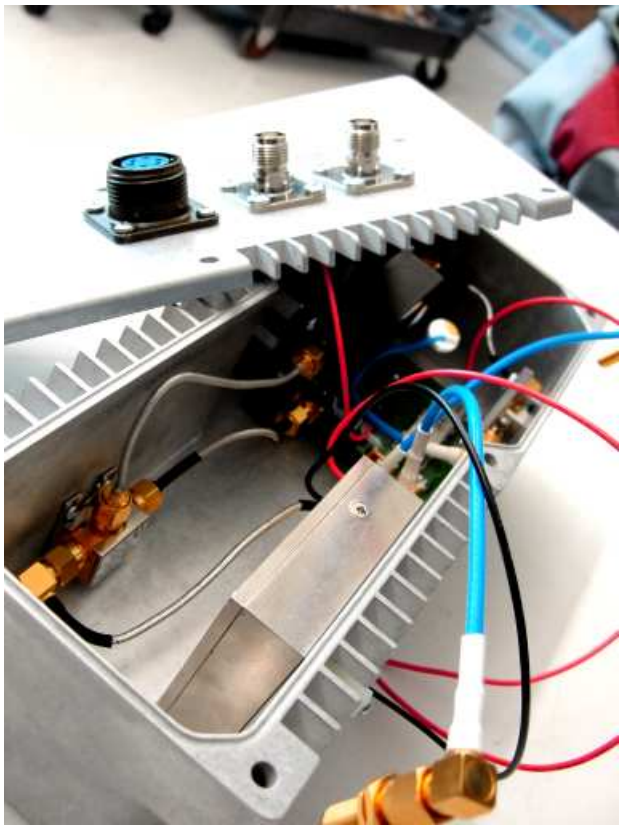

Figure 4.33: A photograph of a prototype down conversion enclosure. Heat fins were cut into the sidewalls to allow for better thermal protection. The DC input, clock input, and IF output ports are located on the lid of the enclosure. Note the groove around the rim that allows a o-ring material to be seated, sealing the enclosure.

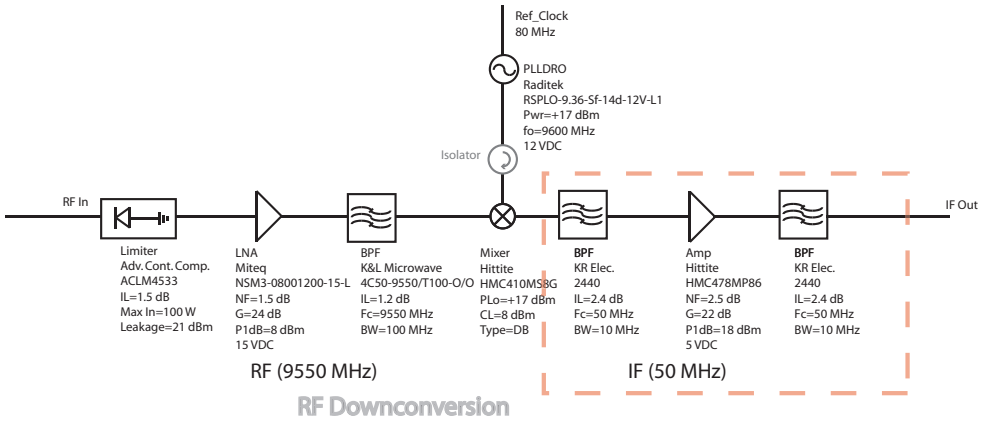

Figure 4.34: A block diagram of the down conversion network. A single stage network was selected to conserve costs and space. The parts within the dashed red box are on a PCB board, also for cost savings. The PLO located inside each down conversion enclosure maintains the coherency of the receive subsystem.

designed to keep overall costs down. Finally the IF signal proceeds to the truck cab and the digital receivers.

Power was delivered to each of the down conversion units via the power distribution box discussed earlier. Once inside the down conversion enclosure, an Advanced Technology eXtended (ATX) cable allows for easy removal of the lid. A wire diagram for the connection as well as the wire colors for the DC cables is given in Figure 4.35.

Following the assembly of each down conversion unit, a set of tests to determine the uniformity of each channel was performed. Some figures of merit regarding the down conversion networks are given in Table 4.7. While there are some outliers in the spectrum of gain values observed across the 36 channels, the difference is not large enough to significantly degrade the performance of the beamforming algorithms. Additionally, calibration schemes will reduce the effect

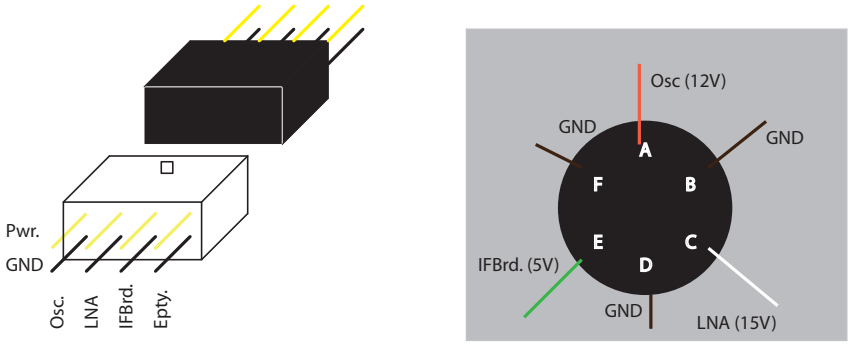

Figure 4.35: A diagram depicting the wire pin-outs for the DC power connectors on the down converter enclosure. Three voltages are utilized within the down converter and an ATX connector allows for easy removal of the enclosure lid.

Table 4.7: RF Down Conversion

Parameter	**Mean Value**	**Std. Dev**	**Units**
Gain	24.23	1.18	dB
Output P1dB	7.79	0.59	dB
Bandwidth	10.72	0.29	MHz
Noise Figure	3.29	-	dB

of inter-channel inconsistencies. While the noise figure is high due to the limiter at the front of the network, it was deemed necessary for the protection of downstream devices.

Finally, the down conversion units were attached to the back of each subarray and the subarrays were installed on the support structure on the pedestal. A photograph depicting the fully completed and installed RF down conversion units is presented in Figure 4.36. Connecting each subarray/down conversion

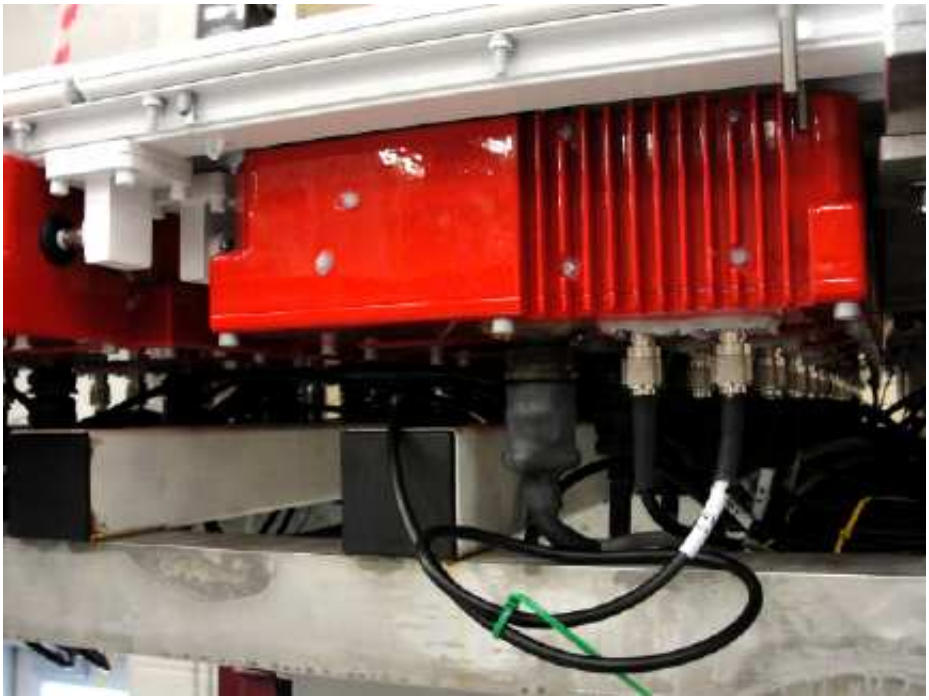

Figure 4.36: A photograph of a fully installed down conversion unit. Note that adjacent subarrays have the enclosures mounted on alternating sides. Labels on each cable ensure the appropriate signals are recorded by the digital receivers.

assembly to the appropriate port on the clock and DC power distribution box was a tedious task and documentation and labeling were essential to ensure data would be recorded properly. A list of each subarray number and the associated down conversion box is presented in Table 4.8. Each clock and IF signal cables

Table 4.8: Subarray/RF Down Conversion Listing

RF Box	**Subarray**	**RF Box**	**Subarray**	**RF Box**	**Subarray**
1	34	13	2	25	32
2	27	14	15	26	7
3	19	15	28	27	24
4	17	16	30	28	4
5	37	17	36	29	23
6	20	18	9	30	11
7	16	19	14	31	29
8	5	20	25	32	10
9	6	21	13	33	21
10	33	22	31	34	22
11	3	23	8	35	12
12	26	24	18	36	35

were cut to the same respective lengths and over 700 feet of coaxial cable was used in the interconnection of the array subsystems. DC power cables were cut to lengths deemed appropriate to not have excessive amounts of cable cluttering the panel. IF signals were bundled and routed to the truck cab where they continued to the digital receivers. A connector block allowing the interconnecting signals to pass through the back wall of the cab while maintaining a weather tight seal was constructed as shown in Figure 4.37. Cable lengths were selected such that the

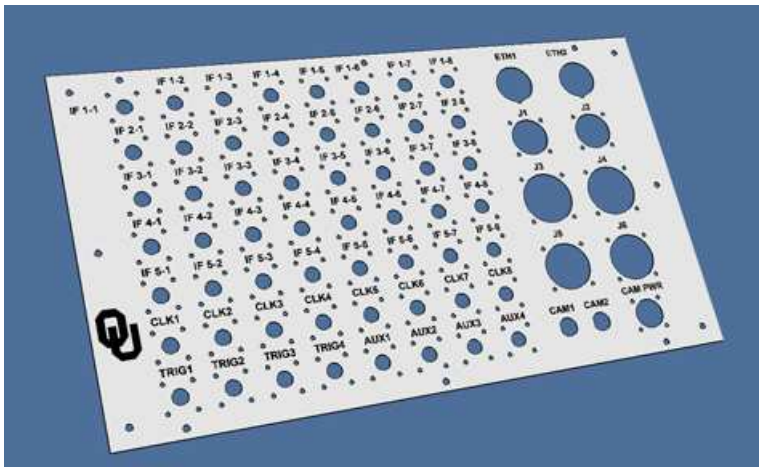

Figure 4.37: An illustration of the plate designed to connect the components within the cab to those without. Many signals pass through the back wall of the cab including AC power, DC power, Ethernet, clock, and IF signals.

pedestal could rotate $\pm 135°$ from a zero position pointing straight off the back of the truck bed. A full illustration of the cable interconnects is given in Figure 4.38.

4.2.3.3 Digital Receivers and Storage

At the heart of the receive chain are the digital receivers. The digital receivers are responsible for converting the IF signal to the baseband I and Q signals, which are then used to derive the radar products discussed in Chapter 2. As mentioned

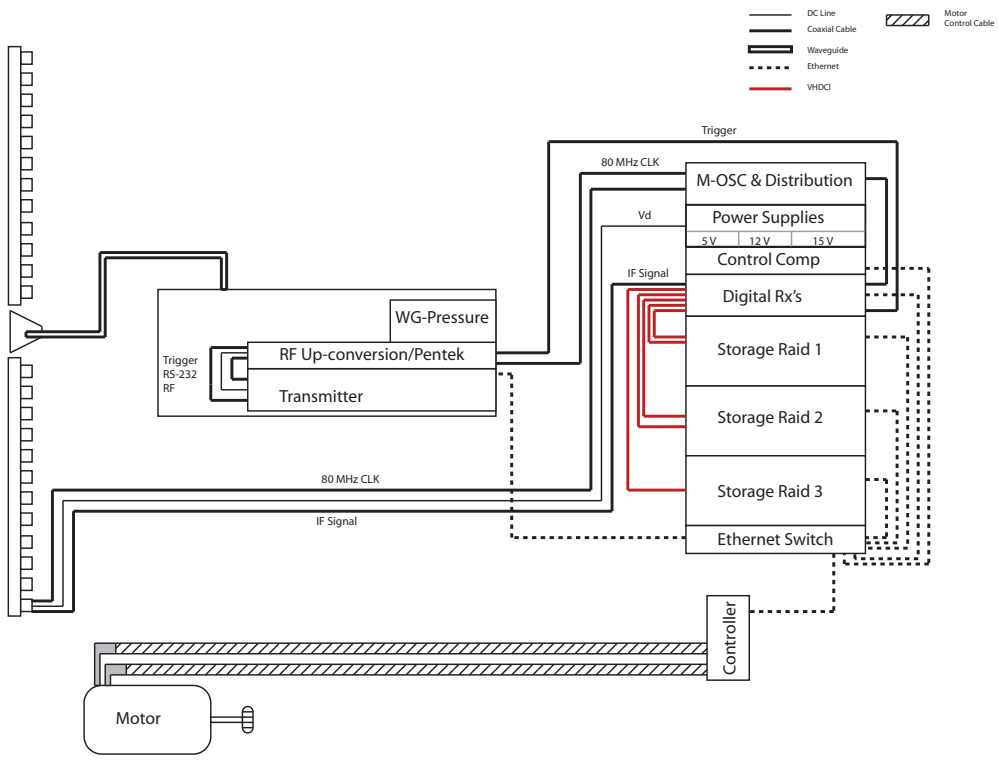

Figure 4.38: An illustration of the general wiring of the AIR. Much of the communication between subsystems is achieved through an Ethernet switch. Specific cables are used to control and power the motor.

previously, digital receiver systems have advantages over analog systems because of the ability to remove I and Q imbalances later through software. Additionally, digital receivers are low cost, robust systems that allow for rapid data collection (Meier et al. 2012). A photograph of a completed digital receiver is given in Figure 4.39.

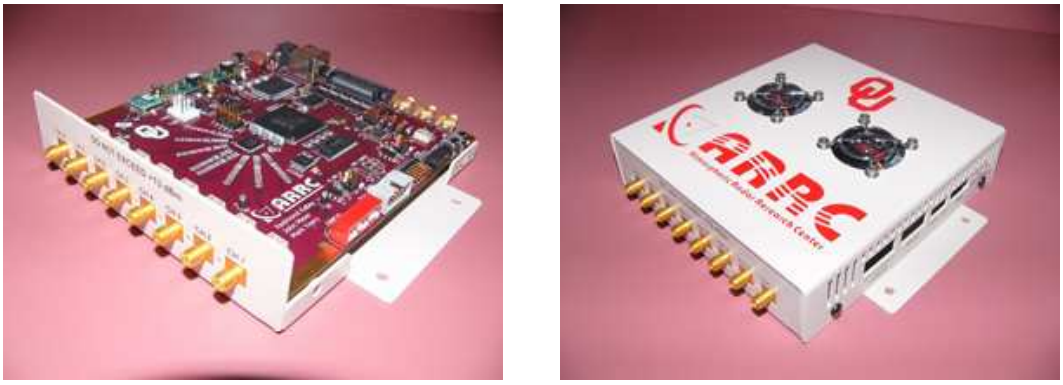

(a) (b)

Figure 4.39: A photograph of the completed 8-channel digital receiver. Five of the units are housed within the truck cab and connect to the storage computers though VHDCI cables and a National Instruments I/O card. An Analog Devices ADC and a Spartan 3A FPGA facilitate the rapid digitization, baseband sampling and data streaming required for the AIR to operate.

The 8-channel digital receivers used on the AIR receive chain were designed and developed at OU (Meier et al. 2012). Multi-channel receivers reduce the per-channel-cost by combining multiple components on a single printed circuit board (PCB). With modern analog-to-digital (ADC) and FPGA chips, efficient processing of the data is possible. High resolution 14−bit digital data are collected through the use of an Analog Devices AD9252 ADC, while the data mixing and processing is completed with a Spartan 3A DSP XC3SD3400A FPGA.

The digital receivers utilize bandpass sampling, which was briefly described in Chapter 2. The principle behind bandpass sampling is that for a given IF frequency, there exist many sampling frequencies that will shift the IF signal to a frequency of $f_s/4$, where f_s is the sampling frequency. In general, $f_s = f_{\mathrm{IF}}/(0.25 + n)$. For this case, $n = 1$ and $f_s = 40$ MHz (Meier et al. 2012). Baseband I and Q signals are produced by multiplying the digitized signal by a 10 MHz digital cosine and sine.

$$cosine = \begin{bmatrix} 1 & 0 & -1 & 0 \end{bmatrix} \tag{4.4}$$

$$sine = \begin{bmatrix} 0 & 1 & 0 & -1 \end{bmatrix} \tag{4.5}$$

Subsequently passing through a cascaded integrator-comb (CIC) filter, the baseband signals are decimated by a factor of eight and the image at 20 MHz is removed. A compensation finite impulse response (CFIR) filter corrects the CIC roll-off and maximizes the SNR by matching the receiver response to the transmit pulse (Meier et al. 2012).

Following the data processing, the data are buffered and passed to the storage system with the predefined header data. In general, the interface between the digital receivers and the radar system includes eight IF inputs, one clock input, a 5-VDC power input, and a very-high-density cable interconnect (VHDCI) cable which carries the digital data to a National Instruments NI PCIe-6537 50-MHz digital I/O card. Two cards are installed in one computer storage unit (with the exception of the third computer), which is a server chassis with a dedicated redundant array of independent disks (RAID) controller allowing eight, 1-TB drives to record the 32-bit, 160-MBs^{-1} data stream produced by each digital receiver. No parity drives are used due to the overhead required.

The data are typically recorded for 2048 range gates for each pulse and data are staggered for each channel in a manner described in Table 4.9. Note that the

Table 4.9: 32-Bit Data Stream

Word	**Sample**	**MS 16 Bits**	**LS 16 Bits**
0	1	Rx A, CH 0, I	Rx B, CH 0, I
1	1	Rx A, CH 0, Q	Rx B, CH 0, Q
2	1	Rx A, CH 1, I	Rx B, CH 1, I
3	1	Rx A, CH 1, Q	Rx B, CH 1, Q
4	1	Rx A, CH 2, I	Rx B, CH 2, I
5	1	Rx A, CH 2, Q	Rx B, CH 2, Q
6	1	Rx A, CH 3, I	Rx B, CH 3, I
7	1	Rx A, CH 3, Q	Rx B, CH 3, Q
8	1	Rx A, CH 4, I	Rx B, CH 4, I
9	1	Rx A, CH 4, Q	Rx B, CH 4, Q
10	1	Rx A, CH 5, I	Rx B, CH 5, I
11	1	Rx A, CH 5, Q	Rx B, CH 5, Q
12	1	Rx A, CH 6, I	Rx B, CH 6, I
13	1	Rx A, CH 6, Q	Rx B, CH 6, Q
14	1	Rx A, CH 7, I	Rx B, CH 7, I
15	1	Rx A, CH 7, Q	Rx B, CH 7, Q
16	2	Rx A, CH 0, I	Rx B, CH 0, I
⋮			

samples are interleaved between master receiver A and slave receiver B as well as channel values and I and Q samples. A 40-kB header begins each file while a 4-kB header precedes each block of pulse data. While many of the values are self explanatory, the UTC time data are in units of seconds-since-January 1, 1900, instead of the typical Unix time, which is referenced to January 1, 1970.

Output file sizes can be selected within a Labview graphical user interface (GUI), which is used not only to control the data recording process performed by the digital receivers and storage computer, but to also monitor the performance of the digital storage subsystem. Data will continue to be recorded until either the user stops the process or a RAID fails to write.

4.3 Calibration

One of the advantages of a digital radar system is the ability to easily calibrate and remove imbalances between I and Q channels. For the AIR, this is especially important because the ability to calibrate the 36 channels determines how well, if at all, the radar will function. Calibration is typically performed at a single range gate and the values are applied for the entire pulse. The time between calibration procedures is a variable that changes from system to system. In some cases, a radar may only need calibrated once before each use. In other cases a calibration may be required between volume scans.

Some calibration schemes require a known source in the far field, either a corner reflector or an active signal source. Others are able to perform the task between scans, requiring little time away from data collection. It is more advantageous to perform calibration *during* data collection if at all possible. Often times a clutter target is all that is required to obtain accurate results. The AIR intends to utilize the final option: *in situ* calibration.

One of the simplest methods for calibration is to set the phase and amplitude of each channel equal to a reference channel. For instance, if channel 0 (CH0) for the AIR is selected as the reference point, each subsequent channel (CH1 to CH35) would be scaled by the amplitude of CH0 and then the phase difference between each channel and the reference would be removed. The problem with this technique is the assumption that all of the signal is originating exactly at broadside, which, in most cases, is not true.

A similar, but more accurate technique involves calculating the correlation between adjacent antenna elements (Attia and Steinberg 1989). The theory of self-coherence is based on the fact that, in cases of incoherent scatterers, a correlation of a spatial sample will reduce to the Fourier transform of the intensity of the illuminating beam, which happens to be the transmit beam. The assumptions are that the incoherent scatterers are statistically uniform and smaller then the resolution volume (Attia and Steinberg 1989). The procedure involves calculating the complex cross-correlation between adjacent elements of the array. Starting with CH0, the phase differences are summed and subtracted from the phase of each channel moving down the array.

While the algorithms specifies incoherent scatterers as necessary for functionality, some strong targets believed to be ground clutter have successfully been used to calibrate the AIR. Further, weather targets should provide an ideal source of incoherent scatterers but mixed results have been obtained. One side affect of the self-cohering algorithm is the angle of strongest return is assumed to be the center of the transmit beam or boresight. While this would seem to be problematic, a simple correction can be applied. Ground clutter occupying the nearest range gates is a useful angular landmark, indicating 0° elevation, or at close to it if terrain is highly variable in the visible scan range. Once an offset is produced,

the beamforming algorithm can produce appropriate range-height indicator (RHI) images.

Now that a complete system description of the AIR has been discussed, a presentation of several data sets collected by AIR will be given in the next chapter.

Chapter 5

Data Collection and Processing

A series of experiments were conducted to explore the capabilities of the AIR. First, the receive subsystem was examined for functionality. Then, actual weather data were collected during several events, including an isolated cell, squall line and supercell. Finally, pulse compression was tested with a fixed target (communication tower) in the far-field with the goal of assessing pulse compression capabilities. A description of the experiments, the environmental conditions and the results are presented in this chapter.

5.1 Point Measurements

5.1.1 Passive Observations with an RF Beacon

Initial tests of the AIR were conducted in the parking lot of 1 Partner's Place building in Norman, Oklahoma. The goal of the experiments was to obtain data by passively recording the receive signals from the 36 array elements. A pair of X-band horns were used to transmit the output of two signal generators, which would serve as sources for the receiver array. A map of the experiment location is given in Figure 5.1. One horn was placed on the balcony of 1 Partner's Place while the second was placed on the roof. The angular separation of the horns at a distance of 0.12 km was approximately 3°. An image showing the view of the test

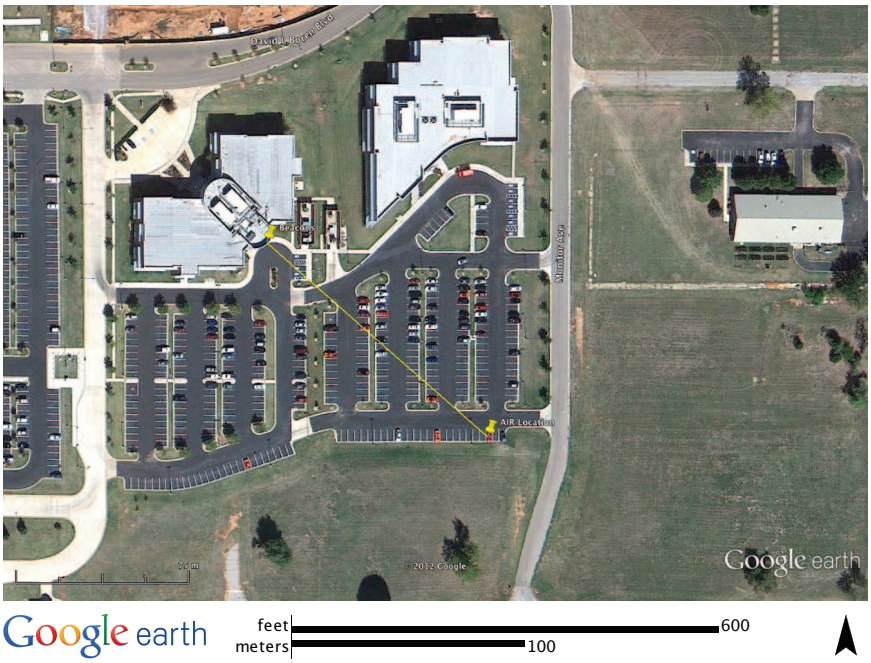

Figure 5.1: An image showing the locations of the AIR and the signal sources for the beacon test. Note that the potential for multipath is high given the arrangement.

beacons from the perspective of the AIR is given in Figure 5.2. After data were

Figure 5.2: A view of the 1 Partner's Place balcony and roof from the AIR. A signal source was placed on the balcony while the other was placed on the roof. The angular separation at this distance was approximately 3°.

recorded with a single source transmitting, Fourier, Capon and RCB techniques were used to analyze the system performance.

Results from the single source test are presented in Figure 5.3. All three techniques resolve the single target and are uniform in the power estimate. The flatness of the RCB results is related to the choice of ϵ, which for this case was set to 9. The calibration technique due to Attia and Steinberg (1989), described in the previous chapter, was used here.

Following the single source tests, the second source on the roof was activated and the results are presented in Figure 5.4. The amplitude estimates for the dual source tests are less satisfactory for the Capon technique, as was expected. Since there are only two point targets and multi-path effects are likely significant, in this case, it is difficult for the Capon algorithm to distinguish a true target from an interfering target. As such, significant attenuation is applied to the true

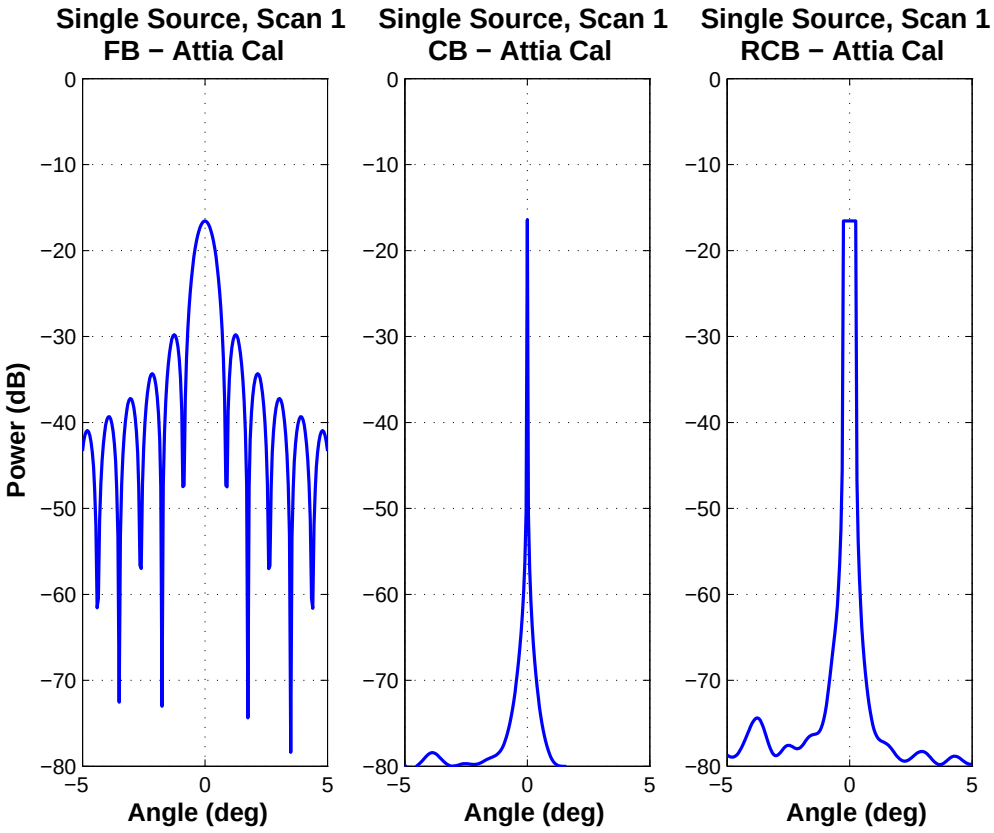

Figure 5.3: Results of the single source beacon experiment. The 36 receive channels of the AIR were used to passively record the signal transmitted by a signal generator and an X-band horn. Fourier, Capon and RCB algorithms were tested during this experiment. All three power estimates agree quite well. Calibration due to Attia and Steinberg (1989) was utilized.

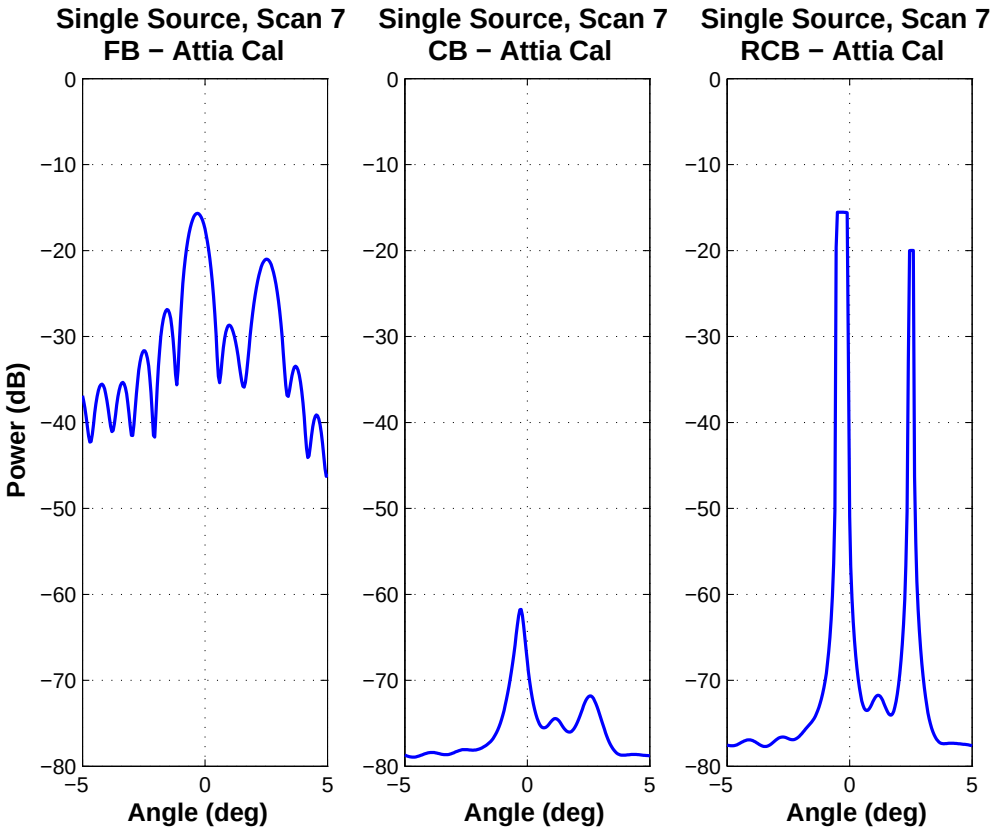

Figure 5.4: Similar to Figure 5.3, except for the dual source test. Both signal sources were active while data were passively recorded. The angular separation of the two sources was approximately 3°. Note that the Capon algorithm produces inaccurate power estimates, likely due to multipath effects and the inability to distinguish between interference and the true signal.

targets, resulting in an underestimated amplitude. The results of this experiment were what initially prompted the study of robust techniques, such as RCB.

Note that the RCB algorithm is able to resolve both targets while providing accurate amplitude estimates. Additionally, the effect of the beamforming sidelobes are mitigated via the adaptive algorithm. Again, $\epsilon = 9$ was chosen for this case. The effect of various epsilon values is shown in Figure 5.5. Increasing ϵ

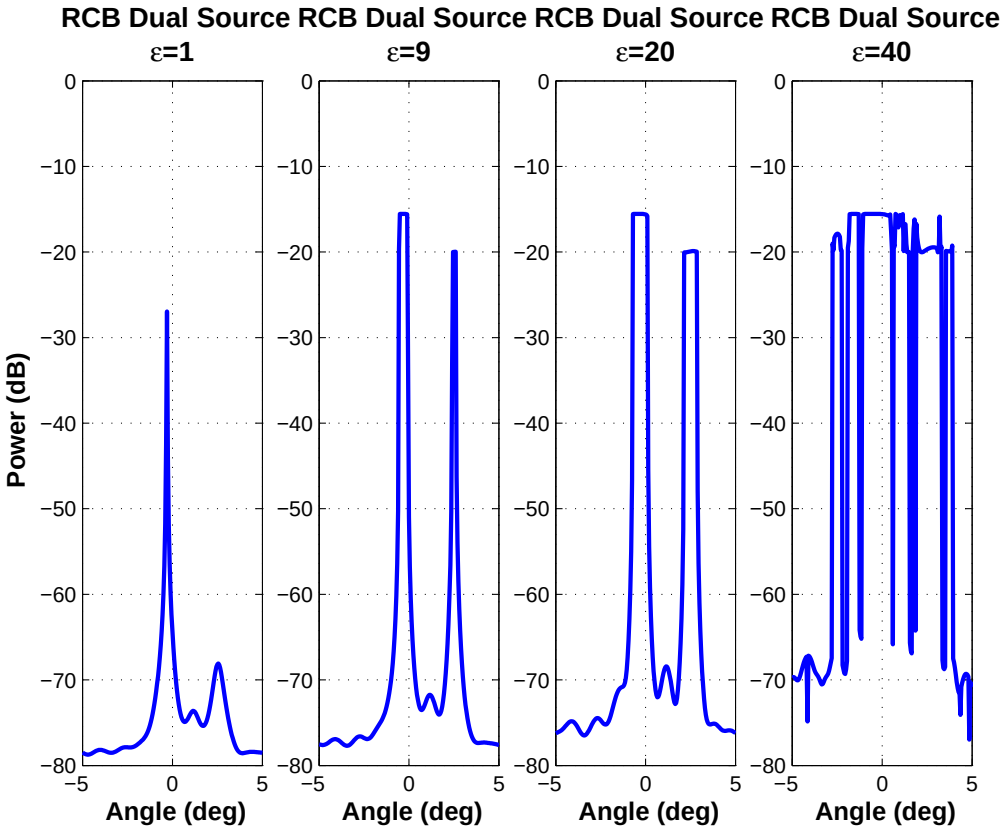

Figure 5.5: The effect of various ϵ values. Increasing the value eventually leads to a degradation of the angular accuracy of the algorithm.

widens the search area for the RCB algorithm and gives a greater chance that the iterative technique will locate the true target. Widening the search space also reduces the resolution of the digital beamforming. Increasing the ϵ value beyond that which is required for accurate results has adverse effects on the beamforming

algorithm and can render the technique unusable. Widening the search area is also responsible for the flat peak visible in the point target experiments for the RCB algorithm. It is believed that the wider search area is essentially like adding ambiguity to the resolution of the RCB algorithm.

It is also important to mention that the RCB and Capon techniques work well in the case of point targets. However, when weather phenomena are observed, distributed power fields make suppression of sidelobes difficult. As a result, the sharp drop in angular power observed in the point source measurements is not observed. Instead, gradients in the power field are smoothed due to the reduced, but still present leakage from sidelobes.

Following the beacon experiments, a series of weather experiments were conducted. Pulse compression had not been tested prior to the weather collections and was thus not used. The following section, however, will discuss the pulse compression experiments performed on a nearby radio tower, but not in chronological order, to finalize the point source measurement portion of this chapter.

5.1.2 Point Target Measurements of a Communication Tower

Leveraging the versatility of the AIR's waveform generator and TWT amplifier, the system is capable of transmitting diverse waveforms to partially regain the loss of sensitivity due to the wide transmit beam. To achieve sensitivity similar to existing mobile radar systems, it was determined that an appropriate pulse width of 8 μs would suffice. Tests were performed along Highway 9 southwest of Norman, Oklahoma near the Newcastle water tower (35.127917N, 97.651306W). A radio tower near Blanchard, Oklahoma was selected as the target. Both long

and short pulses were utilized to facilitate an evaluation of the pulse compression technique.

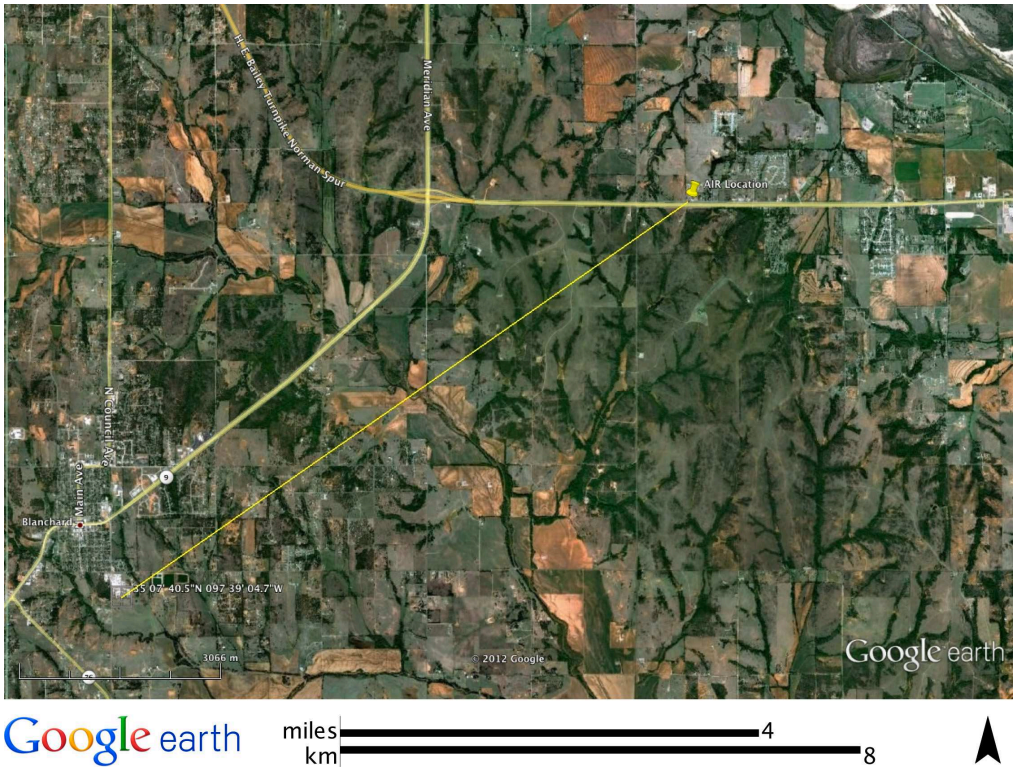

Figure 5.6: An image of the experimental setup for the pulse compression validation experiment. The radar was located in the northern region of the map, near Highway 9, while the radio tower was located just south of Blanchard, Oklahoma. A distance of approximately 11 km separates the AIR and the tower. Due to the terrain, the AIR was deployed below the base of the tower.

During normal operation, the TWT utilized by the AIR is driven into saturation and will thus impart significant distortion on the transmitted waveform. It is often desired to operate the amplifier in the linear region, rather than saturation. Linear operation reduces the amount of distortion on the signal and allows for tapering on transmit. However, in many cases the amplifier is designed to run in saturation to meet output power specifications, as is the case for the

AIR. The waveform must be sampled and recorded for use as the matched filter on the receive data. However, the AIR does not have a burst sampling channel. Instead, the trigger signals were arranged such the digital receivers recorded the leakage from the transmit horn to the 36 receive elements during the transmit burst. The sample time spacing of the digital receivers is 0.2 μs and permits only a few samples to be collected for even a relatively long pulse width. Ideally, a separate channel would be designated as the burst sample and a higher sampling rate would allow for more accurate phase information to be gathered.

Due to the proximity of the receive channels to the transmit horn, saturation of some of the down conversion blocks occurs. Experimental data show that the first four receive arrays nearest the transmit horn are saturated during transmit and are therefore unusable for the burst sampling. Mutual coupling between the remaining channels was ignored during this experiment. The normalized burst signal from the remaining 32 channels was averaged over a dwell and the valid channels. The resulting waveform was saved and used to match-filter the signals for all 36 channels. The results are then calibrated in the normal fashion and beamforming is performed. Results from the pulse compression experiment are presented through the remainder of this section.

Initially, a 1-μs pulse was used to provide a baseline measurement for comparison with the compressed results. RHI spotlight scans for Fourier and RCB algorithms are presented in Figure 5.7. As expected, the radio tower, located approximately 11 km from the radar location appears as a strong, narrow point target. The Fourier algorithm used does not apply a window function so sidelobes along the angular axis are high. The RCB algorithm significantly reduces the sidelobes by approximately 40 dB. Note that the terrain causes the radio tower to appear above the radar horizon. Nearby clutter targets are assumed to be at 0° elevation and were used to align the calibrated beamforming data. A

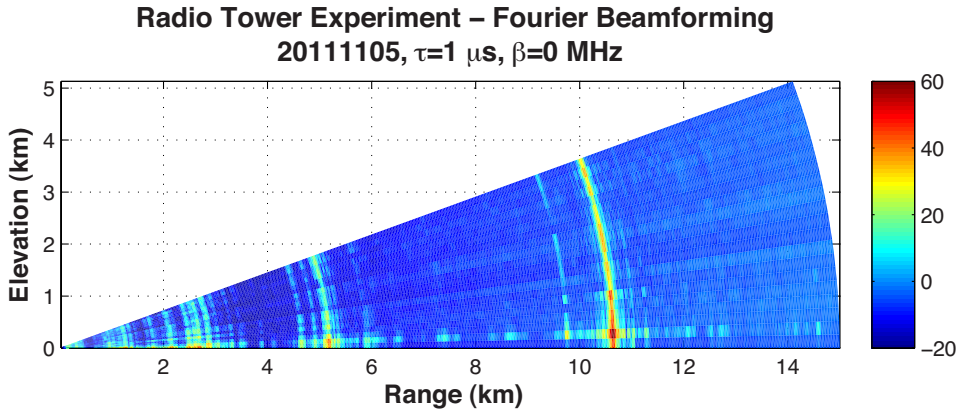

(a)

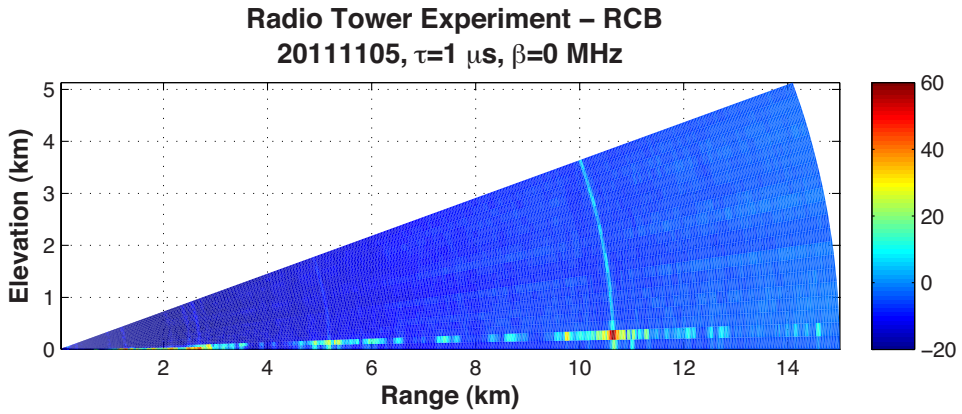

(b)

Figure 5.7: An RHI image of the radio tower experiment using a 1-μs rectangular pulse. Fourier (a) and RCB (b) are used to generate the images. The radio tower appears as the strong target at approximately 11 km. Significant sidelobes due to the beamforming present in the (a) are suppressed by 40 dB in (b). The tower appears in the 1° elevation due to the terrain.

closer view of the radio tower is presented in Figure 5.8 for a 1° elevation angle. As expected, a well-defined peak is present at the approximate location of the

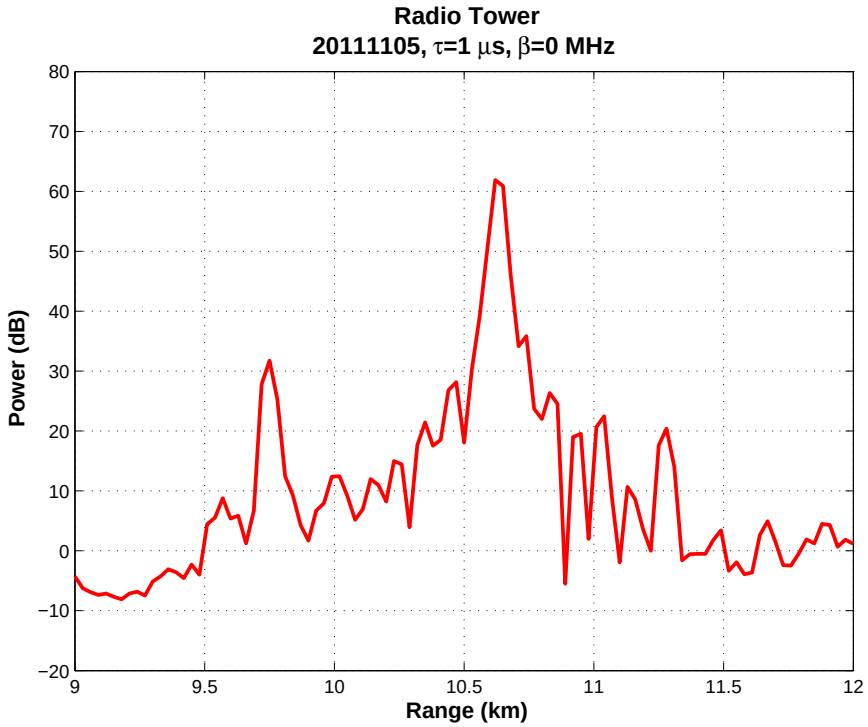

Figure 5.8: A closer view of the radio tower for the RCB case. Note that the location of the tower, indicated by the 60 dB peak at 10.6 km range, is approximate as the trigger signals were not synchronized to provide precise range measurements.

radio tower. The signal timing for the experiment was used only to ensure that the transmitted pulse would be sampled by the digital receivers; no effort was observed ensuring accurate range measurements. Hence, range values will differ as the pulse lengths are changed.

Subsequently, an 8-μs, 5-MHz bandwidth LFM pulse was used and the results are presented in Figure 5.9. As expected, increasing the pulse width produced a decrease in range resolution, meaning the distance between discernible targets is increased. Again, sidelobes are visible in both Fourier and RCB, however, the

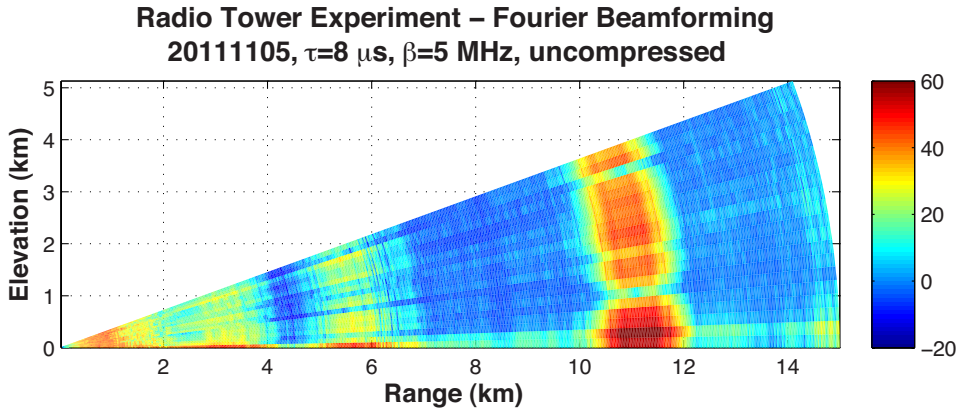

(a)

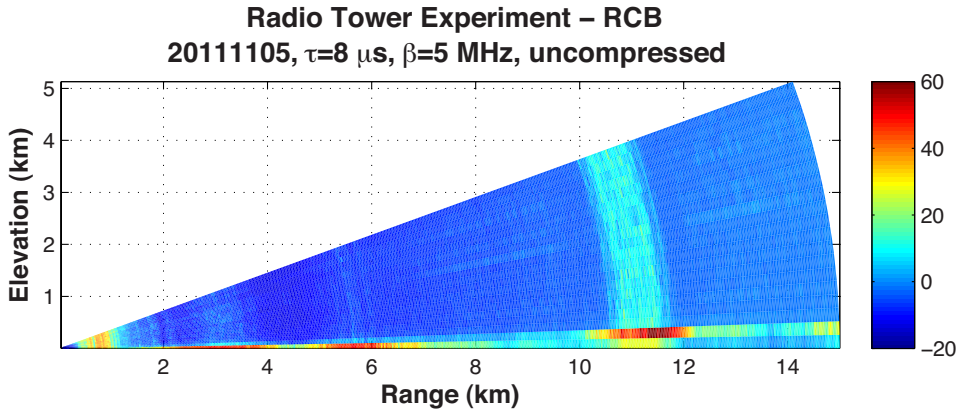

(b)

Figure 5.9: As in Figure 5.7, except for an 8-μs, 5-MHz LFM pulse. The results shown are not compressed and are simply the return power from the long pulse. Note the increased range extent of the radio tower.

RCB algorithm reduces the impact significantly. A closer view of the radio tower for the 1° elevation angle is given in Figure 5.10. Note the large area in range now

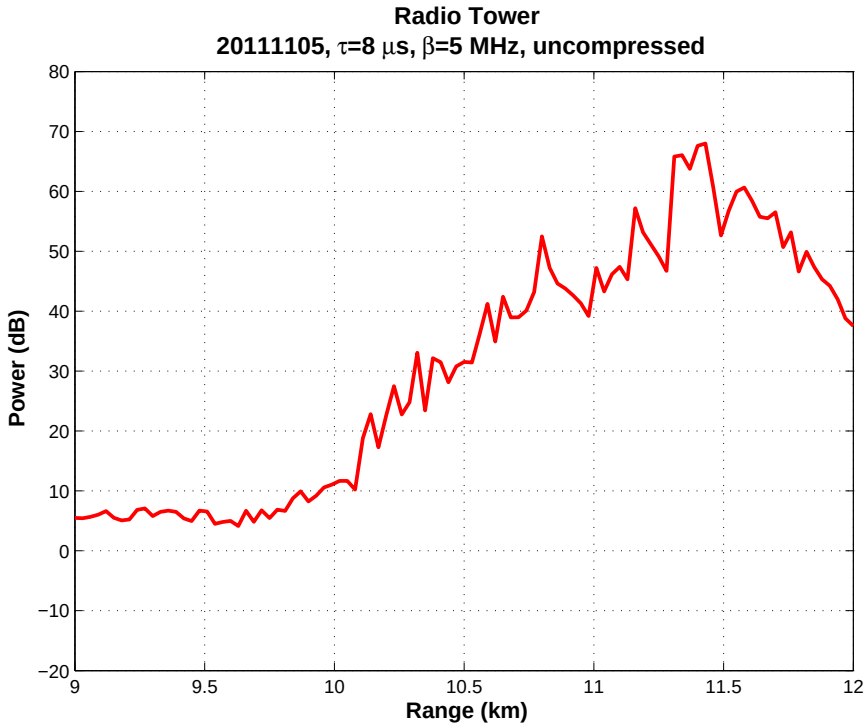

Figure 5.10: As in Figure 5.8, except for an 8-μs, 5-MHz LFM pulse. An increase in the peak power associated with the radio tower is noted as is the significant decrease of range resolution due to the longer pulse width.

occupied by the radio tower. The application of the matched filter is expected to enhance the resolution of the AIR.

As a reference, and to illustrate the effectiveness of the technique, the generated and sampled waveforms are given in Figure 5.11. The generated waveform in Figure 5.11(a) is produced by the waveform generator and is distortion free upon entering the analog up converter. After sampling by the 32 channels, averaging and normalizing, the sampled waveform Figure 5.11(b) was recorded. The waveforms show good agreement, though the sampled waveform appears to have

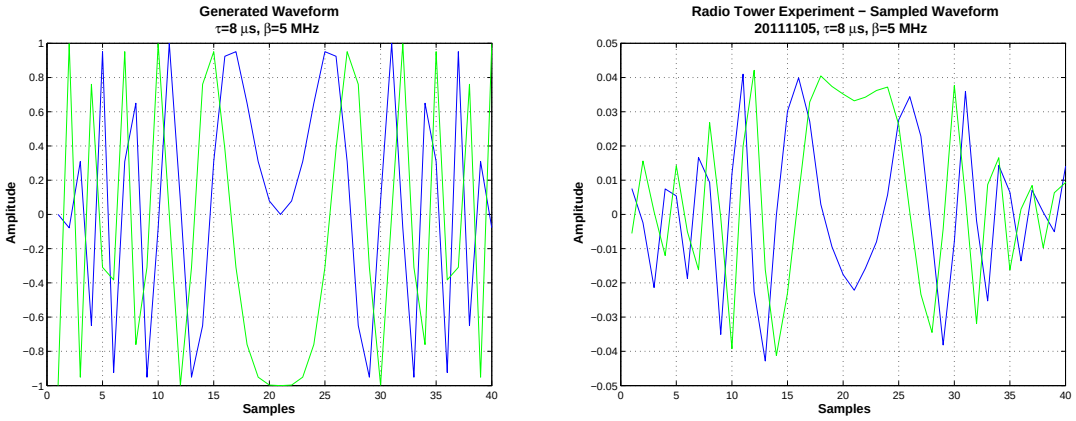

(a) (b)

Figure 5.11: The generated (a) and sampled (b) LFM waveform. The range sampling rate is 0.2 μs giving approximately 40 samples for the 8-μs pulse. Averaging has been performed on the valid channel data to produce the sampled waveform. It appears that some attenuation has been applied to the beginning and end of the sampled waveform, likely due to the up converter and TWT distortion and is not due to any windowing or mismatch filtering.

been attenuated at the beginning and end of the transmission. It is believed that the distortion introduced by the TWT and up converter is responsible for the window function effect.

Initially, a non-windowed matched filter is applied to the received signals and the results are presented in Figure 5.12. Note the improvement in the range extent

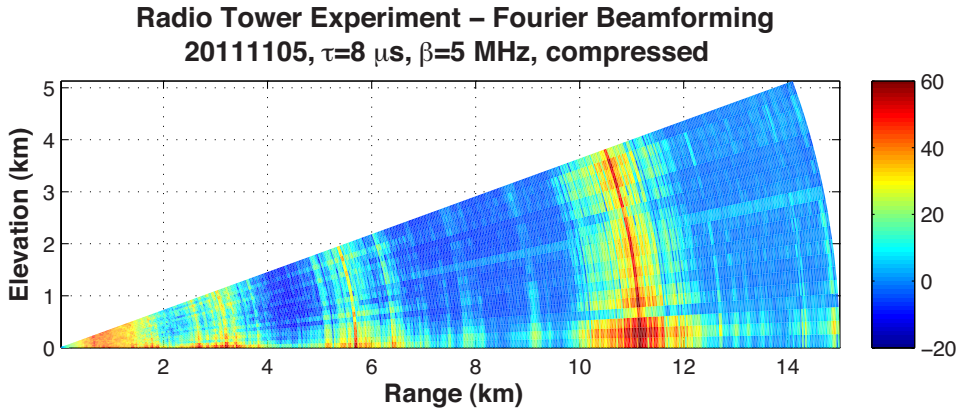

(a)

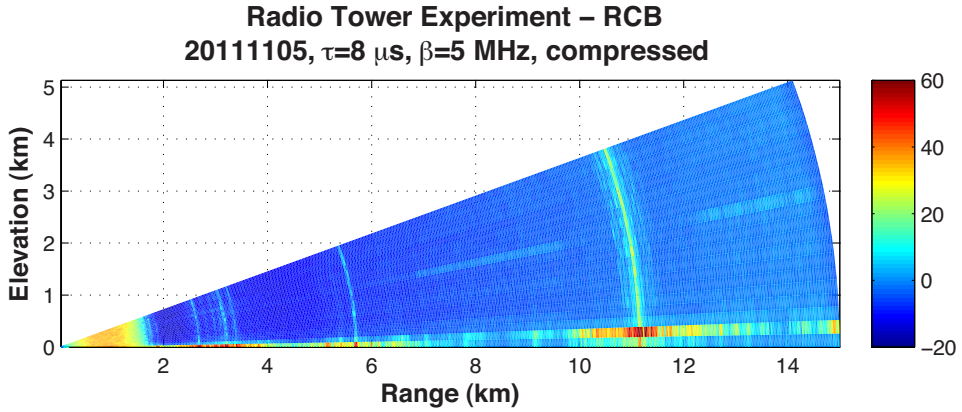

(b)

Figure 5.12: As in Figure 5.9, except a matched filter is applied. Significant reduction in the spatial extent of the radio tower is apparent. Range sidelobes appear to be substantial and threaten to obscure nearby targets.

of the radio tower as compared to Figure 5.9. A closer inspection provided by Figure 5.13 indicates that significant range sidelobes are present. It is important

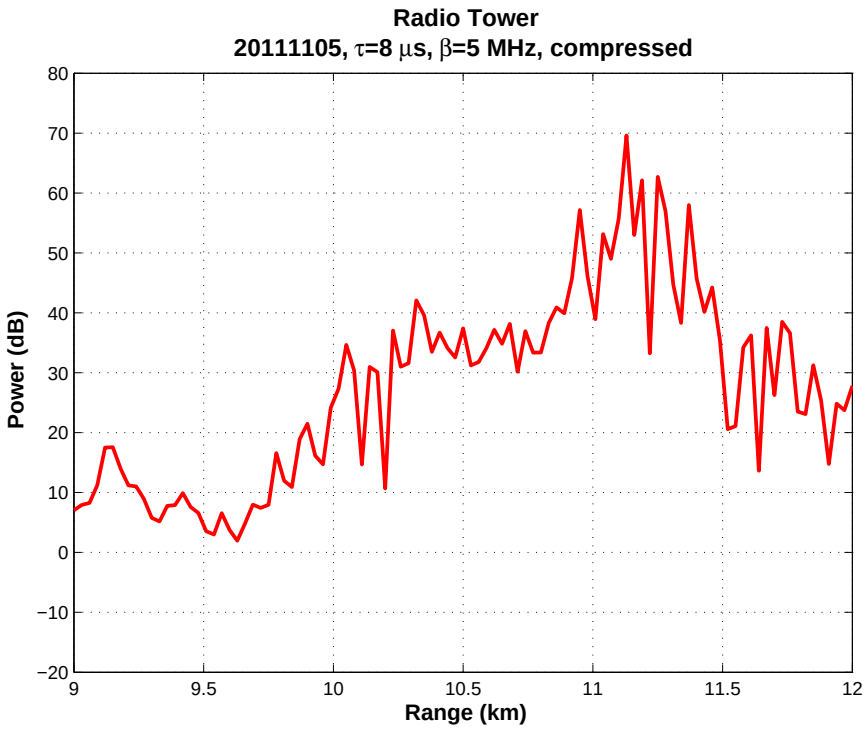

Figure 5.13: As in Figure 5.10, except a matched filter is applied. Approximately 8 dB of sensitivity has been recovered via the pulse compression algorithm from a theoretically expected 9 dB. The discrepancy is likely due to a mismatch between the sampled waveform and the true transmit pulse.

to note the increase in the peak power associated with the radio tower. The 8-μs pulse, after compression, has increased the peak from 62 to 70 dB. It is expected that the pulse width would enhance sensitivity by approximately 9 dB, a discrepancy that is likely accounted for in the window-like affect on the sampled matched filter. To reduce the impact of the significant range leakage present in the compressed signal, a window function is applied to the sampled waveform.

The results of a windowed matched waveform are presented in Figure 5.14. A significant improvement is noted as compared to the unwindowed compression

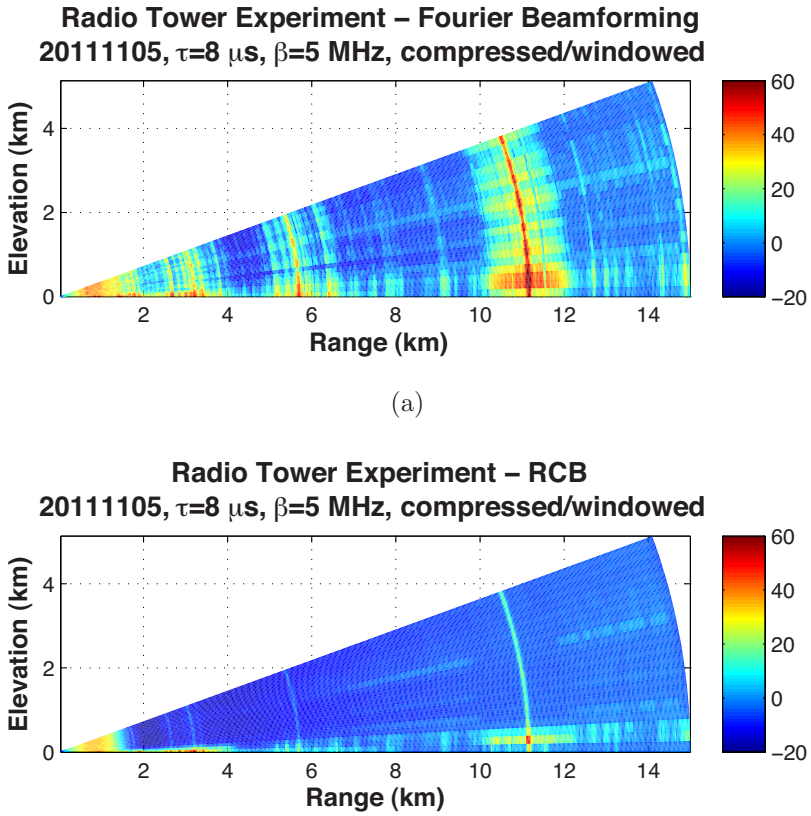

(a)

(b)

Figure 5.14: As in Figure 5.12, except a windowed matched filter is applied. An improvement in the range sidelobes is noted, however, significant leakage remains.

results, especially in the RCB case. A closer inspection of the results are presented in Figure 5.15. Note that a significant loss of sensitivity is incurred as the

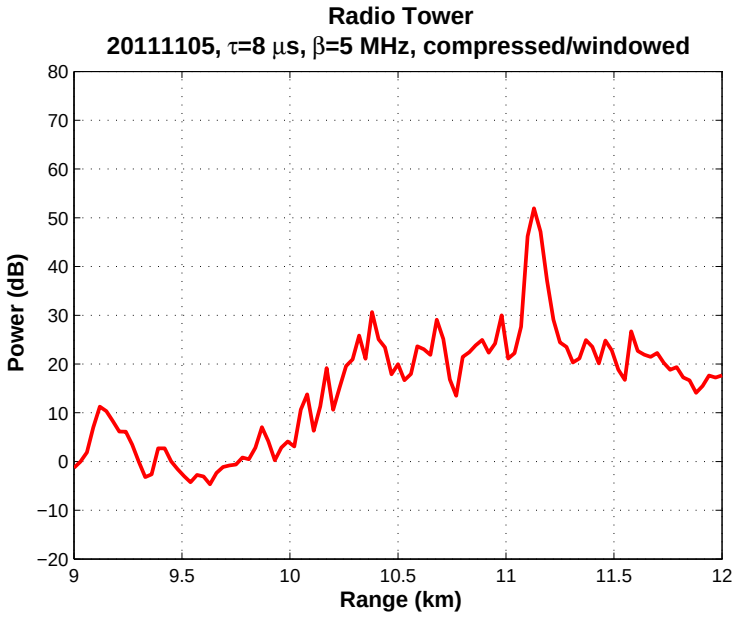

Figure 5.15: As in Figure 5.13, except a windowed matched filter is applied. The range sidelobes have been reduced significantly. Unfortunately, approximately 18 dB of sensitivity is also lost due to the application of the window function.

peak of the radio tower return resides at 52 dB, a loss of approximately 18 dB. While the range leakage has been significantly repressed, the sensitivity losses are unacceptable.

Initial tests of the pulse compression capabilities of the AIR show promise. Small enhancements to the design will allow the performance of the pulse compression algorithm to be improved. Incorporating a dedicated burst pulse sampling channel to record the forward power of the transmit signal will significantly improve the accuracy of the matched filter. Further exploration is required before a final version of the technique can be issued.

5.2 Weather Observations

5.2.1 Isolated Cell

A potentially severe weather event near the city of Norman, Oklahoma on August 8, 2011 provided an ideal case for initial weather data collection with the AIR. The AIR was taken to a location near the Max Westheimer Airport (35.241063N, 97.464681W). The conditions prior to the event were extremely hot and dry with temperatures exceeding 100° F and dewpoints in the mid 60s, as evidenced by the 00Z OUN sounding from August 9, 2011 presented in Figure 5.16. Outflow from

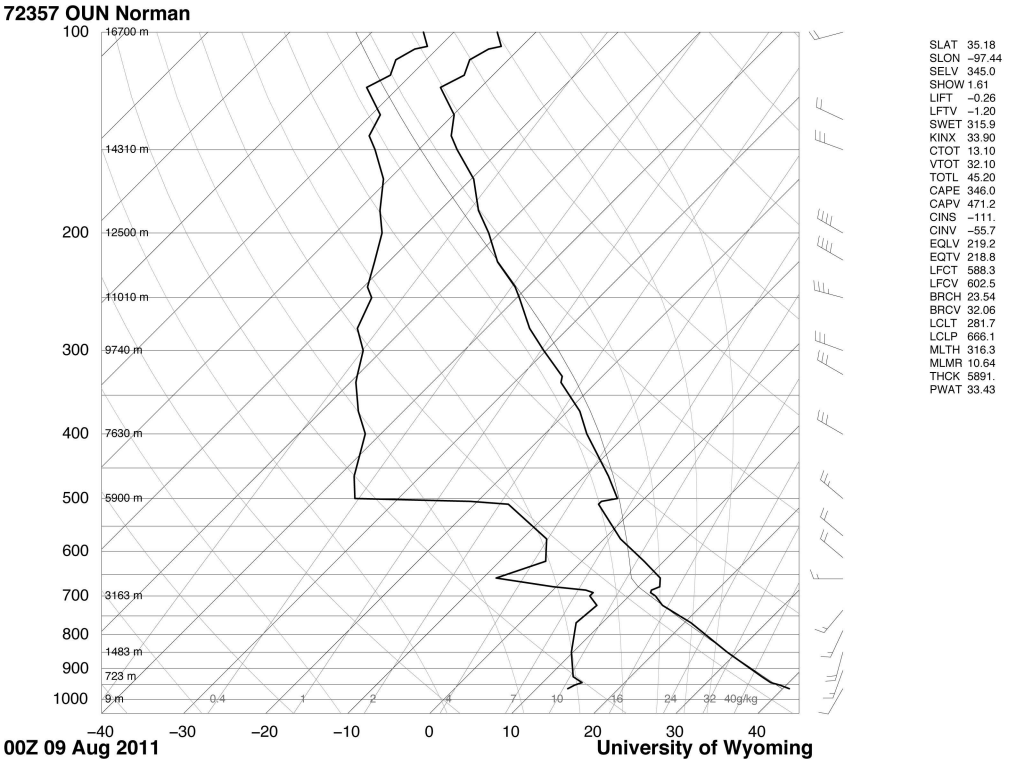

Figure 5.16: The 00Z Skew-T sounding from the OUN station near Norman, Oklahoma. Note the extremely hot surface temperatures and low dewpoints. This, coupled with the dry air aloft, created an environment suitable for high wind events, such as downbursts or derechos.

a previous convective storm to the north of central Oklahoma produced lifting sufficient to initiate isolated cell development. A deep dry layer at mid-levels enhanced convection and also provided a mechanism suitable for significant damaging downburst wind events. Reflectivity and radial velocity images collected with the nearby WSR-88D KTLX during the course of the experiment are presented in Figure 5.17. Several convective cells are visible in the reflectivity image, some of which appear to be merging. A significant outflow boundary is visible in both the reflectivity and radial velocity images as a 20-dBZ and 0 $\mathrm{m\,s^{-1}}$ boundary in the lower portion of the images, respectively.

For this initial test, the AIR was configured to collect a series of RHI images with no azimuthal rotation. Parameters for this data collection campaign are given in Table 5.1. No pulse compression was utilized during this experiment

Table 5.1: August 8, 2011 Isolated Cell Parameters

Parameter	**Value**
PRT	0.8192 ms
v_{a}	9.6 $\mathrm{m\,s^{-1}}$
Dwell	500 Samples
τ	1 μs
Bearing	60°
Time	02:27-02:35 UTC

because the method described in the previous section had not been tested. As such, the sensitivity of the radar system is limited. Therefore, the proximity of the AIR to the weather allows for useful observations to be recorded.

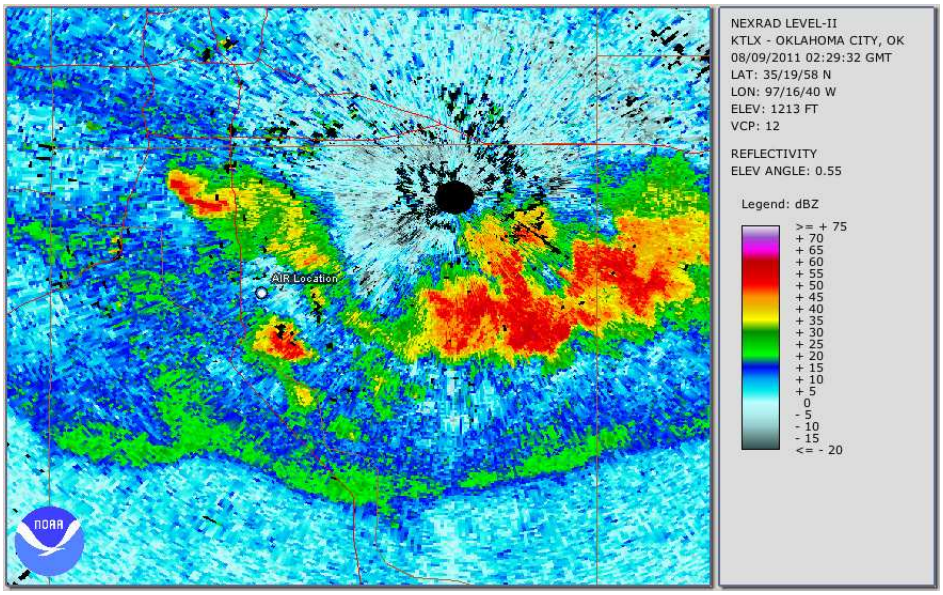

(a)

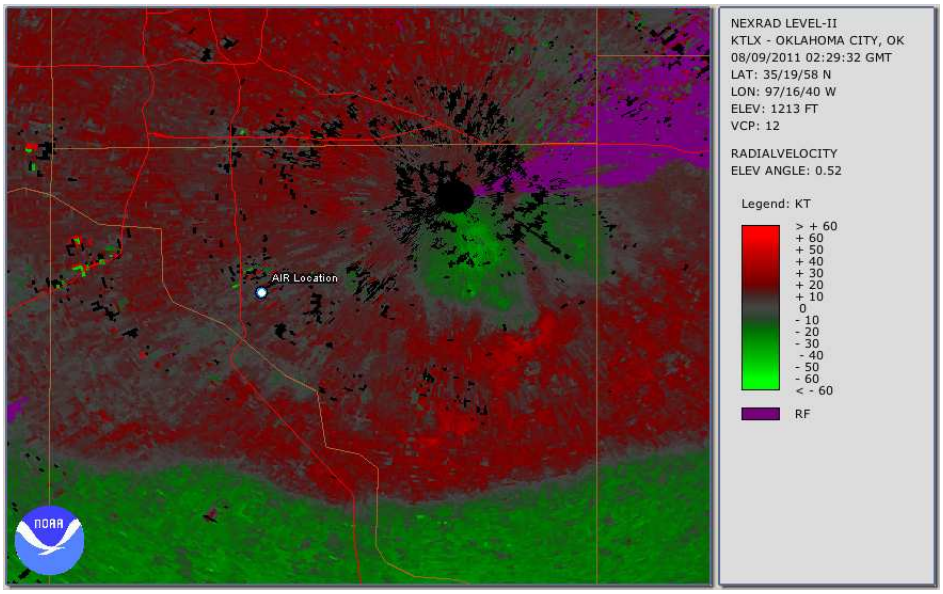

(b)

Figure 5.17: Images of reflectivity (a) and radial velocity (b) measurements collected with the KTLX WSR-88D on August 9, 2011 02:29:32 UTC. The AIR location is indicated by the white dot and the radar recorded a series of fixed-azimuth RHI images at 60° bearing.

An image depicting the return power for 45 RHI images is presented in Figure 5.18 while radial velocity is presented in Figure 5.19. The axes of each image

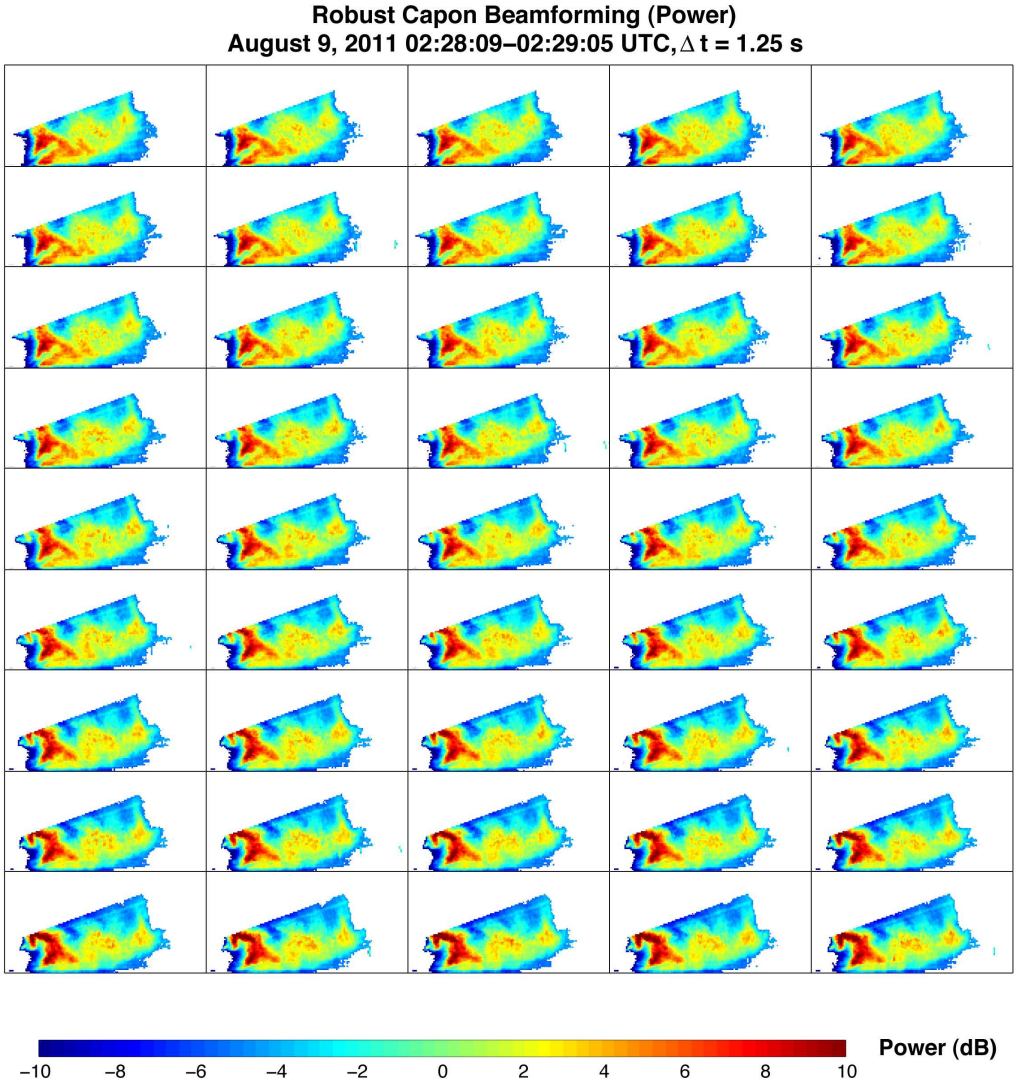

Figure 5.18: A series of RCB-generated RHI images of uncalibrated power recorded by the AIR on August 9, 2011 at 02:28:09 UTC. The time difference between each image is 1.25 s. The height and range extent of each image is 0 to 4 km and 3 to 11 km, respectively. Interesting features within the data include an overshooting region of elevated return power and descending reflectivity cores.

span 3 to 11 km in range and 0 to 4 km in height, while the time difference

between each image is 1.25 s. RCB is used to generate the RHI images with an angular resolution of 0.125°. Data were censored for values of return power below 3-dB SNR. Examining each image in sequence does not yield significant changes in the structure of the return power, which is to be expected for this type of storm. Nevertheless, taken as a whole, the data collection provides a unique view of a cross section of an isolated cell. What appears to be an overshooting core of reflectivity in the forward flank descends into the FOV as time progresses. While much of the motion is likely due to advection of rain through the beam, the temporal resolution is sufficiently high to capture hydrometeor motion in the vertical plane.

Radial velocity images presented in Figure 5.19 further illustrate the capability of the AIR to gather high resolution data. Aliasing is apparent and is expected with the low PRF used to collect these data. A staggered PRT algorithm is necessary given the nature of the phenomena the AIR will observe.

A comparison of the four beamforming algorithms discussed in Chapter 3 was conducted and the results are presented in Figure 5.20. The two Fourier beamforming images, both windowed and not, have a notable ground clutter interference in the first two kilometers due to the beamforming sidelobes. Additionally, the Fourier beamforming case displays significant leakage due to sidelobes, identified by the region of high return power extending above the core of the storm. Both adaptive algorithms reduce the impact of the sidelobes, though some remnants of the leakage are present above the reflectivity core in the RCB case. While the windowed Fourier algorithm appears to remove this effect, a loss of sensitivity is noted, which is not the case with the RCB results.

Further exploration of the isolated cell data yields interesting observations. An enlarged section of the animation plots 1, 16, and 31 taken from Figure 5.18 are given in Figure 5.21. The portion of interest is the descending reflectivity region.

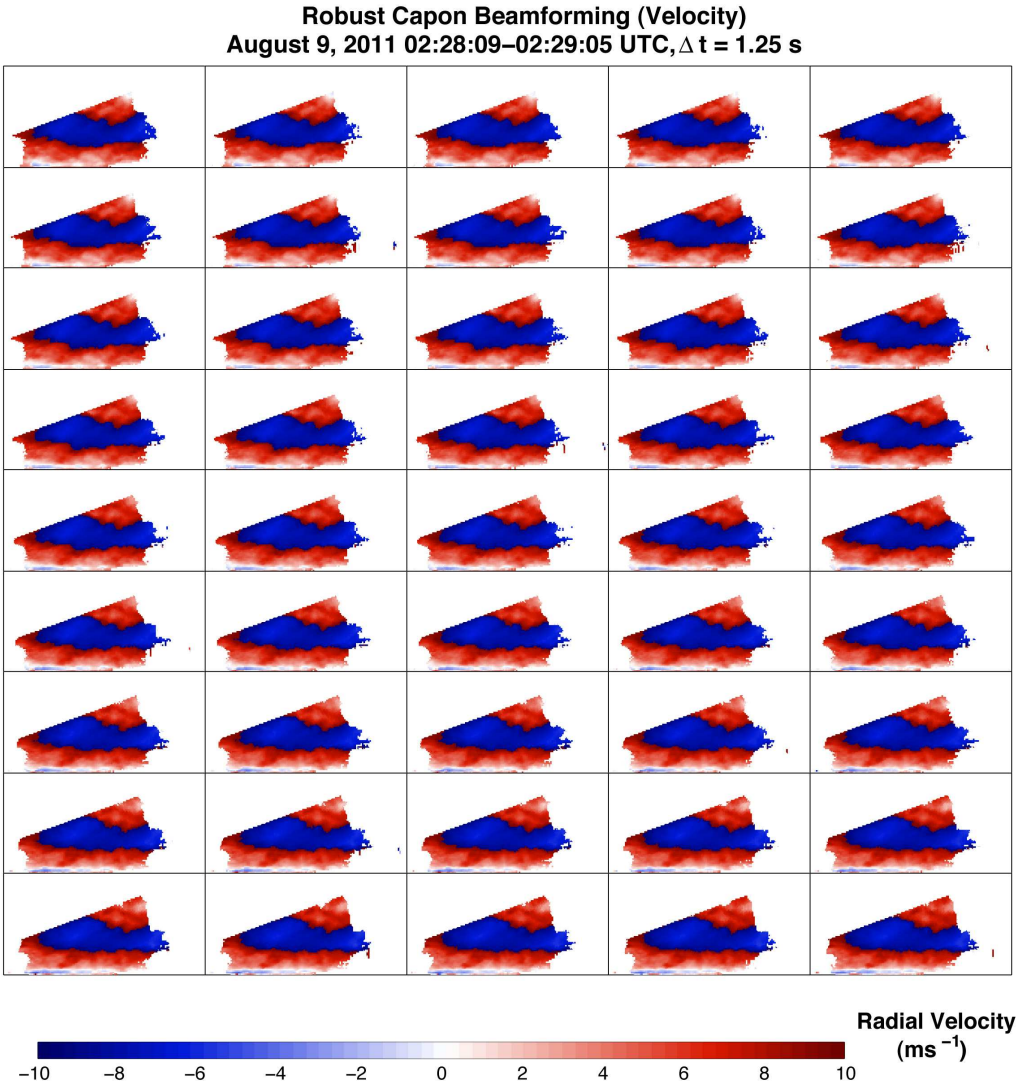

Figure 5.19: A series of RCB-generated RHI images of radial velocity recorded by the AIR on August 9, 2011 at 02:28:09 UTC. The time difference between each image is 1.25 s. The height and range extent of each image is 0 to 4 km and 3 to 11 km, respectively. An aliasing velocity of 9.6 $\mathrm{m\,s^{-1}}$ results in aliasing in the upper regions of the storm, represented by the dark blue patch.

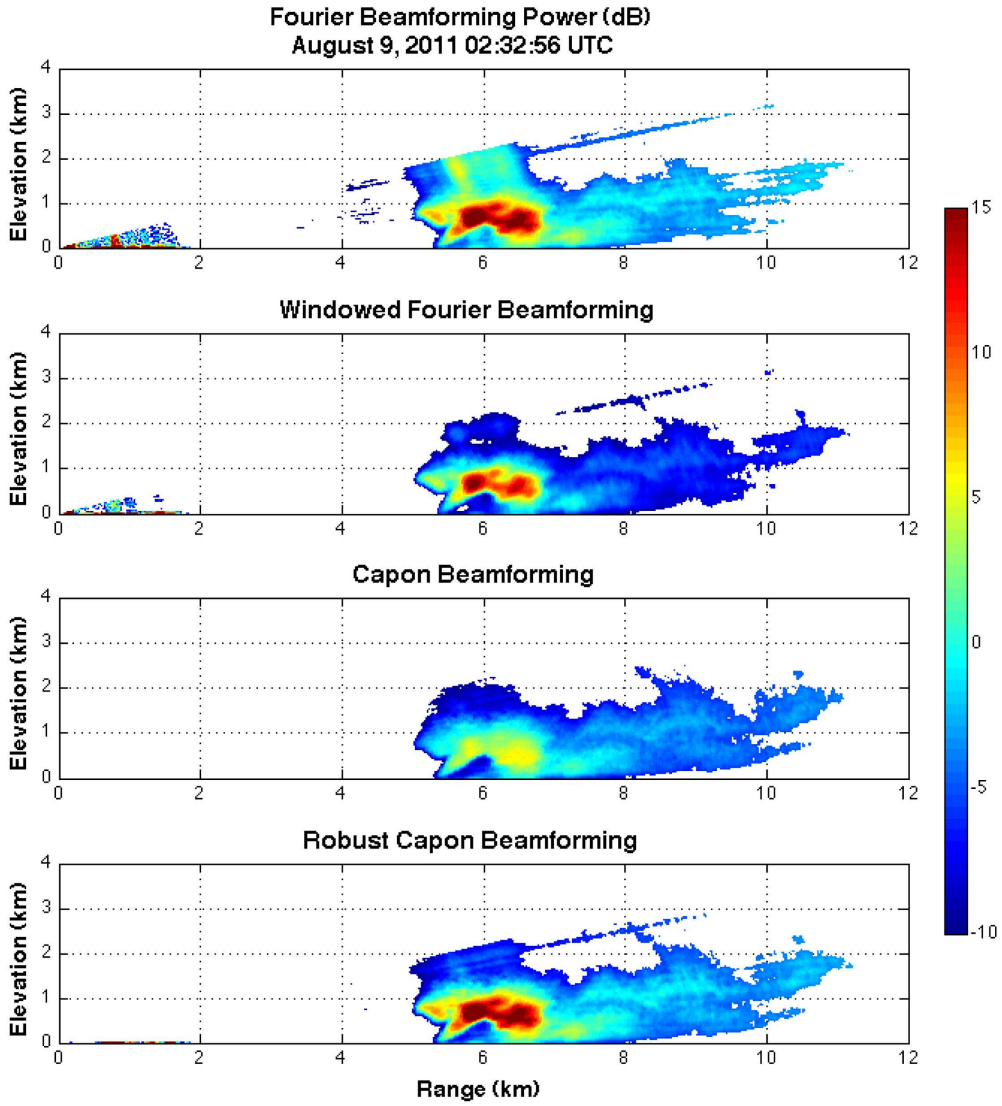

Figure 5.20: A comparison of the digital beamfroming techniques discussed in Chapter 3. Fourier suffers from sidelobe leakage with clutter targets within 2 km, as well as the high reflectivity core near the 6-km range. The remaining techniques significantly reduce the impact of the sidelobe leakage.

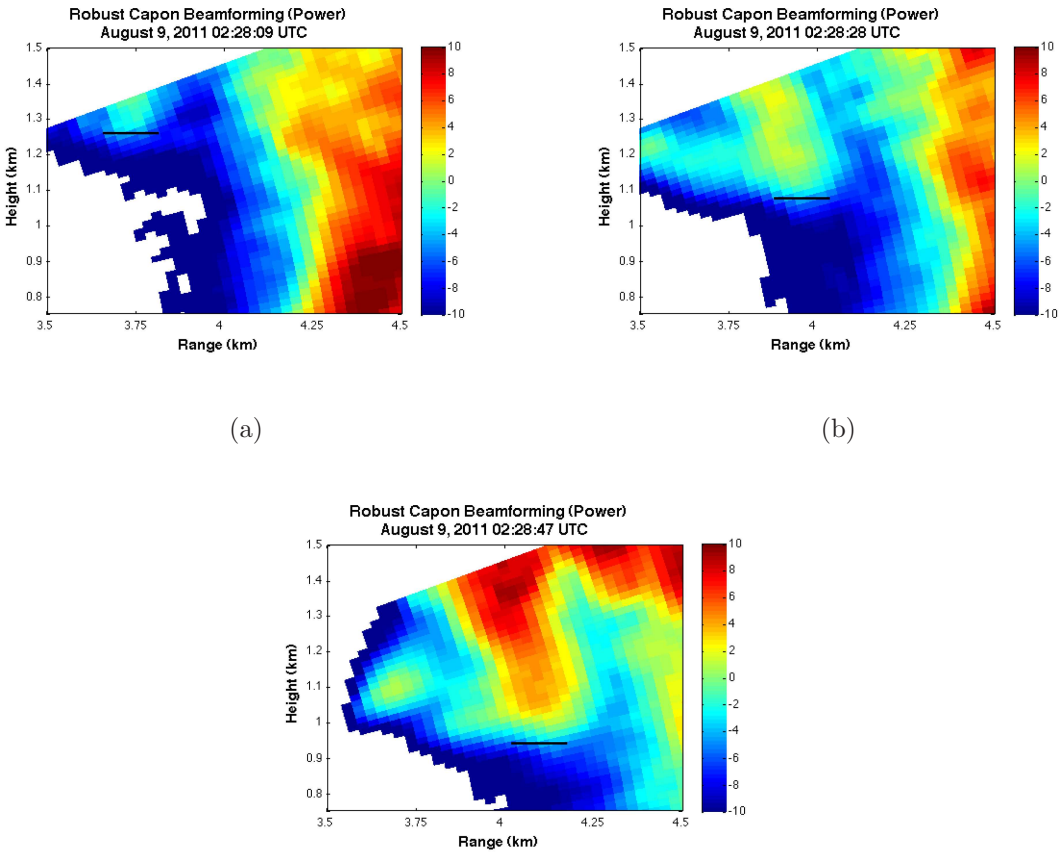

Figure 5.21: Images of the descending rain shaft from Figure 5.18 frame 1 (a), 16 (b), and 31 (c). The black line represents the base of the rain shaft. By measuring the distance the black line moves between frames, a vertical velocity can be determined. In this case, a value of -8 $\mathrm{m\,s^{-1}}$ is estimated.

A black line represents the base of the core and, since the time between scans is known, an approximate vertical velocity of -8 $\mathrm{m\,s^{-1}}$ was determined. More rigorous image processing algorithms could be utilized to obtained automated estimates with a higher degree of accuracy. As mentioned previously, advection likely plays a strong role in the progression of the image. Nevertheless, this exercise serves as an example of the additional dynamic insight provided by the AIR.

5.2.1.1 KTLX Comparisons

Comparisons between the reflectivity and radial velocity retrievals of the AIR and the nearby KTLX radar are presented in Figure 5.22. RHI images were

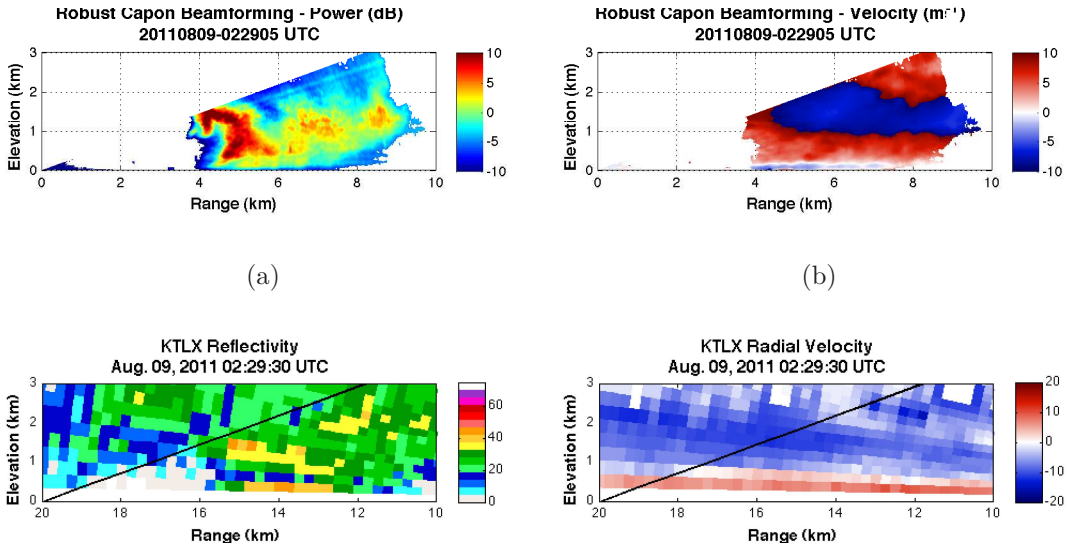

Figure 5.22: A comparison of the AIR power (a) and radial velocity (b) retrievals, and those gathered by KTLX (c) and (d). The diagonal black line in the KTLX images represents the FOV of the AIR. Note that the radial velocity measurements will be inverted for the two radars due to the direction of the beams. Note the velocity image in (b) is aliased in the mid-levels.

constructed from KTLX Level-II data at the 240° azimuth with values interpolated to fill gaps produced by the volume coverage pattern. The black line in Figure 5.22(c) and Figure 5.22(d) represents the FOV of the AIR. Note that the radial velocity measurements produced by KTLX will be reversed as the radars are transmitting toward one another. While it is difficult to compare the images due to the apparent differences in spatial resolution, a general agreement between the return power of the AIR and the reflectivity of KTLX is observed, specifically in the upper portion of the FOV between 4 and 6 km. Given the homogeneity of the radial velocity images, no comparisons other than general agreement are made.

5.2.2 Squall Line

A second data collection for the AIR was conducted on October 17, 2011 approximately 20 km east of Wynnewood, Oklahoma (34.650968N, 96.959406W). A squall line was forecast to develop across central Oklahoma in the afternoon and progress southeastward in the late evening. The 00Z surface map presented in Figure 5.23 indicates that, indeed, a cold front backed by strong winds passed over central Oklahoma. Subsequently, a line of strong thunderstorms was initiated and sustained through the evening. Reflectivity and radial velocity images recorded by KTLX are presented in Figure 5.24. The AIR was located behind the convection, with the line moving toward the southeast. Significant reflectivity returns indicate heavy rain and possibly hail.

Again, the AIR was configured to collect data in the fixed-azimuth RHI mode. Particulars of the data collection are given in Table 5.2. The main difference between the data collection in this case and that of the isolated cell is the dwell time. Changes were made to the data recording software that allowed consecutive

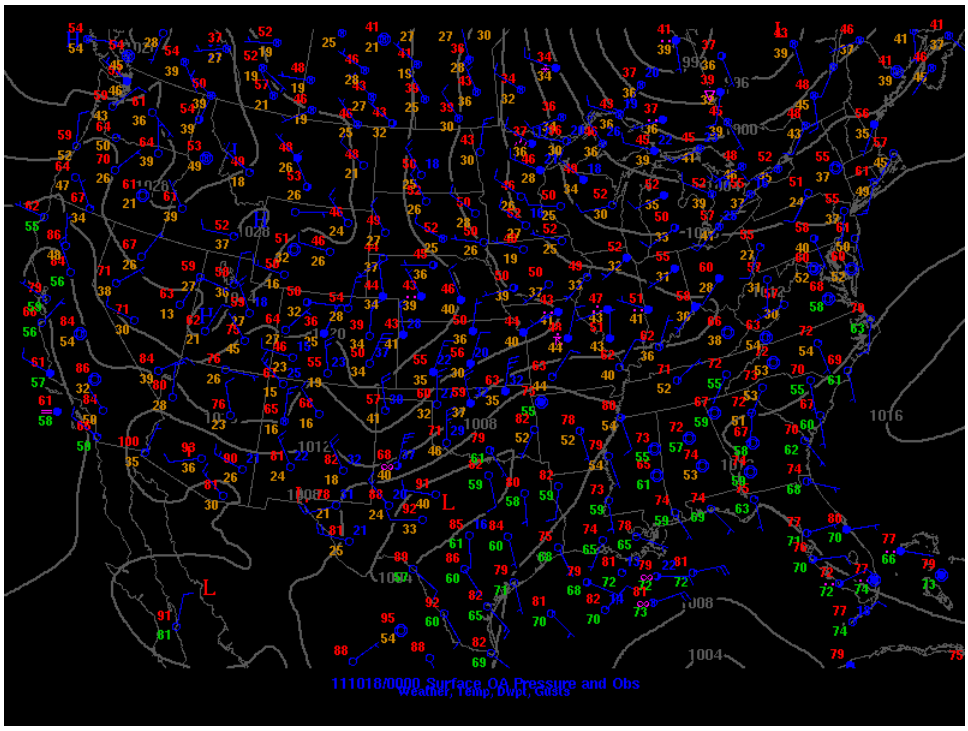

Figure 5.23: The 00Z surface map for October 18, 2011. A cold front backed by strong northerly winds passed through central Oklahoma with temperatures falling approximately 10 to 20° F after the frontal passage. A squall line developed along the frontal boundary and progressed east, southeastward toward Arkansas.

Table 5.2: October 17, 2011 Squall Line Parameters

Parameter	**Value**
PRT	0.8192 ms
v_a	9.6 $\mathrm{m\,s^{-1}}$
Dwell	300 Samples
τ	1 μs
Bearing	170°
Time	00:29-00:57 UTC

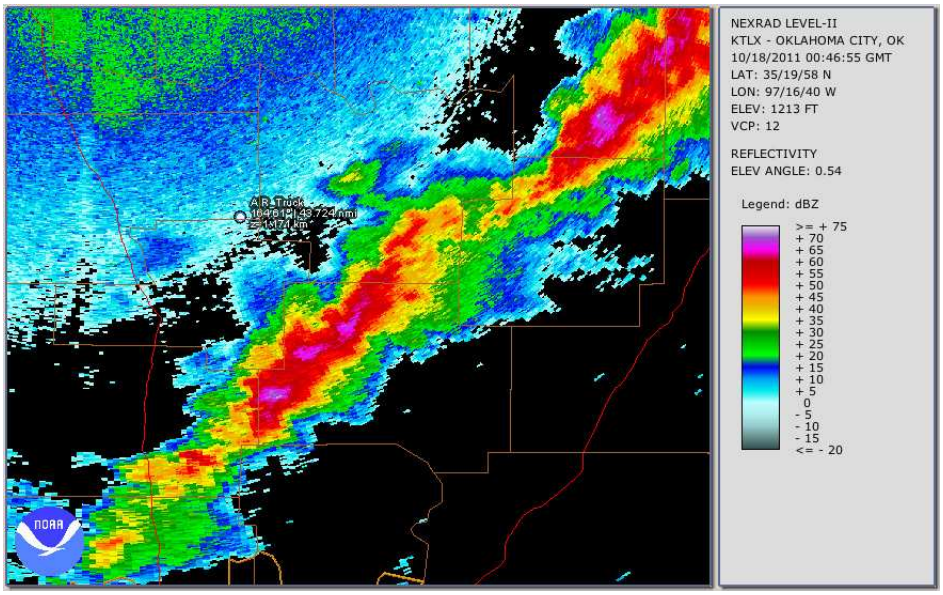

(a)

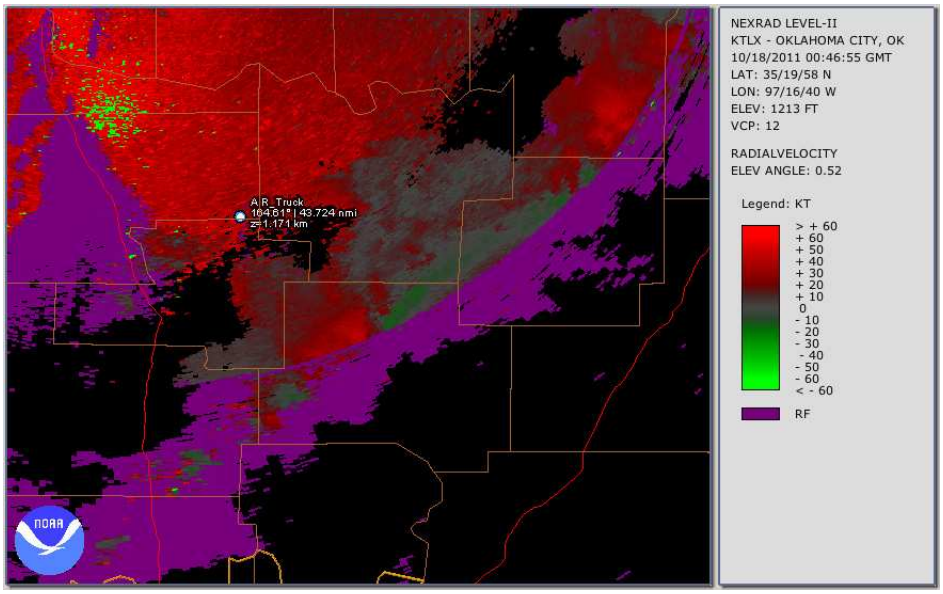

(b)

Figure 5.24: Images of reflectivity (a) and radial velocity (b) measurements collected with the KTLX WSR-88D on October 18, 2011 0:46:55 UTC. The AIR location is indicated by the white dot and the radar recorded a series of fixed-azimuth RHI images at 170° bearing.

RHI images to be collected without a pause between recorded files. Thus, the temporal resolution of the data was increased.

An image, similar to Figure 5.18 is given in Figure 5.25. Again, 45 RHI images are presented with the horizontal and vertical axes representing 15 to 40 and 0 to 12.5 km, respectively. Data were censored for values below 3-dB SNR and RCB beamforming was performed at 0.125° intervals. Note that the temporal resolution of this animation is 3.3 s. Earlier, it was mentioned that the data were collected at a rate higher than the August 8 case. This is indeed true and the full temporal resolution is 0.33 s, meaning that the images within Figure 5.25 are decimated in time. The reason for the abbreviated display is due to the minimal difference between successive images at full resolution.

The red box in Figure 5.25 indicates a region of the image where a demonstration of the full temporal resolution capability of the AIR in the fixed RHI mode will be produced. Similar to enlarging a high resolution image, the data represented by the two images outlined in red can be viewed at a higher temporal resolution, shown in Figure 5.26. As previously mentioned, there is little change between successive images, however, the exercise illustrates the capabilities of the AIR. Data collected during more suitable, quickly evolving phenomena could benefit greatly from the extremely high rate of collection.

Radial velocity images at the decimated and full temporal resolution are presented in Figures 5.27 and 5.28, respectively. Aliasing is prevalent, particularly at the mid and upper levels of the storm, indicating significant motion within the convective core.

One important note regarding the data presented in this section relates to the sensitivity of the AIR. The data were collected at a large distance from the radar and with a 1-μs pulse. As such, the detected power returns are solely due to the strongest parts of the squall line. Regions of light precipitation surrounding the

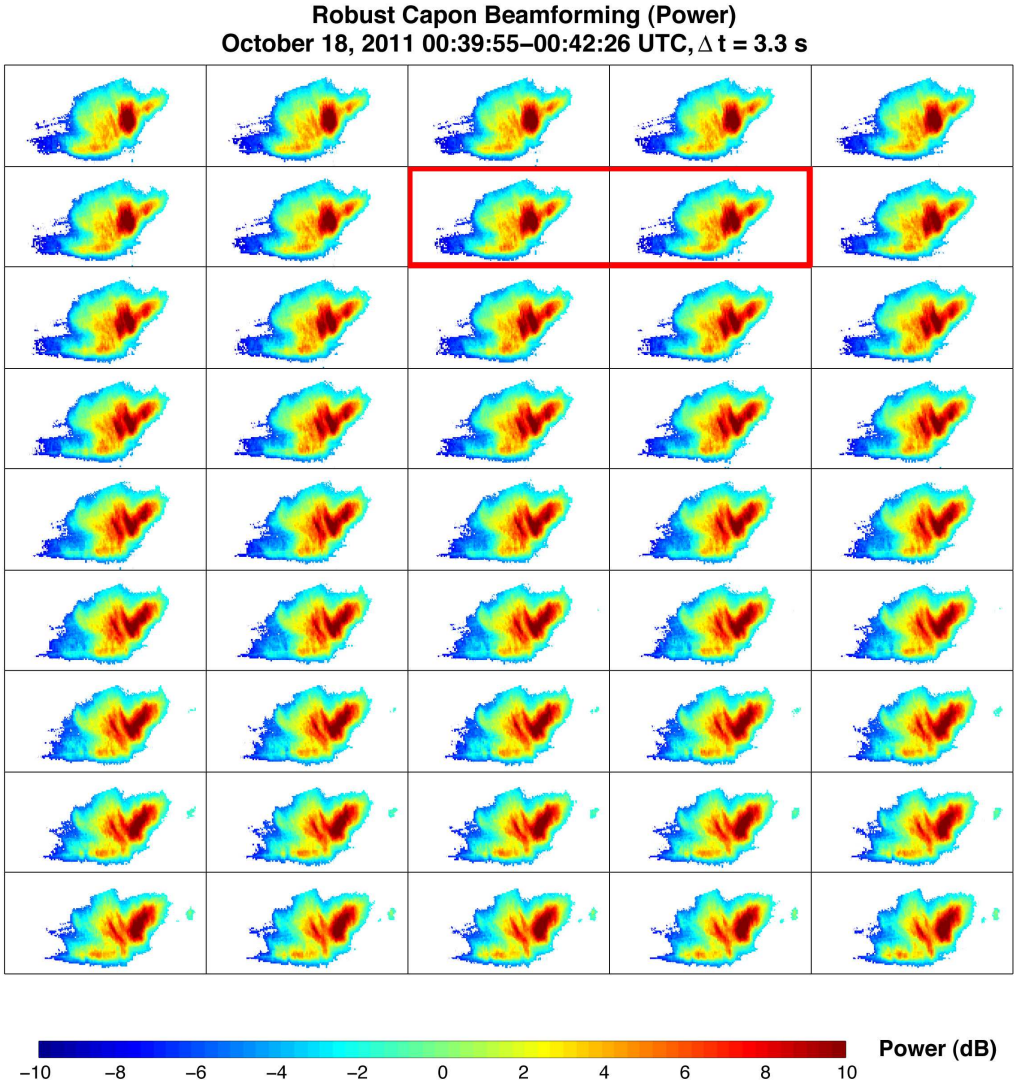

Figure 5.25: A series of RCB generated RHI images of return power recorded by the AIR on October 18, 2011 at 00:39:55 UTC. The time difference between each image is 3.3 s. The height and range extent of each image is 0 to 12.5 km and 15 to 40 km, respectively. The figure represents a decimated view of the full RHI temporal resolution for this collection of data. The red box indicates a region that is expanded for viewing in Figure 5.26.

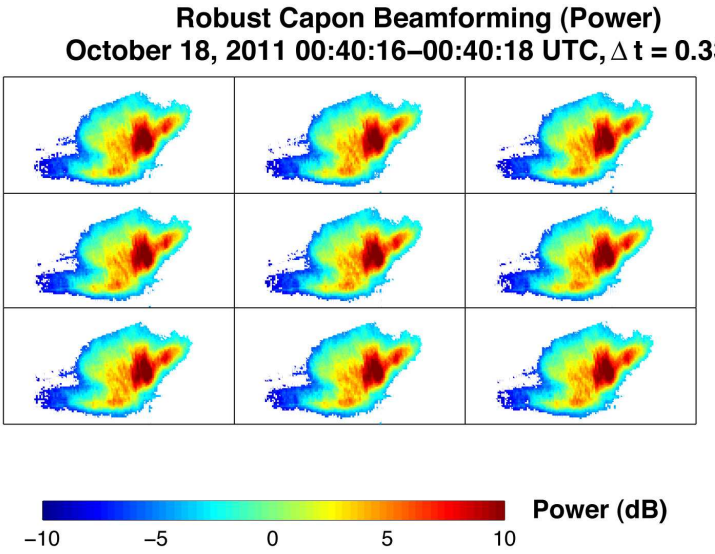

Figure 5.26: A series of RCB generated RHI images of return power recorded by the AIR on October 18, 2011 at 00:39:55 UTC. The time difference between each image is 0.33 s. The figure represents the full temporal resolution of the AIR.

high reflectivity cores are absent from the data presented. Pulse compression is necessary if data collected at these ranges is to be successful. A comparison in the next section illustrates the sensitivity issues.

5.2.2.1 RaXpol Comparisons

For this particular data collection, the AIR was accompanied by another X-band mobile radar system, the RaXpol (Pazmany and Bluestein 2009). The RaXpol is a rapid scanning dish radar capable of collecting RHI images every four to five seconds. The radar was positioned near the AIR and collected data along the same bearing. Results from each radar are presented in Figure 5.29. Note that the lack of sensitivity of the AIR is apparent when compared with the RaXpol. It appears that the AIR is only able to detect signals of approximately 40 dBZ at a range of 35 km. It is worthwhile, however, to compare these data.

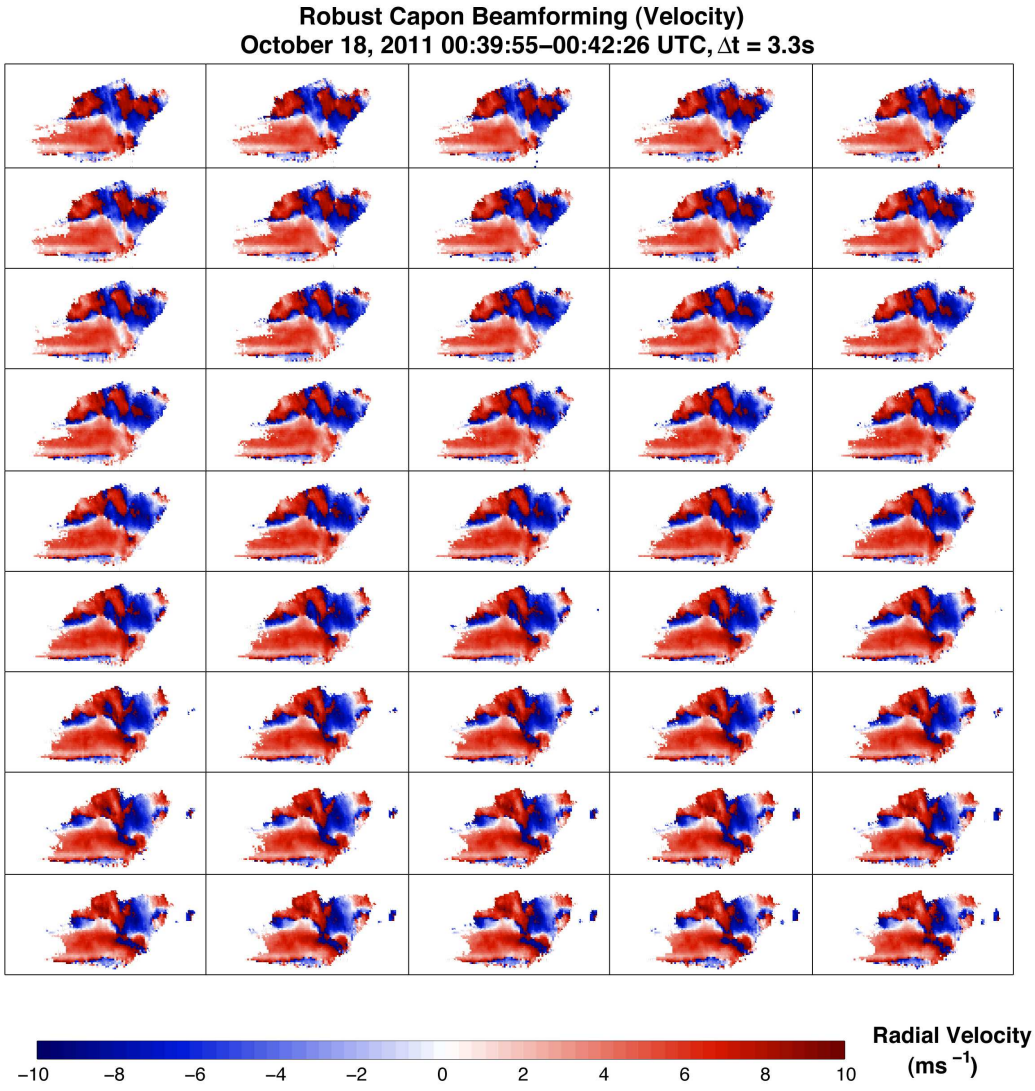

Figure 5.27: A series of RCB generated RHI images of radial velocity recorded by the AIR on October 18, 2011 at 00:39:55 UTC. The time difference between each image is 3.3 s. The height and range extent of each image is 0 to 12.5 km and 15 to 40 km, respectively. The figure represents a decimated view of the full RHI temporal resolution for this collection of data. An expanded view of two of the images is presented in Figure 5.28.

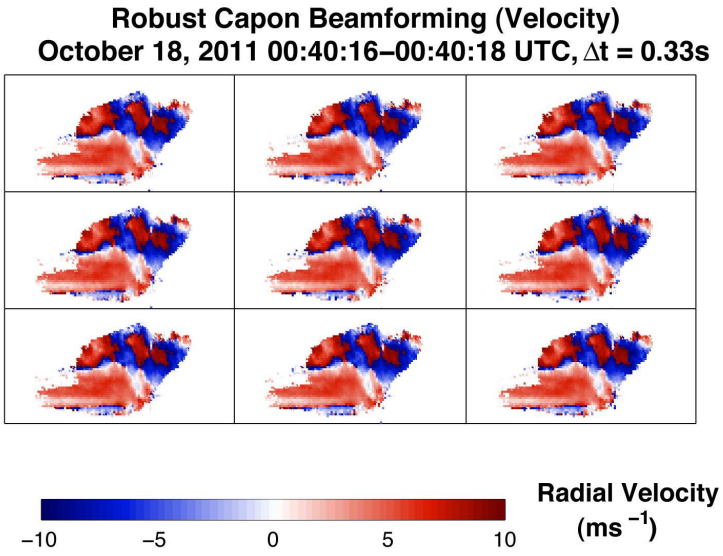

Figure 5.28: A series of RCB generated RHI images of radial velocity recorded by the AIR on October 18, 2011 at 00:39:55 UTC. The time difference between each image is 0.33 s. The figure represents the full temporal resolution of the AIR.

Four images, skipping several scans, are shown in Figure 5.30 for the AIR and are paired with four consecutive scans collected by the RaXpol. The AIR is again displaying a decimated view of the true temporal resolution. The radars were not synchronized prior to the data recording, thus it is possible that a discrepancy may exist between the times shown for each radar. Reasonable agreement is observed between the relative shape of the power returns, however, the sensitivity disparity makes the direct comparison difficult.

Similar to Figure 5.30, an array of images showing the radial velocity measurements is given in Figure 5.31. It is somewhat easier to compare the radial velocity images due to the dynamic nature of the event. Good agreement is observed between the AIR and RaXpol images, especially between 40 and 45 km in range. The time discrepancy may be responsible for the more substantial differences in the radial velocity patterns observed in the images.

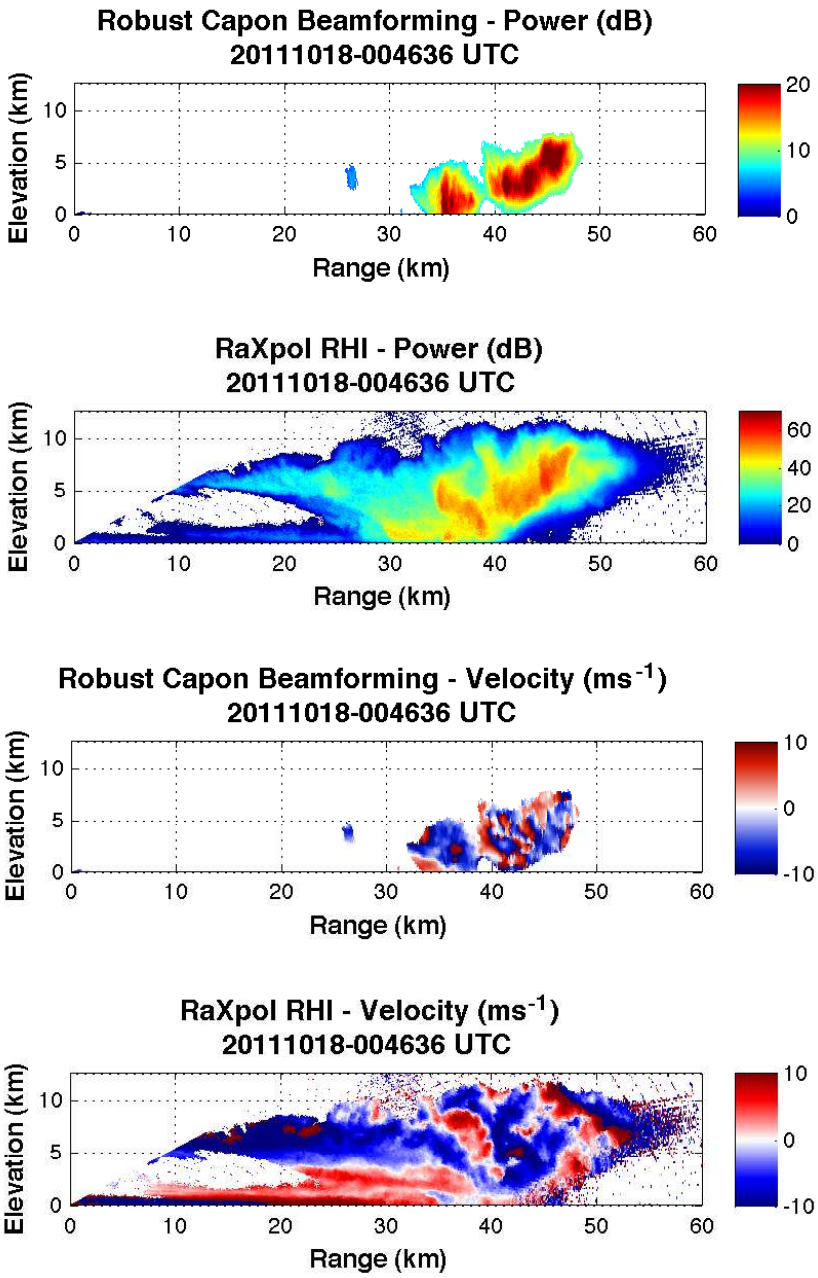

Figure 5.29: Return power and radial velocity data recorded by the AIR and RaXpol mobile radars on October 18, 2011 00:46:36 UTC. The AIR suffers from a loss of sensitivity due to the range to the target storm as well as the short, 1-μs pulse utilized during data collection. Only the high reflectivity cores of the storm are visible, with the lower power signals obscured by the noise. Some agreement between the radial velocity images is noted.

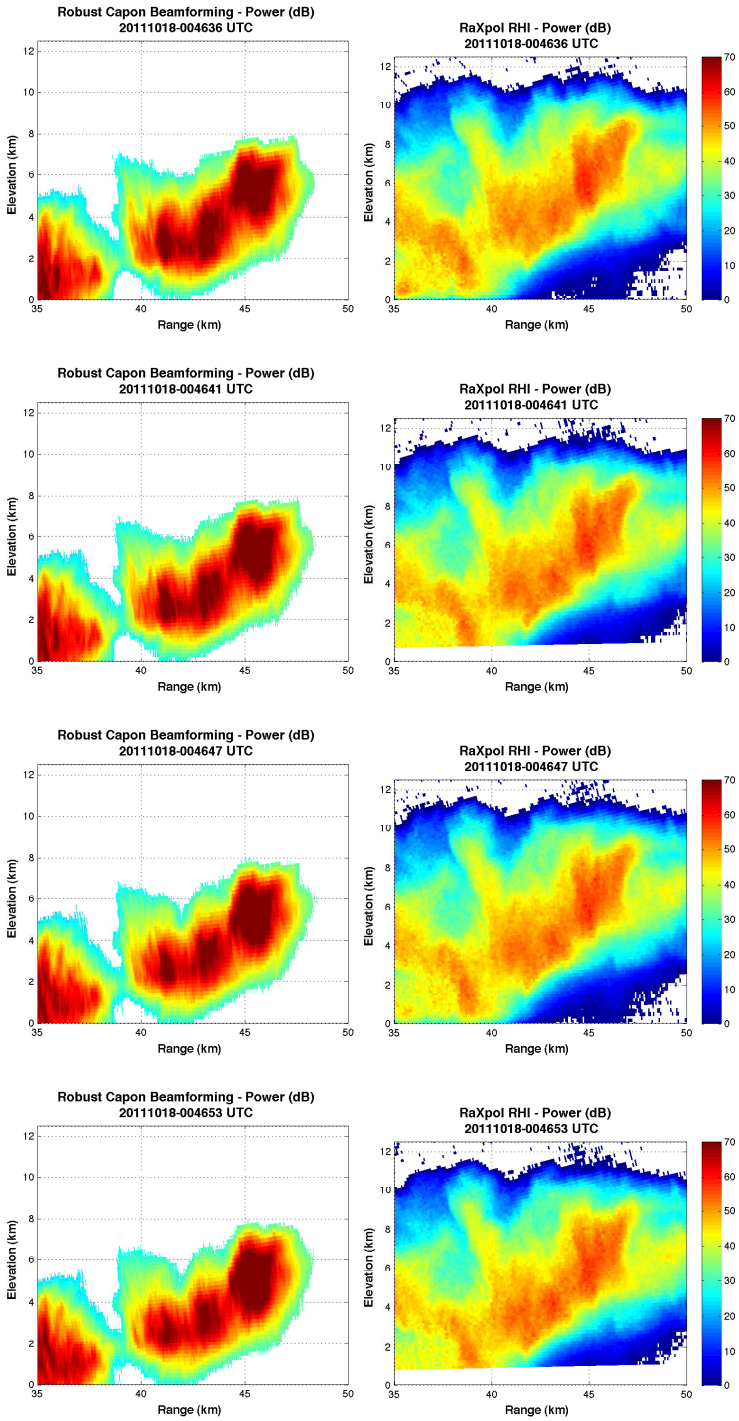

Figure 5.30: Four RHI return power images collected at approximately the same time by the AIR and RaXpol mobile radars. No effort to synchronize the radars was made. Some agreement is observed between the two images, however, only the strongest reflectivity cores are visible with the AIR.

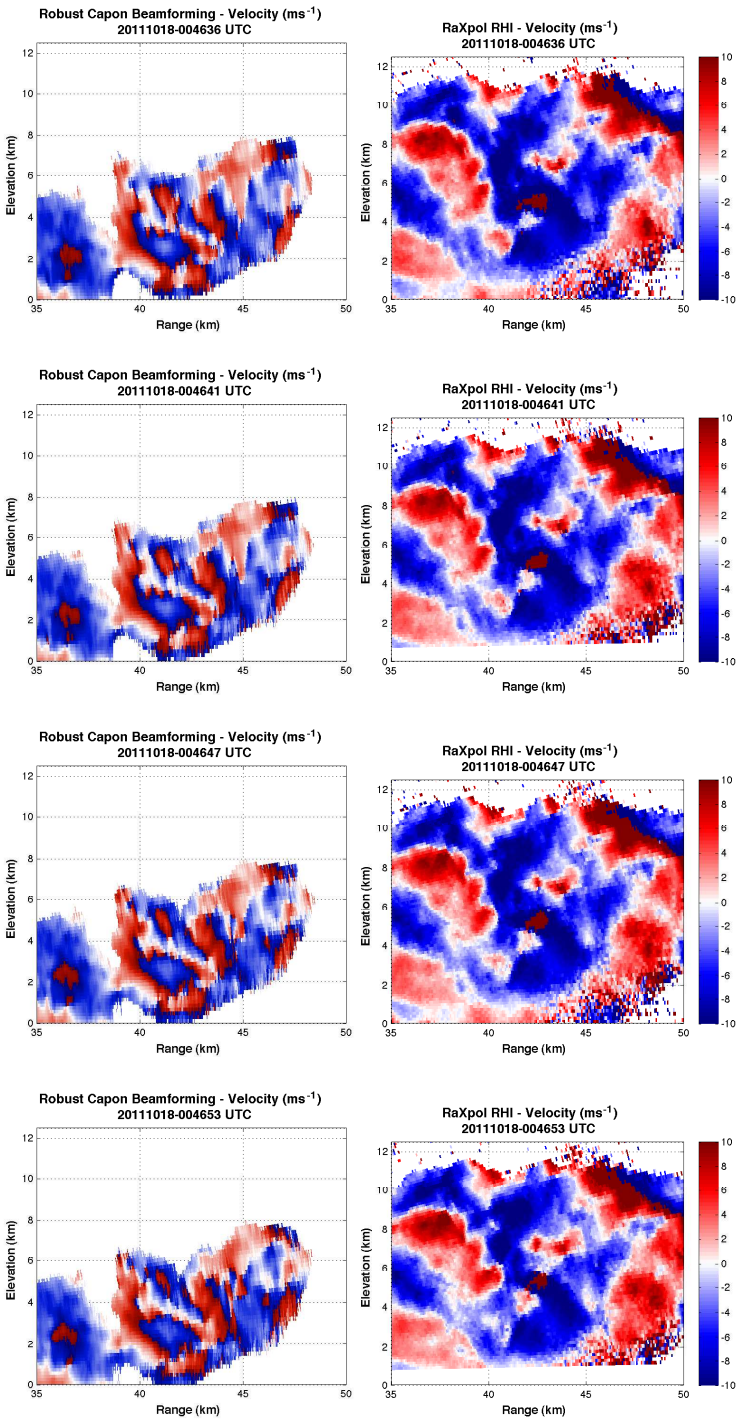

Figure 5.31: Four RHI radial velocity images collected at approximately the same time by the AIR and RaXpol mobile radars. General agreement between the two radars is observed. The time discrepancy between the radars may account for some of the larger differences in spatial correlation.

5.2.3 Supercell

While the capabilities of the AIR were explored in the previous weather collection experiments, an event on November 7, 2011 in southwest Oklahoma provided a scenario that is more representative of the data collections originally envisioned for the AIR. The AIR was deployed to a location near Babbs, Oklahoma (34.942774N, 99.060927W). An outbreak of supercell thunderstorms was predicted for the Texas panhandle/western Oklahoma region. A sounding from 00Z on November 8, 2011 at the OUN site presented in Figure 5.32 reveals that the environment was indeed suitable for sustained supercell development. High dewpoints at low levels

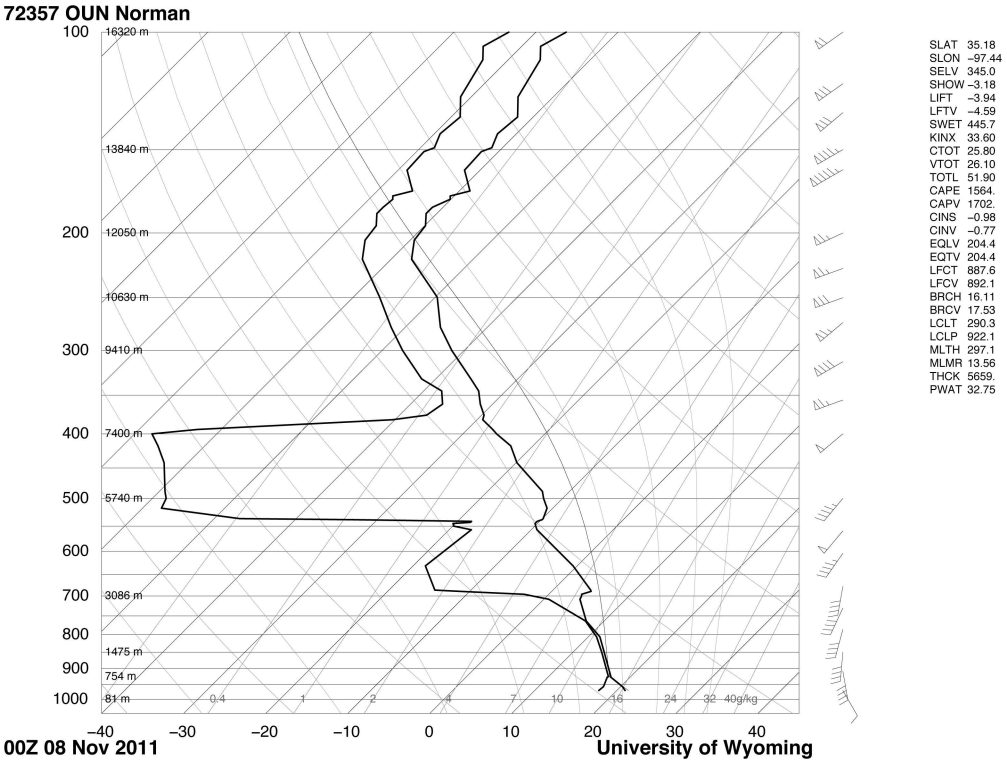

Figure 5.32: A 00Z Skew-T sounding from the OUN site on November 8, 2011. High dewpoints at the surface coupled with southerly winds provided suitable forcing to initiate storms along the dryline. Backing winds at mid-levels created an environment capable of sustaining supercell development and propagation.

and strong southerly winds provided sufficient forcing at the surface. Significant backing of the mid-level winds and a deep dry layer enhanced the possibilities of deep convection, with convective available potential energy (CAPE) values of 1800 KJm^{-1}. Upper-air charts presented in Figure 5.33 further illustrate the state of the environment. As previously mentioned, significant southerly flow at low levels coupled with strong westerlies at mid-levels provided an environment suitable for sustained supercell development. Additionally, the upper-level jet was positioned such that the right-exit region was located over the CAPE maximum, providing a mechanism to enhance convergence at the surface.

Images of the reflectivity and radial velocity measurements recorded by KFDR WSR-88D radar are presented in Figure 5.34 and 5.35. From the image in Figure 5.34, it is apparent that several supercell systems developed within the predicted area, with storm motion proceeding to the northeast. Strong rain and hail were reported with several systems and are indicated by the high reflectivity values in the forward flanks. The storm to the southeast of the AIR location produced a long-lasting tornado.

A closer inspection of the supercell of interest in Figure 5.35 reveals that indeed rotation was observed at low levels. A strong radial velocity couplet located within the supercell is clearly visible in the earlier of the two images, though the rotation weakened over the course of the data collection period.

For this particular data collection, the AIR was configured to collect sectors of azimuthal data, meaning, azimuthal scanning would take place while the beamforming algorithms would produce an RHI at each azimuth angle. Specific parameters of the data collection are given in Table 5.3. As a result, the AIR collected a 40° sector of 20° RHI images once every 6 seconds. Additionally, a staggered PRT algorithm was employed to increase the aliasing velocity of the recorded data. Given the values presented in Table 5.3, an unambiguous velocity

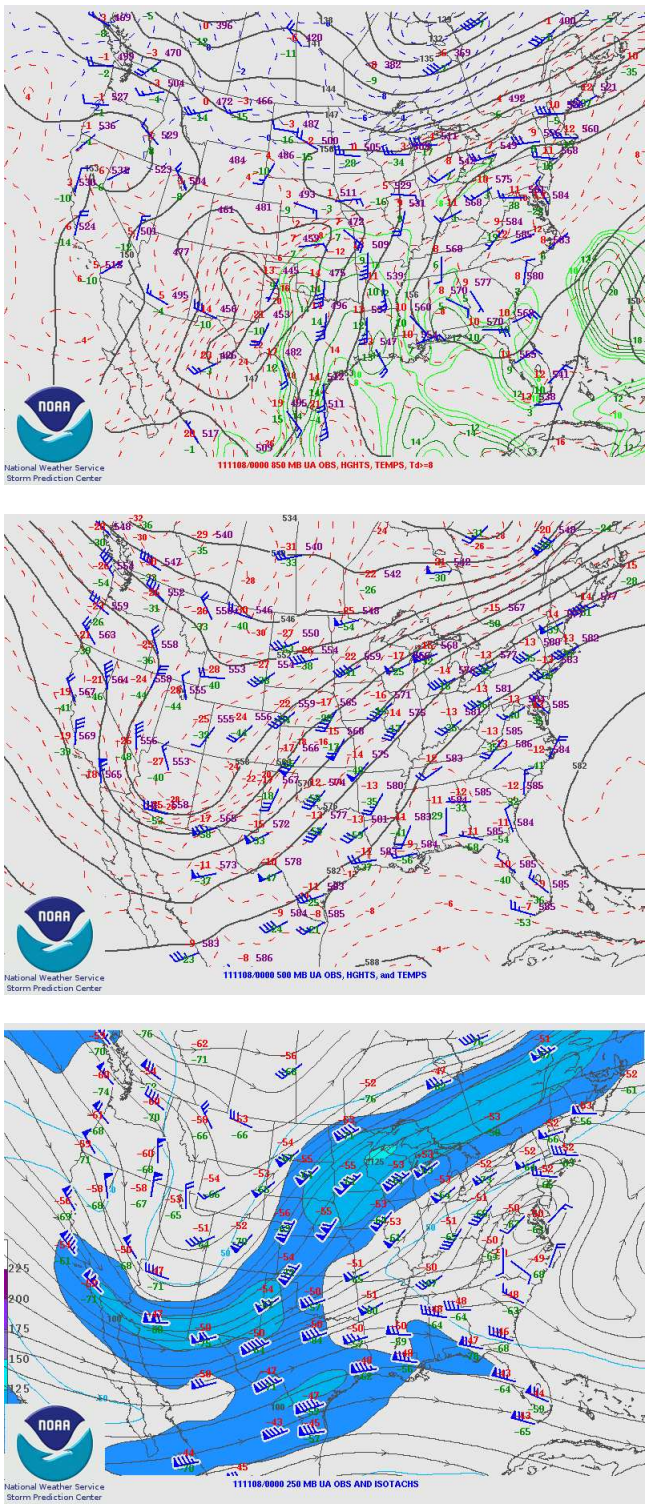

Figure 5.33: Upper air charts for 850, 500, and 250 mb valid for 00Z on November 8, 2011. Note the strong southerly winds at low levels and the location of the right-exit region at the upper levels.

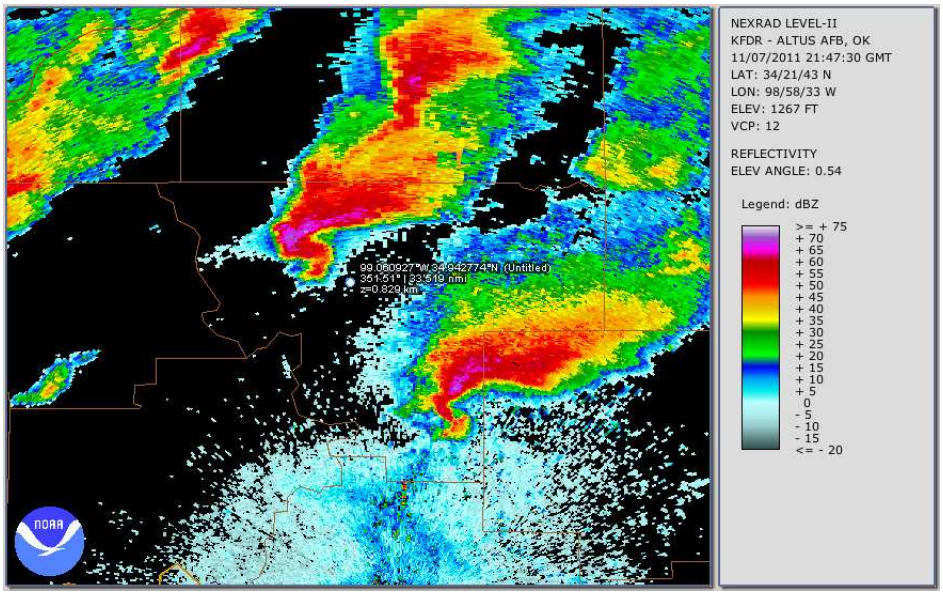

Figure 5.34: An image of reflectivity recorded by the KFDR WSR-88D on November 7, 2011 at 21:47:30 UTC. The AIR location is indicated by the white dot. Several supercells developed in southwestern Oklahoma with some producing tornadoes. The storm directly to the north of the AIR did not produce a tornado, but had a well developed mesocyclone for a brief period.

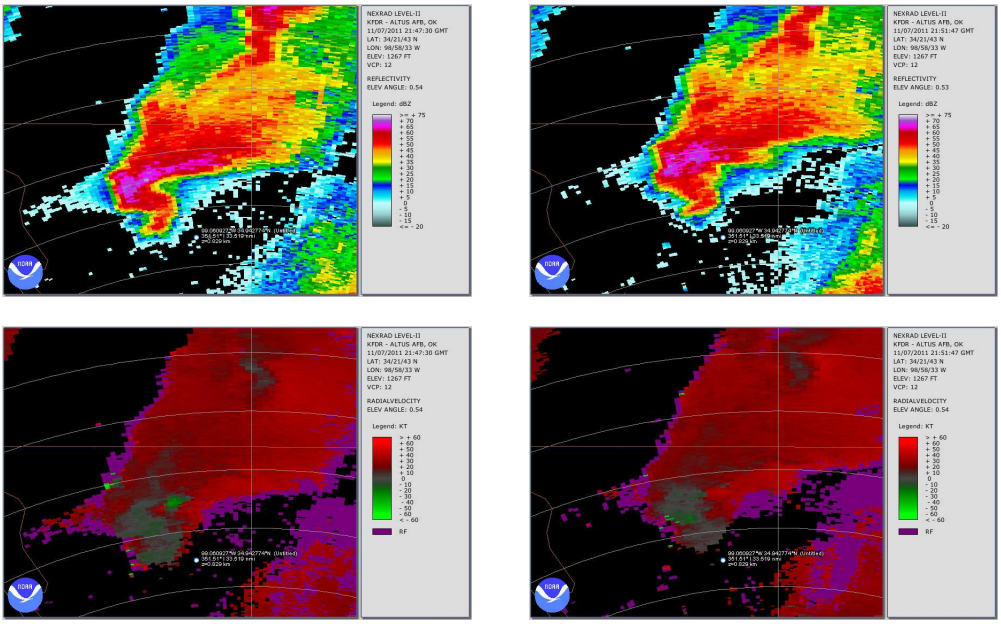

Figure 5.35: Reflectivity and radial velocity images recorded by KFDR at 21:47:30 (left) and 21:51:47 UTC (right). High reflectivity in the forward flank of the storm indicates a high possibility of hail. A strong velocity couplet is visible in the radial velocity image on the left, though it weakens somewhat over the course of approximately 4 minutes. The location of the AIR is indicated by the white dot.

Table 5.3: November 7, 2011 Supercell Parameters

Parameter	**Value**
PRT1	0.4096 ms
PRT2	0.6144 ms
v_{a1}	19.17 $\mathrm{m\,s^{-1}}$
v_{a2}	12.78 $\mathrm{m\,s^{-1}}$
v_{a}	38.33 $\mathrm{m\,s^{-1}}$
Dwell	100 Samples
τ	1 μs
Bearing	-25°to 15°
Time	21:47-21:52 UTC

of 38 $\mathrm{m\,s^{-1}}$ is expected, providing a notable improvement over the previous campaigns. Due to the motion of the antenna in azimuth, the number of samples per dwell is reduced. While many datasets were collected on November 7, the focus of this section will reside on one particular dataset recorded during the time of the KFDR data presented in Figure 5.35.

The results of the experiment are presented in Figures 5.36 through 5.37. Isosurface plots are used to represent the return power of each sector scan, with green, yellow and red indicating values of less than -55, -50 and -45 dB, respectively. Data were processed at 1° intervals in both elevation and azimuth due to the computational burdens of high resolution RCB beamforming. Again, only part of the data are presented due to the high temporal resolution and the time between successive images is 12.5 s. A view of the supercell from the east looking to the west is presented in Figures 5.36 and 5.37. As time progresses, the hook

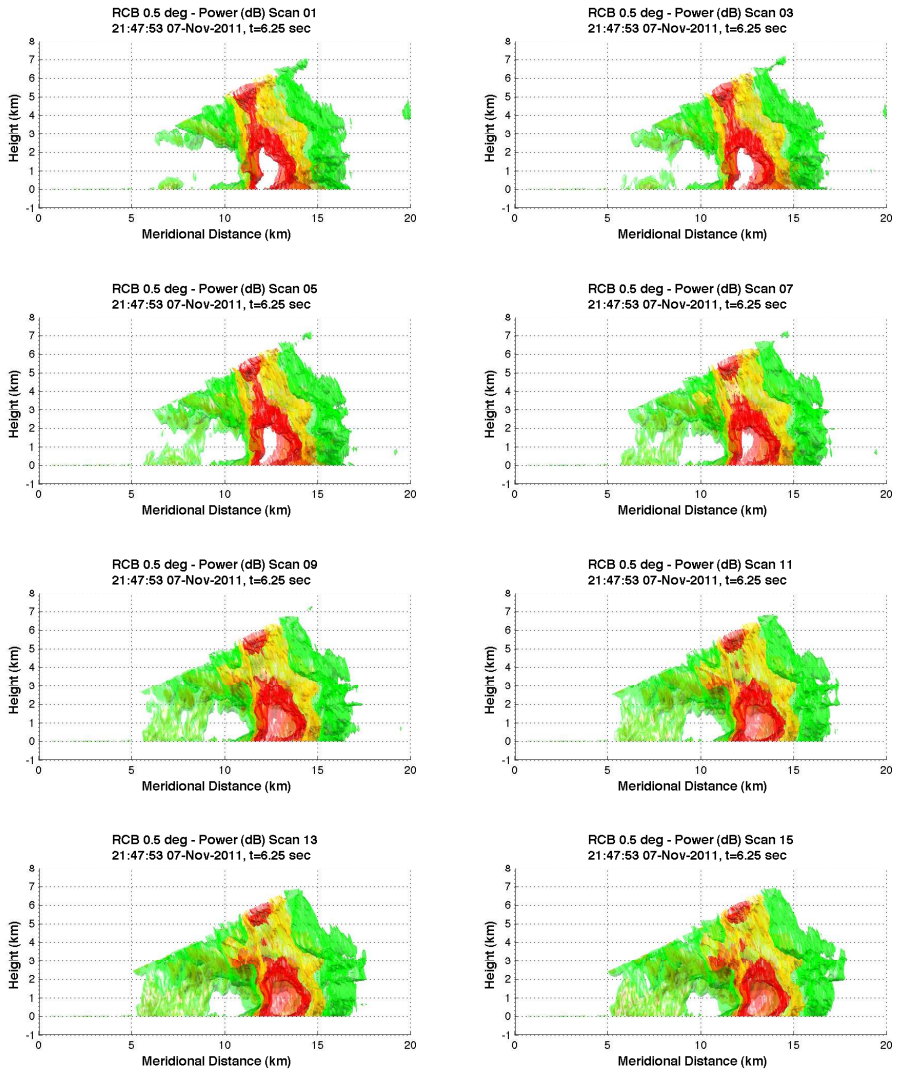

Figure 5.36: Part 1 of a series of images representing the return power recorded by the AIR on November 7, 2011 at 21:47:58 UTC. The images are taken from the east, looking west through the AIR sector FOV. Green, yellow, and red isosurfaces represent power levels of -55, -50, and -45, respectively. The rotating updraft begins to appear through the course of this set of images.

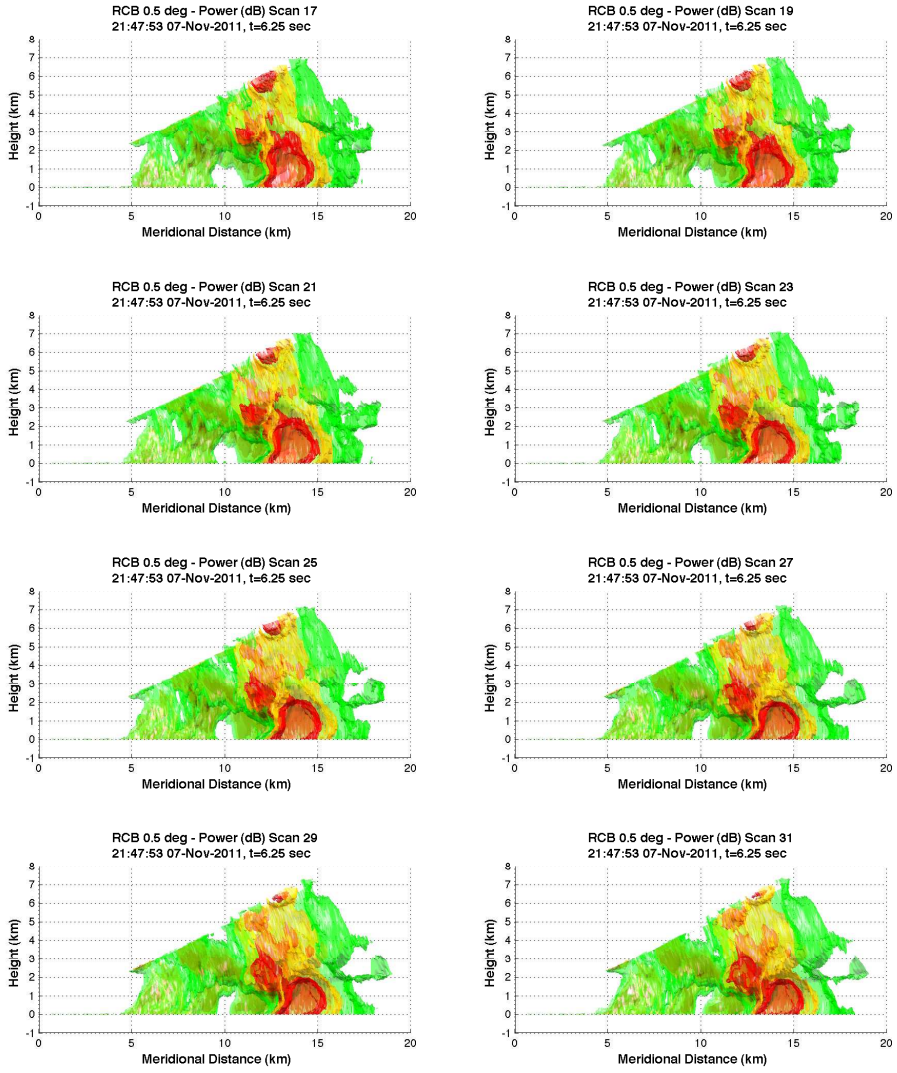

Figure 5.37: Part 2 of a series of images representing the return power recorded by the AIR on November 7, 2011 at 21:47:58 UTC. Green, yellow, and red isosurfaces represent power levels of -55, -50, and -45, respectively. A general motion from the updraft core arcing toward the forward flank is observed. Additionally, descending high reflectivity cores are observed in the forward flank.

echo enters from the far side of the sector. Some rotation is visible within the updraft core. Further, overshooting motion can be observed extending from the updraft arcing toward the forward flank. Descending reflectivity cores are also visible as time progresses.

The same weather event, but viewed from a different angle, is presented in Figures 5.38 and 5.39. From this angle, it is easier to see the forward arcing motion of the reflectivity core as it is lifted, pushed off-axis, and then descends in the forward flank. Sensitivity is again an issue with the data collection due to the 1-μs pulse. Significant losses are incurred through the rain core and eliminate returns beyond 20 km.

A series of PPI plots of the 0° elevation angle are presented in Figures 5.40 and 5.41. Data were not censored for this test. As the collection progresses, the hook echo appears within left edge of the sector. Attenuation is apparent when comparing the images to Figure 5.35. Despite this fact, the details of a highly dynamic section of a supercell are observable. The most interesting feature is a region of anticyclonic rotation that develops at the end of the scan at a meridional and zonal range of 12 and -3 km, respectively.

The associated radial velocity PPI images are presented in Figures 5.42 and 5.43. Velocity data were censored for 3 dB SNR to remove speckled data. A weak velocity couplet is visible at a range of a meridional distance of 12 km and a zonal distance of -3 km. Several other couplets develop and fade throughout the scans indicating the highly dynamic nature of this particular region of a supercell.

RHI images are also useful to examine in supercell cases and a series of images are presented in Figures 5.44 and 5.45, with the associated radial velocity images given in Figures 5.46 and 5.47. Interesting phenomena are observed at this particular azimuth angle including the arching reflectivity region between the updraft core and the forward flank and the rotating updraft itself. Again, attenuation

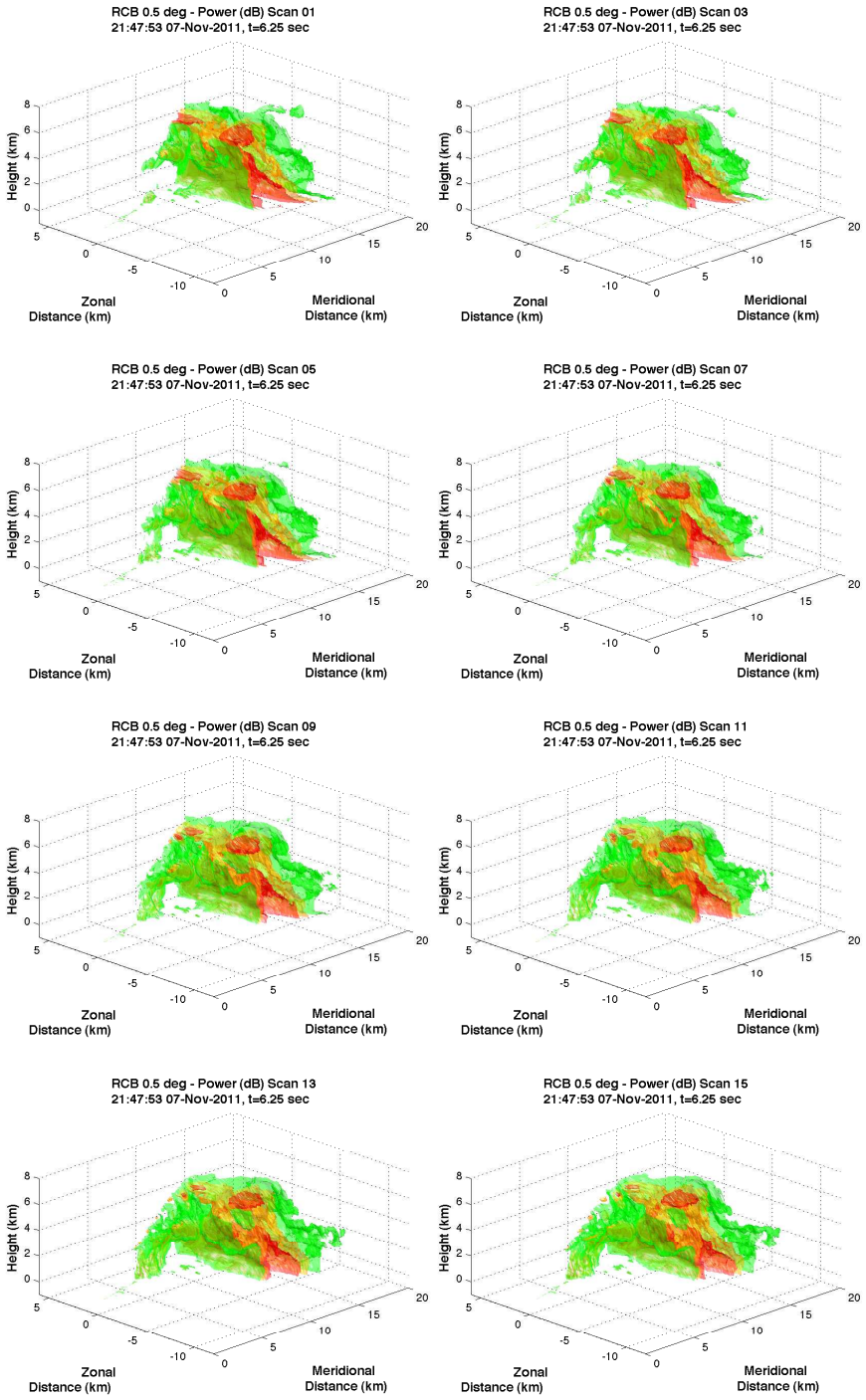

Figure 5.38: As in Figure 5.36 but viewed from the southeast looking toward the northwest from an elevated location. The arcing flow between the updraft core and the forward flank can be observed more readily through these images.

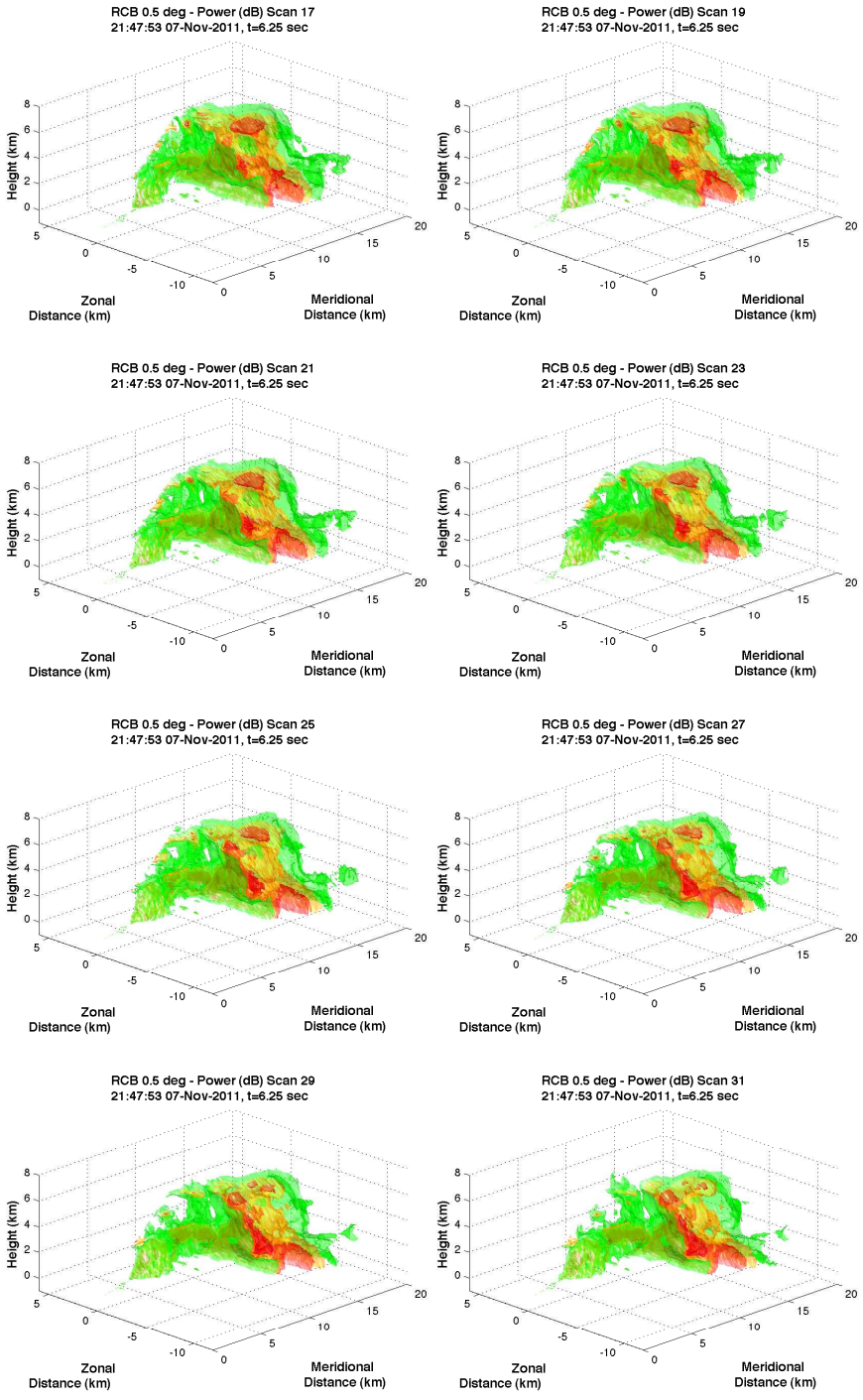

Figure 5.39: As in Figure 5.37 but viewed from the southeast looking toward the northwest from an elevated location.

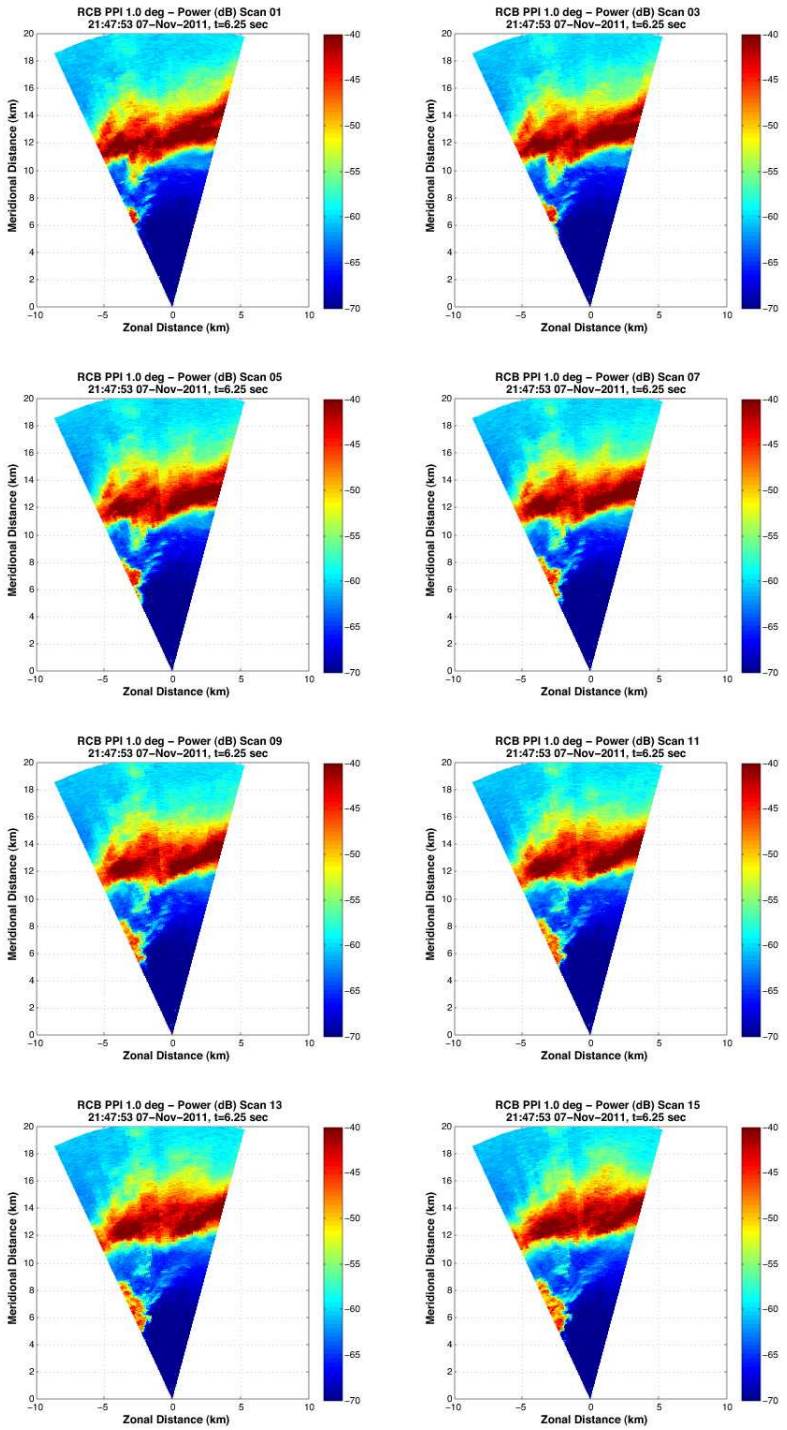

Figure 5.40: Part 1 of a series of PPI images representing the RCB return power recorded at 1° elevation by the AIR on November 7, 2011 at 21:47:58 UTC. The rotating updraft just begins to appear in the lower left side of the sector as the images progress.

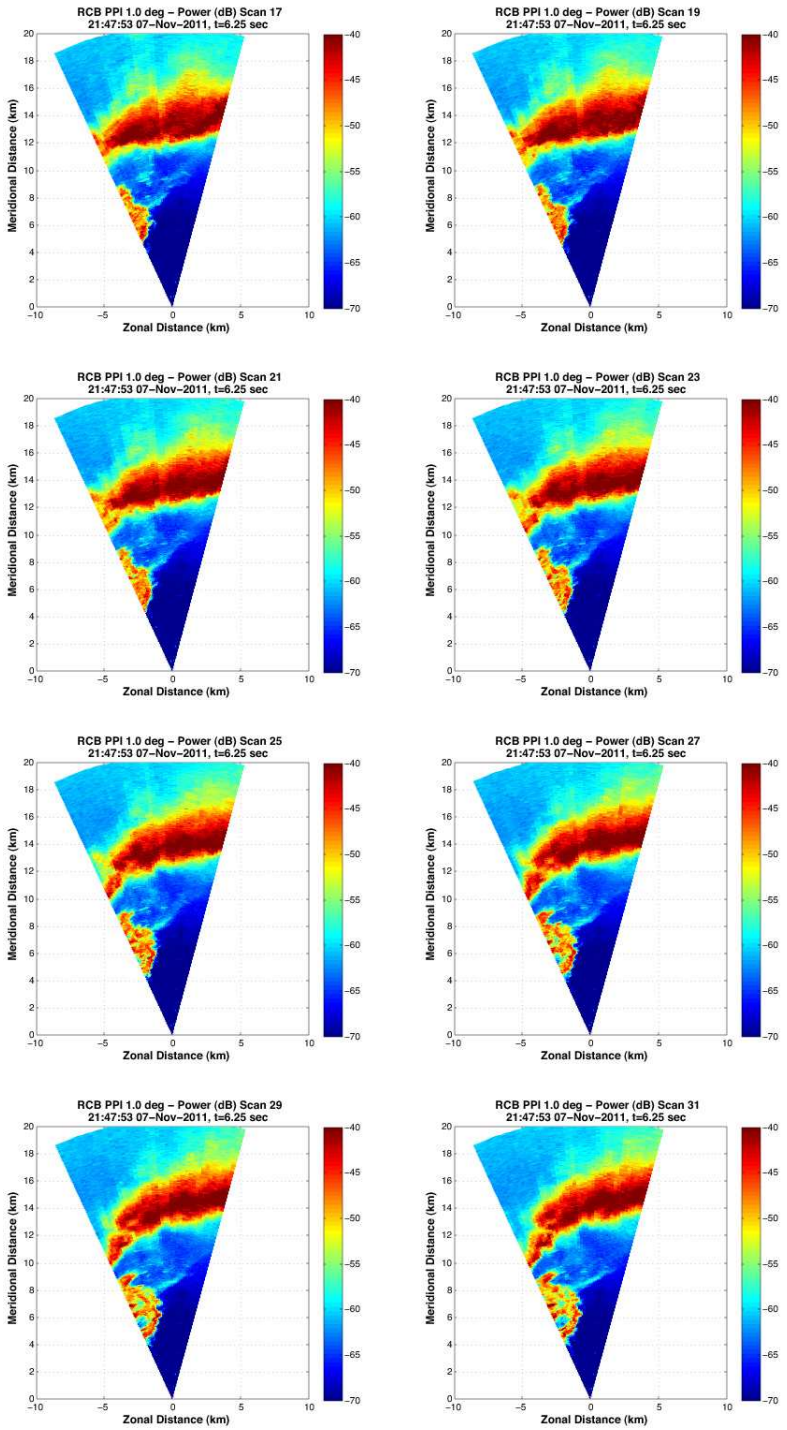

Figure 5.41: Part 2 of a series of PPI images representing the RCB return power recorded at 1° elevation by the AIR on November 7, 2011 at 21:47:58 UTC. The rotating updraft continues to progress into the sector FOV. Anticyclonic rotation is visible at 12 km in meridional range and -3 km in zonal.

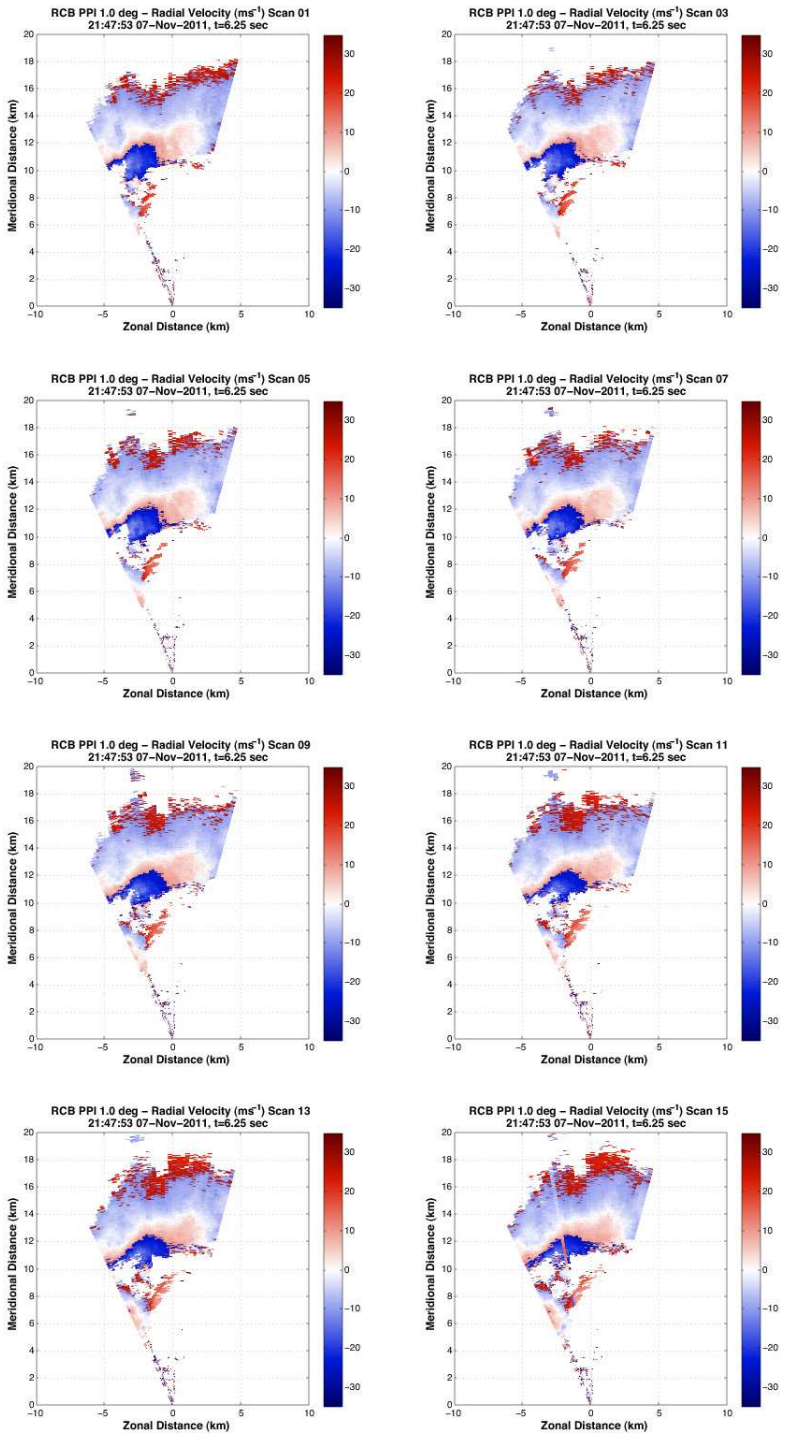

Figure 5.42: Part 1 of a series of PPI images representing the RCB radial velocity recorded at 1° elevation by the AIR on November 7, 2011 at 21:47:58 UTC. The central region of the sector indicates a highly dynamic region of the storm, with high positive and negative velocities in close proximity.

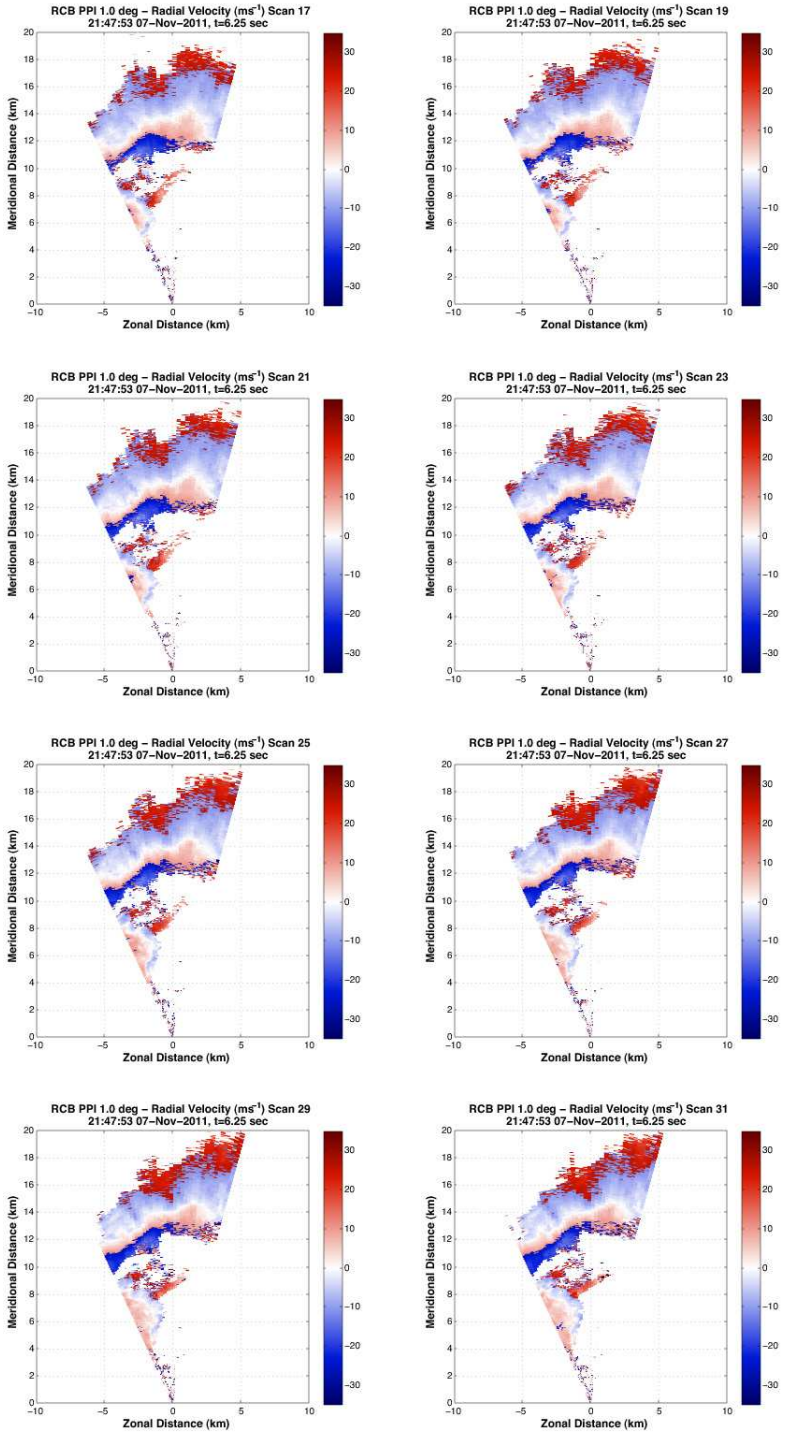

Figure 5.43: Part 2 of a series of PPI images representing the RCB radial velocity recorded at 1° elevation by the AIR on November 7, 2011 at 21:47:58 UTC. The region of anticyclonic rotation is not strong, but some shear in the negative range of velocities is visible at a meridional and zonal range of 12 and -3 km, respectively.

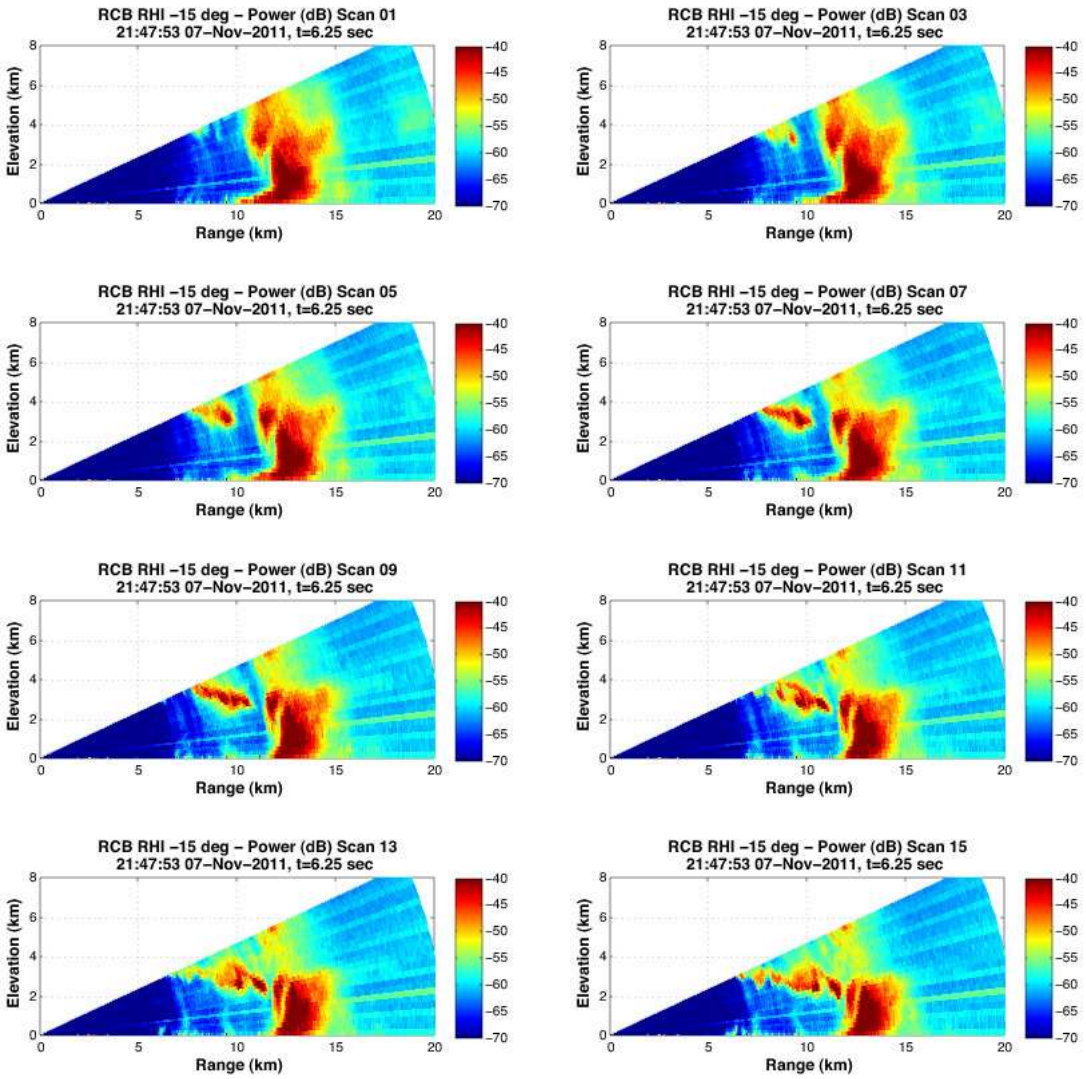

Figure 5.44: Part 1 of a series of RHI images representing the RCB return power recorded at -15° azimuth by the AIR on November 7, 2011 at 21:47:58 UTC. Bands of high reflectivity begin to appear at the upper levels and descend into the heavy rain core located at approximately 13 km in range. Some beamforming artifacts are visible beyond 15 km and appear as regularly spaced beams of elevated power. These artifacts can be removed by subtracting the DC offset.

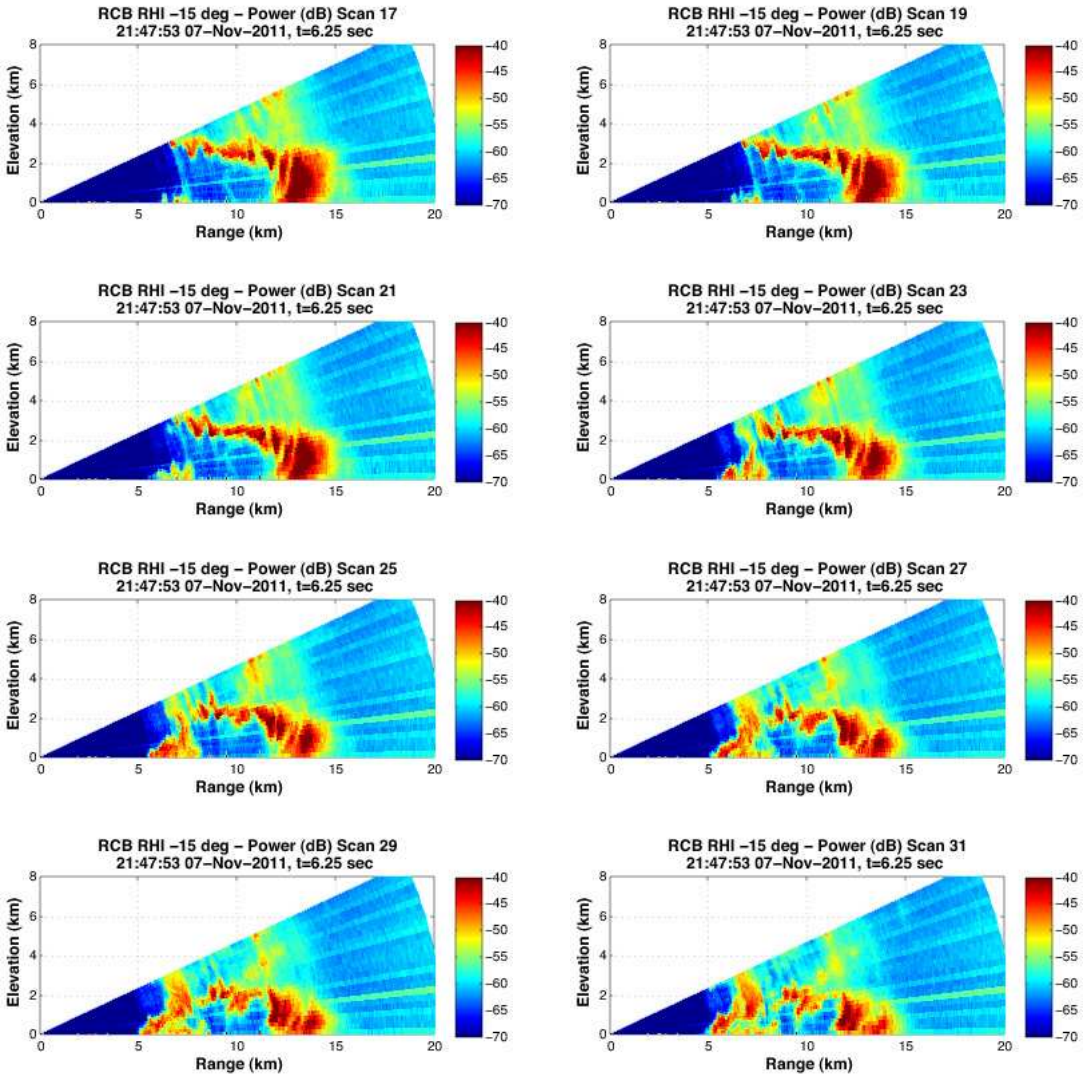

Figure 5.45: Part 2 of a series of RHI images representing the RCB return power recorded at -15° azimuth by the AIR on November 7, 2011 at 21:47:58 UTC. Bands of high reflectivity continue to move into the heavy rain core. The rotating updraft core begins to appear in the RHI plots at a range of 5 km.

and sensitivity issues prevent returns from being recorded past 15 km ranges. Beamforming artifacts are visible beyond the back edge of the storm (15 km) and appear as bands of elevated power, but can be removed by subtracting the DC offset.

Corresponding radial velocity RHI plots are given in Figures 5.46 and 5.47. Within the images, it is possible to identify several features typically associated with super cell storms. First, a region of high negative radial velocities at 10 km in range could represent the outflow boundary produced by the heavy rain in the forward flank. Next, as the wall of the rotating updraft enters the -15° azimuth, high positive radial velocities are observed indicating cyclonic rotation. Finally, after the boundary of the updraft has passed, lower radial velocities are observed, but with opposite polarity. This may indicate the mean motion is different between the near and far sides of the updraft, which would be expected.

The data presented in this section and chapter illustrate the basic capabilities of the AIR. Sensitivity is the primary concern moving forward and pulse compression will be necessary to achieve improved observations of environmental data. The temporal resolution is sufficient for most weather phenomena, even when mechanical azimuthal scanning is utilized. Staggered PRT algorithms are proven effective and are beneficial for storms like the November 7 supercell.

Through the course of the data collection during weather events and the subsequent analysis, influence of the grating lobes has not been observed. The existence has been confirmed by examining the beamforming output for the full $[-\pi, \pi]$ range and observing the aliased patterns. However, at no time has the upper grating lobe produced interference in the lower elevations of the AIR FOV. While this provides some optimism for future cases, it is not necessarily certain that the AIR is immune to grating lobe interference and methods of mitigation through alternative array spacing will be explored further via experimental analysis.

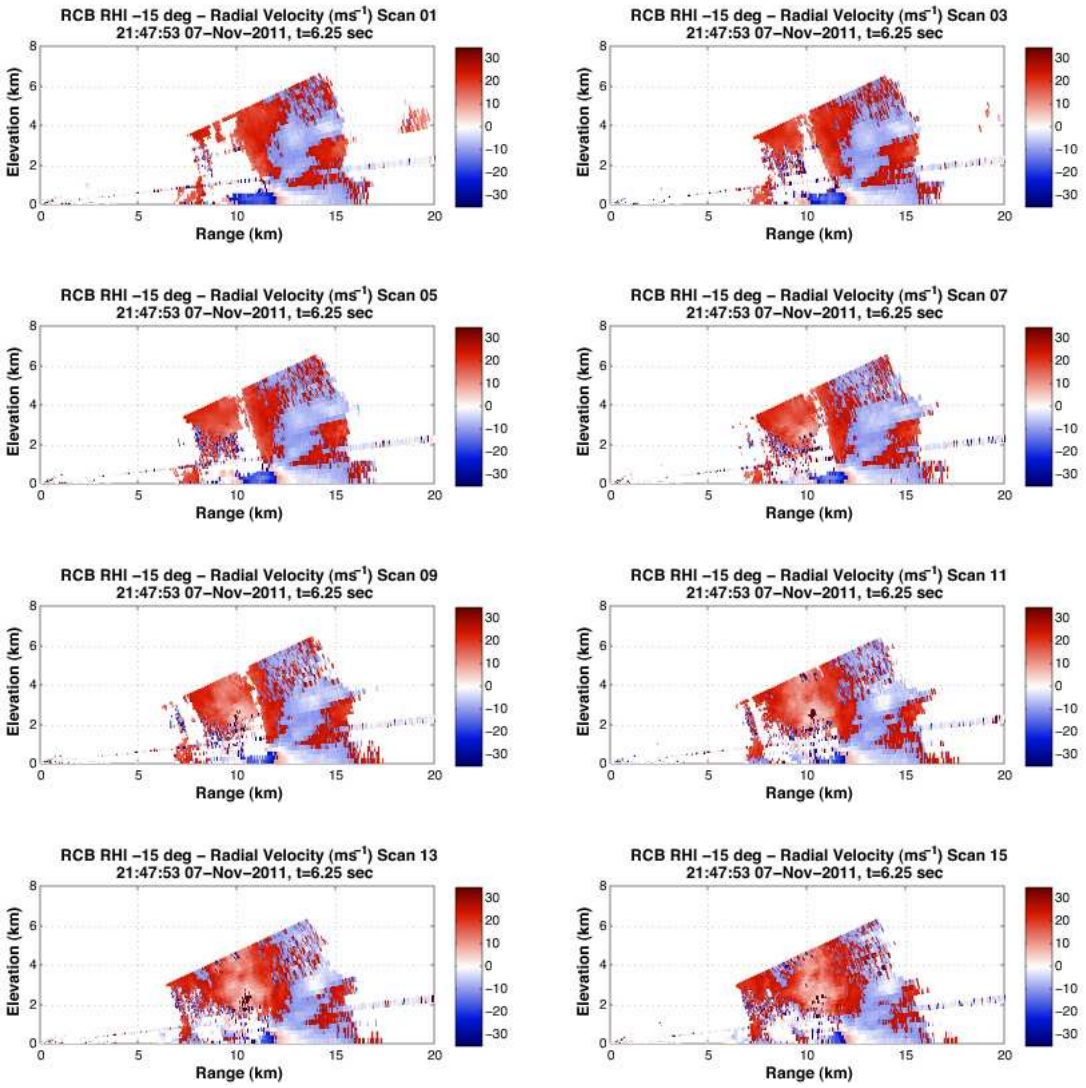

Figure 5.46: Part 1 of a series of RHI images representing the RCB radial velocity recorded at -15° azimuth by the AIR on November 7, 2011 at 21:47:58 UTC. Again the images illustrate the highly dynamic nature of supercell storms. A region of high negative velocity at 10 km could indicate significant convergence at the outflow from the forward flank.

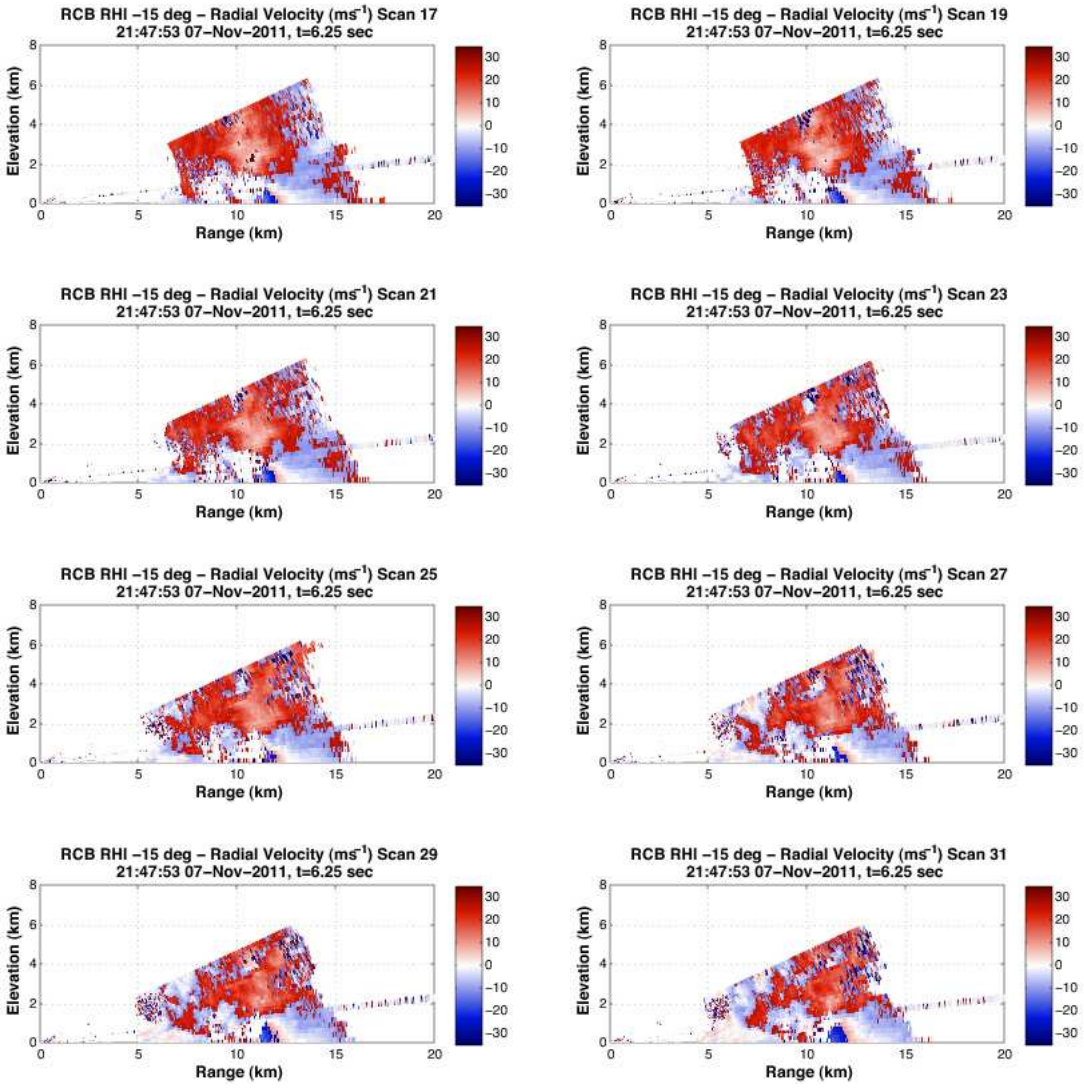

Figure 5.47: Part 2 of a series of RHI images representing the RCB radial velocity recorded at -15° azimuth by the AIR on November 7, 2011 at 21:47:58 UTC. In the final image, the rotating updraft contains an interesting feature in that the relatively low radial velocities are not constant in height and, in fact, reverse polarity. This perhaps suggests that the RHI scan is observing an inner portion of the updraft core.

Chapter 6

Conclusions and Suggestions for Future Work

The motivation behind this work was to explore the feasibility and capabilities of imaging technology for acquiring precipitation data for the study of high-impact severe weather. To facilitate the study, a mobile radar system was designed and constructed that incorporated 36 independent receive elements, which when combined through DBF, were able to produce infinite beams in the elevation axis both simultaneously and instantaneously. The FOV of the radar was defined by the transmit beam, which was narrow in the azimuthal direction and wide in the vertical dimension. Mechanical steering was employed to gather true volumetric data with a temporal resolution of 6 s. Pulse compression techniques were tested on point targets to regain some of the sensitivity lost due to the wide transmit beam.

Many DBF algorithms were utilized and compared, proving the versatility of the system. Analogies between the temporal and spatial domains were discussed and exploited. A calibration technique was also successfully implemented to achieve acceptable phase coherency base on the data alone, without the need to interrupt data collection. The AIR was designed to perform as a research platform and many additional DBF techniques, element spacing arrangements, waveform designs, and interesting phenomena are waiting to be tested.

Specific contributions to the field of radar meteorology were made in several areas. Overseeing the design and construction of the AIR was a significant effort and involved the coordination of many smaller teams. Interacting with the members of each group and ensuring the success of the project was a primary focus throughout the venture. Meteorological imaging radars of the past have typically focused on boundary layer or upper atmospheric phenomena. The AIR's primary focus is to collect precipitation data from severe weather. Applying well defined beamforming techniques, ranging from Fourier to adaptive algorithms like robust Capon and Amplitude and Phase Estimation (APES), to precipitation phenomena was a unique effort and has served to advance the use of adaptive array processing in radar meteorology. Exploration of irregular antenna spacing and drawing from the analogies between temporal and spatial processing led to the development of a technique that reduced the impact of grating lobes by unwrapping angular ambiguities. Ultimately, the author leaves having created a versatile platform capable of producing some of the highest resolution weather data available in the research community today, with opportunities to significantly advance the understanding of rapidly evolving weather phenomena and severe storms.

6.1 Conclusions

Over the coarse of this study, many DBF algorithms were tested and explored as viable options to produce high-resolution radar data. Non-parametric methods, such as Fourier and windowed Fourier beamforming provide accurate power estimates, but suffer from sidelobe leakage and poor resolution. Adaptive algorithms, such as Capon and RCB, provide some relief from the sidelobe issues and increase resolvability, however, the performance of such algorithms is degraded by the observation of distributed targets, like weather. Nevertheless, adaptive

techniques provide the best performance among the DBF choices by significantly reducing the impact of sidelobe interference.

Between the Capon and RCB techniques, RCB provides accurate power and angular estimates. A user defined search space mitigates uncertainties in the steering vector or minor calibration errors. Careful selection of the ϵ parameter must be applied to not degrade the performance of the RCB algorithm. A value too small will approach Capon performance, while a value too large will degrade the power distribution to the point of unsuitability.

A data-dependent calibration technique was discussed and successfully implemented. Images produced by the AIR closely resemble images produced from data gathered contemporaneously by nearby radar systems. Exploiting the spatial correlation between data collected by the array is a viable means of cohering the received signals. Minor errors in pointing angle are resultant from the technique, however, elevation angle offset values are simple to apply. Ground clutter targets provide a distinctive marker for the 0° elevation, though terrain variability must be considered and corrected for.

High temporal resolution is achieved through the simultaneous production of receive beams by the 36 channels. Images produced with 300 sample dwells are formed with resolutions of 0.33 s in a stationary 20° RHI mode. Mechanical scanning provides volumetric updates of a $40° \times 20°$ sector every 6 s. Given the extreme volume of data produced, the AIR is ideal for rapidly evolving phenomena such as tornados. Slowly evolving phenomena do not require high temporal resolution and thus do not benefit from the imaging system. However, the AIR was able to produce images of a mesocyclone case that displayed many dynamic features of supercell storms. It is this subset of weather that the AIR was designed to explore.

Pulse compression techniques were examined briefly on a radio tower to assess the feasibility of the implementation of complex transmit waveforms. The AIR was shown to be able to utilize the leakage from the transmitted signal to match-filter the receive data. Pulse compression will be necessary as was exhibited in the weather data retrievals. Sensitivity was significantly lower than expected and limits the distance with which the AIR can collect high quality data.

The AIR platform has proven to be a tool rich with possibilities for future research and development. Some suggestions for future experiments are discussed next.

6.2 Recommendations for Future Work

- The DBF algorithms discussed in this work merely scratch the surface of those that are available. MMSE and other adaptive techniques exist and can be explored with the AIR. Further, the irregular element spacing discussed theoretically in this work should be implemented with the radar. An assortment of inter-element spacings can be explored via the AIR.

- When mechanically scanning, the radar exhibits some inconsistencies in rotation rates depending on the direction of rotation. As a result, a *jitter* is visible when consecutive volume scans are viewed, despite recording the encoder output values and synching with the scan. Updates to the motor encoder would help to solve this problem, however, synchronization with the data recording software is a likely first step. By utilizing an extra trigger signal, the first pulse of the radar would be produced the exact instant the encoder began to produce values. This would provide a mechanism that might reduce some of the inconsistencies. If an encoder capable of producing azimuth information at the PRF, then the system would be able to remove

jitter by re-binning azimuth angles as needed. Further, a balance between smooth rotation and pointing accuracy is of fundamental importance for weather radar applications and is controlled by the servo amplifier gain parameters. Locating the appropriate balance between these parameters is essential. Finally, the gear backlash can have impacts on the repeatability of the scans and must be checked regularly to minimize pointing errors.

- Wind turbine clutter is a known issue for weather radar networks around the world. Two-dimensional imaging radar systems would be ideally suited to remove the interference produced by wind turbines due to the stationary nature of the FOV. The AIR could be used to explore the feasibility of wind turbine clutter mitigation by utilizing existing spotlight-mode wind turbine clutter mitigation techniques and examining the effectiveness in the presence of severe weather.

- In a similar manner, the multi-function capabilities of imaging systems should be explored. Due to the stationary transmit beam, weather and aircraft targets can be monitored simultaneously. Again, two-dimensional systems are better suited by the elimination of the need to mechanically steer the beam. The AIR can be used to test the multi-function capabilities in the RHI mode and exploring the use of multi-subset processing, which utilizes a particular number of temporal samples to observe weather phenomena (for ground clutter removal and sensitivity), and a different number for aircraft tracking. Testing to explore the feasibility of multi-function deployment should be undertaken.

- Multi-subset processing could also be utilized to improve the update times of strong target echoes by adaptively reducing the samples required for estimation given the strength of the signal from a particular angle. Weak

echoes could utilize very long sample lengths to improve sensitivity while sample sizes could be reduced for strong echoes. The goal is to equate the statistical performance across the resolution volume based on the SNR level.

- Pulse compression is a necessary functionality that will greatly improve the performance of the AIR. Initial tests have shown the feasibility, however, minor additions to the existing hardware would provide better matched filter performance through more accurate sampling of the transmitted waveform. The AIR provides an excellent testbed for the exploration of both temporal and spatial processing applications for remote sensing.

- Polarimetric capabilities of weather radar vastly improve the accuracy of the level-III products. Additionally, the microphysical knowledge gained by the use of dual-polarization radars is substantial. By combining the rapid update rates provided by the AIR with dual-pol capabilities, the AIR could produce new insights into the physical processes occurring within weather phenomena. Tornado debris signatures are also readily identified through the use of dual-pol radars and would be an ideal task for the AIR, which is interested in gathering severe storm data. An upgrade to the AIR antenna elements would facilitate an important gain in meteorological knowledge.

- Space-time adaptive processing (STAP) is a technique typically used to identify targets in clutter filled scenarios, where clutter can be due to the ground or jamming signals (Klemm 2002). The basic principles involve the processing of data in both time and space, utilizing the information in neighboring cells, to improve signal detection by the cancellation of clutter. STAP techniques can be implemented on the AIR platform with the goal of increasing the detectability of weather signals by exploiting the signal statistics of known clutter sources in both time and space.

- Finally, a new technique to extract dynamic parameters for weather modeling via radar data assimilation, called Entropic Balance Theory (EBT) provides another interesting application for imaging systems like the AIR (Sasaki et al. 2012). High temporal resolution data is a necessity for EBT in order to remove microphysical changes in a radar volume due to advection. If temporal resolution and measurement accuracy is high enough, changes in the radar reflectivity (with some assumptions regarding the hydrometeors themselves) can be associated with state changes of liquid water and, thus entropic values. While this is a new, somewhat radical idea, initial results show sufficient promise to continue pursuing further research.

Of course, the AIR should continue to be used as intended: an instrument capable of gathering high resolution data from high-impact, severe weather, like the example shown in Figure 6.1.

Figure 6.1: A photograph of an AIR deployment. A funnel cloud can be observed in the background of the image. Photograph provided by David Bodine.

Bibliography

Ahrens, C. D., 2007: *Meteorology Today: An Introduction to Weather, Climate, and the Environment*. Thomson Brooks/Cole, Belmont, CA.

Attia, E. H. and B. D. Steinberg, 1989: Self-Cohering Large Antenna Arrays Using the Spatial Correlation Properties of Radar Clutter. *IEEE Trans. Antenn. Propag.*, **37**, 30–38.

Battan, L. J., 1959: *Radar Observation of the Atmosphere*. Tech Books, Herndon, VA.

Best, W. H., 1973: Radars Over the Hump: Recollections of the First Weather Radar Network. *Bull. Amer. Meteor. Soc.*, **54**, 205–208.

Bharadwaj, N. and V. Chandrasekar, 2007: Phase coding for range ambiguity mitigation in dual-polarized doppler weather radars. *J. Atmos. Oceanic Technol.*, **24**, 1351–1363.

Biggerstaff, M. I., L. J. Wicker, J. Guynes, C. Ziegler, J. M. Straka, E. N. Rasmussen, A. D. IV, L. D. Carey, J. L. Schroeder, and C. Weiss, 2005: The Shared Mobile Atmospheric Research and Teaching Radar: A Collaboration to Enhance Research and Teaching. *Bull. Amer. Meteor. Soc.*, **86**, 1263–1274.

Bluestein, H., D. W. Burgess, D. Dowell, P. Markowski, E. Rasmussen, Y. Richardson, L. Wicker, and J. Wurman, 2009: VORTEX2: The Second Verification of the Origins of Rotation in Tornadoes Experiment. *5th European Conference on Severe Storms*, Landshut, Germany.

Bluestein, H. B., M. M. French, I. PopStefanija, R. T. Bluth, and J. B. Knorr, 2010: A Mobile, Phased-Array Doppler Radar for the Study of Severe Convective Storms: The MWR-05XP. *Bull. Amer. Meteor. Soc.*, **91**, 579–600.

Bluestein, H. B., S. G. Gaddy, D. C. Dowell, A. L. Pazmany, J. C. Galloway, R. E. McIntosh, and H. Stein, 1997: Doppler Radar Observations of Substorm-Scale Vortices in a Supercell. *Mon. Weather Rev.*, **125**, 1046–1059.

Bodine, D., R. D. Palmer, B. Isom, and B.-L. Cheong, 2009: A New Frontier for Mobile Weather Radar—The Atmospheric Imaging Radar: Meteorological Implications and Requirements. *34th Conference on Radar Meteorology*, AMS, Williamsburg, VA.

Bohren, C. and D. Huffman, 1983: *Absorption and Scattering of Light by Small Particles*. John Wiley and Sons.

Bringi, V. N. and V. Chandrasekar, 2001: *Polarimetric Doppler Weather Radar: Principles and Applications*. Cambridge University Press.

Brookner, E., 1964: Multidimensional Ambiguity Functions of Linear, Interferometer, Antenna Arrays. *IEEE Trans. Antenn. Propag.*, **12**, 551–561.

Brown, R. A. and J. M. Lewis, 2005: Path to NEXRAD: Doppler Radar Development at the National Severe Storms Laboratory. *Bull. Amer. Meteor. Soc.*, **86**, 1459–1470.

Cao, Q., G. Zhang, E. A. Brandes, and T. J. Schuur, 2010: Polarimetric Radar Rain Estimation through Retrieval of Drop Size Distribution Using a Bayesian Approach. *J. Appl. Meteorol. Climatol.*, **49**, 973–990.

Cao, Q., G. Zhang, R. Palmer, and L. Lei, 2011: A new identification and mitigation algorithm for second trip contamination. *Radar Conference (RADAR), 2011 IEEE*, IEEE, 729–733.

Capon, J., 1969: High-Resolution Frequency-Wavenumber Spectrum Analysis. *Proc. IEEE*, **57**, 1408–1418.

Chan, Y. K., M. Y. Chua, and V. C. Koo, 2009: Sidelobes Reductino Using Simple Two and Tri-Stages Non Linear Frequency Modulation (NLFM). *J. Progress In Electromagnetics Research*, **98**, 33–52.

Cheong, B.-L., M. W. Hoffman, R. D. Palmer, S. J. Fraiser, and F. J. Lopez-Dekker, 2004: Pulse Pair Beamforming and the Effects of Reflectivity Field Variations on Imaging Radars. *Radio Sci.*, **39**, 1–13.

Cheong, B. L., M. W. Hoffman, R. D. Palmer, S. J. Frasier, and F. J. Lopez-Dekker, 2006: Phased-Array Design for Biological Clutter Rejection: Simulation and Experimental Validation. *J. Atmos. Oceanic Technol.*, **23**, 585–598.

Cook, C. E., 1964: A Class of Nonlinear FM Pulse Compression Signals. *Proc. IEEE*, **52**, 1369–1371.

Crum, T. D. and R. L. Alberty, 1993: The WSR-88D and the WSR-88D Operational Support Facility. *Bull. Amer. Meteor. Soc.*, **74**, 1669–1687.

Crum, T. D., R. L. Alberty, and D. W. Burgess, 1993: Recording, Archiving, and Using WSR-88D Data. *Bull. Amer. Meteor. Soc.*, **74**, 645–53.

Doerry, A. W., 2006: Generating Nonlinear FM Chirp Waveforms for Radar. Report SAND2006-5856, Sandia National Laboratories, Albuquerque, NM.

Doviak, R., V. Bringi, A. Ryzhkov, A. Zahrai, and D. Zrnic, 2000: Considerations for Polarimetric Upgrades to Operational WSR-88D Radars. *J. Atmos. Oceanic Technol.*, **17**, 257–278.

Doviak, R. J. and D. Sirmans, 1973: Doppler Radar with Polarization Diversity. *J. Atmos. Sci.*, **30**, 737–738.

Doviak, R. J. and D. S. Zrnić, 1993: *Doppler Radar and Weather Observations*. Accademic Press, San Diego, CA, second edition.

Dunlap Jr., O. E., 1946: *Radar: What Radar is and How It Works*. Harper and Brothers, New York, NY, 2nd edition.

Farley, D., 1969a: Faraday Rotation Measurements Using Incoherent Scatter. *Radio Sci.*, **4**, 143–152.

— 1969b: Incoherent Scatter Correlation Function Measurements. *Radio Sci.*, **4**, 935–953.

Farley, D., DT, H. Ierkic, and B. Fejer, 1981: Radar Interferometry - A New Technique for Studying Plasma Turbulence in the Ionosphere. *J. Geophys. Res.-Space*, **86**, 1467–1472.

Forsyth, D. E., J. F. Kimpel, D. S. Zrnic, S. Sandgathe, R. Ferek, J. F. Heimmer, T. McNellis, J. E. Crain, A. M. Shapiro, J. D. Belville, and W. Benner, 2002: The National Weather Radar Testbed (Phased-Array). *18th International Conference on Interactieve Information and Processing Systems (IIPS)*, American Metr. Soc, Orlando,Fla, 140–141.

Fowle, E., 1964: The Design of FM Pulse Compression Signals. *IEEE Trans. Information Theory*, **10**, 61–67.

Fukao, S., 2007: Recent Advances in Atmospheric Radar Study. *J. Meteorol. Soc. Jpn.*, **85B**, 215–239.

Fukao, S., S. Kato, T. Aso, M. Sasada, and T. Makihira, 1980a: Middle and Upper-Atmosphere Radar (MUR) Under Design in Japan. *Radio Sci.*, **15**, 225–231.

Fukao, S., S. Kato, S. Yokoi, R. Harper, R. Woodman, and W. Gordon, 1978: One Full-Day Radar Measurement of Lower Stratospheric Winds Over Jicamarca. *J. Atmos. Terr. Phys.*, **40**, 1331–1337.

Fukao, S., T. Sato, N. Yamasaki, R. Harper, and S. Kato, 1980b: Radar Measurement of Tidal Winds at Stratospheric Heights Over Arecibo. *J. Atmos. Sci.*, **37**, 2540–2544.

Fukao, S., K. Wakasugi, T. Sato, S. Morimoto, T. Tsuda, I. Hirota, I. Kimura, and S. Kato, 1985: Direct Measurement of Air and Precipitation Particle Motion by Very High-Frequency Doppler Radar. *Nature*, **316**, 712–714.

Gage, K., C. Williams, and W. Ecklund, 1994: UHF Wind Profilers - A New Tool for Diagnosing Tropical Convective Cloud Systems. *Bull. Amer. Meteor. Soc.*, **75**, 2289–2294.

Hubbert, J., V. N. Bringi, L. D. Carey, and S. Bolen, 1998: CSU-CHILL Polarimetric Radar Measurements from a Severe Hail Storm in Eastern Colorado. *J. Appl. Meteorol.*, **37**, 749–775.

Hysell, D. L. and R. F. Woodman, 1997: Imaging Coherent Backscatter Radar Observations of Topside Equatorial Spread F. *Radio Sci.*, **32**, 2309–2320.

Ishimaru, A., 1997: *Wave Propagation and Scattering in Random Media*. IEEE Press.

Isom, B., R. Palmer, R. Kelley, J. Meier, D. Bodine, M. Yeary, B.-L. Cheong, Y. Zhang, T.-Y. Yu, and M. Biggerstaff, 2011: The atmospheric imaging radar (air) for high-resolution observations of severe weather. *Radar Conference (RADAR), 2011 IEEE*, IEEE, 627 – 632.

Jakobsson, A. and P. Stoica, 2000: Combining Capon and APES for Estimation of Spectral Lines. *Circuits Systems Signal Processing*, **19**, 159–169.

Jarske, P., T. Saramaki, S. K. Mitra, and Y. Neuvo, 1988: On Properties and Design of Nonuniformly Spaced Linear Arrays. *IEEE Trans. Acoust. Speech*, **36**, 372–380.

Joss, J., J. C. Thams, and A. Waldvogel, 1968: The Variation of Raindrop Size Distributions at Locarno. *Proc. Int. Conf. Cloud Physics*, 369–373.

Klemm, R., 2002: *Principles of Space-Time Adaptive Processing*. The Institution of Electrical Engineers, London, United Kingdom.

Kudeki, E. and F. Sürücü, 1991: Radar Interferometric Imaging of Field-Aligned Plasma Irregularities in the Equatorial Electrojet. *Geophysical Research Letters*, **18**, 41–44.

Kumar, B. P. and G. R. Branner, 1999: Design of Unequally Spaced Arrays for Performance Improvement. *IEEE Trans. Antenn. Propag.*, **47**, 511–523.

— 2005: Generalized Analytical Technique for the Synthesis of Unequally Spaced Arrays with Linear, Planar, Cylindrical or Spherical Geometry. *IEEE Trans. Antenn. Propag.*, **53**, 621–634.

Kumjian, M. R., A. Ryzhkov, V. Melnikov, and T. J. Schuur, 2010: Rapid-Scan Super-Resolution Observations of a Cyclic Supercell with a Dual-Polarization WSR-88D. *Mon. Weather Rev.*, **138**, 3762–3786.

Kurdzo, J. M., J. B. Meier, R. D. Palmer, B.-L. Cheong, and G. Zhang, 2012: Pulse Compression Observations Using the Rapid X-Band Dual-Polarimetric (RaXpol) Mobile Radar. *Extended Abstracts, 28th Conference on IIPS*, AMS, New Orleans, LA.

Laws, J. O. and D. A. Parsons, 1943: The Relation of Raindrop-size to Intensity. *Trans. Amer. Geophys. Union*, **24**, 452–460.

Le, K. D., R. D. Palmer, B.-L. Cheong, T.-Y. Yu, G. Zhang, and S. M. Torres, 2009: On the Use of Auxiliary Receive Channels for Clutter Mitigation With Phased Array Weather Radars. *IEEE Trans. Geosci. Remote Sens.*, **47**, 272–284.

Lei, L., G. Zhang, R. D. Palmer, B. L. Cheong, M. Xue, and Q. Cao, 2009: A multi-lag correlation estimator for polarimetric radar variables in the presence of noise. *34th Conference on Radar Meteorology*, Amer. Meteor. Soc.

Leone, D. A., R. M. Endlich, J. Petričeks, R. T. H. Collis, and J. R. Portert, 1989: Meteorological Considerations Used in Planning the NEXRAD Network. *Bull. Amer. Meteor. Soc.*, **70**, 4–13.

Li, J. and P. Stoica, 1996: An Adaptive Filtering Approach to Spectral Estimation and SAR Imaging. *IEEE Trans. Sig. Proc.*, **44**, 1469–1484.

— 2006: *Robust Adaptive Beamforming*. Wiley-Interscience, Hoboken, New Jersey.

Li, J., P. Stoica, and Z. Wang, 2003: On Robust Capon Beamforming and Diagonal Loading. *IEEE Trans. Sig. Proc.*, **51**, 1702–1715.

Mahafza, B. R., 2000: *Radar Systems Analysis and Design Using MATLAB*. Chapman & Hall, Boca Raton, FL.

Marshall, J. S. and W. Palmer, 1948: The Distribution of Raindrops with Size. *J. Meteorol.*, **5**, 165–166.

Martner, B., D. Wuertz, B. Stankov, R. Strauch, E. Westwater, K. Gage, W. Ecklund, C. Martin, and W. Dabberdt, 1993: An Evaluation of Wind Profiler, RASS, and Microwave Radiometer Performance. *Bull. Amer. Meteor. Soc.*, **74**, 599–613.

Mead, J. B., G. Hopcraft, S. J. Frasier, B. D. Pollard, C. D. Cherry, and D. H. Schaubert, 1998: A Volume-Imaging Radar Wind Profiler for Atmospheric Boundary Layer Turbulence Studies. *J. Atmos. Oceanic Technol.*, **15**, 849–859.

Meier, J., R. Kelley, B. Isom, M. Yeary, and R. Palmer, 2012: Leveraging software defined radio techniques for digital weather radar receiver design. *IEEE Trans. Instrum Measure*, **61**, 1571–1582.

Meischner, P., 2004: *Weather Radar: Principles and Advanced Applications*. Springer, New York, NY.

Melnikov, V. M., R. J. Doviak, D. S. Zrnić, and D. J. Stensrud, 2011: Mapping Bragg Scatter with a Polarimetric WSR-88D. *J. Atmos. Oceanic Technol.*, **28**, 1273–1285.

Metzger, R. S., C. C. Weiss, and A. E. Reinhart, 2011: An Examination of the Structure of Three Tornadoes Using High-Frequency Ka-Band Mobile Doppler Radar. *35th Conference on Radar Meteorology*, Amer. Meteor. Soc., Pittsburgh, PA.

Mie, G., 1908: Contribution to the Optics of Suspended Media, Specifically Colloidal Metal Suspensions. *Ann. Phys.*, 377–445.

Millett, R. E., 1970: A Matched-Filter Pulse-Compression System Using a Nonlinear FM Waveform. *IEEE Trans. Aerosp. Electron. Syst.*, **6**, 73–78.

Mitra, S. K., 2006: *Digital Signal Processing: A Computer Based Approach*. McGraw Hill, New York, NY, third edition.

Oguchi, T., 1983: Electromagnetic Wave Propagation and Scattering in Rain and Other Hydrometeors. *Proc. IEEE*, **71**, 1029–1073.

Palmer, R., M. Larsen, P. Howell, J. Cho, R. Narayanan, and M. Kelley, 1997: A New Spatial Interferometry Capability Using the Arecibo 430-MHz Radar. *Radio Sci.*, **32**, 749–755.

Palmer, R. D., B. L. Cheong, M. W. Hoffman, S. J. Frasier, and F. J. Lopez-Dekker, 2005: Observations of the Small-Scale Variability of Precipitation Using and Imaging Radar. *J. Atmos. Oceanic Technol.*, **22**, 1122–1137.

Palmer, R. D., S. Gopalam, T.-Y. Yu, and S. Fukao, 1998: Coherent Radar Imaging Using Capon's Method. *Radio Sci.*, **33**, 1585–1598.

Palmer, R. D., R. Woodman, S. Fukao, T. Tsuda, and S. Kato, 1990: Three-Antenna Poststatistic Steering Using the MU Radar. *Radio Sci.*, **25**, 1105–1110.

Palmer, R. D., T.-Y. Yu, and P. B. Chilson, 1999: Range Imaging Using Frequency Diversity. *Radio Sci.*, **34**, 1485–1496.

Pazmany, A. L. and H. B. Bluestein, 2009: Mobile Rapid Scanning X-band Polarimetric (RaXpol) Doppler Radar System. *34th Conference on Radar Meteorology*, Amer. Meteor. Soc., Williamsburg, VA.

Pozar, D. M., 2005: *Microwave Engineering*. John Wiley and Sons, Third edition.

Ray, P. S., 1972: Broad-band Complex Refractive Indexes of Ice and Water. *Applied Optics*, **11**, 1836–1844.

Ray, P. S., R. J. Doviak, G. B. Walker, D. Sirmans, J. Carter, and B. Bumgarner, 1975: Dual-Doppler Observations of a Tornadic Storm. *J. Appl. Meteorol.*, **14**, 1521–1530.

Richards, M. A., 2005: *Fundamentals of Radar Signal Processing*. McGraw Hill, Chigaco, IL.

Rogers, R., W. Ecklund, D. Carter, K. Gage, and S. Ethier, 1993: Research Applications of a Boundary-Layer Wind Profiler. *Bull. Amer. Meteor. Soc.*, **74**, 567–580.

Rogers, R. R. and M. K. Yau, 1989: *A Short Course in Cloud Physics*. Butterworth-Heinemann, third edition.

Röttger, J. and H. Ierkic, 1985: Postset Beam Steering and Interferometer Applications of VHF Radars to Study Winds, Waves, and Turbulence in the Lower and Middle Atmosphere. *Radio Sci.*, **20**, 1461–1480.

Rüster, R. and P. Czechowsky, 1980: VHF Measurements During a Jet Stream Passage. *Radio Sci.*, **15**, 363–369.

Ryzhkov, A., S. E. Giangrande, and T. J. Schuur, 2005: Rainfall Estimation with a Polarimetric Prototype of WSR-88D. *J. Appl. Meteorol.*, **44**, 502–515.

Ryzhkov, A. V. and D. S. Zrnić, 1994: Precipitation Observed in Oklahoma Mesoscale Convective Systems with a Polarimetric Radar. *J. Appl. Meteorol.*, **33**, 455–464.

Sachidananda, M. and D. S. Zrnić, 1999: Systematic Phase Codes for Resolving Range Overlaid Signals in a Doppler Weather Radar. *J. Atmos. Oceanic Technol.*, **16**, 1351–1363.

Sasaki, Y., M. Kumjian, and B. Isom, 2012: Entropic Balance Theory and Radar Observation for Prospective Tornado Data Assimilation. *Data Assimilation for Atmospheric, Oceanic and Hydrological Applications*, S. K. Park and L. Xu, eds., Springer, volume 2, chapter Accepted.

Scharfenberg, K. A., D. J. Miller, T. J. Schuur, P. T. Schlatter, S. E. Giangrande, V. M. Melnikov, D. W. Burgess, D. L. Andra, M. P. Foster, and J. M. Krause, 2005: The Joint Polarization Experiment: Polarimetric Radar in Forecasting and Warning Decision Making. *Weather Forecasting*, **20**, 775–788.

Schwarz, C. M. and D. W. Burgess, 2010: Verification of the Origins of Rotation in Tornadoes Experiment, Part 2(VORTEX2): Data from the NOAA (NSSL) X-Band Dual-Polarized Radar. *25th Conference on Severe Local Storms*, Amer. Meteor. Soc., Denver, CO.

Seliga, T. A. and J. B. Mead, 2009: Meter-Scale Observations of Aircraft Wake Vorticies in Preceipitation Using a High-Resolution Solid-State W-Band Radar. *34th Conference on Radar Meteorology*, Amer. Meteor. Soc., Williamsburg, VA.

Shanmugan, K. S. and A. M. Breipohl, 1988: *Random Signals: Detection, Estimation, and Data Analysis*. John Wiley and Sons, USA.

Sinsky, A. I. and C. P. Wang, 1974: Standardization of the Definition of the Radar Ambiguity Function. *IEEE Trans. Aerosp. Electron. Syst.*, **AES-10**, 532–533.

Sirmans, D. and R. J. Doviak, 1973: Pulsed-Doppler Velocity Isotach Displays of Storm Winds in Real Time. *J. Appl. Meteorol.*, **12**, 694–697.

Skolnik, M. I., 2001: *Introduction to Radar Systems*. McGraw Hill, Dubuque, IA, 3rd edition.

Smith, N., 2011: "Weather Radar Shutdown Imminent", The Williston Hearld [Williston, ND], November 18, 2011.

Stoica, P., H. Li, and J. Li, 1999: A New Derivation of the APES Filter. *IEEE Sig. Proc. Letter*, **6**, 205–206.

Stoica, P. and R. Moses, 2005: *Spectral Analysis of Signals*. Pearson Education, Inc., Upper Saddle River, New Jersey.

Strauch, R. G., D. A. Merritt, K. P. Moran, K. B. Earnshaw, and D. van de Kamp, 1984: The Colorado Wind-Profiling Network. *J. Atmos. Oceanic Technol.*, **1**, 37–49.

Sürücü, F., P. M. Franke, and E. Kudeki, 1992: On the Use of Software Beam Synthesis in Multiple-Receiver MF Radar Wind Estimation. *Radio Sci.*, **27**, 775–782.

Tabary, P., F. Guibert, L. Perier, and J. P. du Chatelet, 2006: An operational triple-prt doppler scheme for the french radar network. *J. Atmos. Oceanic Technol.*, **23**, 1645–1656.

Torres, S. M., Y. F. Dubel, and D. S. Zrnić, 2004: Design, implementation and demonstration of a staggered prt algorithm for the wsr-88d. *J. Atmos. Oceanic Technol.*, **21**, 1389–1399.

Ulbrich, C. W., 1983: Natural Variations in the Analytical Form of the Raindrop Size Distribution. *J. Climate Appl. Meteorol.*, **22**, 1764–1775.

van de Hulst, H. C., 1957: *Light Scattering by Small Particles*. John Wiley and Sons.

Venkatesh, V., S. Palreddy, A. Hopf, K. Hardwick, P.-S. Tsai, and S. J. Frasier, 2008: The UMass X-Pol Mobile Doppler Radar: Description, Recent Observations, and New System Developments. *Geoscience and Remote Sensing Symposium, 2008.*, IEEE, Boston, MA, volume 5, 101–104.

Wallace, J. M. and P. V. Hobbs, 1977: *Atmospheric Science: An Introductory Survey*. Academic Press, San Diego, CA, 1st edition.

Warde, D., S. Torres, and B. Gallardo, 2011: Spectral Processing and Ground Clutter Mitigationfor Dual-Polarization Staggered PRT Signals in Doppler Weather Radars. *Extended Abstracts, 34th Conference on Radar Meteorology*, Amer. Meteor. Soc., Pittsburgh, PA.

Weiss, C. C., J. L. Schroeder, J. Guynes, P. Skinner, and J. Beck, 2009: The TTUKa Mobile Doppler Radar: Coordinated Radar and In-Situ Measurements of Supercell Thunderstorms During Project VORTEX2. *34th Conference on Radar Meteorology*, Amer. Meteor. Soc., Williamsburg, VA.

Whiton, R., P. Smith, S. Bigler, K. Wilk, and A. Harbuck, 1998a: History of Operational Use of Weather Radar by US Weather Services. Part I: The Pre-NEXRAD Era. *Weather Forecasting*, **13**, 219–243.

— 1998b: History of Operational Use of Weather Radar by US Weather Services. Part II: Development of Operational Doppler Weather Radars. *Weather Forecasting*, **13**, 244–252.

Woodman, R., D. Sterling, and W. Hanson, 1972: Synthesis of Jicamarca Data During Great Storm of March 8, 1970. *Radio Sci.*, **7**, 739–746.

Woodman, R. F., O. Castillo, G. Michhue, P. Reyes, and S. Villegas, 2003: SOUSY Radar at Jicamarca: System Description. *Tenth International Workshop on Technical and Scientific Aspects of MST Radar*, Piura, Perú, volume 44.

Wurman, J. and M. Randall, 2001: An Inexpensive, Mobile, Rapid-Scan Radar. *30th Int. Conf. on Radar Meteor.*, Munich, Germany.

Wurman, J., J. Straka, E. Rasmussen, M. Randall, and A. Zahari, 1997: Design and Deployment of a Portable, Pencil-Beam, Pulsed, 3-cm Doppler Radar. *J. Atmos. Oceanic Technol.*, **14**, 1502–1512.

Wurman, J. M., 2005: Keynote Talk: A Mobile Rapid-Scan Radar: The Quest for Finer and Balanced Temporal and Spatial Scale Observations. *Extended Abstracts, 32nd Conference on Radar Meteorology*, AMS, Albuquerque, NM.

Yeary, M. B., G. Crain, R. Kelley, J. Meier, R. D. Palmer, T.-Y. Yu, A. Zahari, I. Ivic, and R. J. Doviak, 2011: Phased Array Weather/Multipurpose Radar. *IEEE Aerosp. Electron. Syst. Mag.*, **26**, 12–15.

Yu, T.-Y., M. B. Orescanin, C. D. Curtis, D. S. Zrnić, and D. E. Forsyth, 2007: Beam Multiplexing Using the Phased-Array Weather Radar. *J. Atmos. Oceanic Technol.*, **24**, 616–626.

Zhang, G., R. J. Doviak, J. Vivekanandan, W. O. J. Brown, and S. A. Cohn, 2004: Performance of Correlation Estimators for Spaced-Antenna Wind Measurements in the Presence of Noise. *Radio Sci.*, **39**.

Zhang, G., J. Sun, and E. A. Brandes, 2006: Improving Parameterization of Rain Microphysics with Disdrometer and Radar Observations. *J. Atmos. Sci.*, **63**, 1273–1290.

Zhang, G., J. Vivekanandan, and E. A. Brandes, 2001: A Method for Estimating Rain Rate and Drop Size Distribution from Polarimetric Radar Measurements. *IEEE Geosci. Remote S.*, **39**, 830–841.

Zhang, G. F., R. J. Doviak, D. S. Zrnić, R. Palmer, L. Lei, and Y. Al-Rashid, 2011: Polarimetric Phased-Array Radar for Weather Measurement: A Planar or Cylincrical Configuration? *J. Atmos. Oceanic Technol.*, **28**, 63–73.

Zrnić, D. S., 1975: Simulation of weatherlike Doppler spectra and signals. *J. Appl. Meteorol.*, **14**, 619–620.

Zrnić, D. S. and R. J. Doviak, 1975: Velocity Spectra of Vortices Scanned with a Pulsed-Doppler Radar. *J. Appl. Meteorol.*, **14**, 1531–1539.

Zrnić, D. S., J. F. Kimpel, D. E. Forsyth, A. Shapiro, G. Crain, R. Ferek, J. Heimmer, W. Benner, T. J. McNellis, and R. J. Vogt, 2007: Agile-Beam Phased Array Radar for Weather Observations. *Bull. Amer. Meteor. Soc.*, **88**, 1753–1766.

Appendix A - Refractive Index of Water and Ice

Here a discussion of the complex refractive index associated with both liquid water and solid ice is given based on the work done by Ray (1972).

Recall that m is the complex refractive index and that it is a function of temperature and wavelength through the following relation with the complex dielectric constant:

$$m^2 = \varepsilon_r = \varepsilon' + i\varepsilon''.$$

The complex dielectric for water is calculated from the following set of equations:

$$\begin{aligned}
\varepsilon' &= \varepsilon_\infty + \frac{(\varepsilon_s - \varepsilon_\infty)[1 + (\lambda_s/\lambda)^{1-\alpha}\sin(\alpha\pi/2)]}{1 + 2(\lambda_s/\lambda)^{1-\alpha}\sin(\alpha\pi/2) + (\lambda_s/\lambda)^{2(1-\alpha)}}, \\
\varepsilon'' &= \frac{(\varepsilon_s - \varepsilon_\infty)(\lambda_s/\lambda)^{1-\alpha}\cos(\alpha\pi/2)}{1 + 2(\lambda_s/\lambda)^{1-\alpha}\sin(\alpha\pi/2) + (\lambda_s/\lambda)^{2(1-\alpha)}} + \frac{\sigma\lambda}{18.8496 \times 10^{10}}, \\
\varepsilon_s &= 78.54[1.0 - 4.579 \times 10^{-3}(t - 25.0) + 1.19 \times 10^{-5}(t - 25)^2] \\
&\quad -2.8 \times 10^{-8}(t - 25)^3], \\
\varepsilon_\infty &= 5.27137 + 0.021647t - 0.00131198t^2, \\
\alpha &= -16.8129/(t + 273) + 0.0609265, \\
\lambda_s &= 0.00033836\exp[2513.98/(t + 273)], \\
\sigma &= 12.5664 \times 10^8. \qquad \text{(A.1)}
\end{aligned}$$

The complex dielectric constant for three temperatures (0, 10 and 20°C) and three frequencies (3, 10 and 35 GHz) are given in Table A.1.

		Frequency (GHz)		
		3	10	35
T (°C)	0	(79.6919,25.1976)	(41.8061,41.2107)	(10.2579,19.7567)
	10	(79.6690,18.2257)	(52.7531,38.5035)	(14.0836,24.6402)
	20	(77.9014,13.2354)	(60.2936,33.0685)	(19.2165,29.0939)

Table A.1: Dielectric Constant for Water

A similar set of equations applies to ice and are given as:

$$\begin{aligned}
\varepsilon_s &= 203.168 + 2.5t + 0.15t^2, \\
\varepsilon_\infty &= 3.168, \\
\alpha &= 0.288 + 0.0052t + 0.00023t^2, \\
\lambda_s &= 0.0009990288 \exp\{13200/[(t+273)1.9869]\}, \\
\sigma &= 1.26 \exp\{-12500/[(t+273)1.9869\}. \qquad \text{(A.2)}
\end{aligned}$$

Shown in Table A.2 are the dielectric constant values for ice for the same range of temperatures and frequencies as Table A.1. It is worthwhile to note that the

		Frequency (GHz)		
		3	10	35
T (°C)	-20	(3.1684,0.0008)	(3.1682,0.0003)	(3.1681,0.0001)
	-10	(3.1685,0.0012)	(3.1682,0.0005)	(3.1681,0.0002)
	0	(3.1698,0.0038)	(3.1688,0.0016)	(3.1683,0.0007)

Table A.2: Dielectric Constant for Ice

complex dielectric constant for ice is considerably smaller than those calculated for water.

Appendix B - List Of Symbols

$\mathbf{A}$	signal amplitude vector
A	complex amplitude
A_e	effective aperture
D	drop diameter
D	parabolic dish diameter
$\mathbf{E}$	electric field vector
E	energy
$\mathbf{H}$	magnetic field vector
$H(z)$	filter frequency response
$I(t,r)$	in-phase component of the complex signal
K_m	complex refractive index of water
N	Refractivity
$\tilde{N}$	noise
$N_{\mathrm{DSD}}(\mathsf{D})$	drop size distribution
N_0	DSD number concentration
P	Pressure
P_{w}	water vapor pressure
P_L	power loss due to attenuation
$\hat{P}$	zeroth moment
P_m	$\lvert V(m)\rvert^2$
P_r	return power
P_t	transmitted power
P_{win}	window function power
$Q(t,r)$	quadrature component of the complex signal
Q_a	absorption efficiency
Q_e	extinction efficiency
Q_s	scattering efficiency
R	rainfall rate
$\hat{R}(mT_s)$	estimated weather autocorrelation
$S(r,\theta,\phi)$	power density
$\hat{S}(v)$	estimated weather power specral density
S_{C}	power spectral density, Capon
$\hat{S}_W$	power spectral density, Welch
$\hat{S}_c(\omega)$	power spectral density, correlogram
$S_i(\theta,\phi)$	incident power density
$\hat{S}_p(\omega)$	power spectral density, periodogram

S_r	return power density
$\mathcal{R}$	individual gas constant
T	temperature
T_s	pulse repetition time
$U(t)$	unit step function
$\|V\|$	complex signal amplitude
$VSWR$	voltage standing wave ratio
$W_s(r)$	range weighting function
Z_e	equivalent reflectivity factor
a	earth's radius, 6361 km
a_e	effective earth radius
a	particle radius
$a(\omega)$	steering vector
c	speed of light
d	interelement array spacing
f	frequency
$f^2(\theta, \phi)$	normalized power gain pattern
f_s	sampling frequency
g	directive gain
g_r	receive antenna directive gain
g_t	transmit gain
h	height
h_k	filter coefficients
k	specific attenuation
k_t	total specific attenuation
l	one-way transmission loss
n	refractive index
$\dot{p()}$	probability distribution function
r	range
r_a	maximum unambiguous range
t	time
v_a	aliasing velocity
$v_\mathrm{a}^\mathrm{SPRT}$	staggert PRT aliasing velocity
v_r	radial velocity
$\bar{v}_r$	mean radial velocity
$\hat{v}_r$	first moment
$w(k)$	window function
Δr	range resolution
Γ	reflection coefficient
Λ	DSD slope parameter
$\alpha(\omega)$	APES amplitude at ω
β	bandwidth
γ	Lagrangian parameter
$\delta_{t,s}$	Kronecker delta function

ϵ	user defined parameter, RCB
ε_r	relative permittivity
ε	absolute permittivity
ε_0	vacuum permittivity
ζ	staggered PRT ratio
η	reflectivity
η_0	wave impedance, 377 Ohms
θ	azimuthal angle
$\theta_{3\text{dB}}$	3-dB beamwidth
θ_{e}	elevation angle
θ_{gl}	grating lobe angular location
κ	index of attenuation
λ	wavelength
μ	DSD distribution shape parameter
ν	electromagnetic wave velocity
ρ	density
σ_a	absorption cross section
σ_{an}	absorption cross section
σ_b	backscatter cross section
σ_e	extinction cross section
σ_s	scattering cross section
σ_{sn}	scattering cross section
σ_v	velocity spectrum width
$\hat{\sigma}_v$	second moment
σ^2	statistical variance
τ	pulse width
$\phi(t)$	frequency modulation function
$\chi(t_r, f_d)$	ambiguity function
ϕ	zenith angle
ψ	transmitter phase
ψ_e	echo signal angular phase
ψ_{s}	scattering phase shift
ψ_{t}	transmitted phase
ω	angular frequency
ω_d	angular Doppler shift

Appendix C - List Of Acronyms and Abbreviations

AC	alternating current
ACF	autocorrelation function
ADC	analog-to-digital
AIR	Atmospheric Imaging Radar
AME	Aerospace and Mechanical Engineering
APES	Amplitude and Phase Estimation
ARRC	Atmospheric Radar Research Center
ATX	Advanced Technology eXtended
AWS	Air Weather Service
BTU	British thermal unit
CAPES	Capon and APES
CFIR	compensation finite impulse response
CIC	cascaded integrator-comb
CLEAN-AP	Clutter Environment Analysis using Adaptive Processing
COHO	coherent oscillator
CSWR	Center for Severe Weather Research
DBF	Digital Beamforming
DC	direct current
DFT	discrete Fourier transform
DOA	direction of arrival
DOC	Department of Commerce
DOD	Department of Defense
DOT	Department of Transportation
DOW	Doppler on Wheels
DSD	drop size distribution
DTFT	discrete Fourier transform
EBT	Entropic Balance Theory
EEC	Enterprise Electronics Corporation
FOV	field of view
FPGA	field programmable gate array
GVWR	gross vehicle weigh rating
IF	intermediate frequency
IQ	in-phase and quadrature
JDOP	Joint Doppler Operational Project
JPOLE	Joint Polarization Experiment

LFM	linear frequency modulation
LNA	low-noise amplifier
MDS	minimum detectable signal
MMSE	mimimum MSE
MSE	mean squared error
MST	Mesosphere-Stratosphere-Troposphere
MU	Middle and Upper
NEXRAD	Next Generation [of] Weather Radars
NLFM	nonlinear frequency modulation
NSSL	National Severe Storms Laboratory
NWRT	National Weather Radar Testbed
NWS	National Weather Service
OU	The University of Oklahoma
PCB	printed circuit board
PDF	probability distribution function
PLO	phase-locked oscillator
PRF	pulse repetition frequency
PRT	pulse repetition time
PSD	power spectral density
PSI	pounds-per-square inch
RAID	redundant array of independent disks
RCB	robust Capon beamforming
RF	radio frequency
RHI	range-height indicator
RHS	right hand side
SMA	sub-miniature version A
SMART-R	Shared Mobile Atmospheric Research and Testing Radar
SNR	signal-to-noise ratio
STALO	stable local oscillator
TEP	Turbulent Eddy Profiler
TNC	threaded Neill-Concelman
TWT	traveling wave tube
UHF	Ultra High Frequency
ULA	uniform linear array
UMass	University of Massachusetts-Amherst
UV	ultraviolet
VHDCI	very-high-density cable interconnect
VHF	Very High Frequency
VORTEX2	Verifications of the Origins of Rotation in Tornadoes Experiment 2
VSWR	voltage standing wave ratio
WSR	Weather Surveillance Radar

WSS	wide-sense stationary

Index